Understanding Hydrogel Formation in Dispersions of Carbon black and Carboxymethylcellulose : Rheological, Electrical and Structural Perspectives

Gauthier Legrand

THÈSE

en vue de l'obtention du grade de Docteur, délivrée par

l'École Normale Supérieure de Lyon

École Doctorale N°52
École Doctorale de Physique et Astrophysique de Lyon (PHAST)

Discipline : Physique

soutenue publiquement le 5 juillet 2024, par :

Gauthier Legrand

Understanding Hydrogel Formation in Dispersions of Carbon Black and Carboxymethylcellulose:
Rheological, Electrical and Structural Perspectives

Étude de la formation des hydrogels dans les dispersions de noir de carbone et de carboxyméthylcellulose :
perspectives rhéologiques, électriques et structurelles

Devant le jury composé de :

GENIX, Anne-Caroline	Maître de conférences - HDR	Université de Montpellier	Rapportrice
VERMANT, Jan	Professeur	ETH, Zürich	Rapporteur
COLIN, Annie	Professeur des Universités	ESPCI, Paris	Examinatrice
CARDINAELS, Ruth	Professeure	KU, Leuven & TU, Eindhoven	Examinatrice
COUSSOT, Philippe	Professeur	Université Gustave Eiffel, Paris	Examinateur
MANNEVILLE, Sébastien	Professeur des Universités	LPENSL, Lyon	Examinateur
DIVOUX, Thibaut	Chargé de Recherche - HDR	LPENSL, Lyon	Directeur de thèse

ABSTRACT

Dispersions based on colloids and polymers enable the design of numerous materials, particularly for energy storage. This thesis concerns aqueous dispersions of hydrophobic soot particles, carbon black (CB), using a sodium salt of carboxymethylcellulose (CMC). CMC is a charged, semi-flexible, water-soluble polymer with hydrophobic regions along its chain, forming physical bonds with the CB particles.

We show that it is possible to form CB-CMC hydrogels, i.e., viscoelastic solids over a wide range of CB and CMC concentrations. These hydrogels exhibit two radically different types of behavior on either side of a critical mass ratio between CMC and CB. Below this critical ratio, CB colloids form a percolated network stabilized by CMC, whereas, above this ratio, CB colloids act as physical cross-linkers in the CMC matrix. We report here a detailed picture of these two types of structures through linear and non-linear rheological measurements, coupled with dielectric and structural (X-ray scattering) measurements.

Finally, to elucidate the singular role of CMC within CB-CMC hydrogels, we studied a complementary system consisting of acidified suspensions of CMC that form a gel due to hydrophobic interactions. These studies make use of two complementary techniques, relaxometry and neutron scattering, to shed new light on the role of the polymer within these composite gels.

RÉSUMÉ

Les dispersions à base de colloïdes et de polymères permettent la conception de nombreux matériaux notamment pour le stockage d'énergie. Cette thèse concerne les dispersions aqueuses de particules de suie hydrophobes, du noir de carbone (CB), à l'aide d'un sel de sodium de carboxyméthylcellulose (CMC). La CMC est un polymère chargé, semi-flexible et hydrosoluble qui présente des régions hydrophobes le long de sa chaîne et forme ainsi des liaisons physiques avec les particules de CB.

Nous montrons qu'il est possible de former des hydrogels de CB-CMC, c'est-à-dire des solides viscoélastiques sur une large gamme de concentrations en CB et en CMC. Ces hydrogels présentent deux types de comportements radicalement différents de part et d'autre d'un ratio massique critique entre CMC et CB. En-deçà de ce ratio critique, les colloïdes de CB forment un réseau percolé stabilisé par la CMC, alors qu'au-delà de ce ratio, les colloïdes de CB servent de réticulants physiques dans la matrice de CMC. Nous rapportons ici une image détaillée de ces deux types de structures par le biais de mesures rhéologiques linéaires et non-linéaires, couplées à des mesures diélectriques et structurales (diffusion de rayons X).

Enfin, pour élucider le rôle singulier de la CMC dans les hydrogels CB-CMC, nous avons étudié un système complémentaire constitué de suspensions acidifiées de CMC qui gélifient du fait d'interactions hydrophobes. Ces études mettent à profit deux techniques complémentaires, la relaxométrie et la diffusion de neutron, qui offrent un éclairage original sur le rôle du polymère au sein de ces gels composites

Contents

CHAPTER

1

INTRODUCTION

This thesis focuses on examining water-based dispersions of Carbon Black particles stabilized by Carboxymethylcellulose. We use complementary techniques from different fields of physics and chemistry to grasp the main features of this system. In the introduction chapter of this manuscript, we aim to contextualize the global framework in which this thesis fits. We first present a brief overview of the soft matter field, with a focus on complex fluids. We then offer a more comprehensive discussion regarding the general scope in which water-based Carbon Black dispersions may be included.

A An interdisciplinary approach

A.1 Soft Matter

Soft matter is an interdisciplinary field that explores materials whose properties lie between those of conventional solids and liquids [1]. These *viscoelastic* materials are composed of larger molecules, such as polymers, colloids, and biomolecules. Soft matter encompasses a wide range of phenomena, including the self-assembly of molecules into ordered structures, the flow and deformation of materials under mechanical stimuli, and interfacial interactions. Temperature and entropy appear to be key parameters that often drive the behavior of soft matter systems. Understanding soft matter is crucial for numerous applications across various industries, including pharmaceuticals, cosmetics, food science, and materials engineering, with implications ranging from the design of new materials with tailored properties to the development of advanced drug delivery systems and functional biomaterials [2–4].

Soft matter research is fed by principles from physics, chemistry, materials science, and biology. It is, therefore, fundamentally interdisciplinary and probes orders of magnitudes in time and length scales [5]. Soft matter implies a wide range of experimental, theoretical, and computational complementary techniques to build a consistent understanding of the systems. For instance, rheology is a subfield of soft matter that aims to describe the flow of complex systems typically made of nano- or micrometric entities suspended in a solvent and structured over a mesoscopic scale.

A.2 Rheology

Rheology is a sub-field of soft matter, which aims at describing the flow of complex systems [6]. Prior to tackling such complex systems, we shall first consider the simplest examples encountered in rheology. Ideal solids and ideal liquids are the building blocks of modeling in rheology as their mechanical response is straightforward and fully described by one single parameter. Ideal solids are determined by their elastic constant, which informs on the difficulty to shear a material: at constant force, a material with twice elastic constant stretches twice less. Ideal liquids are determined by their viscosity, which informs on the difficulty of making the material flow: at constant force, a material with twice viscosity flows half as fast. Rheology accounts for both solid-like behavior (elasticity) and liquid-like behavior (viscosity) within a single framework. This *dual behavior* is particularly relevant for substances exhibiting viscoelastic properties, a key concept in complex fluids.

B Building blocks of complex fluids

It is well established that materials are almost never purely solid or liquid. They usually lie in the spectrum between these two extreme cases, they are called “complex fluids" or “soft materials" as they exhibit both solid-like and liquid-like behaviors depending on what the material undergoes. In practice, it may actually mean a lot of things, from the speed applied (e.g., cornstarch dispersions are solid-like at fast deformation), the system age (e.g., cement pastes stiffen with time) to the history of the sample (e.g., shape-memory alloys recover their initial shape after heating). Our everyday life is full of such complex fluids: toothpaste keeps its shape on the toothbrush like a solid but can be easily spread when a sufficient force is applied; rocks in mountains display a brittle failure like solids and they flow over centuries due to their own

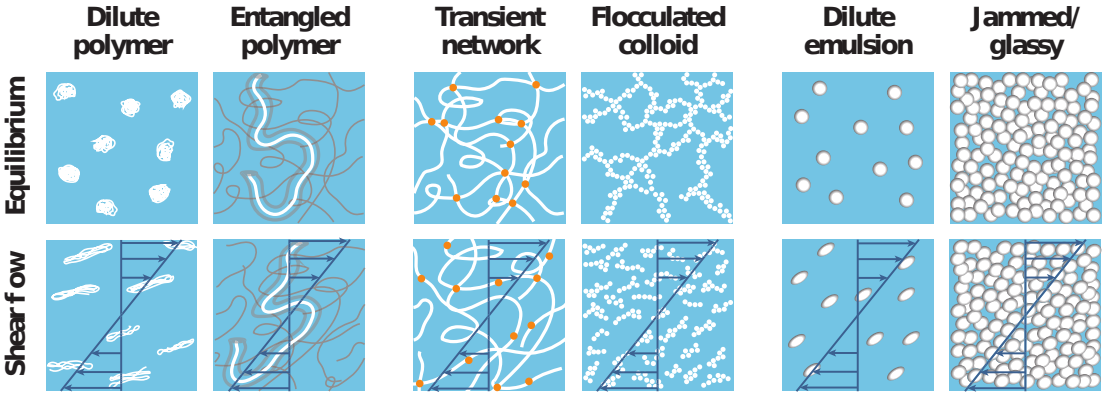

Figure 1.1: Main building blocks of complex fluids and their microstructure. Six major examples encountered in rheology involving polymers, particles, and droplets. Their microstructures are depicted at rest and under flow to emphasize their impact on the rheological properties of complex fluids. Extracted from [7].

weight. These mechanical properties are either a problem that needs to be addressed, e.g., clogging in pipes or hydrology [8, 9]; or some desired properties to ease its use, e.g., 3D printing or food processing [10, 11]. For some applications, both aspects are important, as for flow batteries, which will be described below.

In this viscoelastic framework, the terminology between solid and liquid becomes challenging. A liquid is a material that flows, whereas a solid is a material that keeps its shape indefinitely. As time and length scales matter for viscoelastic materials to differentiate between one behavior or the other, we use meaningful scales depending on the context. In our everyday life, for instance, we arbitrarily consider a viscoelastic material to be a liquid if it flows over a few centimeters over a few minutes. Note, however, that following this definition, some extremely viscous liquids may be mistaken as solids. For instance, in the tar Pitch experiment, bitumen flows with a rate of a drop every decade [12]. Still, this definition is relevant to the practical use of complex fluids, it mostly differentiates materials that can or cannot be poured.

These properties usually arise from the organization of the fluid's smallest entities. In rheology, we aim to bridge the gap between the microstructure and the macroscopic behavior of the fluid in order to fully comprehend and efficiently describe it. Similarities at the macroscopic scale may indeed reveal profound similarities at the microscopic scale. Within this scope, a precise knowledge of the properties at the microscopic scale is thus required. In the following, we shall review the main elementary elements, or building blocks, encountered in soft matter and how they affect the rheological properties at the macroscopic scale, as illustrated in Fig. 1.1.

B.1 Polymers

Polymers are very long molecules with a repeating scheme, which are ubiquitously found in our everyday life in a broad range of systems [15]. They can be found in nature, e.g., the DNA in our cells and cellulose in plant fibers, or synthesized for innovative materials, e.g., plastics or rubber. One should, however, keep in mind that some of them are not harmless and they raise some ecological as well as health concerns. Some synthesized polymers even appear to be ecologically threatening, e.g., PFAS coating agents [16]. Modern rheology tends to include ecological concerns in polymer science, for instance, with research around bio-inspired plastics [17].

One usually considers a polymer as a chain of atoms that can deform. The shape of the polymer in solution depends mainly on its interaction with the solvent, the interactions within the polymer itself, the temperature, its concentration, and its geometry [18]. Most of the time, individual polymers in solution are organized as coils to maximize their entropy. These coils may stretch and unstretch under flow leading to viscoelastic behaviors. Due to these coils, the viscosity of the polymer solution increases as power-laws of the concentration. Such an increase is even more dramatic with large power-laws exponent when polymers are highly concentrated so that they start to feel each other up to a point where the polymer chains are entangled and eventually compressed [18].

The coiling of the polymers and the interactions between the coils are sensitive to the flow undergone by the solution. For sufficiently fast flow, the coils unstretch and align with it, hence the viscosity is lowered. This behavior is known as “shear-thinning". This scenario is very generic, and most polymer solutions exhibit this feature. More generally, the polymer structure is perturbed by the flow, and the flow evolves accordingly (Fig. 1.1). The polymer topology is also an important parameter, as the dynamics at the molecular level are very different for linear, branched, or star polymers. Here, we will only focus on linear polymers. When the interactions within the polymers are strong enough, the polymer solution dramatically changes in nature: it may gelify. A polymer gel is observed when the polymer chains are crosslinked, which forms a percolated network throughout the whole sample. It happens at a large enough concentration and gives the polymeric system an elastic-like behavior. Any of the interactions described below may be at stake for polymers, hence a wide variety of properties.

Finally, polymers in material science can be used in a solution or without solvent in the case of polymer melts. The overall behavior is similar as each system shares the same ideas where polymer interactions and entanglements are the main mechanisms at stake [18].

B.2 Colloidal particles

A colloidal particle corresponds to a particle typically up to the micrometer scale and sensitive to thermal agitation $k_B T$, hence their importance in soft matter. Colloidal particles can be hard or soft particles with various shapes. When dispersed in a solvent, colloids interact with each other through van der Waals forces, which tend to aggregate them [22]. Short-range repulsion is necessary to prevent total aggregation;

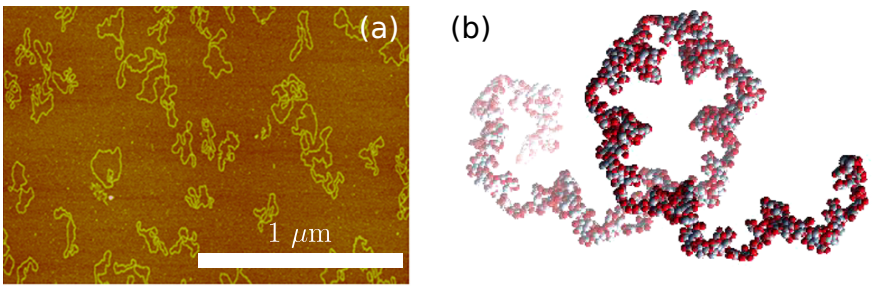

Figure 1.2: Visualization of a polymer in solution. (a) Atomic Force Microscopy image of DNA. Adapted from [13]. (b) Numerical simulation of a 50-monomers long Carboxymethylcellulose, oxygen atoms are represented in red and carbon ones in black (hydrogen is not shown). Adapted from [14].

often, steric or electrostatic repulsion with ions at the colloidal surface fulfill this role. If both attractive and repulsive interactions are present, aggregation is slow and weak enough to be observed experimentally before demixing with the solvent occurs. Colloids are then linked to their neighbors via physical contacts that can easily break and reform.

These colloidal suspensions are not in thermodynamic equilibrium. Due to their small size, colloids undergo Brownian motion, which drives reorganizations in systems composed of these particles; these reorganizations tend to consolidate the gel microstructure in the absence of macroscopic flow — this is referred to as *physical aging* [22]. Moreover, under flow, the mechanical properties of such suspensions evolve over time in a reversible manner [23–25].

At low concentrations or small interaction strength, the particles are well dispersed in bulk, and it corresponds to a homogeneous dispersion that has a liquid-like behavior (Fig. 1.3). It concerns different systems from coffee poured in a cup to mud flowing during a flood. In this framework, the particles mainly interact via repulsive contact forces; the presence of these particles increases the overall viscosity of the dispersion via hydrodynamic interactions mediated by the solvent [26]. The most famous example of such a system is the cornstarch aqueous dispersion [27]. This system behaves like a Newtonian fluid at rest, as water can flow around the micrometric cornstarch particles whose organization remains random. At higher flow rate, the particles tend to organize and align along the flow direction, which lowers the viscosity. This is similar to the shear-thinning behavior observed in polymer solutions. However, due to their hardness, particles start to jam under increasing speed, which inhibits the flow. Frictional contact between the particles eventually leads to a higher rate of energy dissipation and an abrupt increase in the viscosity [28]. Such behavior is known as “shear-thickening" [27].

When the concentration in colloids is sufficient, or the interactions between col-

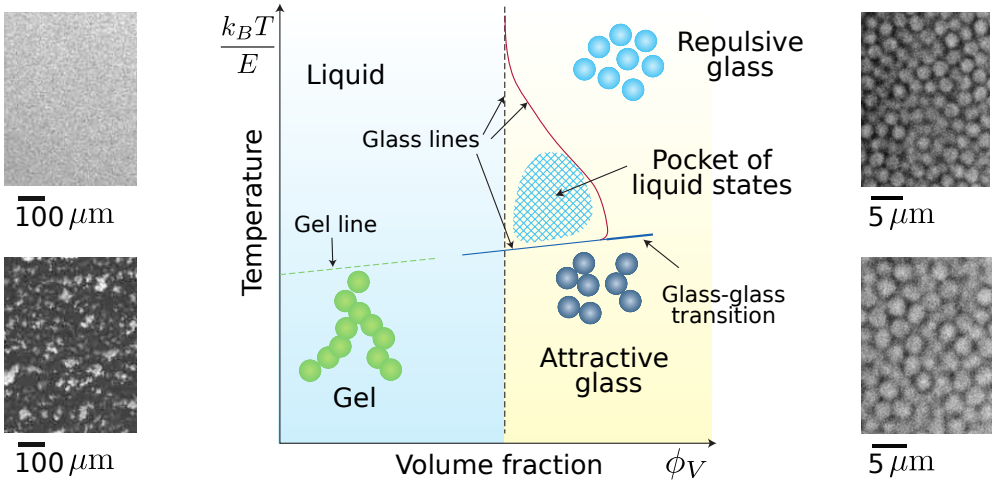

Figure 1.3: Colloidal particles in solution phase diagram. When in solution, colloidal particles can lead to a liquid dispersion, a gel, or glasses depending on the interaction energy E between the colloids (normalized by thermal energy k_BT) and their volume fraction ϕ_V in the solvent. Adapted from [19]. The pictures on the left correspond to optical micrographs of Carbon Black dispersions either in the liquid (top) or in the gel (bottom) phase, adapted from [20]. The pictures on the right correspond to Raman Spectroscopy microscopy of PMMA either in the repulsive glass (top) or attractive glass (bottom) phase. Attraction arises from depletion with the addition of polystyrene, adapted from [21].

loids are attractive enough, particles tend to organize over a longer range (Fig. 1.3). It results in the presence of a flow threshold together with elastic properties at rest, which is referred to as a *yield stress fluid* [29]. At low concentrations, interactions are mainly electrostatic (surface charge of colloids) and hydrodynamic (lubrication of contacts). The resulting structure is called a gel, which is defined as a system that forms a network occupying the entire volume and where particles are locally arrested (do not move freely in the solvent) [19, 30, 31]. When the solvent used is water, the gel is called a *hydrogel*. The structuring mechanism of the particles into a gel is called *percolation* [32], which leads to a heterogeneous structure [33]. Such gels are widely exploited in the food and cosmetics industries because high yield stresses can be achieved with low enough concentrations to have no other effect on the product [22].

Two extreme scenarios are observed in the percolation outcome, depending on the strength of the interactions between the particles [34]. For strong interactions, the system undergoes a phase separation with an arrested network of thick strands of particles within the solvent [Fig. 1.4(a)]. For weak interactions (a few k_BT), the branches are less thick, and there is no phase separation with a fractal network occupying the whole medium. In the latter scenario, the network is transient, and reorganization occurs leading to time-dependent mechanical properties, i.e., physical aging [Fig. 1.4(b)].

When attractive interactions between colloidal particles are too weak, a network cannot be formed a low volume fraction. However, upon increasing the concentration of the dispersion, say more than 58% vol. [19], steric interactions eventually lead to a glass transition yielding a material with solid-like properties. The latter is called a “repulsive glass", as sketched in Fig. 1.3, in which the particles are densely packed, and a structural arrest is observed. Particles are trapped in cages made of their neighbors, from which they cannot escape. If now the attractive interactions were to be larger, the same glassy system would be observed but more spatially heterogeneous, this is called an “attractive glass". Such glassy states are out of equilibrium after an infinite waiting time, and due to thermal activation, the system may eventually reach a crystalline steady state over a long time [36, 37].

The gel-to-glass transition appears to be smooth, and systems in the vicinity of the

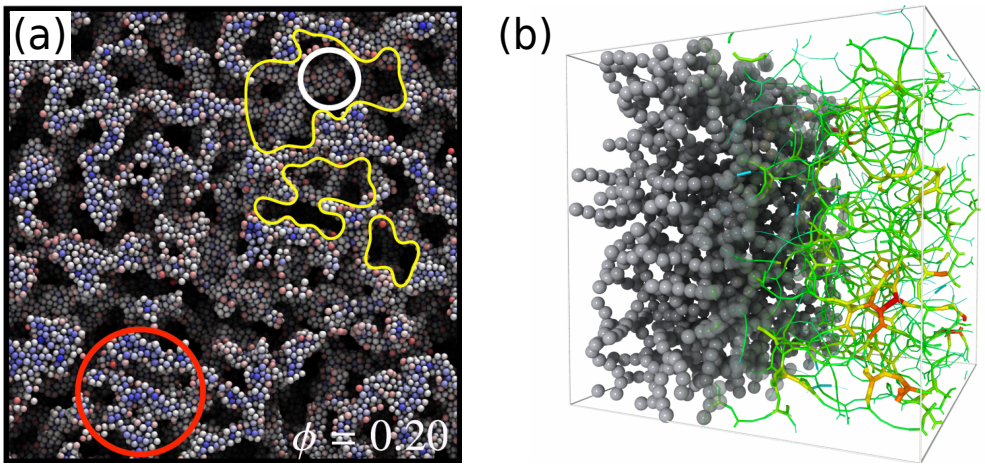

Figure 1.4: Two types of colloidal gels obtained from numerical simulations. (a) In the high interaction regime with phase separation. The emphasized regions highlight the two phases. Adapted from [34]. (b) In the weak interaction regime with the formation of a homogeneous phase. The links correspond to the connectivity of the network. Credits to M. Bouzid, adapted from [35].

transition are actually difficult to sort in one or the other category [38]. They may be referred to as “dense gels" as they are supposedly gels but show lots of similarities with glasses [39]. Especially with the addition of polymers, a colloidal dispersion may be classified as glass even at a low concentration [40]. The main idea behind this glassy description of a gel is well depicted by Keshavarz *et al.* [41], who looked at the aging of weakly attractive colloidal hydrogels and established that, at the particle scale, the network is so dense and connected that it behaves like a glass. They also showed that the glassy to gel-like behavior of their systems continuously evolved as the length scales probed increased. We applied this glassy interpretation of colloidal gels in this manuscript.

Finally, near the sol-gel transition, both polymer and colloidal gels exhibit a very specific behavior. They are known as “critical gels"; their zero shear viscosity diverges and yet their elasticity vanishes at zero frequency [42, 43]. Moreover, at this critical point, the linear viscoelastic properties, which display a broad relaxation spectrum, follow the so-called Winter & Chambon criterion, that we shall encounter later on in this manuscript. Critical gels can be obtained crossing the sol-gel frontier as the system kinetically evolves (i.e., aging) as historically described [42, 43], but also by other means, for instance, by changing the concentration, the pH, or the temperature [44–46]. These critical gels always show the same microstructural feature: they are self-similar over a significant range of length scales [47].

B.3 Other building blocks

Although very common, colloidal particles and polymers are not the only components of complex fluids. A Newtonian fluid such as water can become a complex fluid by the addition of droplets or bubbles, e.g., as in mayonnaise or whipped cream. The former are called emulsions and the latter foams [48, 49]. They are similar to the colloidal systems as the droplets or bubbles can be seen as particles in interaction. Emulsions or foams are even more complex systems because droplets and bubbles are highly deformable objects, and their number is not constant as they are able to merge or split. Moreover, to reach high enough concentrations of droplets or bubbles, they must be stabilized, which is done by adding surfactants to the system that strongly impact their deformability and frictional properties [50].

B.4 From the building blocks to the macroscopic behavior

a Interactions between the building blocks

Interaction energy between particles dictates how they interact at the microscopic level. It is, therefore, crucial to have orders of magnitude in mind, as shown in Fig. 1.5. In the cases of colloidal particles, van der Waals interactions are the most encountered ones. Their typical energy scale is around a few times the thermal energy k_BT (up to 30 k_BT for carbon black particles dispersed in mineral oil [52]). van der Waals interactions stem from instantaneous variations of the electron distributions within the atoms of the particle, which creates multi-pole interactions. They are long-ranged and depend on the dielectric constant of the medium, which can be tuned by the addition of salt for instance.

A stronger interaction is Hydrogen binding, which has the same physical origin but is considered separately from hydroxyl groups OH as the interaction is enhanced

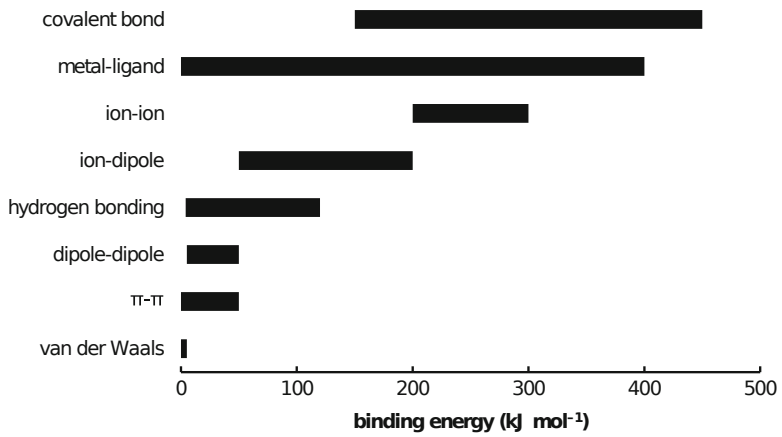

Figure 1.5: Typical interaction energies encountered in soft matter. This should be compared to $k_BT \simeq 2.5$ kJ.mol^{-1} at room temperature. Extracted from [51].

by the difference of electronegativity between the Hydrogen and Oxygen atoms [51, 53]. Its typical energy can reach up to 100 k_BT.

In the presence of charged building blocks, e.g., poly-electrolytes, the Coulomb interaction prevails with a typical energy scale around $200 - 300 k_BT$. It is a short-ranged interaction[1] that tends to gather opposed charges. This type of interaction is highly sensitive to the ionic environment.

Hydrophobic interactions are usually considered for an aqueous solution of spatially heterogeneous polymers that exhibit hydrophilic and hydrophobic regions or patches along their chain[2]. Hydrophobic regions of the polymer tend to minimize their contact with the water, which results in an attractive interaction. Hydrophobic interactions may occur between different species that are at least partially hydrophobic. The orders of magnitude associated are not quite known, and their very existence is even debated [55].

Finally, steric interactions are very short-ranged interactions that prohibit overlapping. This repulsion always dominates at a very short range, but it highly depends on the softness and deformability of the building block considered. For colloidal particles, it can be tuned by the adsorption of polymers onto the surface of solid particles.

b Superposition Principle

Interactions dictate the behavior at the microscale, and the interactions can be modified by several means. For instance concentration plays a major role in the specific behavior of the system, first because of topological concerns but it may interfere with the interactions as well. Actually, any change in any control parameter may have an impact on the dynamics at the macroscale so that it is usually a complex task to decipher the different origins of a macroscopic feature. In that sense, the rescaling principle is a powerful tool that is widely used in rheology, e.g., to evidence at the macroscale minutes differences in the building blocks at the microscale [50]. This manuscript makes no exception and will rely on the use of rescaling to better understand the viscoelastic response of viscoelastic composites.

[1] The Coulomb interaction decays exponentially over the so-called *Debye length*, which depends on the characteristics of the system but is typically around 1 nm [54].

[2] Otherwise it would solely be a polymer in a bad solvent.

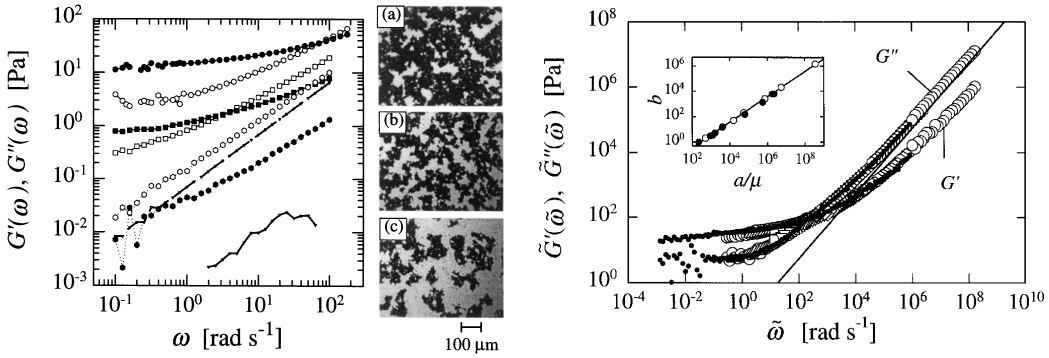

Figure 1.6: Link between microscopic and macroscopic scales. Viscoelastic spectra for Carbon Black suspensions in oil. The spectra and the microstructure continuously evolve with the dispersion concentration above the percolation threshold, which is captured by the rescaled master curve on the right. Adapted from [56].

Far from phase transitions, when a control parameter is changed, the macroscopic properties continuously evolve accordingly. For instance, let us have a look at the mechanical properties (viscoelastic moduli) frequency dependence of an attractive carbon black dispersion in oil and vary its concentration as shown in Fig. 1.6. For each concentration, the data can be rescaled and collapsed onto one single master curve [56]. If the obtained master curve is physically meaningful, it means the rescaling has a profound origin. This is called a "*superposition principle*". This example is called a time-concentration superposition principle as the frequency scale is shifted due to the change of concentration. This translates into an equivalence between a change in the composition and the overall behavior, suggesting some degree of self-similarity in the microstructure of the system.

This rescaling principle is, in fact, way more general and can be applied for any change in the system to describe the impact of the temperature onto the viscoelasticity, e.g., time-temperature superposition principle in polymers [18]; the impact of aging onto the microstructure, e.g., time-connectivity superposition principle in aluminosilicate or ludox colloidal hydrogels [41]; the impact of the composition onto the aging, e.g., salt concentration-time superposition in cellulose nanocrystal hydrogels [57, 58]. Such principle is also used to support universality in *a priori* different mechanisms, e.g., aggregation scenario in colloidal gels [59]. Master curves obtained from such superposition principle are insightful and have appeared extremely often in the field of rheology since the 90s, as shown in Fig. 1.7.

The relevance (or not) of such a superposition principle itself is already extremely insightful. When it applies, the master curve obtained enables us to understand better, on an extended range, the behavior of the rescaled property. For instance, in the work of Trappe *et al.* cited above [56] and reported in Fig. 1.6, the viscoelastic moduli *and* the frequency are both shifted according to the colloid content. The two independent shift factors have a linear relationship, which means that the solid-like response arises from the colloidal network and the liquid-like response from the solvent. This linear relationship has a profound meaning as it comes from the power-law dependence at high frequency of the moduli, which has an exponent of 1 in this example. Costanzo *et al.* [60] studied dispersions of gluten proteins in a water-ethanol solvent at various ratios. The same rescaling is observed, and the moduli shift factor scales as a power-law of the frequency shift factor with an exponent of 0.84, which appears to be the same exponent as in the moduli power-law scaling with the frequency. When

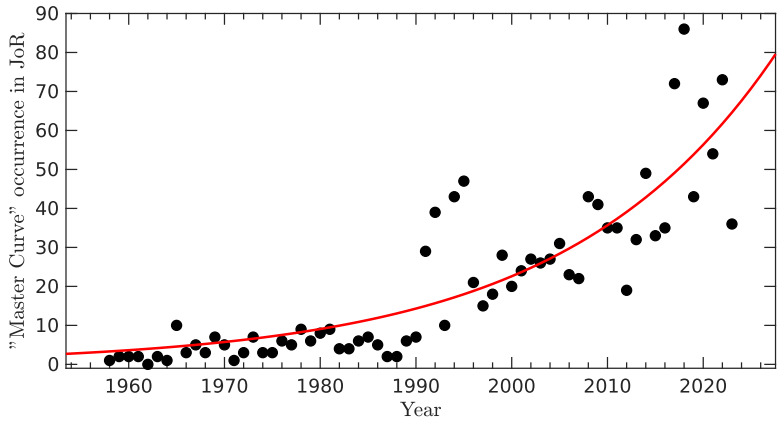

Figure 1.7: Number of articles published in Journal of Rheology where "Master Curve" occurs, as a function of the publication year from 1958 to 2023 (no occurrence was found before). The data approximately follow an exponential increase with a timescale of 22 years as depicted by the red line. Data extracted from https://pubs.aip.org/sor/jor on May, 13th 2024.

both exponents do match, it suggests the gels are critical gels, whose microstructure is self-similar at different scales [61, 62]. This correspondence of the exponents is, however, far from a general result, and it should be checked whenever a superposition principle is conducted. Moreover, the dependence of the shift factors themselves according to the change of the control parameter is interesting, for example the dependence of the shift factor as a function of the temperature gives information on the interaction energy at stake in the system [18]. Finally, such superposition principles can be used to extend the data measured to an experimentally inaccessible range, e.g., the time-temperature superposition principle is applied for polymer melts to measure the viscoelastic modulus over decades of frequencies which would be experimentally challenging otherwise [18].

C Polymer-nanoparticle composites

C.1 A complex, complex system

The tuning possibilities are almost endless when mixing polymers and nanoparticles, and this is no surprise such ternary systems are increasingly studied [63, 64]. The motivation is also to model systems that are closer to systems encountered in real applications, which contain usually more than one compound. Mixing polymers with a colloidal suspension or adding nanoparticles to a polymer melt will substantially alter the way the particles or the polymers interact [65]. The new interactions between the polymers and the nanoparticles depend on many parameters as well, such as the size ratio for instance [66]. It leads to rich phase diagrams as depicted in Figure 1.8.

For polymer solutions, if the polymers do not interact with the particles and are small compared to the particles, it leads to a new effective interaction called *depletion*. It corresponds to the entropy loss when two particles are so close that the polymers cannot access the region in between the particles anymore, and it goes up to a few k_BT [67]. This has been described theoretically in the early 2000s [68]. Another theoretical framework is given for simple cases of polymers that may be adsorbed onto the surface of the particles, polymer bridges between the particles may arise [69, 70]. Even for these simple cases, knowledge of the interactions at the single polymer-particle level

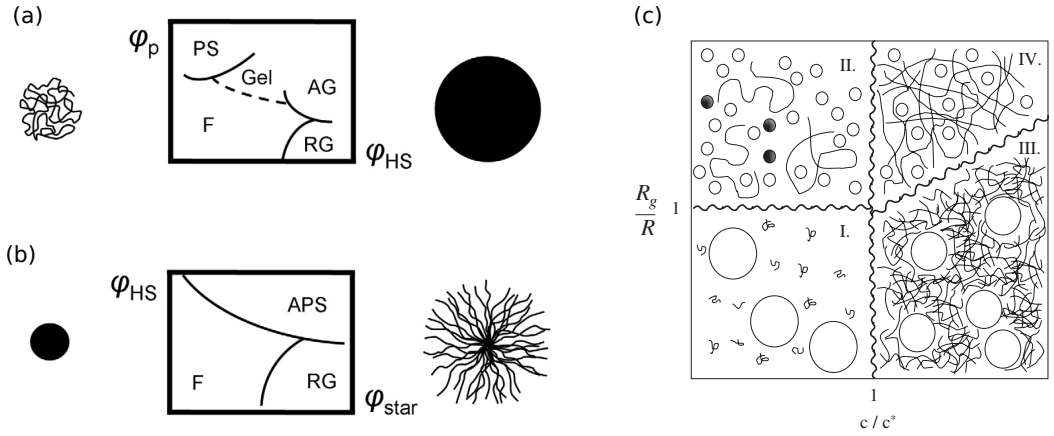

Figure 1.8: Phase diagram of Polymer-nanoparticle dispersions (a) Volume fraction phase diagram of hard-spheres and linear polymer mixtures. (b) Volume fraction phase diagram of hard-spheres and star polymer mixtures. Multiple phases are shown: gel, fluid (F), phase separation (PS), repulsive glass (RG), attractive glass (AG), and arrested phase separation (APS). (c) Polymer-to-particle size ratio vs. polymer concentration phase diagram of hard-sphere and linear polymer mixtures. (a-b) are adapted from [79] and (c) is extracted from [68]. The polymers are considered non-absorbing in each case.

is not sufficient [71]. Furthermore, we shall emphasize the case of systems featuring *associative* polymers. These associative polymers exhibit highly attractive regions distributed along their chain [72–74]. The mixture of nanoparticles and such polymers behave very differently as the colloidal particles may interact a lot with the associating parts of the polymer. In some cases, it leads to changes in the mechanical and structural properties upon shear. For instance, the so-called “shake-gels" dramatically harden upon shear as the attractive regions of the polymers are exposed and bridge the colloidal particles and eventually form an elastic network [75, 76]. This latter case is particularly relevant for this manuscript. We shall finally well mention the case of polymer melts in which nanoparticles can be added as fillers to reinforce the structure [77]. Similar difficulties arise in the prediction of the mechanical properties according to the different interactions between the polymers and the particles [78].

All of the nanocomposite materials cited above have plenty of applications, and they raise major fundamental questions, such as the spatial distribution of the nanoparticles and their impact on the mechanical [80]. The physical origin of the gelation is also a debated question for such systems: are these phenomena driven by entropy or enthalpy [81]? Despite the rich literature on nanocomposites, no systematic investigation of the various existing fillers has been done [81]. It, therefore, has been a thriving research field for the past decades in seeking experimental data to nourish the theoretical and numerical model [82].

C.2 An example of a real system: flow batteries

The present thesis was initially motivated by redox flow batteries, namely the fundamental understanding of the fluid used in such batteries, whose underlying physics is presented here briefly.

Usual redox batteries rely on a chemical reaction where two species are either oxidized or reduced, typically Lithium-based [84]. The chemical reactions occur at the electrodes of two separate bulks. To close the electrical circuit, a membrane is placed

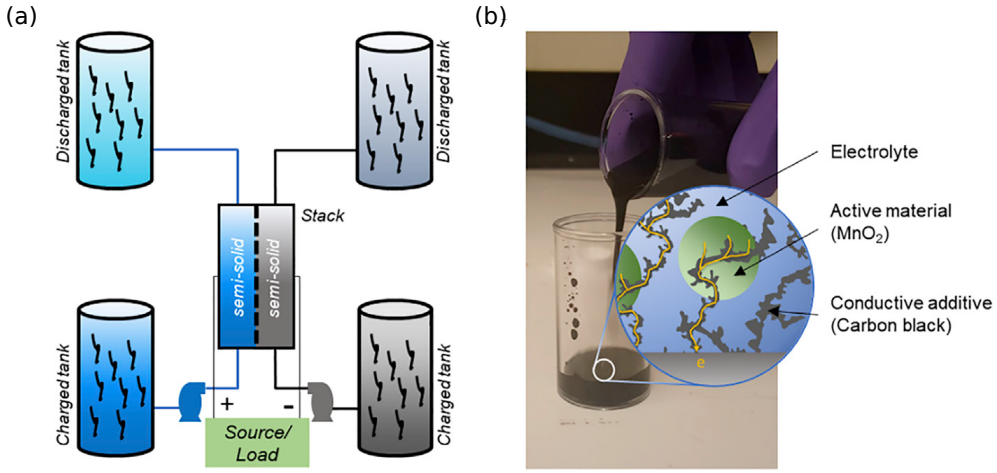

Figure 1.9: Sketch of a flow-battery (a) The tanks of the chemical energy, whose dimensions set the capacity of the battery, are separated from the electrodes, whose dimensions set the power of the battery. (b) Microstructure of a liquid electrode using carbon black as a conductive additive. Adapted from [83].

between the two bulks, which lets Li^+ ions circulate. The chemical reactions occur at the electrode, and one key parameter to increase the power of the battery is the specific area of the electrode: a bigger surface leads to a higher chemical reaction rate, which increases the current delivered. The capacity is set by the amount of chemical reactants, which is ultimately set by the size of the battery. The size of the system sets thus both the power and the capacity of the battery. Flow batteries are built in a slightly different way: the tank and the electrodes are spatially apart. Power and capacity are, therefore, decoupled.

However, the chemical energy stored in the tank must flow to the electrodes where it turns into electrical energy. Both the rheological and electrical properties of the fluids must, therefore, be optimized in order to make the flow battery the most efficient. Using a carbon black dispersion appears to be remarkably clever in that scope. Carbon black particles are electrically conductive and when they form a percolated network touching the electrodes, the whole network becomes an electrode. It significantly increases the specific area of the electrodes, hence the power delivered by the battery. Environmental and cost concerns incited the research around the aqueous dispersion of carbon black particles for this application. Parant *et al.* studied the rheological and electrical properties of different CB aqueous suspensions with the addition of arabic gum and alginate as stabilizers [85]. N'Gouamba *et al.* characterized CB dispersion stabilized by arabic gum and a large concentration of salt ($CaCl_2$) [86]. Dennison *et al.* concentrated a lot the system with CB to disperse stabilize the supension in water, with the addition of a high concentration of salt [87]. Meslam *et al.* and Li *et al.* used surfactants to stabilize the CB dispersion [88, 89]. Porada *et al.* and Hatzell *et al.* looked into activated carbon, which is similar to CB with the difference that it is treated and can be dispersed in water [90, 91]. All of the studies presented above led to yield stress fluids with conductivities around 1 to 100 $mS.cm^{-1}$. In this manuscript we manage as well to stabilize CB particles in water, using only one polymer, yielding promising properties for applications in flow batteries.

D Scope of this manuscript

This project particularly focuses on water-based nanocomposite using Carbon Black (CB) as a conductive nanoparticle and a Carboxymethylcellulose (CMC) as a polymer. CMC is a widely used bio-sourced polymer that receives a flourishing interest in many fields (see Section. 2.B in Chapter 2). Our goal is to understand such an aqueous CB suspension from a more fundamental point of view. Therefore, we did not use any other stabilizer than CMC. This polyelectrolyte has both hydrophobic and hydrophilic regions along its chain, the former stick to the CB and the latter prevent the aggregation of the CB. Compared to the previous studies on water-based CB dispersions reviewed here, the CMC is an *associative* polymer that may gelify on its own.

The goal is to understand how both CB and its dispersing agent, the CMC, interact and organize to form viscoelastic materials with highly variable properties, ranging from non-Newtonian liquids to brittle pastes. In Chapter 3, we explore the phase diagram built on the CB content and CMC concentration with a focus on the hydrogel region. We perform shear rheology, structural, and dielectric characterization to elucidate the link between the microstructure and the viscoelastic properties of the system. In Chapter 4, we look at the impact of large deformations under oscillatory shear and the flow behavior of the CB-CMC hydrogels through coupled rheo-structural and rheo-dielectric experiments. Finally, in Chapter 4, we focus on CMC hydrogels that can be obtained upon acidification, and in the absence of CB particles, in order to elucidate the role of the CMC in CB-CMC hydrogels through a rheological study of both the sol and the gel phases. The sol-gel transition in acidified CMC solutions is examined through rheological and structural experiments, and also by an innovative use of low-field NMR that reveals an original signature of the sol-gel transition.

CHAPTER

2

MATERIALS AND METHODS

This chapter presents the different methods and experimental protocols used in this manuscript to characterize the microstructure and mechanical properties of CB-CMC and CMC samples. The data analysis and their modeling is discussed as well.

A Carbon Black

A.1 Overview

Carbon black (CB) particles are colloidal soot particles produced from the incomplete combustion of fossil fuels. These textured particles of typical size 0.5 μm are made of permanently fused "primary" nodules of diameter 20-40 nm [93], see Fig. 2.1(a). Cheap and industrially produced at large scale, they are broadly employed for their mechanical strength, high surface area, and their electrical conductive properties, even at low volume fractions. Applications include pigments for ink [94, 95], reinforcing fillers in tires and other rubber products [96, 97], electrically conductive admixture in cement [98], conductive materials for supercapacitors [99], biosensors [100–102],

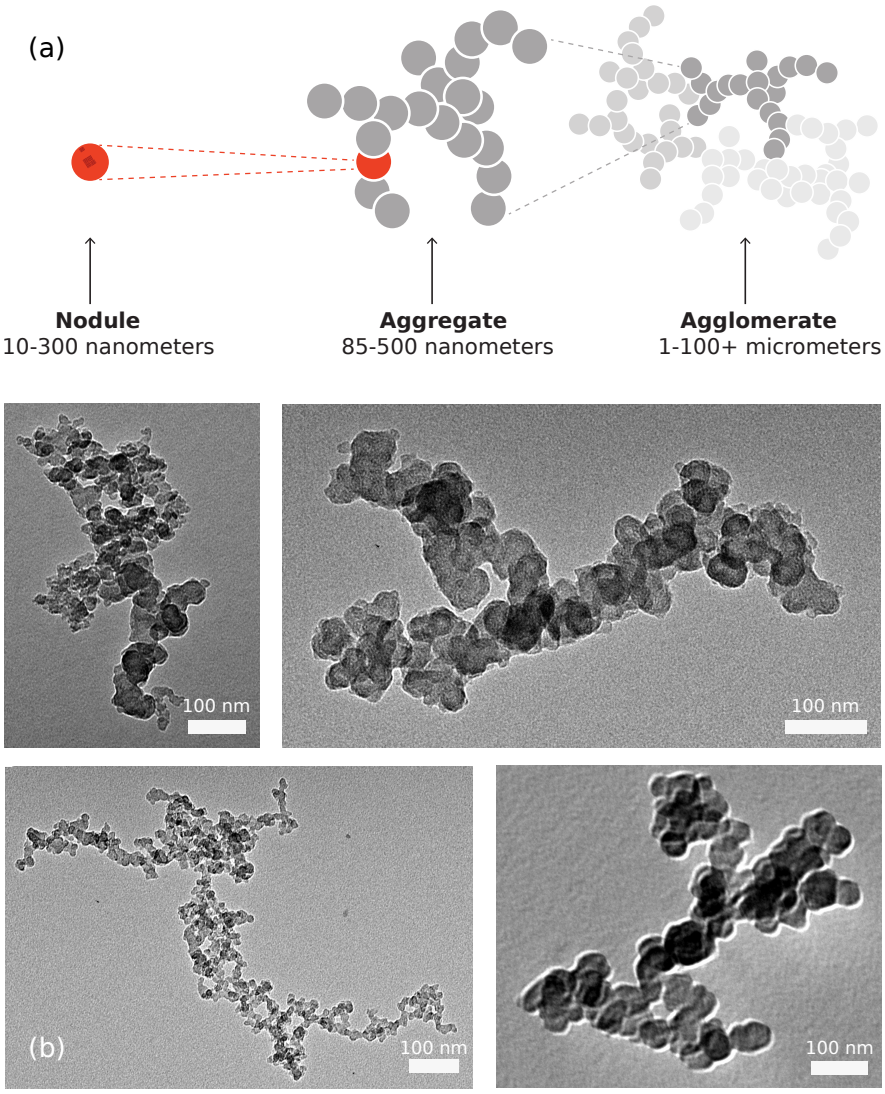

Figure 2.1: Carbon Black structure. (a) Different length scales with Carbon Black nanoparticles. The spheroidal nodule (or primary particle) is the fundamental building block of CB. Nodules are covalently fused into tortuous-shaped aggregates of colloidal size, which may reversibly agglomerate. Extracted from [92]. (b) Transmission Electronic Microscopy (TEM) image of representative aggregates of the CB used in this thesis (Vulcan XC72R). The white bar corresponds to the 100 nm scale.

and electrodes for semi-solid flow batteries [103–107]. Being much cheaper than carbon nanotubes or graphene, CB particles appear promising for applications in energy storage [108], including liquid electrodes for which the ultimate goal is to maximize the conductivity, while minimizing the shear viscosity of the material. In that framework, flow batteries based on aqueous dispersion of carbon black nanoparticles have recently received an upsurge of interest [85, 88, 104, 109, 110].

Due to their hydrophobic properties, carbon black particles are easily dispersed in aprotic solvents such as hydrocarbons [111], where particles interact only via van der Waals forces [112] that correspond to a short-range attractive potential, whose depth is typically about 30 k_BT in light mineral oil [113]. As a result, CB dispersions organize into space-spanning networks even at low volume fractions, and form as soft gels [20, 56, 114] characterized by a yield stress at rest and a highly time-dependent mechanical response under external shear, which involves delayed yielding, heterogeneous flows [115–118], and shear-induced memory effects [119–121].

There are plenty of different CB references with a broad variety of properties regarding the particle and nodule sizes, their morphology characterized by the fractal dimension (how tortuously are the nodules linked). These parameters depend on the manufacturing route of the CB: precursor, temperature, flow rate, and volume fraction [122]. CB particles can also be chemically treated to tweak their surface properties, up to the point of making CB hydrophilic. Various acids or bases can be used in this end [123, 124].

The CB particle used in this thesis is the Vulcan XC72R bought from Cabot. The typical radius size of the aggregate is around 500 nm, 20 nm with a rather small polydispersity ($\pm$5 nm) for the nodules [125], a specific (BET) area 241 m^2/g [126]. Transmission Electron Microscopy (TEM) pictures of this CB are shown in Fig. 2.1(b) and reveal large size and shape distributions.

A.2 Stabilizing Carbon Black particles in water

In the framework of flow batteries, the choice of solvent is a matter of interest. The cheapest and most environmentally friendly is, of course, water. However, CB particles are not stable in such a solvent. Bare CB particles (not treated) are strongly hydrophobic and tend to flocculate rapidly to minimize their contact surface with water, which leads to sedimenting or creaming of CB in aqueous-based solvents [85, 127]. Stabilizing aqueous dispersions of CB particles requires keeping the particles apart, either by electrostatic repulsion or by steric hindrance. In practice, this is achieved in three different ways: (*i*) surface oxidation yielding acidic functional groups [124, 128], (*ii*) functionalization of CB particles with polymers, i.e., polymer grafting chemically onto their surface [129–135] or CB encapsulation through emulsion polymerization [136, 137], and (*iii*) physical adsorption of a polymer dispersant.

The latter method allows reaching CB mass fractions in water as large as 20%, and the dispersants investigated include polyelectrolytes [138], ionic surfactants [139, 140] such as sulfonate surfactants [141–144], sulfonic acids [145, 146], cetyltrimethylammonium bromide (CTAB) [143, 147–150] and chloride (CTAC) [151], non-ionic surfactants [143, 152] such as silicone surfactants [153] or block copolymers surfactants [152, 154, 155], as well as biopolymers such as Arabic gum [85, 156], or polysaccharides [157–160]. From a structural point of view, dispersants adsorb as monolayers onto the surface of CB particles due to hydrophobic interactions, whose strength depends on the molecular structure and weight of the dispersant [144, 159]. Irrespective of the nature of the dispersant, such stabilized CB dispersions generally behave as shear-thinning

fluids [158, 160, 161]. However, depending on the formulation, CB-polymer mixtures may present a solid-like behavior at rest with weakly time-dependent properties [146, 155, 159], suggesting the presence of a percolated network of the CB particles [162].

B Carboxymethylcellulose

Carboxymethylcellulose (CMC) is a semi-flexible anionic polysaccharide derived from the most abundant polymer on earth: the cellulose [163–166]. Its chemical structure is presented in Fig. 2.2. CMC is a water-soluble cellulose ether, which is commonly used as a water binder and thickener in pharmacy, cosmetics, food products[1] [167–170], and as a dispersing agent in semi-solid flow batteries [158], while showing great potential for biomedical applications [171]. The solubility and overall properties of CMC are set primarily by its molecular weight and, to a lesser extent, by its degree of substitution (DS) [168, 172]. The latter is defined as the average number of hydrogen atoms in hydroxyl groups of glucose units replaced by carboxymethyl per unit of repetition of the polymer. It varies typically between 0.4 and 1.2 [167]. With DS= 0 all of the 3 OR groups in the cycle are hydroxyl OH, and with a DS= 3 all of them are carboxymethyl CH_2CO_2Na. The regular cellulose is know to be hydrophobic, when substituted by carboxymethyl groups it promotes its hydrophilicity as they are actually ($CH_2CO_2^-$, Na^+) charged groups. Over a broad range of concentrations, CMC aqueous solutions are shear-thinning viscoelastic liquids [173, 174]. Highly substituted polymers, i.e., for DS $\gtrsim 1$, are hydrophilic and disperse easily in water, yielding rheological features typical of polyelectrolyte solutions [175–178]. However, weakly substituted CMC, i.e., with DS values lower than about 1, display hydrophobic interactions that favor inter-chain association in aqueous solution, yielding larger viscosities. The substituted regions are heterogeneously distributed along the polymer chain.

The concentration c_{CMC} of the CMC in solution dictates the interactions between the polymers [18]. At very low concentrations in the dilute regime, each polymer is independent from one another. When the concentration reaches $c^\star$ the overlap concentration, the polymer coils start to overlap and interactions between them gets stronger. Above $c^\star$ this is the semi-dilute regime. In this regime, the polymer coils can be entangled or not, again depending on the concentration. We define c_e the entanglement concentration such that for $c^\star < c_{CMC} < c_e$ we refer to the semi-dilute unentangled regime and above c_e to the semi-dilute entangled regime. At even larger concentration, one reaches the concentrated regime above $c^{\star\star}$. In this regime the polymers coils

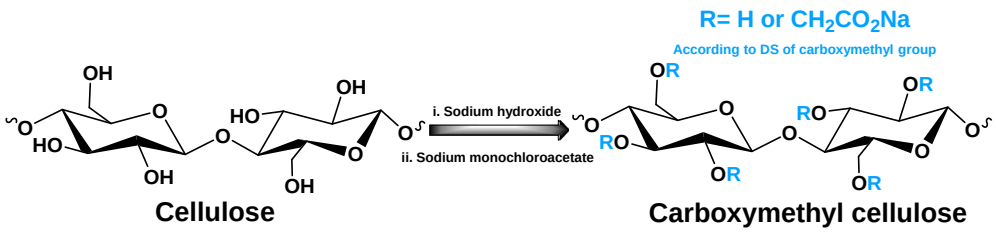

Figure 2.2: Sketch of CMC synthesis route from cellulose. The degree of substitution DS corresponds to the number of R that are CH_2CO_2Na for each cycle (between 0 and 3), averaged over the whole molecule. Adapted from [166].

[1] Food additive registered as E466 or E469.

begin to be squeezed and their size diminishes with c_{CMC}, reducing the number of solvent–monomer contacts. Completely different behavior are to be expected in all of this regimes, as summarized in Fig. 2.3. The critical concentration described above depends on the characteristics of the polymer, namely its molar mass, DS or more generally the intra- and inter-polymer interactions. Namely the hydrophobic interactions and the entanglement have a remarkably big impact onto the mechanical properties. In the present work, we estimated the entanglement concentration $c_e \simeq 0.24\%$ and the concentrated concentration $c^{\star\star} \simeq 2.4\%$ in agreement with [179].

For weakly substituted CMC polymers with DS $\lesssim 0.9$, the hydrophobic regions may lead to the formation of so-called "fringed micelles" in aqueous solution [180], yielding thixotropic and even gel-like properties at high enough concentrations [181–186]. The substitution by carboxymethyl groups is not homogeneous along the polymer chain and blocks of unsubstituted cellulose region are mainly observed for DS $\lesssim 0.9$ [179]. In practice, the gelation of NaCMC solution can be induced by lowering the pH, which decreases the charge density along the CMC chain and promotes the formation of multichain aggregates [187]. At a low enough pH, NaCMC solutions thus behave as soft solids that experience a solid-to-liquid transition at large deformations [188, 189]. Lowering the pH turns the $CH_2CO_2^-$ hydrophilic groups into CH_2CO_2H, which can be somewhat thought of as an effective decrease of the DS.

In this manuscript, we used a sodium salt of carboxymethylcellulose (NaCMC, Sigma Aldrich, $M_w = 250$ kg.mol^{-1} and DS $= 0.9$). Actual values of the batch used were determined to be respectively $M_w = 213 \pm 4$ kg.mol^{-1} using size exclusion chromatography, and DS $= 0.88 \pm 0.02$ using high-field NMR spectroscopy. The radius of gyration of the CMC used was estimated to be around 50 nm [190].

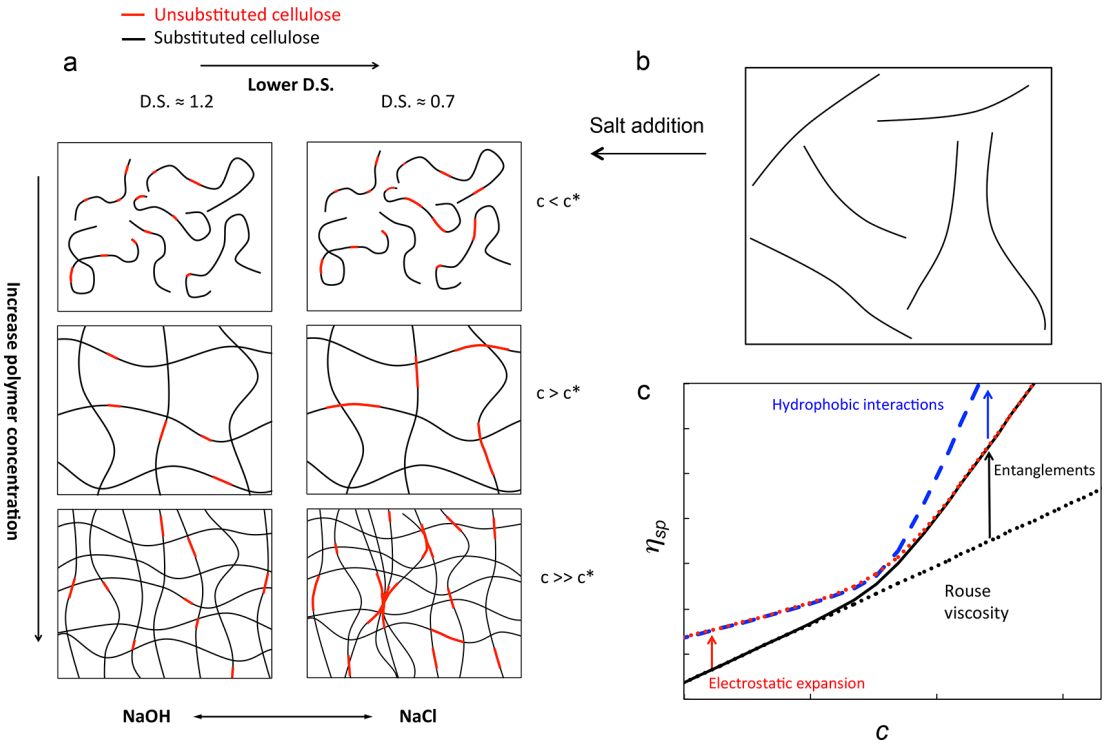

Figure 2.3: Behavior of CMC solutions dependence on key features of the solution such as the polymer concentration, the pH, the DS and the screening of the electrostatic interactions by the addition of salt. Extracted from [179].

C Sample preparation

Samples are prepared by first dissolving sodium carboxymethylcellulose in deionized water. Stock solutions up to 5% wt. are prepared and stirred at room temperature for 48 h until homogeneous, before adding the CB particles (VXC72R, Cabot). Samples are placed in a sonicator bath for two rounds of 90 min separated by a period of 24 h under mechanical stirring. The samples are finally left at rest for another 24 h before being tested. The CMC solution is considered to be the solvent, while CB particles is the dispersed phase. Therefore, we define the CMC weight concentration as $c_{\mathrm{CMC}} = m_{\mathrm{CMC}}/(m_{\mathrm{CMC}} + m_{\mathrm{water}})$ and the CB weight fraction as $x_{\mathrm{CB}} = m_{\mathrm{CB}}/(m_{\mathrm{CB}} + m_{\mathrm{CMC}} + m_{\mathrm{water}})$, where m_{CB}, m_{CMC}, and m_{water} are respectively the mass of CB, CMC, and water in the sample.

In Chapter 5 the pH may be lowered by the addition of HCl. The stock CMC solution are diluted with deionized water and hydrochloric acid solution (Sigma Aldrich). Samples are then placed on a bottle roller for 7 days before being tested at 10 days to limit the impact of ageing (see SI). Final CMC solutions concentrations span from 1 % to 4.5 %. We used a 1 M HCl solution for all the dilutions except for the most concentrated CMC solutions (i.e., 4 and 4.5 %) for which we used a 12 M HCl solution. We checked there is no impact of the HCl solution concentration for a sample at $c_{\mathrm{CMC}} = 1\%$ and $\mathrm{pH} = 1$. The pH of the samples is measured with a pH-meter (Mettler Toledo SevenCompact) and spans between 0 and 7. For CB-CMC solutions the pH is set by the CMC input only, and was found to lay around $\mathrm{pH} = 7 - 8$.

D Rheometry: ways and means

D.1 Linear Viscoelasticity

The description of materials is primarily done by viscosity when dealing with a Newtonian fluid and by Young's modulus when dealing with a Hookean solid. In general cases, the properties of elasticity and viscosity are not exclusive. We then talk about viscoelastic materials [191]. These experimental observations show the need to quantify the elastic and viscous aspects depending on the timescale of the experiment. The complex shear modulus $G^\star$ was introduced to generalize the concepts of Young's modulus and viscosity to viscoelastic fluids by relating stress and strain. Time scales are important for this modulus, so it is naturally defined in the Fourier domain by the equation:

$$\tilde{\sigma}(\omega) = G^\star(\omega)\tilde{\gamma}(\omega) \tag{2.1}$$

where $\tilde{\sigma}$ and $\tilde{\gamma}$ are respectively the Fourier transforms of the shear stress and strain. The complex modulus decomposes into its real part G' called the elastic modulus, which gives the in-phase response and its imaginary part G'' called the viscous modulus, which gives the out-of-phase response. This corresponds respectively to the elastic storage and viscous dissipation of mechanical energy.

A method to measure these two moduli is to apply a sinusoidal deformation with frequency ω and amplitude γ_0 sufficiently small to be in the linear regime, i.e., $\gamma(t) = \gamma_0 \sin(\omega t)$. The stress response is then measured, which in the linear regime, takes the form $\sigma = \sigma_0 \sin(\omega t + \delta)$ where δ, called the loss factor and a function of ω, accounts for any phase shift between deformation and stress. By rewriting the stress, elastic

and viscous moduli defined by (2.2), we obtain:

$$\sigma(t) = \gamma_0 \left[G'(\omega) \sin(\omega t) + G''(\omega) \cos(\omega t) \right] \tag{2.2}$$

where it appears that $G' = \sigma_0/\gamma_0 \cos(\delta)$ characterizes the in-phase response and $G'' = \sigma_0/\gamma_0 \sin(\delta)$ characterizes the out-of-phase response.

Reasoning in the Fourier space with the complex modulus may be hard to grasp, such that using the relaxation modulus $G(t)$ may appear more relevant depending on the context. We shall emphasize that both the complex modulus and the relaxation modulus equivalently characterize a system since both values are related through:

$$G^\star(\omega) = G'(\omega) + iG''(\omega) = \int_{-\infty}^{\infty} i\omega e^{-i\omega t} G(t) \mathrm{d}t \tag{2.3}$$

The simplest experiment to measure it is to apply a deformation γ_0 at a given time from rest and to measure the stress response $\sigma(t)$; the relaxation modulus is then obtained according to $G(t) = \sigma(t)/\gamma_0$. Knowledge of this relaxation modulus then allows evaluating the stress response at a time t given the shear history the fluid has undergone at all times $t' < t$. It reads:

$$\sigma(t) = \int_{-\infty}^{t} G(t - t') \dot{\gamma}(t') \mathrm{d}t' \tag{2.4}$$

which is actually the formal definition of the relaxation modulus. This definition implicitly assumes causality, meaning $G(t' > t) = 0$, what the system *will* undergo has no impact on the current state of the system. The time translation symmetry is assumed as well in this equation: rigorously the relaxation modulus should be written $G(t - t', t)$ as it may depend evolve with time. The failure of the time translation symmetry typically arises from an intrinsic evolution of the system properties with time, e.g., aging or evaporation.

The Fourier domain and the time domain are linked, there are relations between the complex modulus and the relaxation modulus similar to a Fourier transform [192]. These relations require assumptions because one needs to know these moduli over their entire domain of definition. It is, therefore, generally preferable to measure these two quantities independently as needed.

Both moduli have been presented in the linear regime of small deformation amplitudes. In this regime, the moduli do not depend on the amplitude. This is no longer the case in the nonlinear domain where the moduli $G^\star(\omega, \gamma, \sigma)$ and $G(t, \gamma, \sigma)$ also depend on the amplitude [193, 194]. In this regime, deformation may damage the material, and measurement depend on the experimental protocol to characterize the fluid sustainably. For the oscillatory regime, harmonics have also been observed and studied for large amplitudes [193, 195].

These modulus measurements are often carried out using a rheometer, which can impose deformation and measure stress (or vice versa). The technologies differ depending on whether the rheometer operates with strain or stress imposed. The choice of rheometer type depends on the desired precision of the imposed quantity. However, a feedback loop allows imposing strain with a stress-controlled rheometer (and vice versa), but the geometry inertia and the response time of this method prevents its use for certain precise protocols. In practice, the rheometer does not apply deformation or stress but rather rotation or torque. The link between these quantities depends on the geometry in which the sample to be characterized is placed. Three types of geometries are mainly used (Fig. 2.4), with dimensions that can be varied. We used the strain-controlled ARES-G2 and the stress-control MCR302 rheometers for all of the measurements carried out in this manuscript.

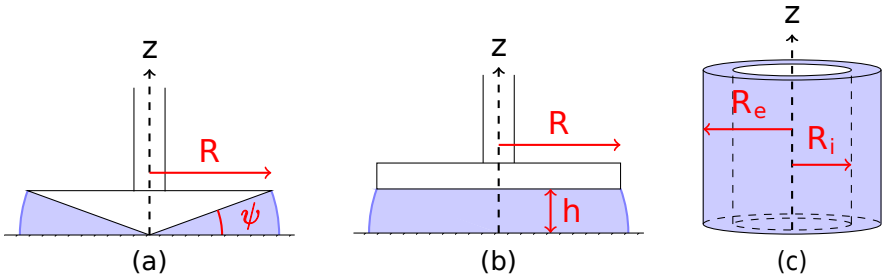

Figure 2.4: Usual geometries used in a rheometer: (a) cone-and-plate, (b) parallel-plate, (c) Couette. The sample is highlighted in lavender. Figure adapted from [196].

D.2 Rheometry

In this manuscript, we mainly used a "cone-and-plate" geometry with a diameter of 40 mm, an angle of 2 °, which consists of a static lower plate on which the sample is placed and then sheared by a mobile cone [Fig. 2.4(a)]. The cone is truncated to avoid solid friction, the truncation is 46 μm for the ARES-G2 and 176 μm for the MCR 302. We used mixed boundary conditions with a rough surface at the rotor and smooth surface at stator with both rheometer. The main advantage of the cone is that it compensates for the higher speed away from the rotation axis by a greater fluid height to be sheared. This allows for a homogeneous shear rate in the sample, which is not true for a "parallel-plate" geometry and only approximately true for a "Couette" geometry [197]. For this reason, the latter geometries were used only in specific experiments when the cone-an-plate could not (e.g., Couette for rheo-SAXS and plate-plate for rheo-electrical setups). The disadvantage of the cone-and-plate geometry is its sensitivity to evaporation because it requires small volumes of fluid. Even a minimal amount of evaporating solvent can significantly change the sample's composition. To limit evaporation, a bell jar can be placed to saturate the atmosphere with the solvent, while limiting the duration of the experiment and the temperature. The temperature is imposed by the lower plate via a Peltier module, which ensures a homogeneous temperature with a precision of a tenth of a degree. If not explicetely precised, the temperature is set to $T = 22°C$.

The rheological protocol applied to all the samples is divided into two consecutive steps: (*i*) a 3 min preshear at $\dot{\gamma} = 500\ s^{-1}$ for most of CB-CMC systems, or $\dot{\gamma} = 50\ s^{-1}$ for the other CB-CMC whose elastic moduli are larger than 10 kPa or for the CMC gels to erase the loading history and rejuvenate the sample; (*ii*) a 20 min recovery during which we monitor the sample linear viscoelastic properties by applying small amplitude oscillations. The rheological characterization is starte afterwards.

Many artifacts can falsify measurements made with a rheometer because it has a limited working range notably by the smallest measurable torque. It is necessary to adapt the parameters of the experimental protocol and the geometry to remain in this working range[2] [198]. If the rotation speed of the mobile part is not constant, care must be taken to remain in the regime where inertia is negligible compared to the measured torque, and here again, the choice of geometry is important (the dimensions and mass of the mobile part influence the moment of inertia). Finally, loading the sample into the geometry has a significant influence on its free surface, and the surface tension can become significant compared to the forces at play in the geometry. It is, therefore, nec-

[2]For example, at fixed stress, a geometry that presents a greater contact surface with the sample allows an increase in the measured stress.

essary to ensure that the sample's contact line is as axisymmetric as possible. Particle sedimentation is also a bias that limits the duration of experiments and the time must not exceed the sedimentation time, which is proportional to the density difference between the particle and the solvent. In this study, the sedimentation time typically equals $\tau_{\text{sink}} = 10^6$ s, much longer than the duration of any experiment (~ 1 h).

D.3 Time-resolved mechanical spectroscopy: Optimally Windowed Chirp

The system might evolve significantly while probing its viscoelastic spectrum. This is quantified by the Mutation number Mu defined as the ratio of the time needed to perform an experiment t_{exp} to the typical evolution time τ_{aging} [199, 200]:

$$Mu = \frac{t_{\text{exp}}}{\tau_{\text{aging}}} \tag{2.5}$$

If $Mu \ll 1$, the system does not evolve much during the time of the experiment so that the system can be seen at rest while the experiment is performed.

The standard way to measure a viscoelastic spectrum is to measure each frequency independently, which is extremely time-consuming, especially for the lowest frequencies and may not respect the $Mu \ll 1$ criterion. The input signal in that case is a sinewave with only one frequency. In the linear regime, the frequencies never interfere and theoretically one can add as much frequencies as wanted into the input signal, each frequency can be easily isolated in the output signal. This concept is very general in physics, but in the case of rheology, it simply means that $G^\star$ can be computed, for instance, with the stress response to whatever input strain, as long as their Fourier transform can be computed [see Eq. (2.1)]. The goal is to scope as many frequencies as possible in the shortest amount of time.

There are, however, experimental and numerical limitations. A very convenient input strain was developed around a chirp signal to get reliable measurements [44]. A chirp signal is a sinewave whose frequency varies exponentially with time so that it probes orders of magnitudes of frequencies in a limited time window. Windowing is applied to the input signal in order to limit finite-size, sampling, and noise effects. This experiment requires are very precise control of the strain. Therefore they are conducted on the strain-controlled ARES-G2 rheometer. A high sampling rate is needed as well for the stress record, we set it to 100 Hz. The parameters of the chirp signal and its windowing were chosen empirically to give spectra with negligible variations

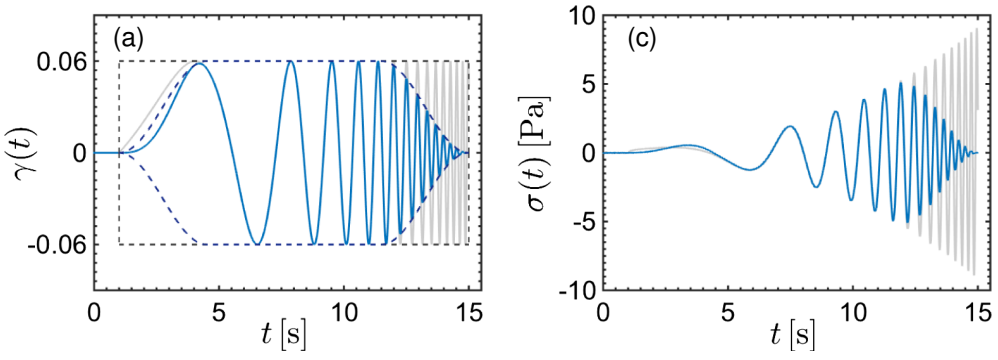

Figure 2.5: Chirp protocol to probe the linear viscoelastic modulus. Input windowed chirp signal for (a) the strain and (b) its stress response. The blue (resp. grey) curves correspond to the data with (resp. without) the windowing. Adapted from [44].

around the spectra measured with a classical frequency sweep. Namely, we set the signal length $T = 25$ s, the lowest frequency $\omega_1 = 0.3$ rad.s^{-1}, the highest frequency $\omega_2 = 30$ rad.s^{-1}, the tapering parameter $r_{\text{OWCh}} = 0.2$ and a waiting time $t_w = 1$ s for all the spectra measured with using the chirp protocol. Note that the mean value of the stress signal was removed to compute its Fourier transform. A typical example of such strain signal and its stress responses is represented in Fig. 2.5.

D.4 Orthogonal superposition

So far, we only considered shear in one direction, when the rheometer is rotating *around* the vertical z axis. As rheometers are usually equipped with a normal force transducer and motor, it can be used to measure the mechanical properties when the sample is sheared *along* the vertical z axis. This is called the orthogonal superposition (OSP), popularized in the 90s thanks to an implementation on classical rheometers [202]. A sketch of the setup is given in Fig. 2.6.

Only oscillatory shear is used with this setup, we note $G^\star_\perp$ the complex modulus measured in the orthogonal direction z of the flow induced by the rotation, and keep the notation $G^\star$ for the modulus in the direction θ of the rotation. We refer to $G^\star_\perp$ as the perpendicular modulus and $G^\star$ as the parallel one. OSP is used either to probe anisotropy by comparison of the mechanical properties along both directions ($G^\star_\perp$ vs $G^\star$) or to probe the evolution of the mechanical properties in the perpendicular direction under a given shear protocol in the parallel direction (namely constant shear rate).

As for the parallel direction, measuring $G^\star_\perp$ requires a precise calibration. However, the perpendicular oscillations create pumping flows, which may have an impact on the perpendicular modulus measurement because of the motion of the geometry. A double wall slotted geometry is used, which is represented in Fig. 2.6(a), is used to minimize this effect [202, 203]. It is engineered to let the fluid flow below and above the shear plane to reduce the impact of the pumping flow on the measurements. It should be noted that such optimization has been shown to work efficiently only for

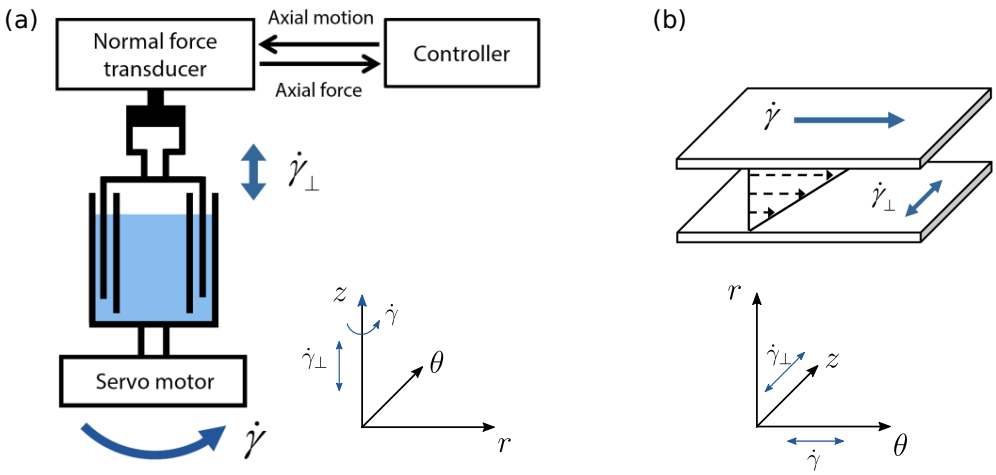

Figure 2.6: Sketch of the OSP setup. (a) Double wall slotted geometry and the feedback loop in the orthogonal direction. (b) Visualization of the two shear planes directions: parallel with a shear in the θ direction, perpendicular with a shear in the z direction. Adapted from [201].

Newtonian fluids, and namely, measurements with yield stress fluids may suffer from further artifacts [203, 204].

D.5 Modeling the mechanical response

We now know how to measure the viscoelastic properties, but the relaxation modulus by itself does not give much information about the physics underlying the system probed. As scientist we aim at interpreting the data to extract meaningful value from the mechanical experiments in order to explain what is actually going on inside the system – usually at the microscopic scale.

For simple elastic solids or viscous liquids, the modeling is quite straightforward: solids are well described by a spring (stiffness g) and liquids by a dashpot (viscosity η), whose constitutive equations that link the stress and the strain are, respectively:

$$\sigma = g\gamma, \tag{2.6}$$
$$G^\star = g, \tag{2.7}$$
$$\sigma = \eta \frac{\mathrm{d}\gamma}{\mathrm{d}t} \tag{2.8}$$
$$G^\star = i\omega\eta \tag{2.9}$$

Of course, this modeling fails for complex fluids that exhibit both solid-like and liquid-like behaviors. Any modeling made of only one spring or one dashpot is doomed to fail since there is no typical timescale implemented in the model, whereas real systems usually have their own characteristic times.

A first attempt to model the mechanical response of complex fluids is to consider a single relaxation time τ, which appears as an exponential decay for the relaxation modulus, i.e., $G(t) = ge^{-t/\tau}$. This is the framework of the canonical Maxwell Model (MM), which describes faithfully viscoelastic fluids with only two parameters g and τ respectively the modulus and time scales. The MM is composed of a serial association of a spring and a dashpot (viscosity $\eta = g\tau$) [Fig. 2.7(a)]. This decomposition in two elements is extremely convenient to interpret the relaxation modulus: each element may arise from two different physical mechanisms that are thus highlighted. Namely, in the case of the MM for polymers (in a solution or as a melt), the spring reveals the strength of the network – i.e., how strongly the polymers are linked, and the dashpot as the viscous dissipation limiting the network dynamics – how difficult it is for polymers to disentangle. The complex modulus in this model reads:

$$G^\star(\omega) = g\frac{i\omega\tau}{1+i\omega\tau} \tag{2.10}$$

Another simple mechanical description is the Kelvin-Voigt Model (KVM), made of a spring and a dashpot that are associated in parallel [Fig. 2.7(b)]. The stress comes independently from both elements. Typically, in some colloidal gels, e.g., CB in oil [56], it is acknowledged that the stress has an elastic contribution from the colloidal network and a viscous contribution from the solvent. The KVM also has two typical scales g and $\tau = \eta/g$. Asymptotically, in the KVM, short timescales correspond to liquid-like behavior, and long timescales correspond to solid-like behavior, contrary to the MM. The dashpot as the viscous dissipation limiting the network dynamics – how difficult it is for the polymers to disentangle. The complex modulus in this model reads:

$$G^\star(\omega) = g(1+i\omega\tau) \tag{2.11}$$

Simple MM and KVM are actually idealized models, and they scarcely capture accurately the experimental data [205]. Real systems usually have several relaxation

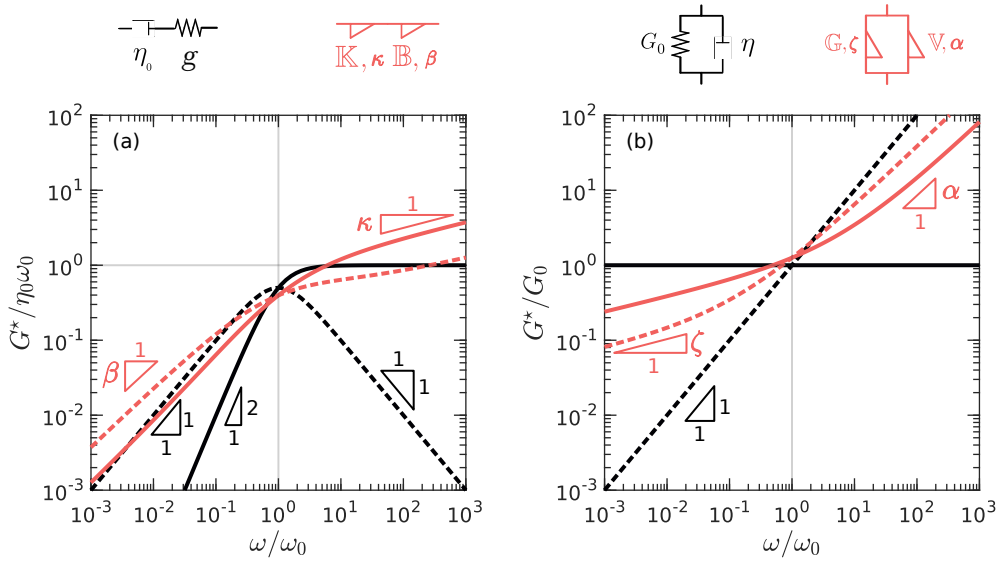

Figure 2.7: Typical viscoelastic spectra in rheology. (a) Regular (black curves) and Fractional Maxwell model with $\beta = 0.8$ and $\kappa = 0.2$ (orange curves) models. (b) Regular (black curves) and Fractional Kelvin-Voigt model with $\alpha = 0.8$ and $\zeta = 0.2$ (orange curves) models. Plots are normalized by the modulus g and time scales τ.

times. The most general case is to assume there is a continuous spectrum of modes for each relaxation time, which contribute independently to the total modulus:

$$G^\star(\omega) = g_e + \int_0^\infty \frac{\mathrm{d}\tau}{\tau} g(\tau) \frac{i\omega\tau}{1+i\omega\tau} \tag{2.12}$$

where g_e is the equilibrium modulus and corresponds to the modulus at rest, i.e., for $\tau = \infty$. This expression should be seen as a continuous sum of Maxwell modes (a discrete sum is a special case of the continuous one). The same expression can be obtained for a sum of Kelvin-Voigt modes, but we will only consider Maxwell modes (moreover, it has been shown that a finite discrete sum of Kelvin-Voigt modes is equivalent to a finite discrete sum of Maxwell modes [206]). The function $g(\tau)$ appears as the relaxation time spectrum and totally determines the linear response of any system: it grasps how much each mode contributes to the total modulus. The problem of characterizing a system in the linear regime boils down to computing $g(\tau)$. However, the relaxation time spectrum cannot, in the general case, be computed from the relaxation modulus or complex modulus, let alone from experimental data [207]. A physically relevant assumption about the functional form of $g(\tau)$ is generally made, e.g., a log-normal distribution [205]. Such a description of the modulus can be very accurate but requires several assumptions and free parameters. In the late 40s, another way of modeling the spectra with fewer parameters flourished, introducing a new building block: the “springpot" [208, 209].

a Fractional models

The springpot is an element that generalizes the spring and the dashpot [210]. It has been popularized by Scott-Blair et al. [208, 211] who wanted to find a way to describe simply power-law scalings, which are ubiquitous in rheology. It is quite usual to observe power laws in viscoelastic spectra, e.g., for critical gel $G' \sim G'' \sim \omega^\alpha$ where $0 < \alpha < 1$ [211]. Power laws with an exponent 1 come from a dashpot, which

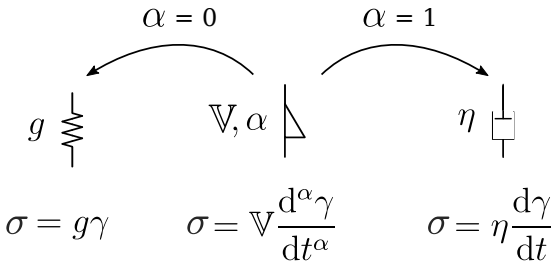

Figure 2.8: (middle) A springpot defined by its quasi-propriety $\mathbb{V}$ and its exponent α. For $\alpha = 0$, the springpot is equivalent to a spring (left), while for $\alpha = 1$ the springpot is equivalent to a dashpot (right).

constitutive equation shows the strain derived one time. Power laws with an exponent 0 come from a spring, which constitutive equation shows the strain derived no time. To get a power law with an exponent α between 0 and 1, it seems like one has to have a constitutive equation where the strain is derived α time. This is where the springpot naturally arises. It is defined by the following constitutive equation and complex modulus:

$$\sigma = \mathbb{V}\frac{\mathrm{d}^\alpha \gamma}{\mathrm{d}t^\alpha} \tag{2.13}$$

$$G^\star = \mathbb{V}(i\omega)^\alpha \tag{2.14}$$

where $0 < \alpha < 1$ and $\mathbb{V}$ is quasi-property expressed in Pa.s$^\alpha$. The operator $\mathrm{d}^\alpha/\mathrm{d}t^\alpha$ is a *fractional derivative* which extends the derivative with non-integer exponents. Although they are physically hard to grasp, fractional derivatives are mathematically well-defined[3]. Its properties are very similar to regular derivatives, namely, in the Fourier space, it turns into $(i\omega)^\alpha$. The springpot is usually sketched as in Fig. 2.8. One should emphasize that in the limit of $\alpha = 0$ (resp. $\alpha = 1$) the springpot is equivalent to a spring (resp. a dashpot). The springpot appears as a powerful tool to model viscoelastic spectra with power-laws since it requires only two parameters, whereas other models using a sum of Maxwell modes usually need lots of free parameters [207]. In this manuscript, we chose to use the least number of free parameters to model the data and try to put as much physics as possible into the model, inspired by Scott-Blair [208]:

"Normally, one is faced with the choice of selecting a large number of true properties or a smaller number of quasi-properties, since it is nearly always possible to express rheological behaviour in terms of true properties provided enough constants are fitted. It is hoped to show that the latter course is by no means always the best."

This new element is a new building block to construct more complex modeling and can be added to regular springs, dashpots, or even other springpots as well. In this thesis both serial and parallel associations of springpots are used; they should be seen as a generalization of the MM or KVM.

Fractional Maxwell Model (FMM)

It is composed of a serial association of two springpots $(\mathbb{K}, \kappa)$ and $(\mathbb{B}, \beta)$. This

[3]Formally the Caputo definition of the fractional derivative is acknowledged [210]. For a smooth function f, it reads $\frac{\mathrm{d}^\alpha f}{\mathrm{d}t^\alpha}(t) = \frac{1}{\Gamma(n-\alpha)}\int_0^t (t-t')^{n-1-\alpha} f^{(n)}(t')\mathrm{d}t'$ with Γ the Gamma function, $n = \lfloor \alpha + 1 \rfloor$ a natural number such that $n - 1 < \alpha \leq n$ and $f^{(n)}$ the n-th derivative of f.

model is used to model viscoelastic liquids that exhibit power laws in their spectra, the complex modulus reads:

$$G^\star(\omega) = \frac{\mathbb{K}\,(i\omega)^\kappa\,\mathbb{B}\,(i\omega)^\beta}{\mathbb{K}\,(i\omega)^\kappa + \mathbb{B}\,(i\omega)^\beta} \tag{2.15}$$

This complex modulus can be written as:

$$G^\star(\omega) = i\omega\eta^\star = \eta_0\omega_0\frac{(i\omega/\omega_0)^{\kappa+\beta}}{(i\omega/\omega_0)^\kappa + (i\omega/\omega_0)^\beta} \tag{2.16}$$

with the two natural scales of frequency ω_0 and viscosity η_0 (or equivalently modulus with $\eta_0\omega_0$):

$$\eta_0 = \left(\frac{\mathbb{K}^{\beta-1}}{\mathbb{B}^{\kappa-1}}\right)^{\frac{1}{\beta-\kappa}} \tag{2.17}$$

$$\omega_0 = \left(\frac{\mathbb{K}}{\mathbb{B}}\right)^{\frac{1}{\beta-\kappa}} \tag{2.18}$$

These two characteristic scales are very useful because they recover meaningful values beyond the quasi-properties, for which it is difficult to give a physical interpretation. Namely, ω_0 is the cutoff frequency of the system and corresponds to a mechanical response dominated by one dashpot or the other. Moreover, the asymptotic behaviors of elastic and loss moduli are useful to keep in mind to recognize the FMM (we assume here $0 < \kappa < \beta$):

$$G^\star(\omega \ll \omega_0) \simeq \eta_0\omega_0(i\omega/\omega_0)^\beta \tag{2.19}$$

$$G^\star(\omega \gg \omega_0) \simeq \eta_0\omega_0(i\omega/\omega_0)^\kappa \tag{2.20}$$

so that for $\omega \ll \omega_0$ (resp. $\omega \gg \omega_0$) the FMM is equivalent to the springpot with the exponent β (resp. κ). This FMM can only model viscoelastic spectra, whose power laws have a higher exponent at low frequencies than the exponent at high frequencies.

Fractional Kelvin-Voigt Model (FKVM)

It is composed of a parallel association of two springpots $(\mathbb{G}, \zeta)$ and $(\mathbb{V}, \alpha)$. This model is used to model viscoelastic solids that exhibit power laws in their spectra, the complex modulus reads:

$$G^\star(\omega) = \mathbb{G}\,(i\omega)^\zeta + \mathbb{V}\,(i\omega)^\alpha \tag{2.21}$$

This complex modulus can be written as:

$$G^\star(\omega) = G_0\left((i\omega/\omega_0)^\zeta + (i\omega/\omega_0)^\alpha\right) \tag{2.22}$$

with the two natural scales of frequency ω_0 and modulus G_0, which have actually the same expression as the ones in the FMM:

$$G_0 = \left(\frac{\mathbb{G}^\alpha}{\mathbb{V}^\zeta}\right)^{\frac{1}{\alpha-\zeta}} \tag{2.23}$$

$$\omega_0 = \left(\frac{\mathbb{G}}{\mathbb{V}}\right)^{\frac{1}{\alpha-\zeta}} \tag{2.24}$$

These two characteristic scales are very useful because they recover meaningful values out of the quasi-properties, for which it is difficult to give a physical interpretation. Namely, ω_0 is the cutoff frequency of the system and corresponds to the transition of a mechanical response dominated by one dashpot to a mechanical response dominated by the other dashpot. The asymptotic behaviors of elastic and loss moduli are useful to keep in mind to recognize the FKVM (we assume here $0 < \zeta < \alpha$):

$$G^\star(\omega \ll \omega_0) \simeq G_0(i\omega/\omega_0)^\zeta \tag{2.25}$$
$$G^\star(\omega \gg \omega_0) \simeq G_0(i\omega/\omega_0)^\alpha \tag{2.26}$$

so that for $\omega \ll \omega_0$ (resp. $\omega \gg \omega_0$), the FKVM is equivalent to the springpot with the exponent ζ (resp. α). This FKVM can only model viscoelastic spectra whose power laws have a lower exponent at low frequencies than the exponent at high frequencies.

Both models are used throughout this manuscript, FMM for viscoelastic liquids below the gelation point or FKVM for most gels. For the latter, the first springpot $(\mathbb{G}, \zeta)$ is actually set to a regular spring G_0 (in this case, the stiffness of the spring sets the modulus scale). Some other gels are not well captured by either of these fractional models because they are fundamentally different: they behave more like glasses.

b Soft Glassy Rheology

The Soft Glassy Rheology (SGR) model was introduced by Sollich et al. in the late 90s [213, 214] to describe a broad range of systems (e.g., dense emulsions and microgels, pastes, colloidal glasses, slurries, paints, etc.) that share only two characteristics: structural disorder and metastability. The purpose of this model is to capture similar features in the mechanical properties in these systems, namely the weak power-law dependence of the elastic and loss moduli as a function of the frequency, with a typical loss factor around 0.1 weakly dependent on the frequency.

The model is inspired by the trap model developed by Bouchaud and Monthus in the 90s [215, 216], in which the reorganization of the microstructure is described as hops in a random energy landscape for each particle degree of freedom as pictured in Fig. 2.9. The shear in the SGR model effectively increases the energy of the particle and promotes hopping. Depending on the so-called "noise temperature" x, the complex modulus has a different frequency dependence. This noise temperature is a fitting parameter that translates the probability for the particles to hop out of their

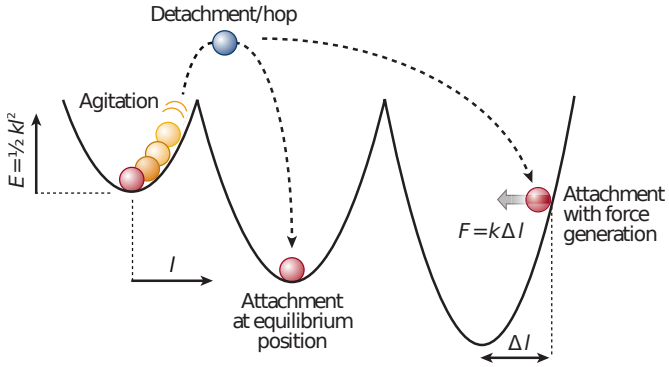

Figure 2.9: Microscopic model for the rheology of glasses. Trap dynamics in a potential well for the soft glassy rheology model. Extracted from [212].

cage formed by their neighboring particles [213, 217, 218]. In the cases considered here $x < 1$ which corresponds to the glass state.

The SGR explicitly includes the “age" of the sample, to be understood as the time elapsed after a reset of the microstructure: the longer the resting time, the more states are explored by the system, which selects the lowest energy ones and the overall mechanical behavior of the system evolves accordingly [219, 220]. The reset of the microstructure is usually done with a “mechanical quench", namely a shear at high shear rate, also known as “shear rejuvenation". The waiting time t_w appears explicitly in the modulus computation.

With this model, they derived the following expression for the complex modulus:

$$G^\star = \mathcal{G}\left(1 - \frac{(i\omega t_w)^{x-1}}{\Gamma(x)}\right) \tag{2.27}$$

where Γ is the Gamma function and $\mathcal{G}$ corresponds to the typical modulus that arises from the well depth in the trap model.

This model is, however, not sufficient to describe the upturn in the high-frequency limit of the loss modulus observed in several systems as the ones encountered throughout this manuscript. For such cases, Brownian motion and solvent viscosity have to be taken into account. The former gives a contribution in both elastic and loss moduli as $c\omega^{1/2}$, which was asymptotically predicted by flow calculations [221] and by a kinetic theory using a hard sphere model [222]. This Brownian contribution has been used successfully to describe suspensions of hard spheres near the glass transition (silica spheres in ethylene glycol) [217, 223]. With these considerations, the complex modulus reads:

$$G^\star = \mathcal{G}\left(1 - \frac{(i\omega t_w)^{x-1}}{\Gamma(x)}\right) + c(i\omega)^{1/2} + \eta i\omega \tag{2.28}$$

Finally, note that this model has been developed to describe glasses but it appears to faithfully describe the behavior of a broader family of systems. Namely, some colloidal gels can be approximated as glasses

D.6 Non-linear rheology

a Framework

So far, $G^\star$ has been solely defined in the linear regime. As a mechanical transfer function, it only makes sense in the linear regime when the frequencies do not mix. In the linear regime $G^\star$ depends only on the frequency so the stress is proportional to the strain, but when the amplitudes are large enough $G^\star$ may also depend on the stress or strain amplitude [193, 194]. This departure from the linear relationship must be measured before any mechanical experiments. Indeed the non-linearities arise from a modification of the system, which is no longer at rest. In the worst-case scenario, this change is non-reversible, and the material can be damaged. Another characteristic of the non-linear regime is the apparition of harmonics in oscillatory shear tests [193, 195]. The first thing to do is, therefore, to determine the extent of the linear regime; the most common way is to apply an oscillatory shear at a fixed frequency and sweep the amplitude from extremely low values to high values. Three different regimes are usually defined: Small, Medium, and Large Amplitude Oscillatory Shear (resp. SAOS, MAOS, and LAOS) [224, 225].

In this work, the strain amplitude is swept and the response stress is recorded. The input strain is a pure sine wave with an amplitude γ_0 and a frequency ω (for simplicity, we set the initial phase to zero). The response stress may have higher frequency terms:

$$\gamma = \gamma_0 \sin(\omega t) \tag{2.29}$$
$$\sigma = \sigma_0 \sum_k a_k \sin(k\omega t + \delta_k) \tag{2.30}$$
$$\sigma = \sigma_0 \sum_k a_k \sin(k\omega t)\cos(\delta_k) + a_k \cos(k\omega t)\sin(\delta_k) \tag{2.31}$$
$$= \sigma_{\text{elast}} + \sigma_{\text{visc}} \tag{2.32}$$
$$\sigma_{\text{elast}} = \sigma_0 \sum_k a_k \sin(k\omega t)\cos(\delta_k) \tag{2.33}$$
$$\sigma_{\text{visc}} = \sigma_0 \sum_k a_k \cos(k\omega t)\sin(\delta_k) \tag{2.34}$$

where σ_0 is the fundamental amplitude, a_k the relative amplitude of the k-th harmonic (such that for the fundamental $a_1 = 1$) and δ_k the phase of the k-th harmonic. The stress can be decomposed into its elastic and viscous parts respectively σ_{elast} and σ_{visc}. One no longer has $\sigma_{\text{elast}} \sim \gamma$ in the non-linear regime because of the harmonics, but still σ_{elast} and γ reach zero and their extremal value at the same time, same goes for σ_{visc} and $\dot{\gamma}$. All values σ_0, δ_k, and a_k depend on the strain amplitude. The frequency dependence is not explicitly written here, but it does play a two-fold role. Firstly, it is the frequency at which the sample is probed, secondly the input energy leading to the breaking of the sample depends on the frequency as well. Unfortunately, they cannot be decoupled during mechanical tests. Finally, as this experiment probes the sample in a state that is not at equilibrium a priori, the shear history plays a role. Namely, the protocol chosen during the strain sweep may impact the results, e.g.,the sweeping rate. To remain consistent, we fixed the sweep protocol to a stepwise sweep, starting from $\gamma_0 = 0.01\%$ applied for two cycles with either 5 or 10 points per decade.

b Strain sweep analysis

In the non-linear regime, one still keeps the same vocabulary for the elastic and loss moduli, but they only refer to effective moduli restricted to the fundamental frequency, i.e., ignoring the harmonics. Namely with the above formalism:

$$G^\star = \frac{\sigma_0}{\gamma_0} e^{i\delta_1} \tag{2.35}$$

The plot of $G^\star$ as a function of the strain γ_0 is already very insightful on the non-linear behavior of the system. The linear regime is the region where both G' and G'' remain constant, strain independent. It yields a linear relation between the stress and the strain amplitudes. For higher amplitudes, G' or G'' may depart from their plateau value, corresponding to a change of the slope in the stress vs strain log-log plot. In the cases encountered in this work at the edge of the linear regime, G' decreases, and G'' may increase or decrease. At even larger amplitudes, they both decrease as the strain amplitude increases. When G'' is a monotonous function of the strain, it is referred to as a type I yielding behavior [226]. On the other hand, for type III, G'' presents an overshoot around the yielding. In some other cases, a so-called “double yielding" may be observed, in which two steps are visible in the plot of G' [227].

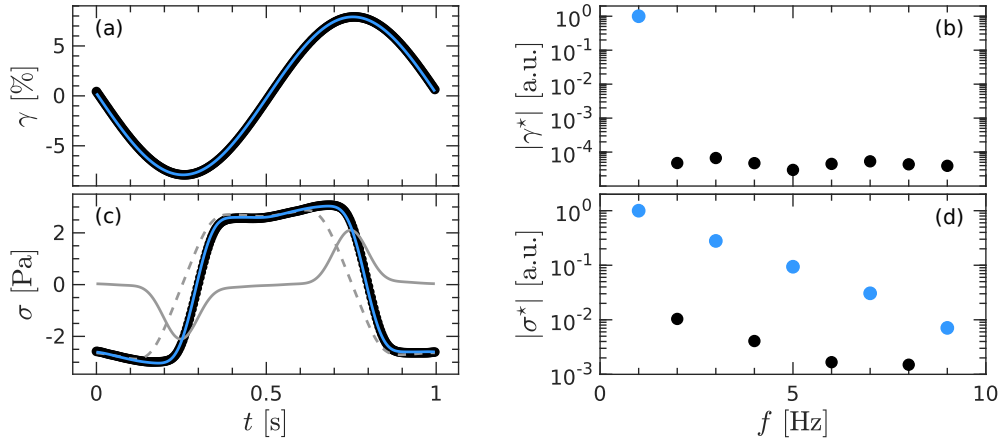

Figure 2.10: Mechanical analysis of one step during a strain sweep of a CB-CMC hydrogel at $c_{\text{CMC}} = 0.01\%$ and $x_{\text{CB}} = 8\%$ with $\gamma_0 = 8\%$ and $f = 1$ Hz. (a) Input strain versus time and (b) its Fourier transform. (c) Output stress versus time and (d) its Fourier transform. The Fourier transforms are normalized by their amplitude at 1 Hz the fundamental frequency. The blue curves in (a) and (c) correspond to the model of the data keeping only the frequencies indicated in blue in their Fourier transform. The grey solid (resp. dashed) line is the elastic (resp. viscous) stress computed thanks to the Fourier decomposition of the stress.

The yield strain γ_y is defined as the crossover point of G' and G''. The LAOS region corresponds to $\gamma_0 > \gamma_y$. However, there are no clear definitions for the SAOS and MAOS, as the departure from the plateau value of G' and G'' is continuous. Similar strategies have been proposed to rationalize the distinction between SAOS from MAOS with the amplitude of harmonics, but the same issue has been encountered, and an arbitrary threshold for their value is required [224]. Here we chose a geometrical definition of the linear regime, determined by a characteristic strain γ_{NL} as the intersection between two power-law fits of G' well before the yielding and right after it. Note that all these definitions depend on the protocol, in particular on the frequency and the number of cycles applied at each step.

Right after yielding, both G' and G'' decrease as a function of γ_0, usually as a power-law which decays faster for G' than for G'' [228]. We note respectively ν' and ν'' the exponents of these power-laws. The potential overshoot in G'' is quantified by $\Delta G''$ as the difference between the maximal value of G'' and its plateau value in the linear region.

c Analysis of LAOStrain waveforms

In the following, we assume there are only odd harmonics in the decomposition described in Eq. (2.31). Indeed, odd harmonics are expect since the stress signal is supposedly in the same direction as the strain. Even harmonics therefore usually correspond to artifacts in the measurement (e.g., slip of the sample at the surface of the geometry or elastic instabilities [224]). We experimentally witnessed the negligible weight of even harmonics in the stress Fourier decomposition Fig. 2.10. The Fourier decomposition is used to express σ_{elast} and σ_{visc}, as they are not accessible directly from the measurements. It turns out that cropping the Fourier decomposition to the 5 first terms precisely describes the data, which corresponds to $k = 1, 3, 5, 7$ and 9 in Eq. (2.31). Computed this way, the goal is to model $\sigma_{\text{elast}}(\gamma)$ and $\sigma_{\text{visc}}(\dot{\gamma})$ in the Lissajous plot. Polynomial descriptions appear to fit the data nicely. To stick with the

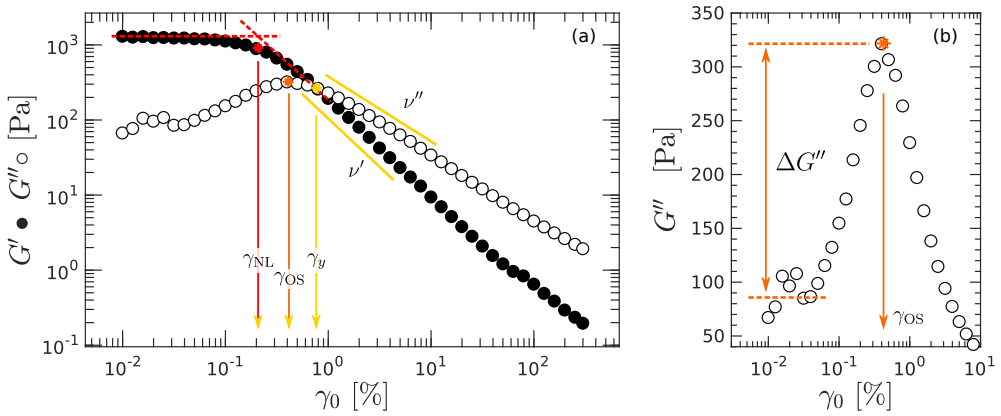

Figure 2.11: Typical strain sweep analysis with a CB-CMC hydrogel at $c_{CMC} = 0.01\%$ and $x_{CB} = 8\%$ at $f = 1$ Hz. (a) G' and G'' as a function of strain γ_0 (neglecting the harmonics in the stress signal). The yellow star corresponds to the yield point, γ_y defined as the crossover between G' and G''. The yellow lines emphasize the power-law exponents of G' and G'' right after the yielding, respectively ν' and ν''. The orange star corresponds to the maximum of the overshoot in G''. The red star is the onset of the non-linear regime γ_{NL} defined as the intersection of the two red dashed lines, power-law approximations of G' well before and near the yielding. (b) Zoom around the overshoot region of G'' to define $\Delta G''$ the difference between the maximum of G'' and its plateau value in the linear regime.

literature, we used the Chebyshev polynomials decomposition [195]. It is equivalent to a regular polynomial fitting with the advantage that the coefficients computed do not depend on the highest order used for the fit (the Chebyshev polynomials base is orthogonal, contrary to the canonical one). The stresses are expressed in the following way:

$$\sigma_{elast}(\gamma) = \gamma_0 \sum_{k,\,\text{odd}} e_k T_k \left(\frac{\gamma}{\gamma_0}\right) \tag{2.36}$$

$$\sigma_{visc}(\dot{\gamma}) = \omega\gamma_0 \sum_{k,\,\text{odd}} v_k T_k \left(\frac{\dot{\gamma}}{\omega\gamma_0}\right) \tag{2.37}$$

with T_k the Chebyshev polynomials of order k (see e.g., [195] for their expression), e_k and v_k the coefficients of order k for the elastic and viscous decomposition respectively. Numerically, these coefficients are computed through a scalar product of the data with each T_k for the first 3 terms $k = 1, 3$ and 5. This is motivated by the negligible amplitude of the coefficients beyond $k = 5$ as shown in Fig. 2.12.

From that, we can compute precisely the following quantities:

$$G_L = \left.\frac{\sigma_{elast}}{\gamma}\right|_{\gamma=\gamma_0} = \sum_{k,\,\text{odd}} e_k \tag{2.38}$$

$$G_M = \left.\frac{\mathrm{d}\,\sigma_{elast}}{\mathrm{d}\gamma}\right|_{\gamma=0} = \sum_{k,\,\text{odd}} k(-1)^{(k-1)/2} e_k \tag{2.39}$$

$$\eta_L = \left.\frac{\sigma_{visc}}{\dot{\gamma}}\right|_{\dot{\gamma}=\omega\gamma_0} = \sum_{k,\,\text{odd}} v_k \tag{2.40}$$

$$\eta_M = \left.\frac{\mathrm{d}\,\sigma_{visc}}{\mathrm{d}\dot{\gamma}}\right|_{\dot{\gamma}=0} = \sum_{k,\,\text{odd}} k(-1)^{(k-1)/2} v_k \tag{2.41}$$

G_L and η_L represent the elastic modulus and viscosity at the largest amplitude during the cycle, whereas G_M and η_M represent, respectively, the elastic modulus and viscosity at zero strain and zero shear rate during the cycle. One should note that $G_L = G_M$ for $\gamma_0 \to 0$ as $e_k = 0$ if $k > 1$ in the linear regime. The same remark applies for η_L and η_M. The very goal of the LAOS intra-cycle analysis is to compare the mechanical properties along the cycle. Here, we only compare the system at extreme strains[4]. This is quantitatively computed with the dimensionless parameters S and T:

$$S = \frac{G_L - G_M}{G_L} \tag{2.42}$$

$$T = \frac{\eta_L - \eta_M}{\eta_L} \tag{2.43}$$

respectively the strain-stiffening and shear-thickening intra-cycle ratios [195]. In the linear regime their are equal to zero, in the non-linear regime they quantify how differently behaves the sample when fully stretched versus non stretched, namely the sign is insightful to understand better the microscopic behavior of the sample.

Finally, another value of interest is the apparent cage modulus [229], meaningful in the case of glassy systems:

$$G_{\text{cage}} = \left.\frac{\mathrm{d}\,\sigma}{\mathrm{d}\gamma}\right|_{\sigma=0} \tag{2.44}$$

which has no simple expression in terms of Chebyshev coefficients and must be computed numerically instead. This modulus appears to be roughly constant along a strain sweep in such materials. It is, therefore, understood empirically as the modulus due to the hopping out of the cage in glassy materials. At zero stress, the particles are assumed to be at the bottom of their trap, hence the slope around this point informs on the stiffness of the cage. One should recall that at zero shear stress, the total stress may contain elastic and viscous stresses that compensate one another. Thus G_{cage} is solely an apparent cage modulus, although in glassy materials the viscous response is negligible. Moreover, the interpretation of G_{cage} as a measurement of the cage elasticity implicitly assumes that the cages have no timescale and reform as soon as the shear rate vanishes.

All of these values have a well-defined mathematical expression, but one should rather visualize them on the Lissajous curves, as depicted in Fig: 2.12.

Remark: the intra-cycle analysis can be done supposedly on any kind of rheometer. In practice, the strain sine waves tend to contain harmonics on a stress-controlled rheometer, which complicates a lot the data analysis. With a stress-controlled rheometer, the intra-cycle analysis is done with a stress sweep instead. Here, we used a strain-controlled rheometer (ARES-G2, TA Instrument) for intra-cycle LAOStrain.

D.7 Continuous shear

a Flow curves: measurement and modeling

Although oscillatory shear experiments are extremely insightful on the system and are a great way to capture its main characteristics, complex fluids are usually submitted to flow for their application. Unfortunately, the link between this oscillatory response and the flow behavior is not straightforward. Therefore, experiments under

[4]Further analysis can be implemented to probe the system at each point along the strain cycle, this is called the Sequence of Physical Processes (SPP) [229]. It has not been conducted on the systems studied in this manuscript yet.

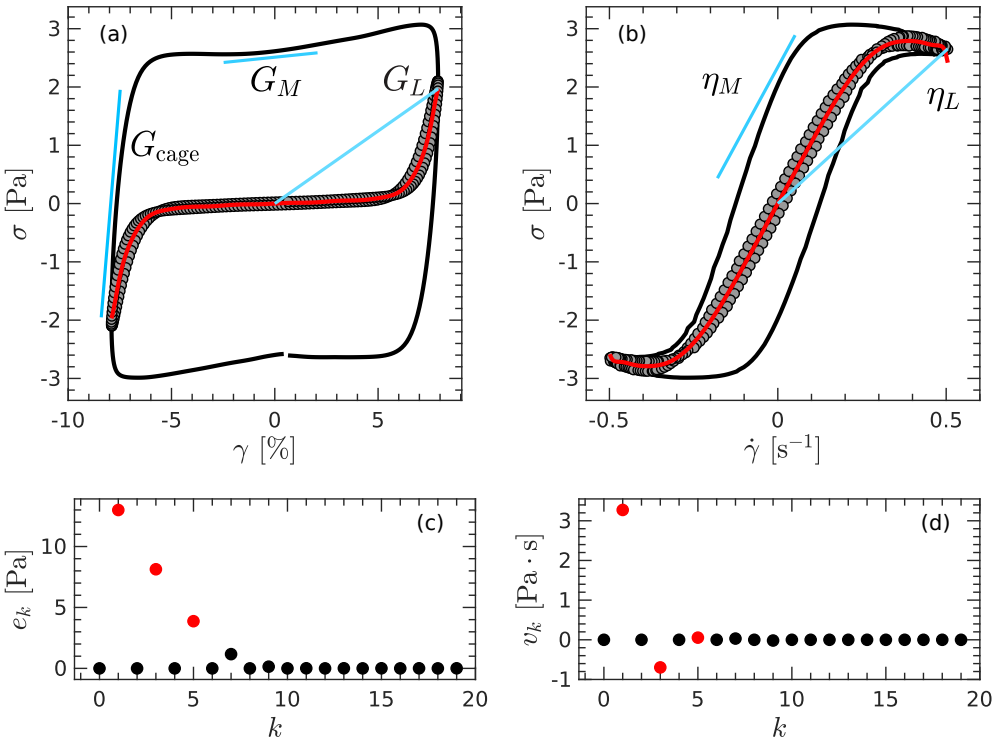

Figure 2.12: Lissajous plots during LAOS of a step at $\gamma_0 = 8\%$ and $f = 1$ Hz during a strain sweep (sample: CB-CMC hydrogel at $c_{\text{CMC}} = 0.01\%$ and $x_{\text{CB}} = 8\%$): (a) stress versus strain and (b) stress versus shear rate. The black lines are the total stress computed approximated by the Fourier decomposition, and the grey cirlces show (a) the elastic and (b) the viscous stresses [see Eq. (2.29) to (2.34) and Fig. 2.10]. The slope of the blue curves indicates either G_M, G_L, G_{cage}, η_M or η_L, as defined in Eq. (2.38)-(2.41) and Eq. (2.44). The red curves are the Chebyshev description of the data with the coefficients for $k = 1, 3, 5$ plotted below. Chebyshev coefficient (c) e_k for the elastic stress and (d) v_k for the viscous stress as a function of the Chebyshev order. The red points correspond to $k = 1, 3, 5$ used to describe the data in (a) and (b).

continuous flow, i.e.,continuous shear (as opposed to oscillatory shear), must be conducted to complete the characterization of any system. This is usually done through flow curves for which a constant shear rate $\dot{\gamma}$ is applied the resulting stress σ is measured. The flow curves correspond here to the plot σ vs $\dot{\gamma}$, as represented in Fig. 2.13.

For yield stress fluids such as the one studied in this thesis, the flow curves have several features: (i) at very low shear rates the stress is independent on $\dot{\gamma}$ and the plateau value is called the yield stress σ_y, (ii) above this stress plateau σ increases with $\dot{\gamma}$ and may not decrease[5] [197]. In other words, to make the system flow, one needs to apply a stress above σ_y, and it flows more as the stress increases.

There are several models to describe the flow curves of gels and in order to extrapolate the flow behavior. The two that we shall discuss here are the Herschel-Bulkley (HB) [230] and the Three Components (TC) [231] models, which express the stress as

[5]Thermodynamics prohibits σ to decrease with $\dot{\gamma}$ in a stationary state. In some cases, it can be observed but it translates instabilities.

a function of the shear rate according to:

$$\text{HB:} \quad \sigma_{\text{HB}} = \sigma_y + \sigma_y \left(\frac{\dot{\gamma}}{\dot{\gamma}_c} \right)^n \tag{2.45}$$

$$\text{TC:} \quad \sigma_{\text{TC}} = \sigma_y + \sigma_y \left(\frac{\dot{\gamma}}{\dot{\gamma}_c} \right)^{1/2} + \eta_{\text{bg}} \dot{\gamma} \tag{2.46}$$

with σ_y the yield stress, $\dot{\gamma}_c$ a critical shear rate[6], n the Herschel–Bulkley exponent (typically $0 < n < 1$), and η_{bg} a background viscosity depending on the solvent[7]. Both models were empirically constructed to account for the yield stress together with a potential shear thinning behavior, i.e.,the effective viscosity $\eta = \sigma/\dot{\gamma}$ decreases with $\dot{\gamma}$. The main discrepancy between HB and TC is their physical meaning: in HB the $\dot{\gamma}^n$ term has no clear interpretation, whereas in TC the $\dot{\gamma}^{1/2}$ term is correlated to plastic events and the linear term is due to the continuous phase viscosity.

We compared both models for the CB-CMC hydrogels using the relative error $\epsilon_{\text{rel}} = |\sigma_{\text{HB}} - \sigma|/\sigma$ or $\epsilon_{\text{rel}} = |\sigma_{\text{TC}} - \sigma|/\sigma$ for two representative samples [Fig. 2.13]. Although both models yield similar values for σ_y, the relative error is significantly larger for the TC than the HB model, which confirms the visual intuition that the HB model captures the flow curve better. We shall, from now on, only consider the HB model to describe the flow curves.

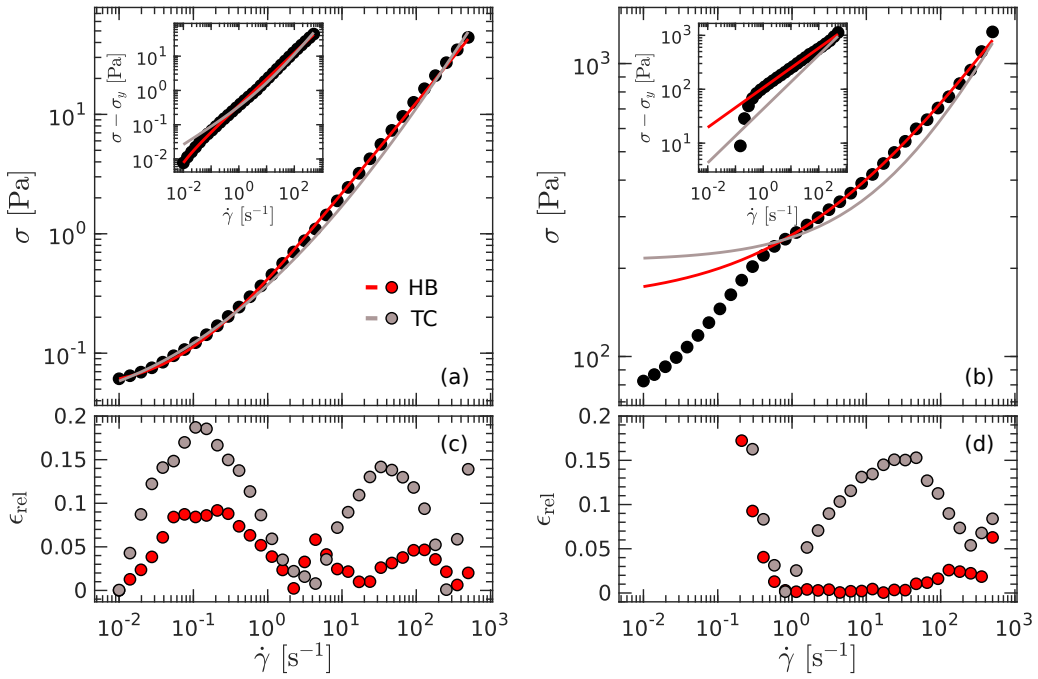

Figure 2.13: Comparison of the Herschel-Bulkley and the Three Components models. Flow curve for a CB-CMC hydrogel at $c_{\text{CMC}} = 1\%$ & $x_{\text{CB}} = 6\%$ (a) and at $c_{\text{CMC}} = 3\%$ & $x_{\text{CB}} = 10\%$ (b) measured from $\dot{\gamma} = 500$ to $0.01\ \text{s}^{-1}$, 7 steps of 10 s each per decade to ensure the stationary state is reached. The red (resp. grey) curves are the best HB (resp. TC) fitting of the data. The inset shows $\sigma - \sigma_y$ as a function of $\dot{\gamma}$ with σ_y the yield stress extracted from the fits to emphasize the better agreement of the HB model to the data. (c)-(d) Corresponding relative error $\epsilon_{\text{rel}} = |\sigma_{\text{HB}} - \sigma|/\sigma$ or $\epsilon_{\text{rel}} = |\sigma_{\text{TC}} - \sigma|/\sigma$ as a function of $\dot{\gamma}$ plotted below each flow curve.

[6]For HB one usually uses instead $K = \sigma_y/\dot{\gamma}_c^n$ for the prefactor before $\dot{\gamma}^n$.
[7]Note that these equations hold for $\sigma > \sigma_y$ and only consider positive values for σ and $\dot{\gamma}$.

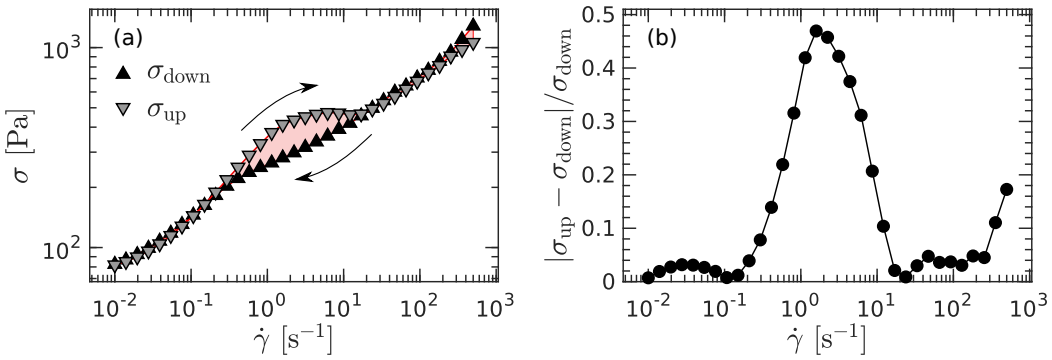

Figure 2.14: Hysteresis in a flow curve for a CB-CMC hydrogel at $c\_\text{CMC} = 3\%$ & $x_{\text{CB}} = 10\%$. (a) Flow curves measured from $\dot{\gamma} = 500$ to 0.01 s^{-1} in black and from $\dot{\gamma} = 0.01$ to 500 s^{-1} in grey. For each flow curve, there are 7 steps per decade, during each step the shear rate is applied for 10 s. The red area corresponds to the are between the two ramping protocols. (b) Relative difference between the stress measured during the ramp up and the ramp down. The area under this curve corresponds to A_σ.

Note that some slip may occur during the flow curve, which is visible in Fig. 2.13(b) by the characteristic change of curvature around $\dot{\gamma} = 0.5$ s^{-1} [232, 233]. Wall slip of the sample is a crucial topic in rheology, but out of the scope of this work. Therefore we did not consider the data for $\dot{\gamma}$ below the onset of wall slip, as they are not representative of the system intrinsically.

The way the flow curve is measured has a huge influence on the flow curve [120, 234]. Here we chose an arbitrary protocol as a compromise between the time taken for each measurement and the limitation of transient effect. The flow curves are measured starting from the highest values of $\dot{\gamma}$ with 7 steps of 10 s per decade. Then, the same experiment is repeated with the same parameters but by starting from the lowest value of $\dot{\gamma}$. Hysteresis between the ramp down and the ramp up of the shear rate may be observed as represented in Fig. 2.14. It arises from several physical mechanisms; the most cited ones are either transient response of the stress, shear-banding, or thixotropy [235, 236]. We quantify this hysteresis through A_σ the normalized area enclosed by the two flow curves:

$$A_\sigma = \frac{1}{\log\left(\dot{\gamma}_{\text{max}}/\dot{\gamma}_{\text{min}}\right)} \int_{\dot{\gamma}_{\text{min}}}^{\dot{\gamma}_{\text{max}}} \left| \frac{\sigma_{\text{up}} - \sigma_{\text{down}}}{\sigma_{\text{down}}} \right| \mathrm{d}\log\dot{\gamma} \tag{2.47}$$

where σ_{down} (resp. σ_{up}) corresponds to the stress computed in the ramp down (resp. up) of $\dot{\gamma}$ between its two extremal values $\dot{\gamma}_{\text{min}}$ and $\dot{\gamma}_{\text{max}}$. Note this definition differs from the one given in [235] as we want here to normalize the area by the typical stress value which depends on the composition–hence the division by σ_{down}, and by the size of the shear rate range–hence the division by $\log\left(\dot{\gamma}_{\text{max}}/\dot{\gamma}_{\text{min}}\right)$. The function whose integral results in A_σ is plotted in Fig. 2.14(b).

Finally, for some systems, there is an equivalence between the linear oscillatory viscoelasticity through the complex viscosity $|\eta^\star(\omega)| = |G^\star(\omega)|/\omega$ and the viscosity $\eta(\dot{\gamma})$ measured under flow. This is referred as the empirical Cox-Merz rule [237], which claims:

$$|\eta^\star(\omega = \dot{\gamma})| = \eta(\dot{\gamma}) \tag{2.48}$$

where the complex viscosity is evaluated at $\omega = \dot{\gamma}$. It means that the timescale excited is the governing parameter for these systems. This rule blurs the line between con-

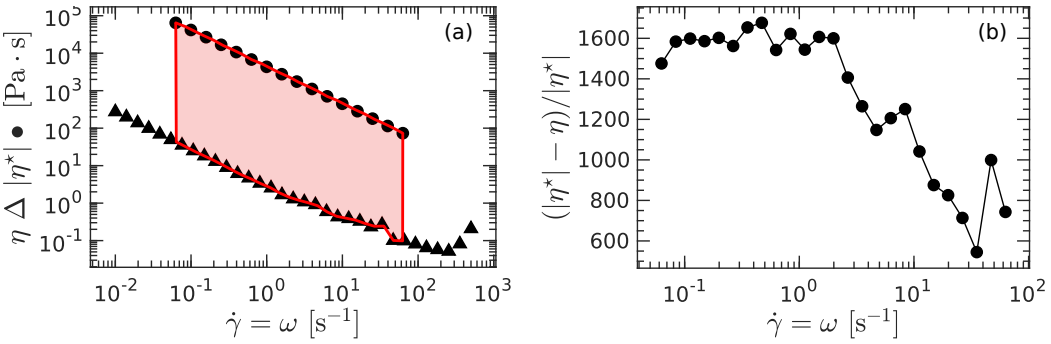

Figure 2.15: Verification of the Cox-Merz rule for a CB-CMC hydrogel at $c_{CMC} = 0.01\%$ & $x_{CB} = 8\%$. (a) Viscosity under flow η versus $\dot{\gamma}$ during the ramp down in triangles, complex viscosity $|\eta^\star|$ versus ω in circles. (b) Relative difference between the two viscosities when $\omega = \dot{\gamma}$, after resampling of the data. The area under this curve corresponds to A_η.

tinuous and oscillatory shear but should really be understood as a phenomenological observation that applies in some cases but is clearly not a general law. For the CB-CMC hydrogels this rule may or may not be verified as plotted in Fig. 2.15. Similarly to the computation of A_σ we define, A_η which quantifies the departure from this rule as the area between the two viscosities:

$$A_\eta = \frac{1}{\log\left(\dot{\gamma}_{max}/\dot{\gamma}_{min}\right)} \int_{\dot{\gamma}_{min}}^{\dot{\gamma}_{max}} \left| \frac{|\eta^\star(\omega = \dot{\gamma})| - \eta(\dot{\gamma})}{|\eta^\star(\omega = \dot{\gamma})|} \right| \mathrm{d}\log\dot{\gamma} \tag{2.49}$$

Where $\dot{\gamma}_{max}$ and $\dot{\gamma}_{min}$ are chosen to maximize the length of the integration where the condition $\omega = \dot{\gamma}$ is achievable. This area is computed numerically using linear interpolation of the $|\eta^\star(\omega)|$ and $\eta(\dot{\gamma})$ curves so that they are defined on the same abscissas.

b Flow Cessation

Finally, we also look at the mechanical behavior when the shear is stopped. The protocol is sketched in Fig. 2.16(a) and presented here. The sample is sheared for 1200 s to reach a steady state characterized by the steady state shear rate $\dot{\gamma}_{SS}$ and stress σ_{SS}. The stress relaxation is recorded as a function of time for 1200 s as well. It eventually reaches a steady state with a non-zero stress, which we call the residual stress σ_{res}. We ensured the rheometer efficiently applied the set shear rate during this process as shown in Fig. 2.16(b). The rheometer reaches a steady state within 0.03 s with a negligible undershoot, transient effects due to the rheometer are therefore not considered.

E Electrical properties

In the context of conductive fluids, their behavior under any electrical stimuli must be understood, as must their mechanical properties. Namely, it is crucial to know the typical values for the electrical resistance and the timescales since they crucially determine the application.

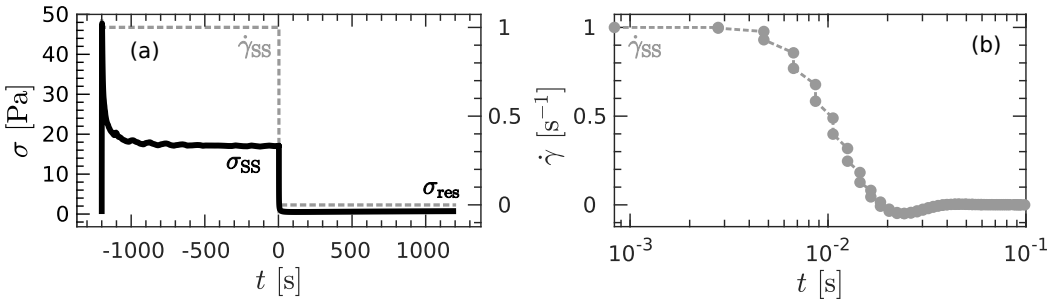

Figure 2.16: Shear protocol during a flow cessation experiment. (a) Stress versus time for a steady state prepared at $\dot{\gamma} = 1$ s^{-1} for 1200 s in the left axis. The steady-state stress σ_{SS} and the residual stress σ_{res} are the plateau values represented in the plot. The right axis shows the shear rate applied corresponding to a step from 0 to $\dot{\gamma}_{SS} = 1\ s^{-1}$ at t =-1200 s. The shear is stopped at $t = 0$. (b) Zoom on the transient regime between the steady state at $\dot{\gamma}_{SS}$ and the full arrest of the flow around $t = 0$, which takes about 0.03 s with the ARES-G2 rheometer used for this experiment.

E.1 Measuring the dielectric properties of complex fluids

Similarly to the rheology section, the goal is to measure the transfer function built on two observables: here, we consider the current I and the voltage U (or $I^\star$ and $U^\star$ in the Fourier space). They are linked through the following equation in the linear regime:

$$U^\star = Z^\star I^\star \tag{2.50}$$
$$Z^\star = Z' - iZ'' \tag{2.51}$$

where we introduced the complex modulus $Z^\star$, that we decompose in its real and imaginary parts Z' and Z''. Z' corresponds to the resistive part, which is responsible for energy loss. Z'' corresponds to the capacitive part, which can store energy. The plot $Z^\star$ as a function of the frequency is the impedance spectrum and can be seen as the electrical fingerprint of the system. Formally, mechanical and electrical algebra are equivalent, considering the following translation given in Table 2.1.

The problem boils down to measuring $Z^\star$ in order to fully describe the linear electrical properties of a system. To do so, the trivial way is here again to apply either U or I and measure the other quantity as a function of the frequency. More subtle protocols with several frequencies at the same time can be conducted but were not enabled by the software (EC-Lab) used here. In practice, the sample is put in a cylindrical cell

Mechanics	Dielectrics	Physical meaning
σ	U	Driving force
$\dot{\gamma}$	I	Flow
$\sigma^\star = G^\star\gamma^\star$	$U^\star = Z^\star I^\star$	Governing equation
G'	Z''	Stored energy
G''	Z'	Dissipated energy
Spring g	Capacitance C	Building block for stored energy
Dashpot η	Resistor R	Building block for dissipated energy
Springpot $\mathbb{V}, \alpha$	Constant Phase Element Q, n	Quasi-property

Table 2.1: Correspondence between the mechanical and the electrical world.

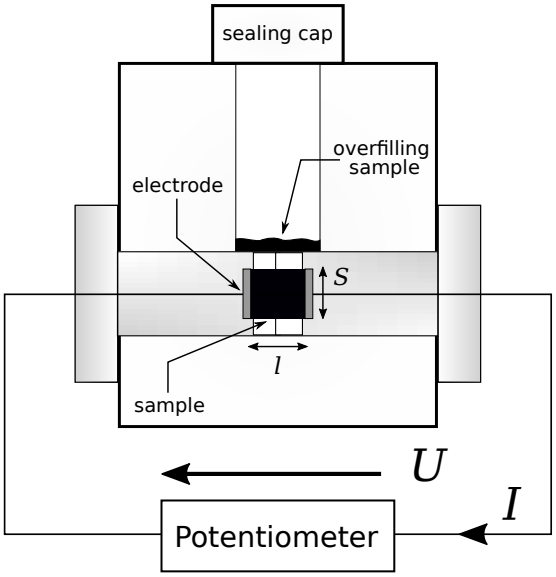

Figure 2.17: Sketch of the dielectric cell. The potentiometer (SP-300 Potentiostat, Biologic) is plugged into a platinum cell within a Teflon box.

embedded in a Teflon box, both caps of the cylinder are made of platinum electrodes to ensure a good electrical contact with the sample. Teflon seals are used to keep the height of the cylinder constant between the different experiments. With a surface of the cap of around $S = 0.5$ cm^2 and a length of around $l = 1$ mm, each experiment scans a sample volume of about 0.05 mL. Yet, to avoid air bubbles and to limit evaporation in the cylinder, the cell is filled with a larger volume of sample ($\simeq 5$ mL), and then the electrodes are screwed so the joints touch. The overfilling impact on the measurement has been reduced thanks to limited contact between the measured sample and the overfilled one through a submillimetric hole in the joints to let the sample flow while screwing the electrodes.

The cell is then connected to a nano-ammeter, itself connected to a potentiometer (SP-300 Potentiostat, Biologic). The measuring protocol is created via the software EC-Lab. To measure an electrical spectrum, the potentiometer applies an alternative voltage to the cell and measures the current going through it. The complex impedance is computed from the amplitude ratio and the phase shift between the two signals. This computation is accurate only in the linear regime, where the voltage is low enough to neglect any electrochemical reactions (e.g., water electrolysis occurs beyond about 1.23 V) or any non-linear dielectric response. To determine this linear regime, we applied a voltage of increasing amplitude at $f = 0$ Hz (DC) and checked the departure from linearity in the current response to the voltage [Fig. 2.18]. Thereafter the amplitude voltage is set to 10 mV.

Computing the impedance depends, however, on the geometrical characteristics of the cell. The relevant value is actually the complex conductivity $\sigma^\star_{\text{elec}}$, defined by:

$$Z^\star = \frac{l}{S\sigma^\star_{\text{elec}}} \tag{2.52}$$

where $l/S = k$ is the cell constant, a purely geometric value (neglecting finite-size effects, as in rheology). Note here that we consider $\sigma^\star_{\text{elec}}$ as a scalar value, in the most general case it should be described as a matrix – so as to capture anisotropy in the

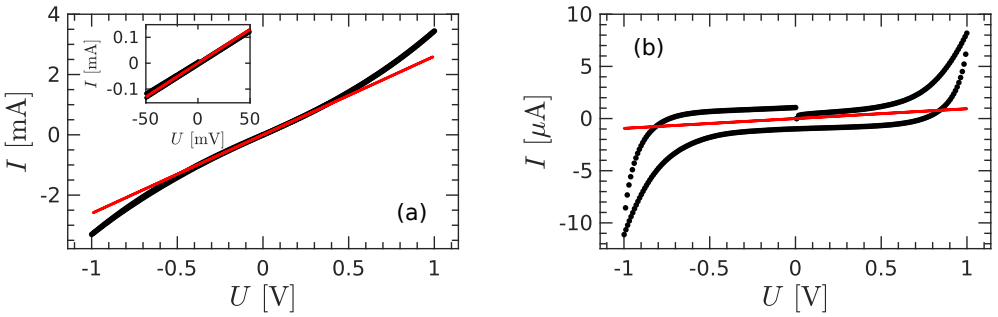

Figure 2.18: Cycla-voltametry experiment: Current as a function of the applied voltage of aqueous solution with $x_{CB} = 8\%$ and (a): $c_{CMC} = 0.1\%$, (b): $c_{CMC} = 2\%$. The inset in (a) is a zoom around 0 V. The red lines correspond to the best linear fit of the data around 0 V. The voltage cycle is a triangular signal starting at 0 V with an amplitude of 1 V and a ramp speed of ± 20 mV per second. Note the change of units for the current: the latter sample is one order of magnitude less conductive, which is captured by the slopes of the red curves (a): 2.6 $m\Omega^{-1}$ and (b): 0.9 $\mu\Omega^{-1}$. The cycle may not be enclosed due to transient response at the beginning of the experiment.

material's electrical properties. Equivalently the complex permittivity $\epsilon^\star$ can be computed from the impedance:

$$Z^\star = \frac{l}{i2\pi f \epsilon^\star S} \tag{2.53}$$

with f the frequency, so that $\sigma^\star_{elec} = i2\pi f \epsilon^\star$. Both conductivity and permittivity can be used, it only depends on the point of view: the former is mostly used when the cell is seen a resistive path whereas the latter corresponds to a capacitance.

In any case, the constant cell k must be determined precisely. The actual dimensions of the cell are unknown and the cell requires to be calibrated using KCl solutions of known concentration and conductivity (Certified conductivity OIML Standard Solution from Radiometer Analytical). Measurements were performed at room temperature at $T = 22 \pm 1°C$. The electrical impedance of these solutions is reported in Fig. 2.19, and fitted by the following equation:

$$Z^\star(f) = R_{ion} + \frac{1}{Q(i2\pi f)^n} \tag{2.54}$$

which corresponds to the impedance of the electrolyte R_{ion} in series[8] with the impedance Z_{CPE} of a constant phase element (CPE) of parameters Q and n modeling the electrode-electrolyte interface [238] (see Section 2.E.2 for more details about the modeling). The cell constant k is then computed to match the expected ionic conductivity σ_{ion} at the given temperature and concentration in KCl so that $k = R_{ion}\sigma_{ion}$. The results yield a cell constant $k = 0.37 \pm 0.01$ cm^{-1}, as shown in the inset in Fig. 2.19. Finally, the fit yields the following values $Q = 1.6 \pm 0.1 \times 10^{-5}$ $\Omega^{-1}.s^{-n}$ and $n = 0.88 \pm 0.01$, independent of the KCl concentration.

E.2 Modeling the electrical response

The complex impedance has already been reported in similar systems as the ones studied in this thesis with CB as well but with different solvents and with additives

[8] The wires and the contact at the interface of the electrodes may add a small resistance (at most around 1 Ω [Fig 2.25]) in series that was neglected compared to the large values obtained.

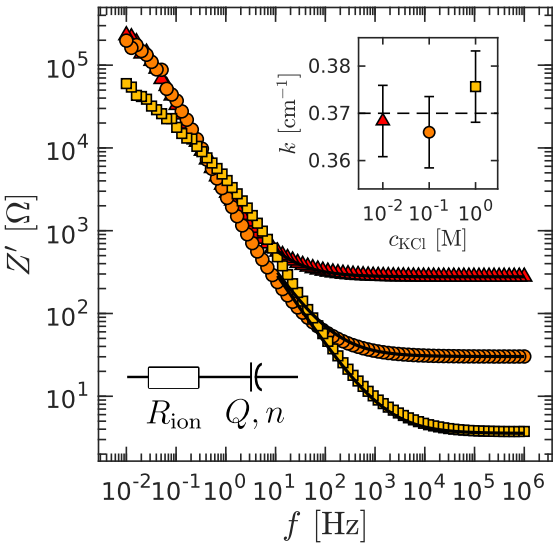

Figure 2.19: Calibration of the dielectric cell. Real part Z' (resistance) of the electrical impedance vs frequency of KCl solutions as measured with the conductivity cell for three different KCl concentrations: $c_{KCl} = 10^{-2}$ M (▲), 10^{-1} M (●), and 1 M (■). The black lines are the best fits of the data with Eq. (2.54) for $f > 10$ Hz. Inset: cell constant k vs. KCl concentration, yielding $k = 0.37 \pm 0.01$ cm^{-1}. The sketch shows the electrical model used to fit the data, in this case with $Q = 1.6 \pm 0.1 \times 10^{-5}$ $\Omega^{-1}.s^{-n}$ and $n = 0.88 \pm 0.01$, independent of the KCl concentration. See Section 2.E.2 for more details.

[106, 239]. The impedance all follow the same shape: a low-frequency plateau value for the real part and a bell-shaped curve for the imaginary part. It corresponds to a semi-circle in a Nyquist representation. Note that the imaginary part can be chosen either negative or positive depending on the convention chosen in Eq. (2.51) where the sign before Z'' may change. The simplest way to describe such systems is to consider two independent paths for the current to flow: either through the network of conductive particles (namely CB) or through charge accumulation at the interface of the electrodes. The main discrepancy between electronic and ionic charge carriers is the ability of electrons to cross the electrode, whereas the ions cannot [240]. The electronic path is thus quite straightforward and can be modeled by a bare resistance. On the other hand, the charge accumulation at the interface arises from the transport of ions in the bulk or electrons in the circuit, both as a response to the electric field. This is reminiscent of a capacitance where the medium between the electrodes is a conductor; physical mechanisms are thus more complex and cannot be modeled by a capacitor. This framework introduces an ionic double layer close to the interfaces: due to the voltage, each electrode is electrically charged, which perturbs the distribution of ions close to the surface. Such double layers have a frequency-dependent response when an oscillating field is applied and is well captured by a Constant Phase Element (CPE) [238, 241–244]. CPEs have a complex impedance including a power-law dependence on the frequency, which is characterized by an exponent n typically between 0 and 1, along with a prefactor Q (expressed in $\Omega^{-1}.s^n$):

$$Z^\star_{CPE} = \frac{1}{Q(i2\pi f)^n} = \frac{\cos(n\pi/2)}{Q(2\pi f)^n} - i\,\frac{\sin(n\pi/2)}{Q(2\pi f)^n} \tag{2.55}$$

CPEs have a constant phase angle independent of the frequency, hence their name. The spectral and temporal behaviors of this CPE are represented in Fig. 2.20. They are the equivalent of the spring-pot element in rheology [211]. The CPE is a generalization of the classic capacitor; in fact, for $n = 1$, one recovers the case of a capacitor (Q is then the capacitance), and for $n = 0$ the case of a resistance (Q is then the conductance). For n between 0 and 1, the CPE corresponds to an element whose behavior is intermediate between that of a resistor and a capacitor. CPEs were first introduced in the context of particle suspensions to model the electrode-electrolyte interface as an imperfect

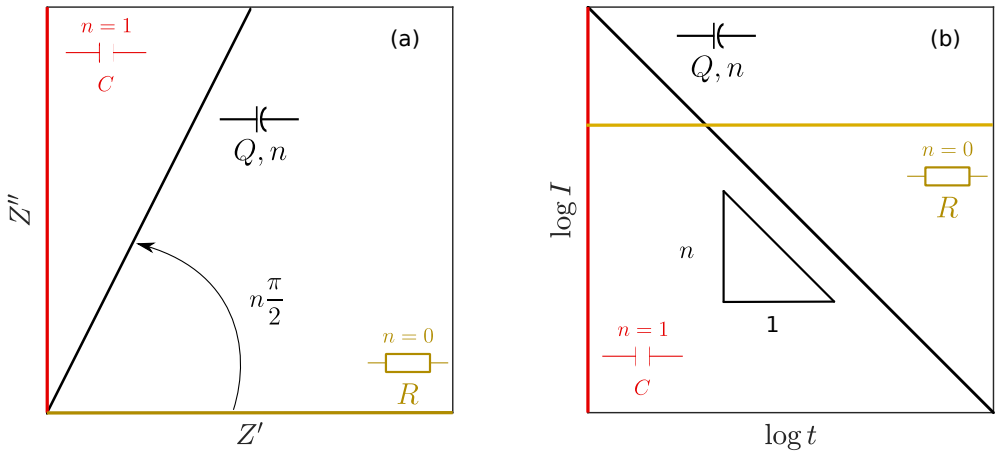

Figure 2.20: Constant Phase Element for different values of n. The extreme cases $n = 0$ in orange and $n = 1$ in red correspond respectively to a resistor and a capacitor. (a) Nyquist plot of the complex impedance, which has a constant phase $n\pi/2$. (b) Current response to a step voltage at $t = 0$ which is a power-law with an exponent n, and the red curve represents a Dirac delta function.

capacitor. Indeed, for $n < 1$, the real part of Z_{CPE} is non-zero, which induces energy losses and testifies to the imperfect nature of the capacitor. The physical interpretation of this peculiar impedance is not clear to date, the main hypothesis is that it comes from (i) heterogeneities at the surface of the electrode due to roughness or irregular current distribution, and/or (ii) subdiffusion processes of ions in the double layer [241, 242, 244].

To fully describe the behavior of the double layer, a resistance R_{ion} is added to the CPE to account for the electrolyte resistance, which quantifies how difficult it is for the ions to move. The full impedance in a cell filled with a sample with electronic and ionic charge carriers is represented in Fig. 2.21(e), and its expression reads:

$$Z^\star(f) = R_{\text{CB}} \frac{1 + R_{\text{ion}} Q (i2\pi f)^n}{1 + (R_{\text{CB}} + R_{\text{ion}}) Q (i2\pi f)^n} \tag{2.56}$$

The two resistances can be converted into electrical conductivities, respectively $\sigma_{\text{CB}} = k/R_{\text{CB}}$ and $\sigma_{\text{ion}} = k/R_{\text{ion}}$, with k the cell constant. With this model one can precisely extract the contribution in conductivity due to the CB network, which is highly informative on its microstructure. Moreover, it clearly appears that the low-frequency limit is the relevant range to probe the CB network since $Z^\star \simeq R_{\text{CB}}$ for small frequencies. A natural cutoff frequency f_c appears in Eq. (2.56):

$$f_c = \frac{1}{2\pi \left[Q \left(R_{\text{CB}} + R_{\text{ion}} \right) \right]^{1/n}} \tag{2.57}$$

Note that this cutoff frequency corresponds to the position of the maximum of Z'', which can be estimated quite easily.

To follow the dynamics of σ_{CB} as a function of time during a mechanical test, a constant voltage is applied and the current is recorded; it formally corresponds to the zero frequency limit in Eq. (2.56). The cutoff frequency appears here as the smallest time resolution by such a protocol: $1/f_c$ represents the electrical response time of the system. If the timescale is smaller than $1/f_c$, one will not be able to decouple the time-dependence of R_{CB} to the time-dependence response. In other words, the system

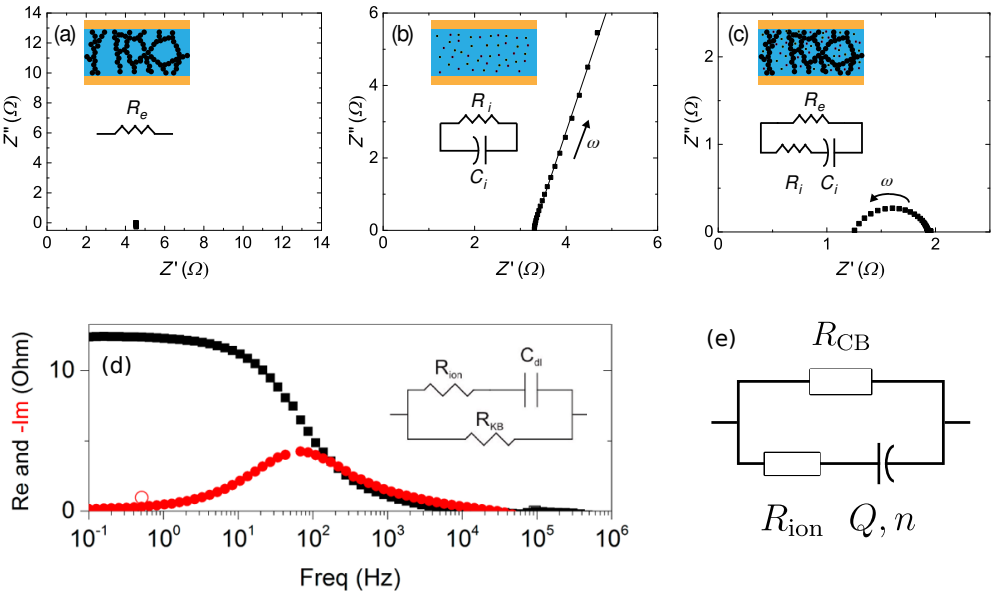

Figure 2.21: Complex impedance in different canonical systems. Nyquist plot of the complex impedance for a system with: (a) only electronic transport with a suspension of CB in oil, (b) only ionic transport with a KCl solution, (c) both with a suspension of CB in a strongly ionic aqueous solution (lithium polysulfide). Frequency ranges from $\omega = 2\pi f = 10^2$ to 10^4 rad $\cdot$ s^{-}1. Adapted from [239]. (d) Bode plot of the complex impedance for a CB suspension in organic solvent with a high concentration of $LiPF_6$. Adapted from [106]. (e) Equivalent electric circuit used in this thesis: R_{ion} and R_{CB} are resistors; Q, n is a CPE with an exponent n and a prefactor Q.

must be in a quasi-stationary state so that the response of the system to the electrical excitation is faster than the physical evolution of the system. A numerical resolution can be conducted to check the relevance of this framework. The knowledge of the complex impedance in the Fourier space can be translated into the time space with the following differential equation:

$$(R_{CB} + R_{ion})Q\frac{d^n U}{dt^n} + U = R_{CB}R_{ion}Q\frac{d^n I}{dt^n} + R_{CB}I \tag{2.58}$$

where d^n/dt^n is a fractional derivative and R_{CB} may evolve in time. The Matlab function "MT_FDE_PI1_Im" [245] was used to solve this fractional differential equation numerically, where the input is a step function for the voltage $U(t) = U_0\mathcal{H}(t)$ with $\mathcal{H}$ the Heaviside step function, and $R_{CB}(t) = R^0_{CB}(1 + \epsilon f_c t)$, so that ϵ characterizes the speed of the time evolution in R_{CB} and R^0_{CB} the typical initial value for R_{CB}.

To solve this equation, initial values are needed for $I(t)$ and its first derivative. They are computed thanks to the initial value theorem in the Laplace space, with $\tilde{i}$ (resp. $\tilde{u}$) is the Laplace transform of I (resp. U). We first assume R_{CB} constant for the

sake of simplicity.

$$I(t=0^+) = \lim_{s\to\infty} s\tilde{i}(s) \tag{2.59}$$

$$= \lim_{s\to\infty} s\frac{\tilde{u}(s)}{R_{CB}}\frac{1+(R_{CB}+R_{ion})Qs^n}{1+R_{ion}Qs^n} \tag{2.60}$$

$$= \lim_{s\to\infty} s\frac{U_0}{sR_{CB}}\frac{1+(R_{CB}+R_{ion})Qs^n}{1+R_{ion}Qs^n} \tag{2.61}$$

$$= U_0\frac{R_{CB}+R_{ion}}{R_{CB}R_{ion}} \tag{2.62}$$

$$\frac{dI}{dt}_{|t=0^+} = \lim_{s\to\infty} s\left(s\tilde{i}(s) - I(t=0^-)\right) \tag{2.63}$$

$$= \lim_{s\to\infty} s\left(\frac{U_0}{R_{CB}}\frac{1+(R_{CB}+R_{ion})Qs^n}{1+R_{ion}Qs^n} - 0\right) \tag{2.64}$$

$$= \infty \tag{2.65}$$

Both initial conditions are consistent with the intuition one can have on the system if the CPE is considered as a capacitor: at short time scales the capacitor is equivalent to a wire and the whole circuit is equivalent to R_{CB} in parallel association with R_{ion}. It suggests that the same initial conditions can be applied in the case of time-dependent R_{CB}, for which the relevant value is thus $R_{CB}(t=0)$. The numerical resolution of the current $I(t)$ response to a step voltage $U(t) = U_0\mathcal{H}(t)$ is plotted in Fig. 2.22 (a) for different speeds in the evolution of R_{CB} with the typical values of R_{ion}, Q and n. The effective value of the CB resistance $R_{CB}^{eff} = U_0/I$ is compared to the actual value of R_{CB} input in the simulation in Fig. 2.22 (b). For $\epsilon < 1$, the effective and the real values are comparable when $f_c t \gtrsim 1$: the current faithfully follows the evolution of R_{CB} after a transient regime because the response time is smaller than the typical evolution time of R_{CB}. However, for $\epsilon = 10$, R_{CB}^{eff} underestimates the real value because there is

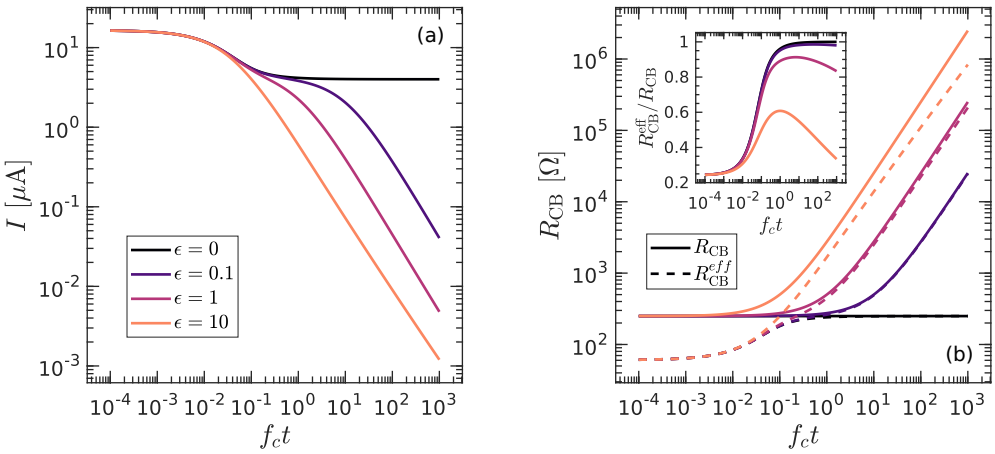

Figure 2.22: Numerical resolution of the response to a step voltage $U(t) = U_0\mathcal{H}(t)$ applied with $U_0 = 1$ V to the electric circuit sketched in Fig. 2.21(e) with $R_{ion} = 80\ \Omega$, $n = 0.8$, $Q = 2.10^{-5}\ \Omega^{-1}.s^n$ and $R_{CB}(t) = R_{CB}^0(1+\epsilon f_c t)$ with $R_{CB}^0 = 250\ \Omega$ and $f_c = 85$ Hz. The parameters have been chosen to match the typical values found for the system studied in this manuscript. Colors encode the values of ϵ, lighter colors correspond to larger values of ϵ from 0 to 10 and the timescale is normalized by the cutoff frequency f_c. (a) Current going through the circuit. (b) Actual R_{CB} input in the code (solid lines) and the effective computed value extracted from the current $R_{CB}^{eff} = U_0/I$ (dashed lines); the inset shows the ratio R_{CB}^{eff}/R_{CB}.

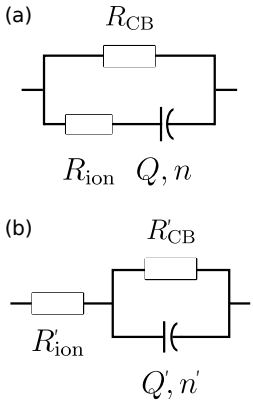

Figure 2.23: Equivalence between two models. Two equivalent representations of the same electrical impedance with different electric circuits when the parameters are well chosen. (a) Model used in the manuscript and commonly acknowledged in the literature. (b) Equivalent circuit, which physical interpretation is less straightforward.

a lag between the current response and the evolution of R_{CB}. We demonstrated here that dynamic dielectric experiments are physically limited by a threshold set by the response time of the equivalent electrical circuit: the smallest timescale reachable is indeed determined by the cutoff frequency of the circuit. A feature that remains unexplained here is the long-term behavior of R_{CB}^{eff}, which seems to start slowly drifting away from R_{CB} when $f_c t \gtrsim 1$. For slow enough dynamics, i.e., small ϵ, the feature is extremely small: a drop of less than 1% at the longest time computed here with $\epsilon = 0.1$. This effect disappears when $n = 1$, which suggests this is not a numerical error.

One should emphasize that the equivalent electric circuit is not unique: with two resistors and a CPE one can recall the same total impedance by changing the values of the building blocks of the circuit. In Fig. 2.23(b), the complex impedance reads:

$$Z^\star(f) = \frac{(R'_{CB} + R'_{ion}) + R'_{CB}R'_{ion}Q'(i2\pi f)^{n'}}{1 + R'_{CB}Q'(i2\pi f)^{n'}} \tag{2.66}$$

This model is strictly equivalent to the one in Fig. 2.23(a) with the impedance given in Eq. (2.56) when:

$$R'_{CB} = R_{CB}\left(\frac{R_{CB}}{R_{CB} + R_{ion}}\right) \tag{2.67}$$

$$R'_{ion} = R_{ion}\left(\frac{R_{CB}}{R_{CB} + R_{ion}}\right) \tag{2.68}$$

$$Q' = Q\left(\frac{R_{CB} + R_{ion}}{R_{CB}}\right)^2 \tag{2.69}$$

$$n' = n \tag{2.70}$$

In the present work, we observe that $R_{ion} \ll R_{CB}$, which leads to $R'_{ion} \simeq R_{ion}$, $R'_{CB} \simeq R_{CB}$, $Q' \simeq Q$, and $n' \simeq n$. In other words, both models are expected to lead to indistinguishable fits of the impedance spectra and to the same set of physical parameters.

E.3 Rheo-Impedance Spectroscopy

In flow batteries fluids are scarcely at rest. It is, therefore, of great interest to understand the evolution of the dielectric properties in regard to the flow undergone by the fluid. Naturally, the best way appears to conduct coupled electrical and mechanical

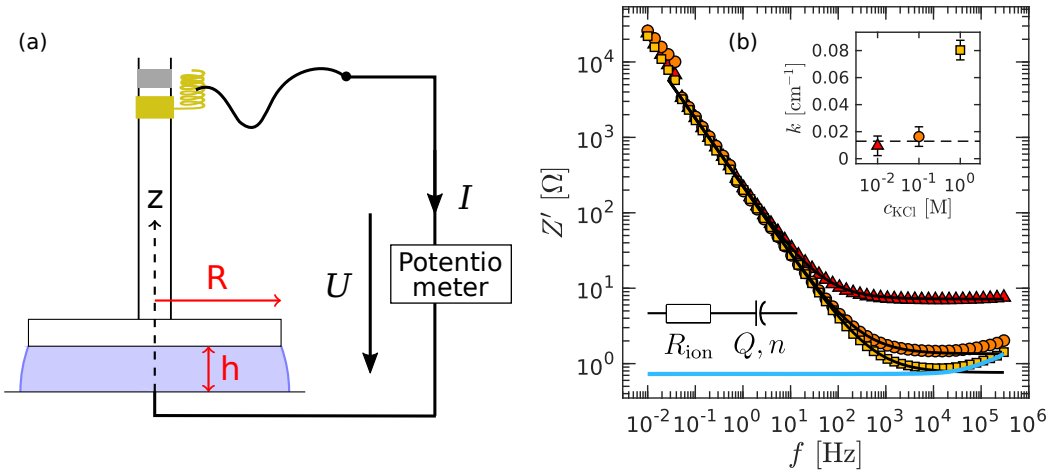

Figure 2.24: Rheo-electrical setup. (a) Sketch of the rheo-electric setup. All cables are clamped except the wire between the spring (colored in gold) and the plug represented by the black dot. The grey zone at the top of the rotor is an insulator to prevent any current from going through the electronics of the rheometer. (b) Real part Z' (resistance) of the electrical impedance vs frequency of KCl solutions as measured in the rheometer dielectric geometry (parallel plate, diameter $d = 40$ mm and gap $h = 1$ mm) for three different KCl concentrations: $c_{\text{KCl}} = 10^{-2}$ M (▲), 10^{-1} M (●), and 1 M (■). The black lines are the best fits of the data with Eq. (2.54) for $f > 10$ Hz. The blue line corresponds to the data for a liquid metal (Gallium-Indium alloy). Inset: cell constant k vs. KCl concentration, yielding $k = 0.013 \pm 0.005$ cm^{-1} (excluding the value computed from $c_{\text{KCl}} = 1$ M, which data are within the setup limitations). The sketch shows the electrical model used to fit the data, in this case with $Q = 1.3 \pm 0.1 \times 10^{-4}$ Ω^{-1}.s^n and $n = 0.90 \pm 0.1$, independent of the KCl concentration.

measurements within a rheometer. For the sake of simplicity, we use a 50 mm diameter parallel-plate geometry [see Fig. 2.24(a)]. The constant gap simplifies the interpretation of the electrical response. The upper and bottom plates become in this setup the electrodes. The biggest challenge arises from the electrical contact at the rotor (upper plate), which must not alter the mechanical measurements [239]. In this work, we used a commercial setup from Anton Paar. To ensure electrical contact, the tip of a loosened coper wire is stuck between two loops of a tight spring, which is attached to the rotor. The other end of the wire is fixed to the rheometer, its total length (~ 5 cm) and diameter (~ 0.5 mm) are chosen to limit the impact on mechanical measurements.

We used the same protocol as in Section 2.E.1 to obtain the cell constant of the rheometer. We will stick to the same gap $h = 1$ mm used in the calibration for most of the experiments. The calibration yields a cell constant $k = 0.013 \pm 0.005$ cm^{-1} for the parallel-plate geometry with a diameter $d = 40$ mm and a gap $h = 1$ mm, as shown in Fig. 2.24(b). The fitting parameters were estimated to $Q = 1.3 \pm 0.1 \times 10^{-4}$ Ω^{-1}.s^n and $n = 0.90 \pm 0.1$, independent of the KCl concentration. The blue horizontal line corresponds to Z' for an EGaIn alloy (Gallium-Indium eutectic 75.5%-24.5% wt. from ThermoFisher), which is a liquid metal at room temperature. It was used to estimate the low impedance limit of this setup. This alloy behaves as an extremely low resistor so that the impedance measured, loaded with it, is an image of the impedance of the setup itself. The lowest impedance measurable with this setup is around 0.8 Ω for frequencies below 10 kHz and 1-2 Ω for frequencies between 10 kHz and 1 MHz. The imaginary part of the impedance with the Ga-In alloy is an order of magnitude below. The wire will indisputably add a torque to the mechanical measurement, to evaluate this contribution we let the rheometer oscillate at $f = 1$ Hz and measure an

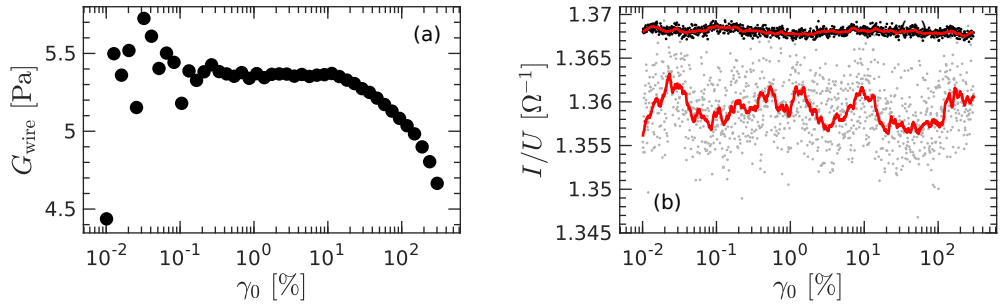

Figure 2.25: Rheo-dielectri experimental limitations. (a) Amplitude of the elastic modulus G_{wire} computed for the rheo-electric setup without any sample loaded, as a function of the strain amplitude during an oscillatory shear at $f = 1$ Hz. This modulus arises from the torque contribution of the wire, which represents the lowest value measurable with this setup. (b) Influence of the strain amplitude during an oscillatory shear at 1 Hz on the measurement of the current I in an EGaIn alloy when a constant voltage U is applied: 100 mV in black and 10 mV in gray. The red curves correspond to a moving average of the data over 1% of the total signal. The gap is set to 1 mm.

effective modulus as a function of the strain amplitude. The effective modulus G_{wire} is estimated around 5 Pa with an empty loading in the rheometer [Fig.2.25 (a)], it decreases at large amplitudes when the wire unfolds. For further experiments, we shall remain in the framework of moduli way above 5 Pa, which means not all systems will be suitable for this setup. The electrical connection induces an error in the mechanical measurement, we also need to check the other way around. During an experiment the wire will move, which could have an impact on the electrical measurements as well. We check this in with an EGaIn alloy loading and see how the electrical measurements are influenced by the oscillations during an oscillatory shear at $f = 1$ Hz, as a function of the oscillation amplitude. A constant voltage (10 or 100 mV) is applied, and the current is measured [Fig.2.25 (b)]. Although fluctuations are visible, they are not correlated to the strain amplitude, which means the electrical measurements can be safely assumed to be independent on the mechanical protocol.

Two typical measurements are done with this setup: static and dynamic measurements. For the static one, the goal is to probe the sample at a particular step of the mechanical protocol, e.g., to compare the state before and after a strain sweep. In this case, a full dielectric spectrum is recorded in the rheometer; the results and analysis are the same as the ones described above with the dielectric cell. On the other hand, to probe precisely the dynamics of the system under a controlled shear protocol, the full dielectric spectrum is not accessible as it takes too much time to measure. Instead we record the current I as a function of time as a response to an applied constant voltage U_0. It corresponds to the zero-frequency conductivity:

$$\sigma_{\text{DC}}(t) = k\frac{I(t)}{U_0} \tag{2.71}$$

as detailed in the above Section 2.E.2. Time synchronization is ensured by a triggering from the rheometer to the potentiometer. Eventually, the signal σ_{DC} versus t undergoes a spectral analysis, allowed by the high-frequency rate available with the potentiometer (typically 100 Hz). We note $\sigma^{\star}_{DC}$ its Fourier transform, which is normalized so that $|\sigma^{\star}_{DC}(f = 0)|$ and σ_{DC} have the same mean value. Ultimately they are expressed in the same units. To study the time-dependence of the spectral response, we look at the signal through the lens of a time-frequency plot as shown in Fig. 2.26(e), which

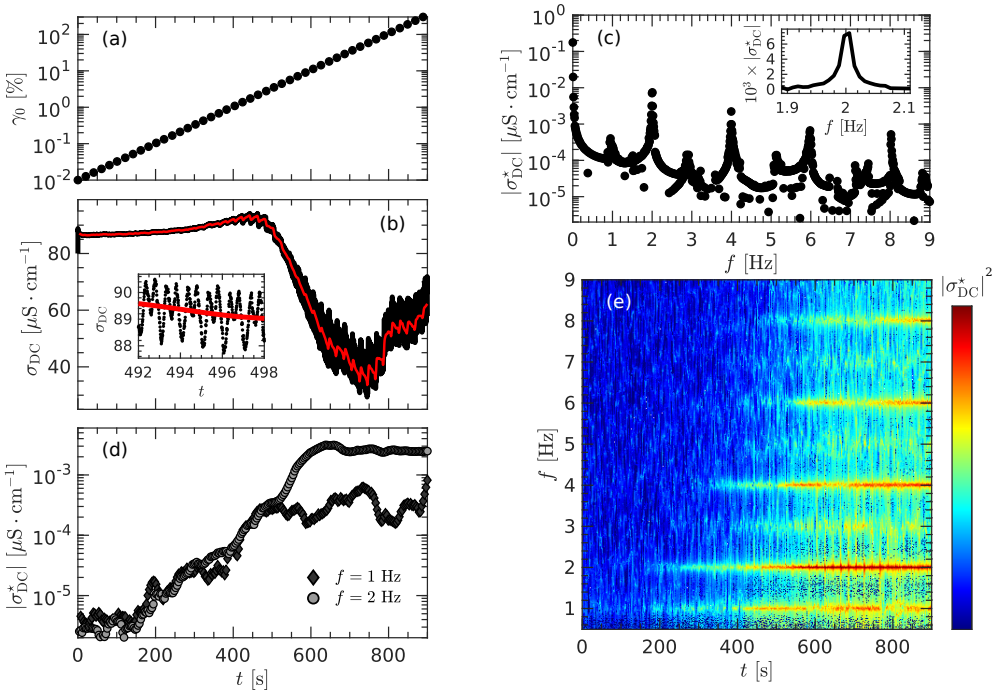

Figure 2.26: DC electrical dynamic response of a CB-CMC gel ($c_{CMC} = 0.01\%$ and $x_{CB} = 4\%$) during a strain sweep under oscillatory shear at $\omega = 2\pi$ rad/s ($= 1$ Hz). (a) Strain amplitude as a function of time. (b) Conductivity as a function of time: raw data σ_{DC} in black and the zero-frequency component of its Fourier transform $|\sigma^\star_{DC}(f = 0)|$ in red. The inset emphasizes the high sample rate with a zoom of the data between $t = 492 - 498$ s. (c) Fourier transform of the signal σ_{DC} around $t = 800$ s. The inset shows the typical broadness of the peaks with a zoom around $f = 2$ Hz. (d) Time dependence of the 1 Hz (dark diamonds) and 2 Hz (grey circles) components of $|\sigma^\star_{DC}|$. (e) Time-frequency plot of the power spectrum $|\sigma^\star_{DC}|^2$, which value is encoded by the color bar (log spacing from 10^{-12} in blue to 10^{-2} in red). The zero frequency is not represented as its amplitude is at least 3 orders of magnitude above any other frequency.

basically corresponds to computing the Fourier transform of the signal over a moving window along the signal. The size of the window sets the temporal and frequency resolutions, here we chose a window of 15 s as a compromise between both. Ultimately, the time dependence of $|\sigma^\star_{DC}(f = 0)|$ is exactly $\sigma_{DC}(t)$. When an oscillatory shear is applied, the electrical signal contains only multiples of the shear frequency, as observed in Fig. 2.26. To study these harmonics, their amplitude is averaged over the broadness of the peak [Fig. 2.26(c)-(e)], as this feature mainly comes from the choice of the window for the Fourier Transform. We set the average over 0.05 Hz on each side of the peak for all frequencies.

F Low-field Nuclear Magnetic Resonance

Nuclear Magnetic Resonance (NMR) is widely used to characterize chemical compounds as it is highly sensitive to the environment of the nuclei probed. Here the said nucleus is the one of the hydrogen atom ^{1}H (or proton), similarly to the usual high-field NMR experiments. With NMR we measure the response of the proton spin to a magnetic excitation. We note $\boldsymbol{M}_0$ the average direction of the spins. The sample is put in a strong constant magnetic field $\boldsymbol{B}_0$, which aligns the protons spin with the

direction of $\boldsymbol{B}_0$. The spins precess around this axis, which sets a resonant frequency, known as the Larmor frequency [246]. A second magnetic field $\boldsymbol{B}_1$ is applied to the sample, but this one rotates[9] in the xy plane, perpendicular to the direction z of $\boldsymbol{B}_0$. If the rotation frequency is equal to the resonant one, the direction of the spins is shifted out of the z direction towards the xy plane. Then, B_1 is turned off and the spin relaxes towards the z direction. The time during which B_1 is applied is set so that the spin direction M_0 is in the xy, which maximizes the signal measured. It is called a $\pi/2$-pulse, and it corresponds to the first step in Fig. 2.27. Then $\boldsymbol{M}_0$ is let to relax towards the z direction and we measure the component $M_{0,xy}$ of $\boldsymbol{M}_0$ in the xy plane which is usually described by an exponential decay according to the Bloch equations. We extract from this transverse[10] relaxation time T_2.

This protocol corresponds to a Free Induced Decay (FID). In practice, the FIDs are not trustworthy for large values of T_2 because of the spatial heterogeneities in $\boldsymbol{B}_0$ [246]. As depicted in Fig. 2.27, in this case, each spin relaxes differently, and it impacts the averaged $M_{0,xy}$ is not representative of the real relaxation. To avoid this issue we apply at a time T_E after the initial pulse a π-pulse: $\boldsymbol{B}_1$ is turned on for twice the time of the $\pi/2$-pulse. After this second pulse, each individual spin is flipped. Then the sample is let to relax for another T_E, and the heterogeneities are compensated thanks to this flip (if the heterogeneity accelerates the spin decay before the π-pulse, it will slow it after and vice-versa). We now have a faithful measurement of $M_{0,xy}$ at time $t = 2T_E$, this is known as the Spin Echo. From this point, we can repeat the process and apply a π-pulse at $t = 3T_E$ in order to measure $M_{0,xy}$ at $t = 4T_E$, and so on and so forth to eventually record the full relaxation of $M_{0,xy}(t)$. T_E appears thus as the sampling rate of the measurement. This is the Carr-Purcell-Meiboom-Gill (CPMG) echo train procedure [247, 248], which is generally used to measure large values of T_2 where the heterogeneities have a huge impact.

This low-field NMR is a more accessible version of the high-field NMR used in chemistry. The principle remains the same but the values of B_0 are larger in the latter case. With a high enough amplitude, the magnetic heterogeneities can be examined and linked to the chemical structure. In this case, a Fourier analysis of the decay after a $\pi/2$-pulse is performed [246].

For the experiments conducted in this manuscript we use a low-field NMR pulsed spectrometer (Bruker Minispec mq20), at a 20 MHz proton resonance frequency. The

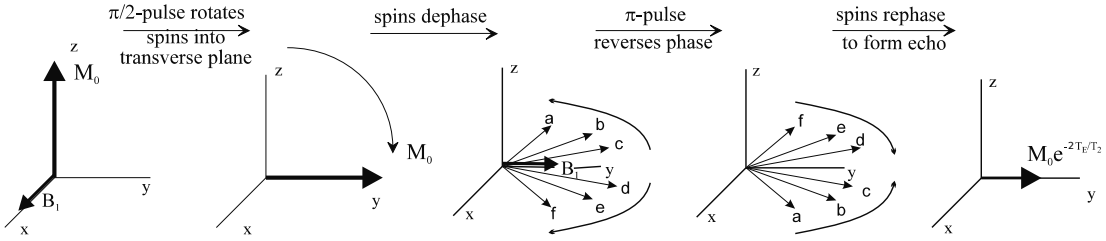

Figure 2.27: Spin relaxation in a NMR experiment. Sketch of the spin echo procedure in a heterogeneous medium. The referential frame is the rotating frame following the rotation of $\boldsymbol{B}_1$. Each letter a-f corresponds to an individual spin, which is submitted a different value of $\boldsymbol{B}_0$ due to spatial heterogeneities. For the sake of clarity, only the components in the xy plane of the spins and $\boldsymbol{M}_0$ are represented. Adapted from [246].

[9] In practice an oscillating field is applied along just one direction x or y, as the resonance is sharp it is equivalent to a rotating field.

[10] The relaxation time along the z axis is T_1.

samples are placed into a tube with a diameter of 1 cm, and filled up to a height of ca. 3 mm, to limit spatial heterogeneities of the magnetic field. The echo time was estimated to 1 ms, and the signal at short times was systematically adjusted to be between 60% and 100% intensity, ensuring optimal statistics without any risk of saturation. We measure T_2 for different temperatures from 283 K up to 343 K thanks to a BVT 3000 heater working with nitrogen gas. Prior to each experiment, the temperature was stabilized for 10 min.

G Small-Angle Scattering (SAS)

G.1 General overview

a Scattering measurements

Scattering experiments all rely on the interaction between waves and matter and are extremely insightful on the structure at the nanoscale to microscale in the material probed. The waves can be either electromagnetic waves with different wavelengths (X-rays, light), or particle waves (neutron). In each case, the scattering arises from the difference in the way the wave interacts with the components in the system, which is quantified by the contrast factor $\Delta\rho$, expressed in [m^{-2}]. The intensity of the scattered wave depends on the diffraction angle θ represented in Fig. 2.28 and corresponds to the angle between the incident wave and the diffracted one. The physically relevant parameter is the scattering wave vector $\boldsymbol{q}$, whose amplitude is given by:

$$|\boldsymbol{q}| = \frac{4\pi \sin\theta}{\lambda} \tag{2.72}$$

with λ the wavelength of the incident wave [250]. Defined this way, the wave vectors can be compared with different sources. In the isotropic, binary, and monodisperse case with only one kind of scatterer described in this work, only the amplitude of $\boldsymbol{q}$ matters, and $\Delta\rho$ is constant. The scattered intensity $I(q)$ per unit volume can be written as:

$$I(q) = \Delta\rho^2 \phi V_{\text{part}} P(q) S(q) \tag{2.73}$$

where ϕ is the volume fraction of scatterers, V_{part} is the volume of one scatterer, P and S respectively the form and structure factors are normalized such that $P(q \to 0) = 1$ and $S(q \to \infty) = 1$. Both are discussed in more detail in the following.

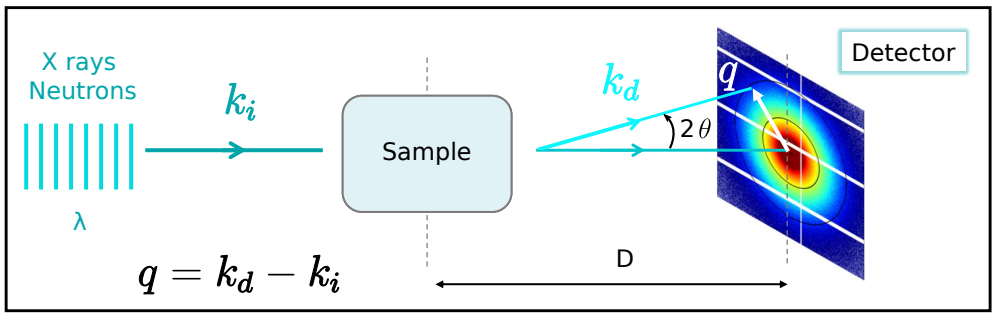

Figure 2.28: Sketch of a small angle scattering setup. The incident beam can either be neutrons or X-rays with a wavelength λ. The scattering wave vector $\boldsymbol{q}$ is the difference between the incident beam wave vector $\boldsymbol{k}_i$ and the scattered one $\boldsymbol{k}_d$, which has an angle 2θ from $\boldsymbol{k}_i$. The detector is at a distance D from the sample. Adapted from [249].

b Form factor

The form factor describes the individual particles. In the diluted regime ($\phi \to 0$), the scattering intensity and the form factor are equivalent (as $S(q) \to 1$). For the monodisperse case where all the particles are identical, the form factor is expressed as:

$$P(q) = \frac{1}{V_{\text{part}}^2} \left| \int_{V_{\text{particle}}} e^{-i\boldsymbol{q}\cdot\boldsymbol{r}} \mathrm{d}^3\boldsymbol{r} \right|^2 \tag{2.74}$$

where the integration is computed among all positions $\boldsymbol{r}$ within the volume of a particle V_{particle}. This general equation is usually difficult to compute, apart from simple geometry, e.g., spheres and rods [250]. To overcome this issue, one may consider two asymptotic cases: the low-q and the high-q regimes.

Guinier regime: low-q limit

The Guinier approach proposes to describe any shape as a sum of different equal-sized spheres. It is especially relevant in the low-q limit since it corresponds to a large scale point of view far from the details at small scales. In this framework, the form factor can be approximated to:

$$P(q) \simeq 1 - \frac{1}{3}(qR_G)^2 \tag{2.75}$$

where R_G is the radius of gyration of the particle, which corresponds to its typical size (for a sphere of radius R, $R_G = \sqrt{3/5}R$). This equation corresponds to a Taylor expansion of P as a function of q, which holds for $qR_G \lesssim 1$. Note that this expression is equivalent to the expression often encountered $P(q) \simeq \exp(-(qR_G)^2/3)$ in the low-q regime.

Porod regime: high-q limit

In the case of a sharp interface between the particle and the surrounding medium, the high-q limit of the form factor decays as a power law of the wave vector:

$$P(q) \simeq Kq^{-(6-D_s)} \tag{2.76}$$

where D_s is the fractal dimension of the surface, which ranges between $D_s = 2$ for a smooth interface and $D_s = 3$ for a rough surface.

c Structure factor

The structure factor is q-dependent when the scatterers are in a large enough amount to interact with each other (recall $S(q) \to 1$ when $\phi \to 0$). It can be shown [250] that the structure factor is an image of the radial distribution function $g_{\text{corr}}(\boldsymbol{r})$, which is related to the probability of finding a particle at a position $\boldsymbol{r}$ from a particle:

$$S(q) = 1 + \phi \int_V e^{-i\boldsymbol{q}\cdot\mathrm{r}} [g_{\text{corr}}(\boldsymbol{r}) - 1] \mathrm{d}^3\boldsymbol{r} \tag{2.77}$$

where the integration is made over the volume V probed by the beam [250]. The ϕ factor in the second term is reminiscent of the fact it is a pair-interaction factor. The link between the g_{corr} and S is not straightforward, however one can get the typical correlation length scale r_{max} between particles from the scattering intensity thanks to

the so-called "Bragg condition" [250]. It states that $r_{peak} \simeq 2\pi/q_{peak}$ where q_{peak} is the position of the possible peak of scattering intensity. It also implies that in order to measure correlations over this distance, the setup should reach wave-vector amplitude below $q_{low} \simeq 2\pi/r_{peak}$.

d Key additional concepts in scattering

Polydispersity

In the case of polydisperse particles, a size distribution must be added to account for the different contributions of each particle [250]. The structure factor does not change as long as the interactions do not depend on the size of the particles. The overall expression of the scattering intensity, however, includes new terms accounting for the size distribution:

$$I(q) = \underbrace{\Delta\rho^2\phi \left\langle V_{\text{part}} P(q) \right\rangle S(q)}_{\text{average scattering term}} - \underbrace{\Delta\rho^2\phi (S(q)-1)\Xi(q)}_{\text{correction term}} \tag{2.78}$$

where $\langle ... \rangle$ is the average over the particle size and Ξ tends to 0 when the polydispersity vanishes, which corresponds roughly to some kind of the variance of the form factor due to the size distribution[11].

Invariant

It should be noted that the following expression is an invariant for a given composition:

$$Q_{\text{SAS}} = \int q^2 I(q) \mathrm{d}q = cte \tag{2.79}$$

It corresponds to the mean-square density fluctuation over the whole system and depends only on the composition of the sample [250]. In this manuscript, we define a restricted computation of Q_{SAS} over a range δq:

$$Q_{\delta q} = \int_{\delta q} q^2 I(q) \mathrm{d}q \tag{2.80}$$

We typically set $\delta q = [q_a \; q_b]$ with $q_a = 2.10^{-3}$ nm^{-1} and $q_b = 4.10^{-2}$ nm^{-1}. These values were chosen for CB-CMC hydrogels in SAXS, such that $Q_{\delta q}$ for $q > q_b$ corresponds to the form factor and remain constant, and $Q_{\delta q}$ for $q < q_a$ is experimentally unreachable. One therefore has:

$$Q_{\text{SAS}} = \underbrace{\int_0^{q_a} q^2 I(q) \mathrm{d}q}_{\text{experimentally inaccessible data}} + \underbrace{Q_{\delta q}}_{\text{measurable data}} + \underbrace{\int_{q_a}^{\infty} q^2 I(q) \mathrm{d}q}_{\text{constant term}} \tag{2.81}$$

With Q_{SAS} being a constant, any change in $Q_{\delta q}$ must be compensated by the first term in Eq. (2.81), which corresponds to out-of-frame data.

Background

The solvent itself may lead to a scattering pattern. The background also includes the incoherent scattering, which arises from the fluctuations in the contrast factor and

[11] Formally $\Xi(q) = \left\langle \left| \frac{1}{V_{\text{part}}} \int_{V_{\text{particle}}} e^{-i\boldsymbol{q}\cdot\boldsymbol{r}} \mathrm{d}^3\boldsymbol{r} \right|^2 \right\rangle - \left| \left\langle \frac{1}{V_{\text{part}}} \int_{V_{\text{particle}}} e^{-i\boldsymbol{q}\cdot\boldsymbol{r}} \mathrm{d}^3\boldsymbol{r} \right\rangle \right|^2$.

does not depend on q. It also accounts for diffraction by the holder. The total scattering intensity reads then:

$$I_{\text{tot}} = I_{\text{sample}} + I_{\text{empty}} + I_{\text{solvent}} + I_{\text{incoherent}} \tag{2.82}$$

In the data analysis, the background must be cautiously removed to make sure one only looks at I_{sample}. The procedure is described in Section 2.G.2.a.

Multiple types of scatterers

In the case of a three-component system, such as the water-based CB-CMC solutions under study, the total scattered intensity is more complicated [251–253]. It is basically the sum of the scattering intensity of the solvent intensity together with the scattering intensity of each component a and b, to which a cross term is added. It corresponds to the correlation between a and b, which gives rise to a cross term proportional to the geometrical average of both volume fractions of each component.

$$I(q) = \underbrace{\Delta\rho_a^2 \phi_a V_{\text{part,a}} P_a(q) S_a(q)}_{\text{scatterer a}} + \underbrace{\Delta\rho_b^2 \phi_b V_{\text{part,b}} P_b(q) S_b(q)}_{\text{scatterer b}} + \underbrace{2\Delta\rho_a \Delta\rho_b \sqrt{\phi_a \phi_b} I_{\text{ab}}(q)}_{\text{cross term}} \tag{2.83}$$

This equation is usually simplified by discarding the cross term, as it is often negligible when one term dominates the other because of the scaling with $\Delta\rho$ and ϕ.

e Differences between Neutron ans X-ray scattering

In this work, Small Angle X-ray Scattering (SAXS) and Small Angle Neutron Scattering (SANS) have been conducted. We shall discuss here the main differences between SAXS and SANS. First of all, scattering is only visible if the waves are not absorbed by the sample probed. This is why light scattering is unfortunately not possible for carbon black dispersions. SAXS and SANS have similar wavelengths so that the q ranges are roughly the same for comparable sample-to-detector distances. At the ESRF (ID02), the wavelength is $\lambda_{\text{SAXS}} = 0.1$ nm and the detector can move from 0.8 m to 31 m so that the wave-vectors available are within 10^{-3} to 60 nm^{-1}. At the ILL (D22) the wavelength is either $\lambda_{\text{ILL}} = 0.6$ nm or $\lambda_{\text{ILL}} = 1.2$ nm and the detector can move from 1.3 m to 18 m so that the wave-vectors available are within 1.5x10^{-3} to 10 nm^{-1}.

The main reason why SAXS and SANS experiments are complementary is due to the prefactor $\Delta\rho^2$ in Eq. (2.73). This contrast factor depends on the interaction of the wave with the sample and its different components. The *contrast factor* depends either on the difference in electronic densities of the scatterers and the solvent for SAXS or on the difference in nuclei densities of the scatterers and the solvent for SANS[12]. As suggested by the notation, the contrast factor is in fact the difference of scattering length densities (SLD) $\rho_{\text{scatterer}}$ of the scatterer and the SLD of the background $\rho_{\text{background}}$ (typically the solvent):

$$\Delta\rho = \rho_{\text{scatterer}} - \rho_{\text{background}} \tag{2.84}$$

To have the best measurements, $\Delta\rho$ must be as large as possible, which may be hardly achievable in some cases where the SLD of the scatterer and the solvent are too close. As the SLD are not the same with X-rays and neutrons (see Fig. 2.29), SAXS and SANS may yield different contrast.

[12] The dependence is, however, non-trivial for SANS as presented in Fig. 2.29.

A huge advantage of the SANS is the possibility to play with the SLD of the background, especially when the solvent is water. Light water H_2O and heavy water D_2O have similar interactions with the surrounding compounds in the sample, but their SLD are very different. When mixed, the SLD of the background $\rho_{\text{background}}$ can vary between ρ_{H_2O} and ρ_{D_2O} following a simple mixing rule. If the SLD of the scatterer lies between these values, the contrast factor vanishes for the right proportion of light to heavy water. This is called *contrast matching*. It is extremely useful when the sample contains several species: one can match the SLD of the solvent with one compound at a time to measure the scattering intensity of the remaining one only.

This feature is of particular interest in the polymer-nanoparticle system under study here. In SAXS the contrast is so large between the CB and the solvent that the scattered intensity measured is clueless on the structure of the polymer. Hence the goal the SANS experiments conducted aimed at matching the CB to magnify the signal of the polymer. To evaluate the right volume ratio of heavy-to-light water $r_{\text{water}} = V_{D_2O}/(V_{H_2O} + V_{D_2O})$, tabulated values of SLD are helpful but not adequate since the exact chemical composition of the CB is not known. The contrast matching is therefore determined experimentally. The scattering intensity is measured for samples at different r_{water} but fixed volume fraction of CB and CMC so that $x_{CB} = 0.01\%$ and $c_{CMC} = 2\%$ at $r_{\text{water}} = 0$. Contrast matching occurs when the scattering intensity is minimal. In Fig. 2.30, one clearly sees that the contrast is never achieved event at $r_{\text{water}} = 1$; the SLD of the CB (Vulcan XC72R in this case) is higher than the one of D_2O[13]. Experiments have still been conducted with maximized contrast matching, unfortunately the CB particles scatter so much that it overtakes all other source of scattering.

Contrast matching is not available with SAXS, forchanging the electron cloud of an atom-making ion would alter too much its physical and chemical properties. However

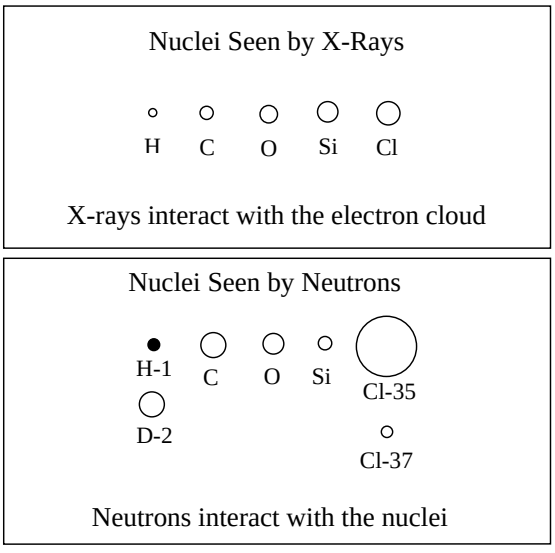

Figure 2.29: Visual representation of the scattering length density (SLD) for different atoms with (top) X-ray and (bottom) neutron scattering. The proton H-1 is black to remind its SLD is negative. Figure adapted from [254].

[13] In fact $\sqrt{I} \sim |\rho_{CB} - \rho_{\text{background}}|$ so that the sign is undetermined. The uncertainties in the data do not allow us to discriminate whether $\rho_{CB} - \rho_{\text{background}}$ is positive or negative at the maximum r_{water}. In any case, the contrast matching occurs at $r_{\text{water}} > 1$.

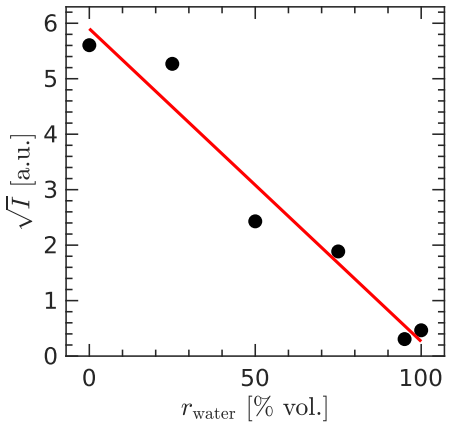

Figure 2.30: Determination of the matching ratio for a SANS experiment for a CB-CMC mixture at $c_{\text{CMC}} = 2\%$ & $x_{\text{CB}} = 0.01\%$. The square root of the intensity (averaged over the first decade of q) is plotted against the D_2O-to-H_2O volume ratio r_{water}. The red line is the best linear fit of the data leading to a contrast at $r_{\text{water}} = 1.2 \pm 0.1$.

the flux is usually way bigger in SAXS than in SANS, which enables to have a sufficiently coherent incident beam required for X-ray Photon Correlation Spectroscopy (XPCS), which will be described in Section 3.B.3. Both in SAXS and SANS, we chose to only consider relative intensities so that the prefactors are meaningless, and the scattering intensities are therefore expressed in arbitrary units.

G.2 Analysis of the scattering intensity profiles

a Background removal

The total scattering intensity contains the diffraction pattern of the solvent that should be removed. Here, we focus on the signal data analysis in SANS for acidified CMC solutions, obtained with the smallest wavelength ($\lambda = 6$ Å). The scattering intensity was measured for the samples and the solvent (H_2O) in the same conditions. The data are plotted in Fig. 2.31(a) for the solvent and an acidified CMC solution at $c_{\text{CMC}} = 2\%$ and pH $= 0.9$. The intensity is exported already reduced, that is to say, the holder scattering intensity I_{empty} is already subtracted [see Eq. (2.82)]. Therefore, the reduced scattering intensity reads:

$$I_{\text{reduced}} = I_{\text{CMC}} + I_{\text{H}_2\text{O (CMC)}} + I_{\text{incoherent (CMC)}} \tag{2.85}$$

The contribution of the solvent $I_{\text{H}_2\text{O (CMC)}}$ and the incoherent scattering $I_{\text{incoherent (CMC)}}$ can be measured separately without polymer. In the dilute regime we consider here with ϕ the volume fraction of CMC close to zero, $I_{\text{H}_2\text{O (CMC)}} = (1-\phi) I_{\text{H}_2\text{O}}$ where $I_{\text{H}_2\text{O}}$ is the scattering intensity of the solvent alone. The same goes for $I_{\text{incoherent (CMC)}}$ since the incoherence is mainly due to the protons being much more abundant in water. In the following, the incoherent scattering intensity will be included in $I_{\text{H}_2\text{O}}$, which corresponds to considering the reduced intensity of water.

One has to remove $(1-\phi) I_{\text{H}_2\text{O}}$ from the reduced signal to get the proper sample scattering intensity. Since the value of ϕ is hard to evaluate, a quantity $\kappa I_{\text{H}_2\text{O}}$ is removed from the reduced data, where κ is unknown (close to 1 in the polymer concentration regime targeted here). The evolution of the scattering spectrum according to this parameter κ is shown in Fig. 2.31(b-e) for a solution at $c_{\text{CMC}} = 2\%$ and pH $= 0.9$.

The value of $\kappa = 0.99$ was chosen to fulfill the two following criteria: (*i*) no plateau in the high q-range that would be physically meaningless, and (*ii*) no negative values on a significant range of q.

The lowest q values were obtained with another wavelength $\lambda = 11.5$ Å and merged with the $\lambda = 6$ Å data set for $q < 5 \times 10^{-3}$ Å^{-1} (data for $q > 5 \times 10^{-3}$ Å^{-1} obtained at $\lambda = 11.5$ Å were discarded as their are redundant with the data at $\lambda = 6$ Å but with a lesser signal-to-noise ratio). This introduces an arbitrary factor in the scattering intensity, corrected in Fig. 2.32. The vertical shift introduced was chosen so that the data at both wavelengths overlap in the lowest q range accessible. The data at $\lambda = 11.5$ Å for $q > 3 \times 10^{-3}$ Å^{-1} were then removed to get only the correctly shifted data. The background intensity is negligible in this range of wave vectors, and no further treatment was applied.

Similar treatment is done in SAXS, with the advantage that the incoherent scattering is negligible and the CB scatters a lot so that the background have a rather small contribution. However, in SAXS we extensively studied the polymer-CB dispersions, a ternary system. The protocol is a bit trickier to get the scattering intensity of the CB only. One has to subtract the water and the CMC signals with an arbitrary factor for each. Formally it reads:

$$I_{\mathrm{CB}} = \underbrace{I_{\mathrm{raw}}}_{\text{raw signal}} - \underbrace{\kappa^{\mathrm{CB}}_{\mathrm{H_2O}} I_{\mathrm{H_2O}}}_{\text{background}} - \kappa^{\mathrm{CB}}_{\mathrm{CMC}} \underbrace{\left(I^{\mathrm{CMC}}_{\mathrm{raw}} - \kappa^{\mathrm{CMC}}_{\mathrm{H_2O}} I_{\mathrm{H_2O}} \right)}_{=I_{\mathrm{CMC}},\ \text{CMC only}} \tag{2.86}$$

The three κ constants were chosen according to the protocol detailed above and reported in Fig. 2.33(a)-(c). It ensures that the form factor of the CB is accessible on a reasonable q range in order to normalize the intensities properly. In the q range of the CB form factor, the signal must be the same regardless of the composition, apart from a vertical shift due to the change in volume fraction[14]. The cross term related to the spatial correlation of the CB and the polymer can not be removed and may explain

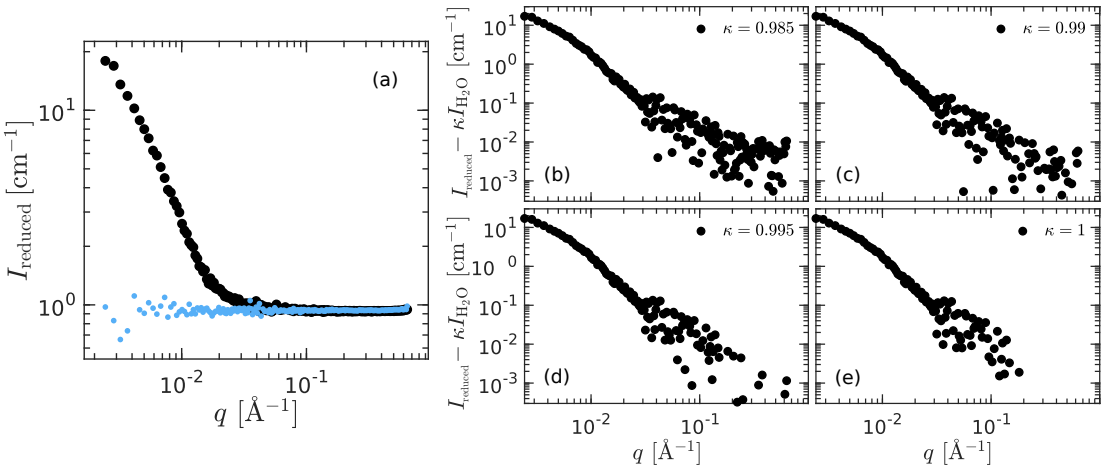

Figure 2.31: Protocol to remove the solvent background in the scattering intensity. (a) Reduced scattering intensity as a function of the wavevector q (neutron wavelength $\lambda = 6$ Å). Black circles correspond to a solution of CMC at $c_{\mathrm{CMC}} = 2\%$ and pH $= 0.9$ in H_2O. The blue dots correspond to pure H_2O. A fraction κ of the pure H_2O scattering intensity is subtracted to the CMC solution scattering intensity: (b) $\kappa = 0.985$, (c) $\kappa = 0.99$, (d) $\kappa = 0.995$, and (e) $\kappa = 1$.

[14] As long as ϕ is close to 0, which is the case here.

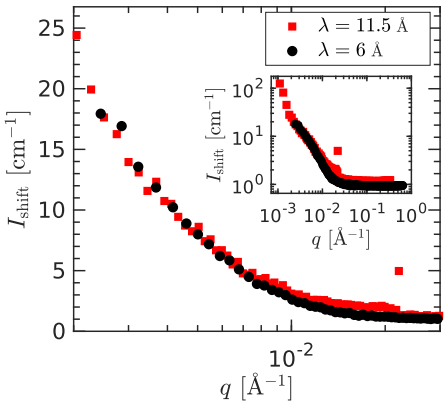

Figure 2.32: Protocol to rescale the scattering intensity at different source wavelengths. Reduced radially-averaged scattering intensity as a function of the wave number q for a solution of CMC at $c_{CMC} = 2\%$ and pH $= 0.9$ in H_2O, for two different neutron wavelengths $\lambda = 11.5$ Å (red squares) and $\lambda = 6$ Å (black circles). The data for $\lambda = 11.5$ Å were shifted vertically by a factor 0.9 to overlap the data at $\lambda = 11.5$ Å in the lowest q range. The inset shows the same data on the full q range in a log-log scale.

the signal at high q, which departs from a Porod regime. It seems to be especially true in the very diluted regime [Fig. 2.33(d)], in which the relative contribution of CB itself is not predominant. We used a CMC solution at $c_{CMC} = 2\%$ for all the compositions, even at different polymer content. We therefore assume that the configuration of the polymer is same regardless of the concentration. This hypothesis is relevant in this q range since one probes structure within the polymer, which is not much affected by its actual concentration. This framework is supported by the previous work of C. Lopez and R. Colby on similar CMC suspensions [179, 255], which reports the same shape for the scattering intensity of the CMC as the one plotted in the inset in Fig. 2.33(a).

b Form Factor of CB particles

The form factor must be measured in the zero concentration limit of scatterers. In this framework, the scatterers will not aggregate and will remain isolated in the solvent. It implies that the particles must be stable in the solvent. Here we only focus on the form factor of CB particles, as the form factor of the polymer we used were not accessible.

The form factor should not depend on the solvent, for normalization simplicity we first attempted to extract the form factor from a diluted solution of CB in a CMC solution at $c_{CMC} = 2\%$. At lower polymer concentrations the CB particles are too hydrophobic and form aggregates, similar to what happens with CB dispersed in water. Unfortunately, even at $x_{CB} = 0.01\%$ the CB particles are not isolated, which is exhibited by the absence of a low-q plateau for the solid line in Fig. 2.33(d). Instead, we used the data from Dagès et al. [256] on the same CB Vulcan XC-72R with mineral oil for solvent. The data were shifted vertically so that they match around $q = 0.1$ nm^{-1} to account for the change in SLD with another solvent.

The form factor is described by a polydisperse mass fractal model, following the analysis detailed in [125, 256]. The mass fractal model is based on the decorrelation in fractal objects, which scales as a power-law of the distance and an exponent related to the fractal dimension [257–259]. We did not take into account the form factor of the single nodule since its typical size is way smaller than the size of the CB particle,

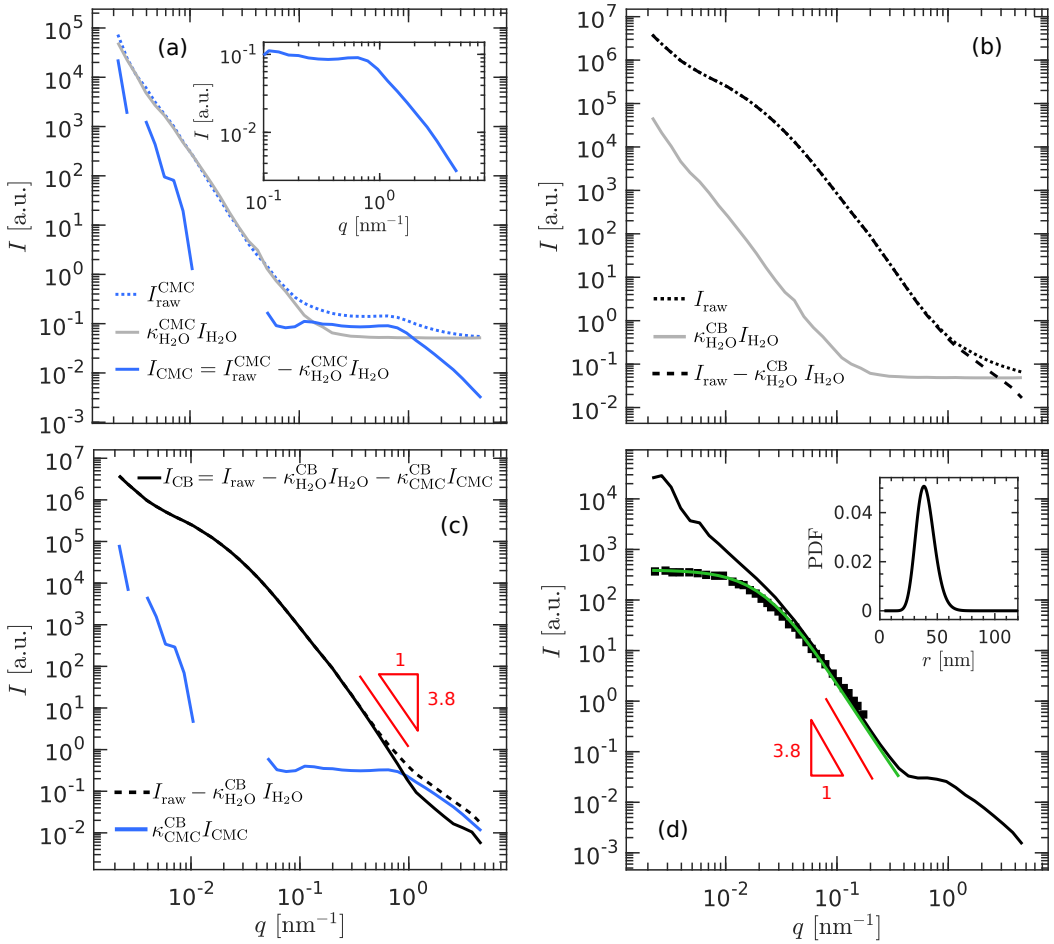

Figure 2.33: Protocol to extract the scattering intensity of the CB only. The grey curves correspond to the water signal I_{H_2O}, the black ones to the CMC ($c_{CMC} = 2\%$), the blue ones to the CB signal ($x_{CB} = 8\%$ and $c_{CMC} = 2\%$) and the red line shows a slope of -3.8. (a) Removal of water background to the CMC scattering intensity. The inset shows a zoom of the CMC signal after the water removal. (b) Removal of water background to the CB-CMC scattering intensity. (c) Removal of CMC background to the CB-CMC scattering intensity, after water removal on each. (d) Scattering intensity of a CB-CMC solution at $c_{CMC} = 2\%$ and $x_{CB} = 0.01\%$ in water after the protocol detailed in (a)-(c), plotted as a solid black line. The squares correspond to the data extracted from [256] in mineral oil, rescaled to match the solid line at $q = 0.1$ nm^{-1}. The green curve is the fit of the latter data following Eq. (2.87)-(2.90) with $r_0 = 40$ nm, $p = 0.2$ and $d_m = 2.87$. The inset shows the Schulz size distribution used in the form factor computation.

therefore out of the relevant q range for our study. The polydispersity is modeled by a Schulz distribution of sizes similarly[15] to [125]. In this framework, the scattering intensity is modeled by the following set of equations:

[15]Note that in this work the polydispersity was considered on the nodules rather than the whole CB particles as done here.

$$P_r(q) = \Gamma(d_m - 1) r^{d_m} \frac{\sin[(d_m - 1)\ \tan^{-1} qr]}{qr[1 + (qr)^2]^{(d_m-1)/2}} \tag{2.87}$$

$$P(q) = \int_0^\infty w(r) P_r(q) \mathrm{d}r \tag{2.88}$$

$$w(r) = \frac{1}{\mathrm{Norm}} \left(\frac{r}{r_0}\right)^z \exp\left(-(z+1)\frac{r}{r_0}\right) \tag{2.89}$$

$$z = (1 - p^2)/p^2 \tag{2.90}$$

with Γ the gamma function, r the size of the particle, d_m the mass fractal dimension of the particle, r_0 the mean value of the size particle, z an exponent related to the polydispersity p, and Norm a normalization factor. The computed scattering intensity is plotted in green in Fig. 2.33(d). Particular attention should be given to r_0, it should be understood as a correlation lengthscale rather than the typical size of a CB particle, which is around 5 times larger than r_0 according to the TEM pictures [Fig. 2.1(b)].

The form factor does not describe well the scattering intensity for $q \gtrsim 0.2$ nm^{-1}, it might be due to the cross term between CMC and CB [Fig. 2.33(d)].

c Structure Factor of CB particles

With the model to describe the form factor P, we can compute an apparent structure $S_{\text{app, abs}} = I/P$. This is only an apparent structure factor as this value is determined indirectly from experimental data. Moreover, this value is normalized at $q = 0.1$ nm^{-1} to account for the potential prefactor due to the different volume fraction of scatterer. We shall note the normalized apparent structure factor S_{app}, which is plotted in Fig. 2.34. This value of q for the normalization corresponds to a regime where we assume to probe length-scales within the CB, i.e., the structure factor should be equal to 1. This hypothesis is supported by the fact that S_{app} is flat in this region.

Unfortunately we did not find yet an efficient way to analyze the structure factors thus obtained. We instead investigate the Kratky representation of the scattering in-

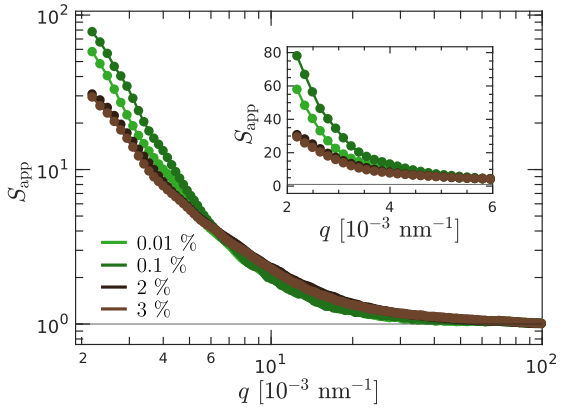

Figure 2.34: Apparent structure factor S_{app} of CB-CMC mixture at $x_{\text{CB}} = 6\%$ and $c_{\text{CMC}} = 0.01\%$ (light green), 0.1% (dark green), 2% (dark brown) and 3% (light brown). The data are normalized by their value at $q = 0.1$ nm^{-1} to account for the potential difference in volume fraction of CB. The inset shows a zoom of the data from $q = 2.10^{-3}$ nm^{-1} to $q = 6.10^{-3}$ nm^{-1} in a lin-lin plot. The black lines correspond to $S_{\text{app}} = 1$.

tensity Iq^2 vs. q, which gives results more straightforward to interpret. The analysis of the structure factors is left as a promising perspective for future work.

d Quantitative analyze of the data

In the case of the polymer neutron scattering, we managed to find a relevant mathematical description to model the data. We used the empirical Guinier-Porod fit function, developed by B. Hammouda [260], and more recently added to the SasView application[259]. The obtained function is plotted in Fig. 2.35 and is defined as follows:

$$\begin{aligned} I(q < q^*) &= G/q^s \exp\left(\frac{-q^2 R_g^2}{3-s}\right) \\ I(q > q^*) &= D/q^m \end{aligned} \tag{2.91}$$

where s and m are the power-law exponents at low q (Guinier regime) and high q (Porod regime), respectively. R_g is the apparent radius of gyration that relates to q^*, m, and s through:

$$q^* = \frac{1}{R_g}\sqrt{(m-s)(3-s)/2} \tag{2.92}$$

$$d^* = 2\pi/q^* \tag{2.93}$$

Moreover, to ensure continuity of $I(q)$, the prefactors G and D in the low-q and high-q, respectively, are related to each other through:

$$D = G\ \exp\left(\frac{-q^{*2}R_g^2}{3-s}\right) q^{*m-s} = \frac{G}{R_g^{m-s}}\ \exp\left(-\frac{m-s}{2}\right)\left(\frac{(m-s)(3-s)}{2}\right)^{\frac{m-s}{2}} \tag{2.94}$$

However, for the CB-CMC suspensions, we did not manage to find a relevant model. Indeed as the CB particles used are big, the q range available to study the structure is quite small: typically between $q = 3.10^{-3} - 2.10^{-2}$ nm^{-1}. With less than a decade, fitting the data does not make much sense. We decided instead to extract specific q values that arise from a Kratky plot of the data, as shown in Fig. 2.36. Namely,

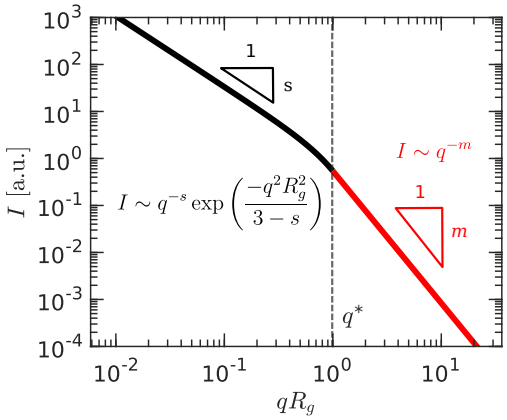

Figure 2.35: Guinier Porod model for scattering intensity as a function of the normalized wavevector qR_g. The dashed line correspond to $q = q^\star$, the black curve to the first part of the fit for $q \leqslant q^\star$ and the red curve to the second part of the fit for $q \geqslant q^\star$. For this plot $s = 1.5$ and $m = 2.8$.

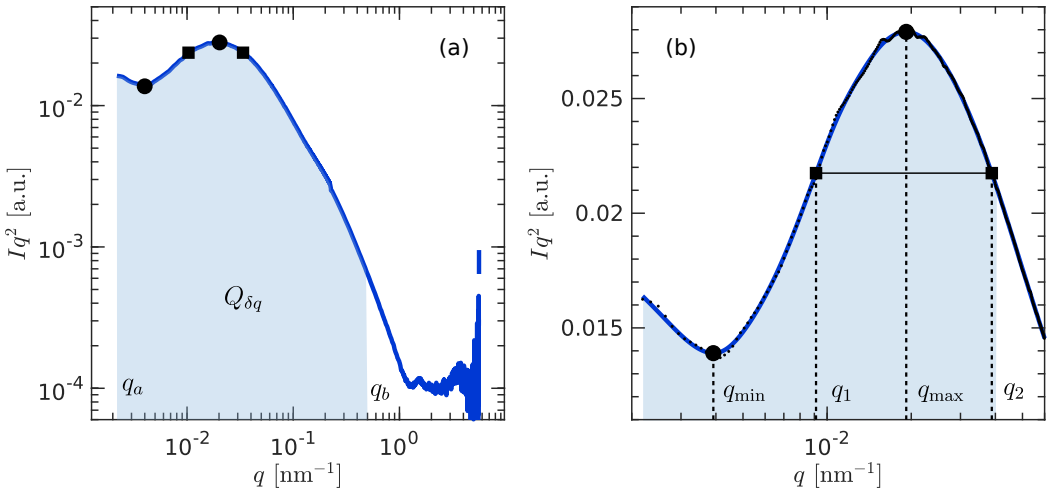

Figure 2.36: Kratky plot of the scattering intensity Iq^2 vs q of a CB-CMC mixture at $c_{CMC} = 2\%$ and $x_{CB} = 8\%$. The black circles correspond to the extrema in the region of interest ($q < 0.06$ nm^{-1}), the black squares correspond to the definition of q_1 and q_2. (a) Full data set. (b) Zoom in the region of interest. The dotted lines show the definition of $q_{\max}, q_{\min}, q_1$ and q_2. The shaded area represents the area computed for $Q_{\delta q}$ defined in Eq. (2.79), from $q_a = 2.10^{-3}$ nm^{-1} to $q_b = 4.10^{-2}$ nm^{-1}.

the position of the maximum and minimum of Iq^2 respectively $q_{\max}$ and $q_{\min}$, are noteworthy as they inform on the correlation lengths. The broadness of the maximum peak is also studied through q_1 and q_2. The former corresponds to the inflection point of the Iq^2 vs. q curve for $q_{\min} < q < q_{\max}$. The latter is the abscissa where Iq^2 has the same value as at q_1 but on the other side of the maximum, i.e., for $q > q_{\max}$. The broadness of the peak is reported through the ratio q_2/q_1. Finally we shall also study the partial integral of the invariant $Q_{\delta q}$ as defined in Eq. (2.79), which is represented by the shaded area in Fig. 2.36.

G.3 Rheo-SAS

During static SAS experiments, the shear history of the sample is not controlled. To avoid this issue, the best way is to put the sample in a rheometer to control exactly its shear history, through a shear rejuvenation step. It is also extremely insightful to correlate the changes in the scattering intensity spectrum with the shear undergone by the sample. The scattered wave must go through the sample within the rheometer. The setup is sketched in Fig. 2.37. In both rheo-SANS and rheo-SAXS experiments, we used a Couette geometry, with a hollow inner bob to absorb the X-ray or neutron beam as little as possible. Time synchronization between the rheometer and the scattering measurements are insured thanks to a triggering of the scattering by the rheometer. The background intensities are averaged over a long time and at a high shear rate to limit the impact of flaws in the rotational symmetry of the geometry.

G.4 X-ray Photon Correlation Spectroscopy (XPCS)

X-ray Photon Correlation Spectroscopy (XPCS) combines the principles of X-ray scattering and signal correlation to study the dynamics at the nanoscale. In an XPCS experiment, the intensity of scattered X-rays forms speckle patterns on the detector, which are recorded as a function of time. As for the SAXS, these diffraction patterns

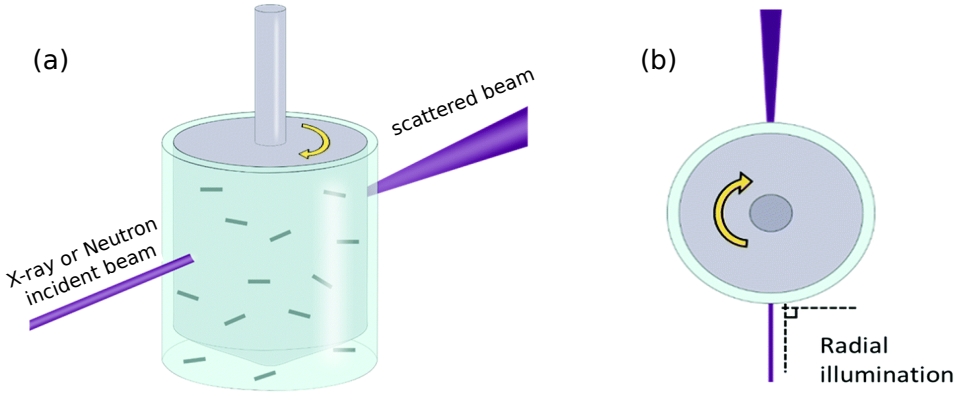

Figure 2.37: Rheo-SAS setup. (a) Schematic illustration of the Couette cell submitted to beam. (b) Top-view schematic highlighting the radial illumination of the dispersions, perpendicular to the flow direction and parallel to the velocity gradient. Adapted from [261].

arise from the interference of X-rays scattered from different regions of the sample, but for XPCS one focuses on the fluctuations of the speckle patterns. By analyzing their temporal evolution, XPCS can provide insight into the dynamics of the sample at various length scales. Several processes may be at stake: particle motion, diffusion, or structural rearrangements.

To quantify the intensity fluctuations, the intensity auto-correlation function g_2 of the speckle pattern is computed as a function of time t (time from the start of the experiment), lag-time Δt (delay between two speckle patterns), and wave-vector q. The samples studied in this work are isotropic, so that g_2 may only depend on the amplitude of the wave vector and not on its direction. Formally g_2 is defined as follows:

$$g_2(q,t,\Delta t) = \frac{\langle I(q,t)I(q,t+\Delta t)\rangle}{\langle I(q,t)\rangle \langle I(q,t+\Delta t)\rangle} \tag{2.95}$$

where I is the scattering intensity and $< \ldots >$ denotes ensemble average. In fact, the samples are usually assumed to be ergodic, and for practical reasons, the average is taken instead over the different directions of the scattering wave vectors, which is reasonable in the present isotropic case [262]. The intensity auto-correlation function is expected to be maximal (fully correlated) when $\Delta t = 0$ since the system is compared to itself at the same time. With increasing values of Δt, the correlation decreases as the system explores different micro-states that are statistically different from one another[16] up to the point where $g_2(q,t,\Delta t) = 1$ as $\Delta t \to \infty$. Indeed, in soft matter, systems are never fully arrested, and long-time memory cannot be achieved at the nanoscale, at least because of the thermal noise in the Brownian systems studied here.

The way the correlation decays and how it depends on the wave vector is extremely insightful. In non-stationary systems, the decay also depends on t, but it raises loads of technical questions that will not be addressed here. Two signatures of non-stationarity can be observed, which are depicted in Fig. 2.38. The correlation function may shift with time, which leads to an apparent change in the decay time [Fig. 2.38(a)-(b)]. The correlation function may also exhibit some peaks of correlation at specific times, which makes the time average non-relevant [Fig. 2.38(c)-(d)]. In both cases, this

[16] The two intensities $I(q,t)$ and $I(q,t+\Delta t)$ become uncorrelated so that $\langle I(q,t)I(q,t+\Delta t)\rangle = \langle I(q,t)\rangle \langle I(q,t+\Delta t)\rangle$ and $g_2(q,t,\Delta t) = 1$.

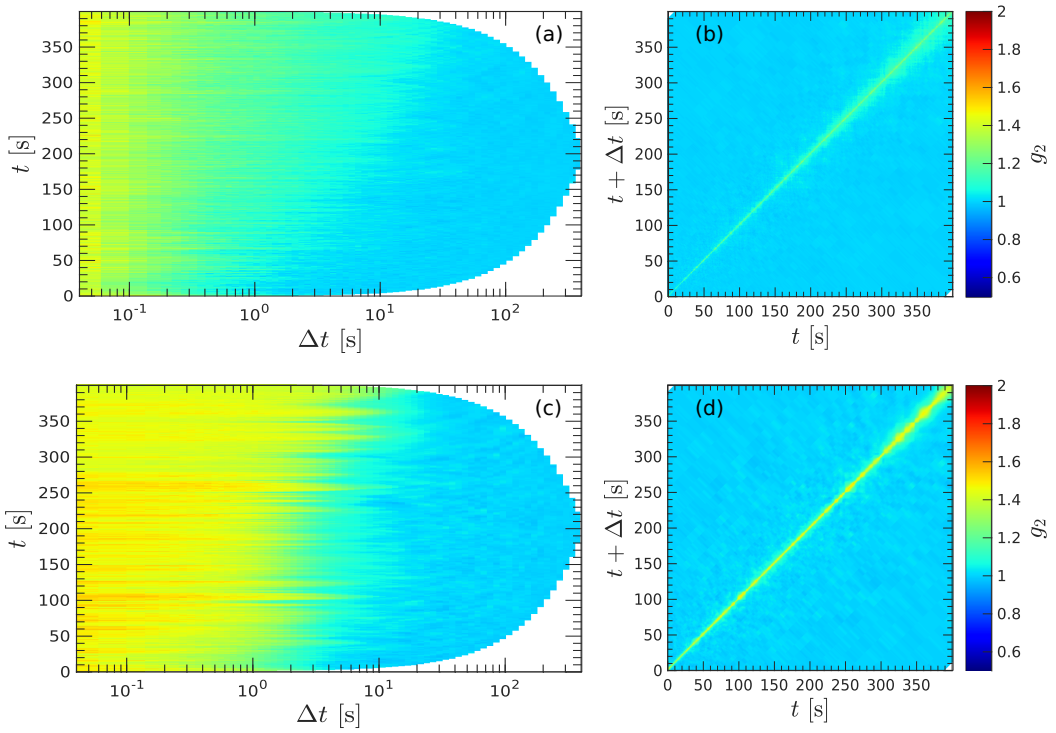

Figure 2.38: Correlation function g_2 at $q = 0.01$ nm^{-1} as a function of time t and delay time Δt of CB-CMC dispersions. Warmer colors indicate larger values of g_2 as shown in the color bar on the right, the data are not rescaled. Top panel: $x_{CB} = 2\%$ and $c_{CMC} = 2\%$ (a) Map of g_2 in the $(\Delta t, t)$ plane, with the x axis in log scale. (b) Map of g_2 in the $(t, t + \Delta t)$ plane. Bottom panel: $x_{CB} = 4\%$ and $c_{CMC} = 2\%$ (c) Map of g_2 in the $(\Delta t, t)$ plane, with the x axis in log scale. (d) Map of g_2 in the $(t, t + \Delta t)$ plane.

usually means that the sample is not at equilibrium, either because the sample itself has not reached a steady state, or because it reacts with the X-rays used for the measurement. In the experiments presented here, the non-stationarity is attributed to the reaction between the X-rays and the polymer, which creates free radicals that change the dynamics probed by the XPCS [263]. To limit this effect, the experiments should not last too long (typically a few minutes) and the incident X-ray flux should have a low intensity. Unfortunately, it leads to lower statistics to compute the correlation function, and the latter is therefore noisier.

Henceforth, we shall consider stationary measurements so that the correlation function $g_2(q, \Delta t)$ depends on q and Δt only. A typical example is shown in Fig. 2.39(a). When the data are too noisy, the correlation function may not remain bounded between 0 and 1. Explicitly, for $\Delta t \to \infty$, g_2 reaches a plateau value that is not zero due to a residual correlation in the noise. This makes the analysis more challenging since it adds a free parameters to the fit of the correlation function. In the ideal case of a Brownian particle in a Newtonian fluid, the correlation function decays exponentially $g_2 - 1 \sim \exp(-\Delta t / \tau_{\text{Brownian}})$, with only one timescale $\tau_{\text{Brownian}} = 6\pi\eta R_H / k_B T q^2$, with η the solvent viscosity, R_H the hydrodynamic radius of the particle, $k_B T$ the thermal energy and q the wave-vector [264]. This is, in fact, the diffusive timescale, which is inversely proportional to the diffusion coefficient $D = k_B T / 6\pi\eta R_H$ and proportional to the square of the length scale $1/q^2$.

In general, there is a distribution of several timescales at stake, which arises from

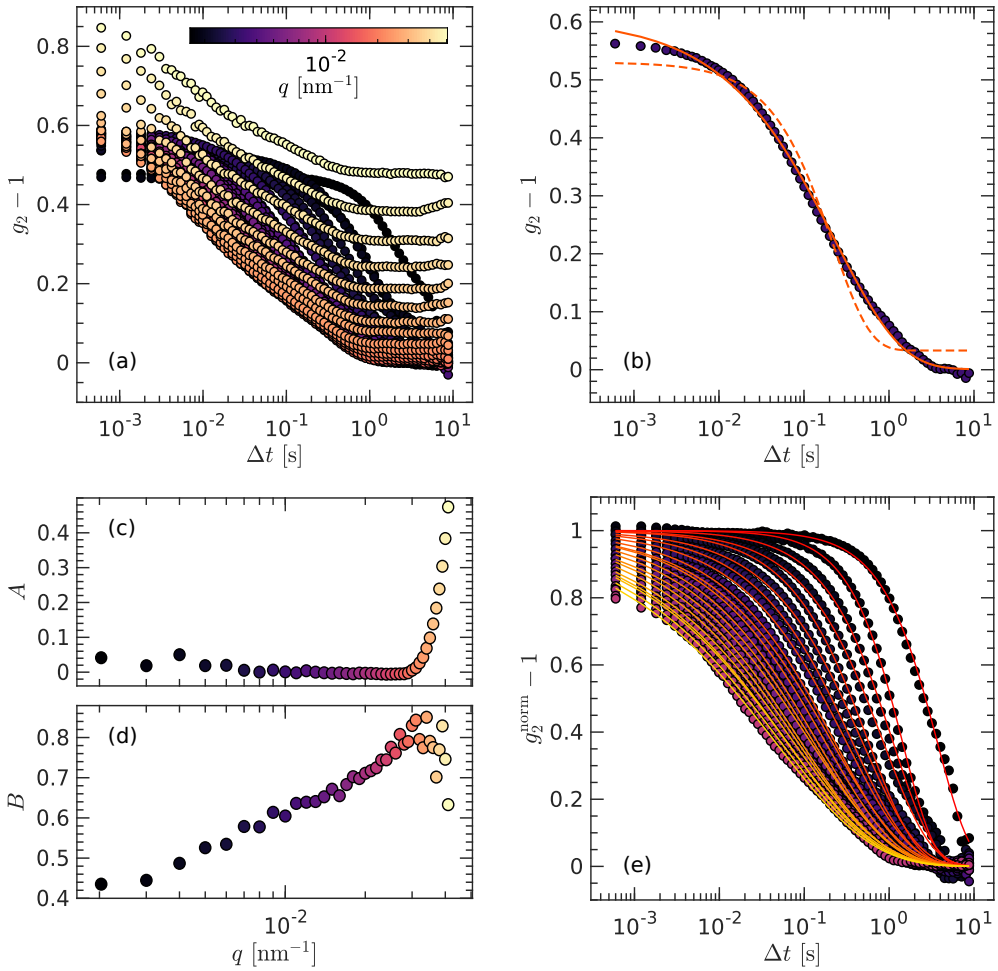

Figure 2.39: XPCS analysis of a CB-CMC dispersion at $x_{\mathrm{CB}} = 2\%$ and $c_{\mathrm{CMC}} = 2\%$. (a) Raw intensity auto-correlation function g_2 as a function of delay time Δt for different wave-vector amplitude q, brighter colors indicate higher values of q as shown in the color bar, ranging from $q = 2.10^{-3}$ to 4.10^{-2}nm^{-1}. (b) g_2 at $q = 0.01$ nm^{-1}, the solid line corresponds to the best fit of the data according to Eq. (2.96), with $A = 0$, $B = 0.60 \pm 0.01$, $\beta = 2.3 \pm 0.1$ and $\tau = 0.44 \pm 0.02$ s. The dashed line corresponds to the best fit of the data according to Eq. (2.96) with β fixed to 1, i.e., regular exponential decay, $A = 0.03 \pm 0.01$, $B = 0.50 \pm 0.02$, and $\tau = 0.22 \pm 0.03$ s. (c) A parameter as a function of q. (d) B parameter as a function of q. (e) Normalized intensity auto-correlation function as a function of Δt for different q using the A and B parameters shown in (c) and (d). Wave-vector values range from $q = 2.10^{-3}$ to 2.10^{-2} nm^{-1}, due to low statistics at high q the data are too noisy and are not represented here.

different physical mechanisms and the analysis of the full decorrelation is a challenging problem [265]. Here, we focus on a simpler approach where the decay is described by only one main timescale. However, in order to be consistent with the data, the decay is described by either a *stretched* or a *compressed* exponential function: $g_2(q, \Delta t) - 1 = \exp(-(\Delta t/\tau)^\beta)$, with, respectively, $\beta < 1$ and $\beta > 1$. Note that the timescale τ and the exponent β depend on q. To account for the biases described above, the intensity auto-correlation functions are fitted using the following equation:

$$g_2(q, \Delta t) - 1 = A + B \exp(-(\Delta t/\tau)^\beta) \tag{2.96}$$

where A corresponds to the noise correlation at large lag-time, and B is the contrast factor due to the coherence of the detector, which are not physically meaningful

to study the system. Hence, we shall focus only on the normalized intensity auto-correlation function:

$$g_2^{\text{norm}}(q, \Delta t) - 1 = \frac{g_2(q, \Delta t) - 1 - A}{B} \tag{2.97}$$

and look for the q-dependence in τ and β. The parameters A and B are extracted from the fit of the g_2 raw data with Eq. (2.96). An example of this numerical analysis is shown in Fig. 2.39. Thanks to the normalization, one can clearly see the expected q dependence on the decay timescale: higher values of q lead to faster decay. Indeed, higher q correspond to smaller length scales, which relax faster since they have to move less to decorrelate. Moreover, the fact that the decay timescale indeed depends on q proves that this feature is not due to an artifact in the measurement, and truly probes the dynamics of the scattering particles. Finally, A and B are both increasing functions of q, which is consistent with the noise interpretation since the statistics get lower as q increases. More quantitative results are discussed in Section 3.B.3.

CHAPTER

3

VISCOELASTICITY OF CB-CMC HYDROGELS: A DUAL ORIGIN

In the present chapter, we aim at understanding the main properties of CB aqueous dispersions stabilized by CMC. Varying the contents of CB and CMC, we unravel a rich phase diagram, which we characterize by rheometry and electrical impedance spectroscopy. Our results allow us to identify two different types of CB-CMC hydrogels, whose microstructures are sketched and extensively discussed. The outline of the chapter is as follows: the first section, Section 3.A, aims at introducing the system with the different phases encountered, especially the hydrogel phase. The second section, Section 3.B, discusses the impact of the composition on the gel linear properties. A focus on the dynamic properties is addressed in Section 3.C.

A Phase diagram

The large variety of dispersants used so far in CB dispersions is in stark contrast with the limited knowledge regarding the link between the microstructure and rheological properties of the resulting composite materials. Among the open questions, it remains to disentangle the respective contributions of the CB and the dispersant to the macroscopic mechanical properties of the mixture, and whether the CB particles form a percolated network on their own, or if they are bridged by the polymeric chains. We investigated the phase diagram of CB-CMC mixtures in the following section in order to make progress on this question. We first discuss qualitatively the outcome of dispersing carbon black (CB) nanoparticles in a solution of carboxymethylcellulose (CMC). In practice, we observe four different phases that are summarized in the phase diagram reported in Fig. 3.1. We emphasize that such a phase diagram of the polymer/carbon mixture is a *non-equilibrium* state diagram whose boundaries depend on the details of the sample preparation. For low CB and CMC concentration, the aqueous dispersion is unstable and the CB particles sediment within about 20 min [Fig. 3.1(b)]. On the one hand, increasing the CMC concentration beyond about 10^{-2}% allows stabilizing the CB particles, yielding a viscoelastic liquid stable over weeks [Fig. 3.1(c)]. On the other hand, increasing the content in CB particles confers gel-like properties upon the samples, i.e., the sample shows a solid-like behavior at rest and for small deformations, while it flows for large enough stresses [Fig. 3.1(d)]. Finally, for CB content larger than about 10%, the sample behaves as a strongly elastic paste, with a fragile behavior to the touch [Fig. 3.1(e)].

In the present work, we focus on the hydrogel phase, which is observed over the entire range of CMC concentrations explored, and for CB content ranging between a few % and about 15%. In order to quantify the gel rheological properties, we measure its linear viscoelastic properties through small amplitude oscillatory shear. The ratio of the viscous to the elastic modulus measured at $\omega = 2\pi$ rad.s^{-1}, i.e., $G''/G' = \tan\delta$, also known as the loss factor, is reported in Fig. 3.2(a). Similar representation of G' and G'' are shown in Figs. 3.2(b) and (c) respectively. Such a phase diagram built

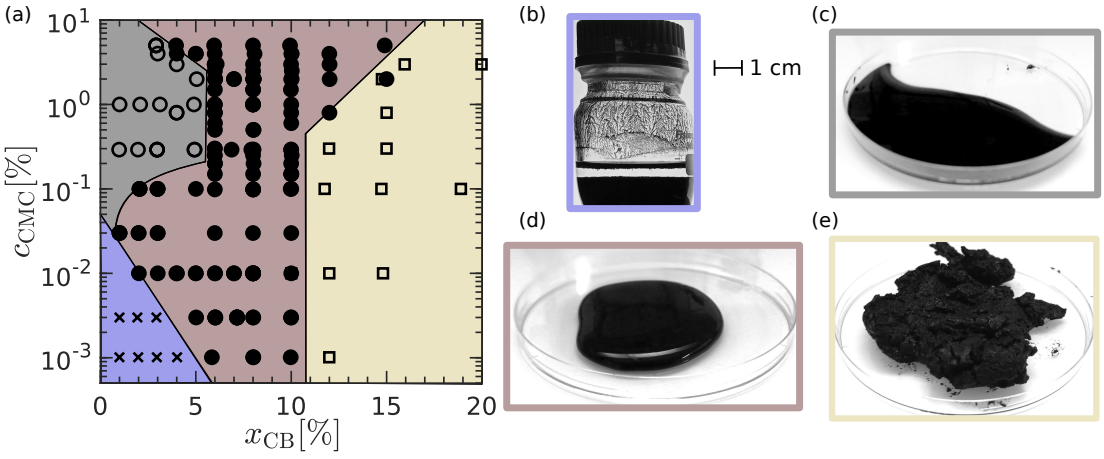

Figure 3.1: (a) **Phase diagram of aqueous CMC-CB dispersions** as a function of the CB solid weight fraction x_{CB} and the CMC weight fraction c_{CMC}. Pictures of (b) demixed phase [blue region and $\times$ symbols in (a)], (c) the viscoelastic liquid phase [grey region and $\circ$ symbols in (a)], (d) the viscoelastic solid phase [red region and $\bullet$ symbols in (a)], (e) brittle paste phase [yellow region and $\square$ symbols in (a)].

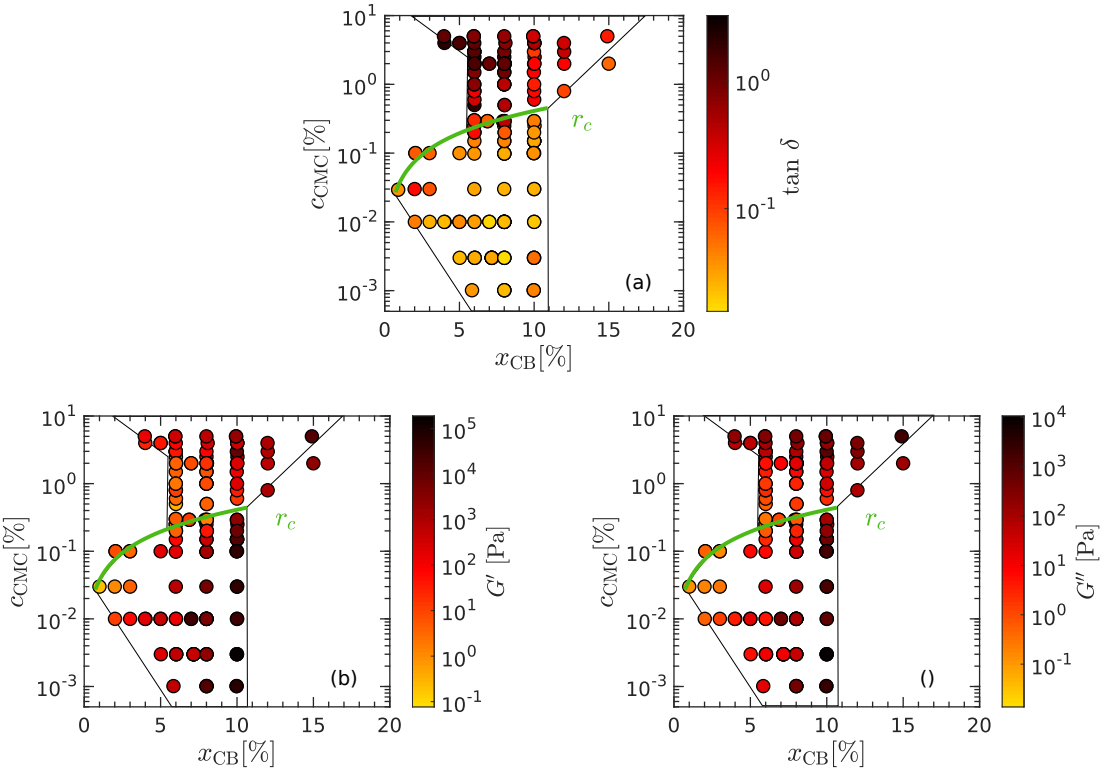

Figure 3.2: Hydrogel region of the phase diagram of aqueous CMC-CB dispersions as a function of the CB solid weight fraction x_{CB} and the CMC weight fraction c_{CMC}. The green curve corresponds to $r = r_c$, and separates two regions in the gel phase with samples of different microstructures. Color levels code for the loss factor $\tan\delta = G''/G'$ (a), the elastic modulus G' (b) and the loss modulus G'' (c) in the gel phase determined by small amplitude oscillatory shear at $\omega = 2\pi$ rad.s^{-1}.

upon the loss factor highlights two different regions, which correspond to samples that mainly differ by their CMC concentration. Samples with a lower CMC concentration display relatively less viscous dissipation ($\tan\delta \lesssim 0.1$) than samples with the highest CMC concentration ($\tan\delta \gtrsim 0.1$). This observation suggests that CMC-CB hydrogels come in two different flavors, depending on the polymer content. We quantify these qualitative results by studying the scaling of the viscoelastic and electrical properties of the samples, with respect to the CMC concentration and the CB content.

We now discuss the impact of the CMC concentration at fixed CB content, which corresponds to a vertical cut in the phase diagram reported in Fig. 3.1(a). We shall first look into the eletrical properties. Electrical measurements are performed in AC mode in a cylindrical cell made of Teflon (thickness of about 1 mm, and surface of about 0.5 cm^2). The inner sides are made of metal and act as electrodes that are connected to a multi-frequency impedance analyzer (SP-300 Potentiostat, Biologic). A decreasing ramp of frequency allows determining the frequency dependence of the sample impedance $Z^*(f) = Z' - iZ''$, which real and imaginary part, Z' and Z'' respectively, are shown in Fig. 3.3 for a sample containing $c_{\mathrm{CMC}} = 0.15\%$ & $x_{\mathrm{CB}} = 8\%$. The resistance Z' shows a decreasing step shape, while the reactance Z'' displays a bell-shaped curve. Overall, the complex impedance measured experimentally can be well fitted

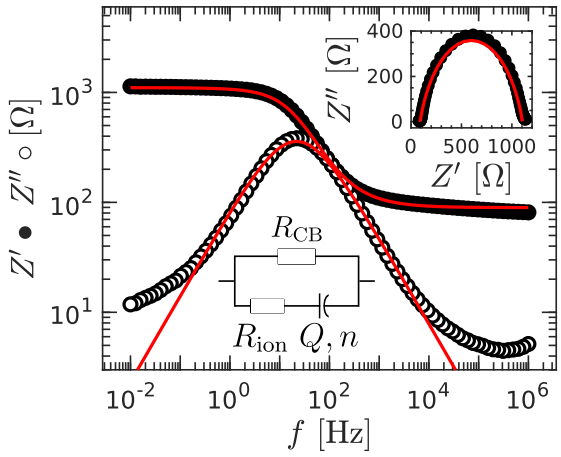

Figure 3.3: Frequency dependence of the resistance Z' (•) and reactance Z'' (○) of a CMC-CB dispersion. Inset: Nyquist plot Z'' vs. Z' for the same data. Measurement performed in AC mode by ramping down the frequency from $f = 10^6$ Hz to 10^{-2} Hz. Each point is averaged over two cycles. The red continuous curves in both the main graph and the inset show the best fit of the data for Z' and Z'' simultaneously by Eq. (3.1), which corresponds to the electrical circuit sketched in the main graph with $R_{ion} = 97\ \Omega$, $R_{CB} = 1.1\ \text{k}\Omega$, $n = 0.78$, and $Q = 1.8 \times 10^{-5}\ \Omega^{-1}.\text{s}^n$. Data obtained on a sample composed of $c_{CMC} = 0.15\%$ & $x_{CB} = 8\%$.

by:

$$Z^*(f) = R_{CB}\frac{1 + R_{ion}Q(i2\pi f)^n}{1 + (R_{CB} + R_{ion})Q(i2\pi f)^n} \tag{3.1}$$

which corresponds to the simple circuit sketched as an inset in Fig. 3.3, and classically reported in the literature for describing the electrical response of CB or carbon nanotube dispersions [105, 110, 121, 266, 267]. Equation (3.1) accounts for the additive contributions of the ions in solution, and an electronically-conductive percolated network of CB particles. More precisely, the circuit comprises a resistance R_{CB} modeling the percolated network of CB particles, in parallel with two elements, namely a resistance R_{ion} accounting for the ionic conductivity of the sample in series with a constant phase element (CPE) characterized by a dimensionless exponent n, and a parameter Q. CPE were first introduced in the context of particulate suspensions [268] and model the electrode-electrolyte interface as an imperfect capacitor [243, 244]. Although such a modeling fails to describe the dependence of $Z''(f)$ at very low and very high frequencies, potentially due to some parasitic inductance, it does account very well for $Z'(f)$ over eight orders of magnitude in frequency.

Fitting the impedance spectra to Eq. (3.1) yields four parameters, R_{CB}, R_{ion}, Q and n. The two resistances can be converted into electrical conductivities, respectively $\sigma_{CB} = k/R_{CB}$ and $\sigma_{ion} = k/R_{ion}$, with k the cell constant determined by independent measurements on KCl solutions of different concentrations (here $k = 0.37 \pm 0.01\ \text{cm}^{-1}$, see Fig. 2.19 in Chapter. 2). The parameters Q and n are weakly sensitive to the CB and CMC content, and their typical values are $Q \simeq 17 \times 10^{-6}\ \Omega^{-1}.\text{s}^{-n}$ and $n \simeq 0.75$, as discussed in more details in section 3.C (see Fig. 3.16). In the following we focus on σ_{CB}, which is used as a proxy for probing the existence of a space-spanning percolated network of CB particles in the sample, and therefore provides some insights on the microstructure of the CB-CMC dispersions.

The same vertical cut in the phase diagram can be done to study the mechanical properties. The dependence of G' with the CMC concentration is pictured in

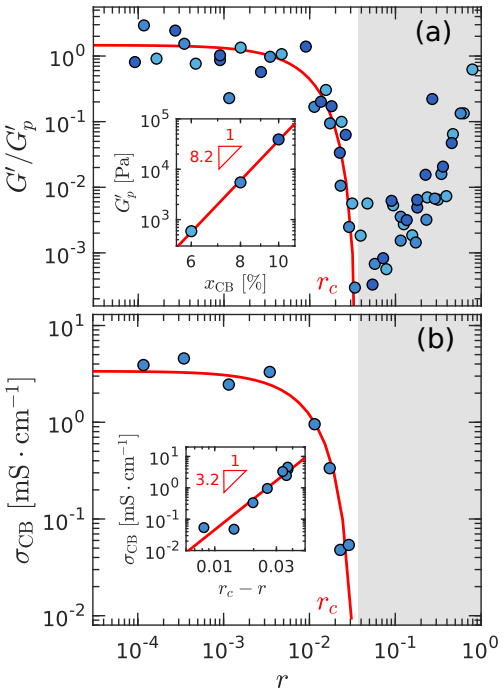

Figure 3.4: Evidence for a transition between two rheological and electrical regimes. (a) Normalized elastic modulus G'/G'_p measured at $\omega = 2\pi$ rad.s^{-1} vs. mass ratio $r = m_{CMC}/m_{CB}$. Each data point has been measured 1200 s after a shear rejuvenation step (see Section 2.D.2 in Chap. 2). Color encodes the CB content x_{CB}: 6% (•), 8% (•), and 10% (•). The plateau elastic modulus G'_p is defined as the average value of G' over the range $10^{-4} \leqslant r \leqslant 10^{-2}$. The red curve is the best power-law fit of G'/G'_p vs. $r_c - r$ with $r_c = 0.037$, yielding an exponent 3.8 ± 0.5. Inset: G'_p vs. x_{CB}. The red line is the best power-law fit of the data, yielding an exponent 8.2 ± 0.6. Inset: G'_p vs x_{CB}. (b) Electrical conductivity σ_{CB} of the CMC-CB dispersions vs. mass ratio $r = m_{CMC}/m_{CB}$, with $x_{CB} = 8\%$. The red curve is the best power-law fit of σ_{CB} vs. $(r_c - r)$ with $r_c = 0.037$, yielding an exponent 3.2 ± 0.8.

Fig. 3.4(a), as a function of the mass ratio $r = m_{CMC}/m_{CB} = c_{CMC}\,(1 - x_{CB})\,/x_{CB}$, which represents the effective number of CMC molecules per CB particles. At low CMC concentrations, we observe that the elastic modulus G' is constant $G' = G'_p$, independent of r over about two decades of CMC concentration, i.e., $10^{-4} \leqslant r \leqslant 10^{-2}$. For $r > 10^{-2}$, the elastic modulus drops abruptly by about 3 orders of magnitude for increasing CMC concentration within a narrow range of r values, reaching a minimum value at $r = r_c \simeq 0.037$. Finally, for $r > r_c$, increasing the CMC concentration translates into an increase of G', which scales roughly as a power-law function of r. This evolution of G' over the whole range of r is robust, as evidenced by the data reported in Fig. 3.4(a) for three different CB content, namely $x_{CB} = 6$, 8 and 10%.

These observations unambiguously confirm the trends determined thanks to the loss factor and show that the linear elastic properties of CMC-CB hydrogels have two distinct origins depending on the relative content in CB and CMC. For $r < r_c$, the gel elastic properties are set by the amount of CB particles [see inset in Fig. 3.4(a)] and independent of the CMC concentration, whereas for $r > r_c$, the elastic modulus is an increasing function of the CMC concentration, irrespective of the CB content. Moreover, these results suggest that the gel microstructure is drastically different on each side of r_c. To get more insights on the hydrogel microstructure, we build upon the fact that the CB particles are electrically conductive.

We have performed AC electrical measurements on a series of gels with a fixed CB content ($x_{CB} = 8\%$) and over a broad range of CMC concentrations. For each gel, we determine its electrical conductivity σ_{CB}, associated with the possible percolated network of CB particles (see section Material and methods for details about electrical measurements). The data are reported in Fig. 3.4(b). We observe that the electrical conductivity shows a similar dependence upon the CMC concentration to that of the elastic modulus. For $r < r_c$, the electric conductivity is high, i.e., $\sigma_{CB} \simeq 10$ mS.cm^{-1}, independent of the CMC concentration, whereas for $r > r_c$, the electric conductivity

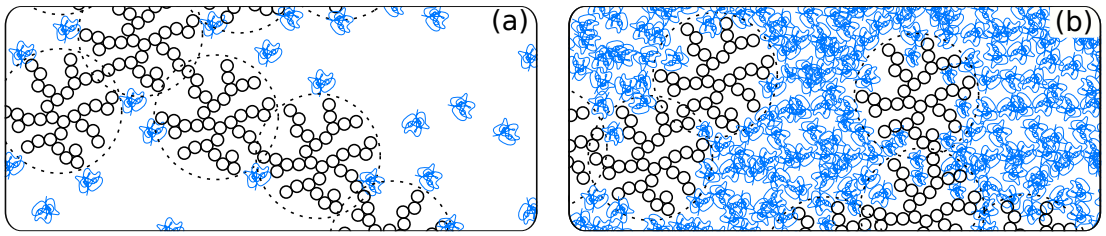

Figure 3.5: Sketch of CMC-CB hydrogels microstructure in (a) the colloid-dominated regime $r < r_c$, and (b) the polymer-dominated regime $r > r_c$. The black solid circles represent the primary CB nodules, which form the unbreakable fractal CB particles that are individually identified by dashed circles, while the blue coils represent CMC macromolecules.

drops by 3 orders of magnitude down to a negligible value following a power-law of $r_c - r$, with an exponent 4.6 [see inset in Fig. 3.4(b)].

These results demonstrate that CB particles form a space-spanning network for $r < r_c$, turning the sample into an electrically conductive material. In contrast, the negligible electrical conductivity ($\sigma_{CB} \lesssim 10^{-3}$ mS.cm^{-1}) observed for $r > r_c$ points towards a microstructure in which the CB particles are isolated as individual particles or clusters. We can further conclude that these isolated particles or clusters serve as physical cross-linker, which provide solid-like properties to the CMC matrix, for CMC dispersions alone behave as viscoelastic liquids regardless of the CMC concentration [173, 174]. These two different microstructures are sketched in Fig. 3.5. Finally, note that the transition from a gel network in which the elasticity is set by the CB particle alone to a gel network in which the elasticity results from the polymer network physically cross-linked by CB particles occurs over a narrow range of r values. The value $r_c \simeq 0.037$ corresponds to the critical amount of polymer required to decorate all the CB particles, such that further addition of CMC only viscosifies the solvent. Within this framework, the evolution of the sample microstructure from $r < r_c$ to $r > r_c$ is akin to a de-percolation transition, as reported in silica-styrene-butadiene nanocomposites [269].

Justification for the scaling of G' with c_{CMC} for $r < r_c$:

The elastic modulus of CMC-CB hydrogels for $r < r_c$ is a decreasing function of the CMC concentration, as shown in Fig. 3.6(a). To highlight the power-law scaling between the elastic modulus and the CMC concentration, the horizontal axis is rescaled using a critical CMC concentration c_c. To be consistent with the scaling as a function of r and the unicity of r_c, irrespective of the CB content, c_c must depend on x_{CB} following $c_c = r_c x_{CB}/(1 - x_{CB})$. With $r_c = 0.037$ as in Fig. 3.6(b), the power-law exponent between $\mathcal{G}_0$ and $c_c - c_{CMC}$ for each CB content are the same and equal to $\xi = 3.8 \pm 0.5$ as expected according to Fig. 3.4.

In the next section 3.C, we show that $\mathcal{G}_0 \sim (r_c - r)^{\xi}(x_{CB} - x_c)^{\beta}$. One should note that $1/x_{CB} - 1 \simeq 1/x_{CB}$ for $x_{CB} \ll 1$, such that at low CB content:

$$(r_c - r)^{\xi}(x_{CB} - x_c)^{\beta} = (c_c - c_{CMC})^{\xi}(1/x_{CB} - 1)^{\xi} x_{CB}^{\beta} \tag{3.2}$$

$$\simeq (c_c - c_{CMC})^{\xi} x_{CB}^{\beta-\xi} \tag{3.3}$$

As shown in Fig. 3.10(d), the best power-law fit of $\mathcal{G}_0$ as a function of x_{CB} at fixed CMC concentration yields to an exponent 4.7 ± 0.7, which is compatible with $\beta - \xi = 4.4$.

The fact that the more CB in the solution, the higher c_c, emphasizes that the relevant parameter is r. Indeed, if the transition between the two regimes were only due

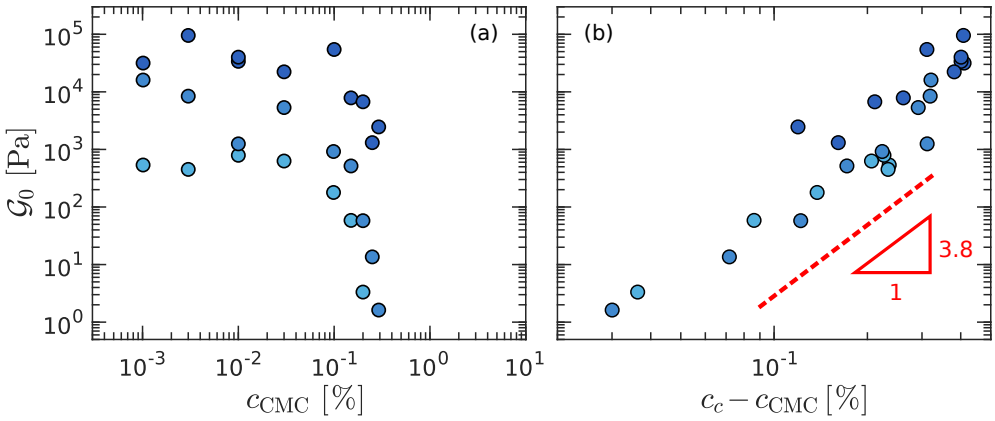

Figure 3.6: Critical CMC concentration for the depercolation transition. (a) Elastic modulus G' at $\omega = 2\pi$ rad.s^{-1} as a function of c_{CMC} for different CB contents $x_{CB} = 6\%$ (•), 8% (•), and 10% (•). (b) Same data plotted as a function of $c_c - c_{CMC}$ where the critical CMC concentration c_c was computed using $r_c = 0.037$ leading to $c_c = 0.24,\ 0.32,\ 0.41\%$ for resp. $x_{CB} = 6,\ 8,\ 10\%$. The red dotted line indicates a slope of 3.8, which is expected according to the scaling in Fig. 3.4.

to the polymer concentration, increasing the CB weight fraction would increase the effective concentration of polymer everywhere else, leading to a lower c_c, which is not what is observed here.

B Properties of CB-CMC hydrogels

Having identified two different microstructures on each side of r_c, we now determine in detail their respective linear viscoelastic properties, namely their linear viscoelastic spectrum and the impact of the CB content. Then we will discuss the electrical linear properties as a function of the composition.

B.1 Polymer-dominated regime ($r > r_c$)

We first report on the properties of gels obtained for $r > r_c$, whose microstructure is a viscoelastic matrix of CMC, physically cross-linked by CB particles dispersed individually or as clusters [see Fig. 3.5(b)].

We first characterize the gel linear viscoelastic properties by determining its viscoelastic spectrum over three decades of frequencies ω. Figure 3.7(a)-(c) show the viscoelastic spectrum for $x_{CB} = 6, 8$ and 10% at fixed CMC concentration $c_{CMC} = 2\%$. These three viscoelastic spectra all display a finite plateau modulus in the zero frequency limit, confirming that these mixtures behave as soft solids at rest. Moreover, for these three spectra $G''(\omega)$ displays a power-law dependence, at least over two decades in frequency. Both behaviors are well captured by a *fractional* Kelvin-Voigt model, which consists in a spring of stiffness G_0 in parallel with a spring-pot element [210, 270] characterized by a quasi-property $\mathbb{V}$ (dimension Pa.s$^{\alpha}$) and an exponent $0 < \alpha < 1$ [see inset in Fig. 3.7(a) for a sketch of the mechanical model]. Such a fractional element, which was first introduced by Scott-Blair [211] to describe the power-law spectrum of protein gels plays the same role as the CPE element used to describe the impedance spectra, an gives raise to a constant mechanical phase with

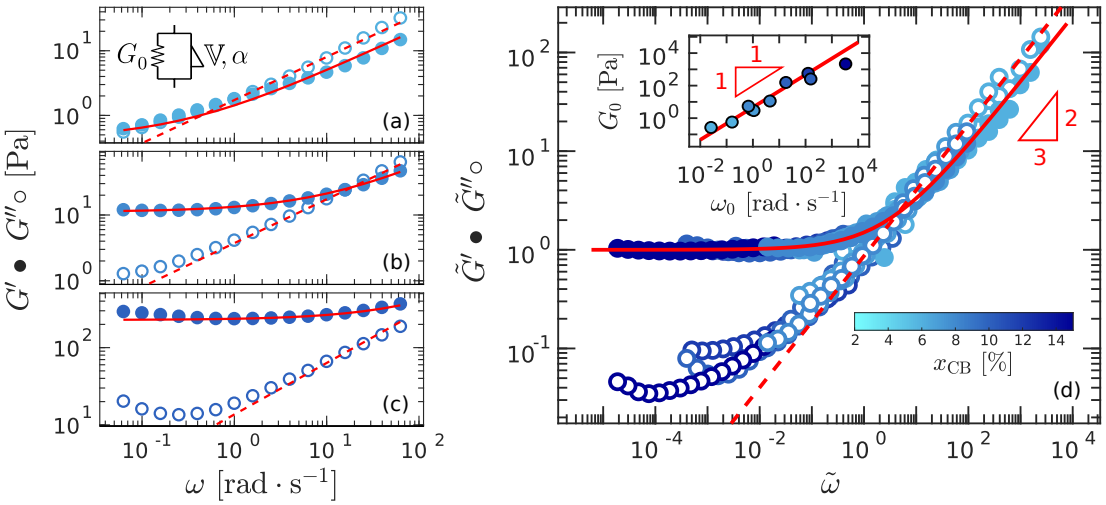

Figure 3.7: Viscoelastic spectrum in the polymer-dominated regime. Frequency dependence of the elastic and viscous moduli, G' and G'' resp., of CMC-CB dispersions with three different CB contents x_{CB} = (a) 6%, (b) 8%, and (c) 10% with $c_{CMC} = 2\%$. The red curves are the best fits of the data to a fractional Kelvin-Voigt (FKV) model [see Eq. (3.4)], which is sketched in (a). (d) Master curve for the frequency dependence of the viscoelastic moduli of CMC-CB dispersions, obtained by normalizing both the moduli and the frequency: $\tilde{G}' = G'/G_0$, $\tilde{G}'' = G''/G_0$, and $\tilde{\omega} = \omega/\omega_0$ with $\omega_0 = (G_0/\mathbb{V})^{1/\alpha}$ for different CB contents ranging from 6% to 15% with $c_{CMC} = 2\%$. The red curves correspond to the normalized FKV model $\tilde{G}^\star = 1 + (i\tilde{\omega})^\alpha$ with $\alpha = 2/3$. Inset: G_0 vs. ω_0; the red continuous line is the best linear fit of the data.

$\tan\delta = \alpha\pi/2$. The fractional Kelvin-Voigt model yields the following expression for the complex modulus:

$$G^\star = G_0 + \mathbb{V}(i\omega)^\alpha, \tag{3.4}$$

which real and imaginary parts correspond to the red fits in Fig. 3.7(a)–(c) determined simultaneously. This fit function relies only on two dimensional parameters, namely the elastic modulus G_0 and the characteristic frequency defined as $\omega_0 = (G_0/\mathbb{V})^{1/\alpha}$. Remarkably, all spectra obtained by varying the carbon content between 6 and 15% at fixed $c_{CMC} = 2\%$ can be described by varying G_0 and $\mathbb{V}$, while fixing $\alpha = 2/3$.

Such a robust description allows us to propose a universal master curve for the viscoelastic spectrum obtained at various CB contents, by using the following set of normalized coordinates: $\tilde{G}' = G'/G_0$, $\tilde{G}'' = G''/G_0$, and $\tilde{\omega} = \omega/\omega_0$ [Fig. 3.7(d)]. This master curve is, in turn, well described over 8 orders of magnitude of reduced frequency by the fractional Kelvin-Voigt model pictured as red lines in Fig. 3.7(d). The power-law dependence of both $\tilde{G}'$ and $\tilde{G}''$ with an exponent 2/3 in the high-frequency limit is in remarkable agreement with the value computed by Zimm for dense polymer suspensions and polymer solids taking into account Brownian motion and hydrodynamic interactions [271, 272]. This observation strongly suggests that CB particles contribute mainly to the low-frequency part ($\tilde{\omega} \ll 1$) of the viscoelastic spectrum, whereas the CMC entangled network dominates the high-frequency response ($\tilde{\omega} \gg 1$). This result, together with the fact that CB-CMC hydrogels are not electrically conductive for $r > r_c$, provide robust evidence that in the regime $r > r_c$, the gel microstructure consists of a CMC viscoelastic matrix in which CB particles are dispersed without forming a percolated network, while serving as cross-linkers.

Finally, note that the master curve is robust and holds for different CMC concentrations. Viscoelastic spectra of CB-CMC hydrogels with c_{CMC} varying between 2 %

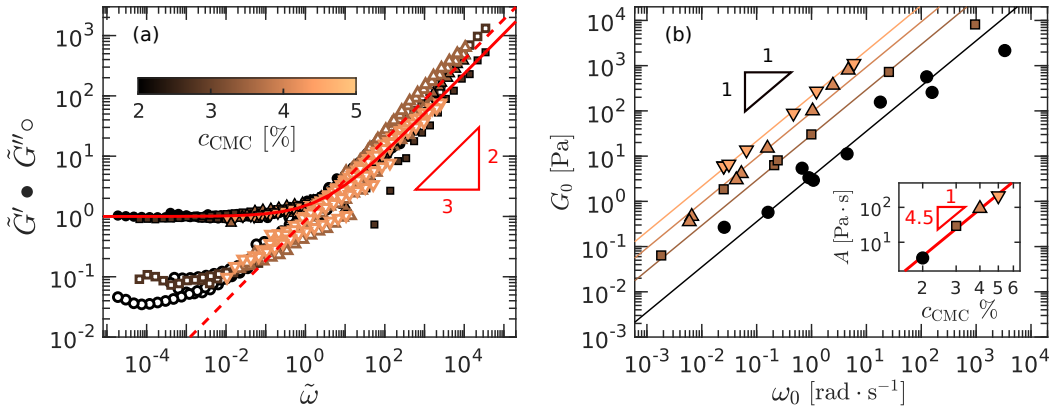

Figure 3.8: Generalization of the master curve for different CMC concentration within the polymer-dominated regime. (a) Master curve for the frequency dependence of the viscoelastic moduli of CB-CMC hydrogels for $c_{CMC} = 2\,\%$ (•), 3 % (■), 4 % (▲), and 5 % (▼) and different CB contents ranging between 5 % and 15 %. The red curves correspond to the normalized FKV model $\tilde{G}^\star = 1 + (i\tilde{\omega})^\alpha$ with $\alpha = 2/3$. (b) Scaling between the two normalization factors G_0 and ω_0. The solid lines show the best linear fits of the data $G_0 = A\omega_0$. Inset: A vs. c_{CMC} best described by a power-law fit with an exponent 4.5 ± 0.8 shown as a red line.

and 5 % and x_{CB} varying between 5 % and 15 % can be superimposed on the same master curve as that reported in Fig. 3.7, using the modulus (G_0) and frequency (ω_0) parameters extracted from the fit of each spectra by a fractional Kelvin-Voigt model (FKV). The general master curve is shown in Fig. 3.8(a). The modulus G_0 grows linearly with the frequency ω_0, with $G_0 = A\omega_0$ as shown in Fig. 3.8(b). The shift factor A increases as a power-law of the CMC concentration with an exponent of about 4.5 [see inset in Fig. 3.8(b)].

Interestingly, a similar master curve was reported for CMC-polydispersed silica hydrogels [273]. Although the impact of the CMC concentration was not determined, the scaling factor G_0 was reported to increase as a power law of the silica content with an exponent 3.15 compatible with the value $\zeta = 3.0 \pm 0.5$ reported in Fig. 3.9. This comparison suggests that the nature and specific properties of the suspended nanoparticles, e.g., shape and size, have little or no influence on this exponent, which is mainly controlled by CMC. Moreover, the viscoelastic spectrum of CMC-silica hydrogels show a power-law in the high-frequency limit, with an exponent 0.56 that is compatible with the Zimm scaling $\alpha = 2/3$ reported in the present work. Note that this exponent is not universal, and depends on the polymer-solvent interaction. For instance, the viscoelastic spectrum of polyacrylamide-silica hydrogels obtained for various contents in silica particles can also be rescaled onto a master curve that shows a high-frequency response that is a power law with an exponent 0.74 [274].

We now discuss the dependence of the plateau modulus G_0 that characterizes the gel elasticity as a function of both the CB content and the CMC concentration. As reported in Fig. 3.9, all our experimental results collapse on a master curve when G_0 is plotted as a function of $c_{CMC}^{\chi}(x_{CB} - x_c)^{\zeta}$. On the one hand, the gel elasticity increases as a power-law of the particle content relative to the mechanical percolation threshold x_c, which depends on the CMC concentration (see inset in Fig. 3.9) and was determined from the phase diagram in Fig. 3.1. In practice, the onset of rigidity decreases weakly for increasing polymer concentration, from $x_c = 5\%$ at $c_{CMC} = 1\%$ to $x_c = 4\%$ at $c_{CMC} = 5\%$. On the other hand, the gel elasticity increases as a power law of the CMC concentration, with an exponent $\chi = 2.4$. This scaling is strongly reminis-

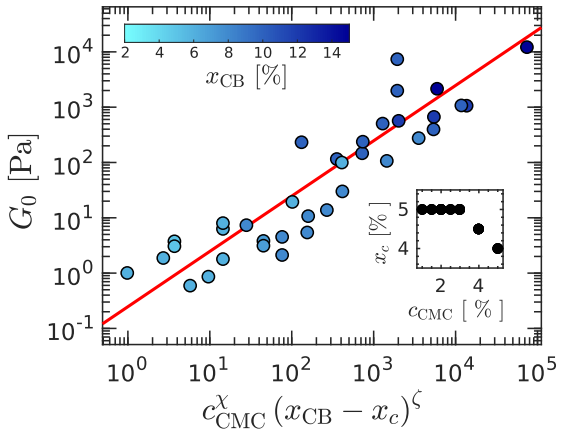

Figure 3.9: Scaling of the elastic modulus in the polymer-dominated regime. G_0 vs $c_{CMC}^{\chi}(x_{CB}-x_c)^{\zeta}$ for $r > r_c$, where $\chi = 2.4 \pm 0.4$ and $\zeta = 3.0 \pm 0.5$. The inset shows the threshold of CB content x_c as a function of c_{CMC} inferred from the sol-gel transition in the phase diagram reported in Fig. 3.1. The red line shows the best linear fit of the data.

cent of the concentration dependence predicted for the plateau modulus of entangled polymer solutions, for which an exponent $7/3 \simeq 2.33$ was derived by Colby, Rubinstein and Viovy [275]. In the present case, for $r > r_c$, CMC are indeed in an entangled regime, which is reported for $c_{CMC} \gtrsim 0.16\%$ [177]. This result further supports the idea that, for $r > r_c$, the elasticity of the CMC-CB hydrogel has two independent physical origins: a first contribution from the entangled CMC, and a second one from the CB particles, which serve as cross-linkers and inhibit the long-time relaxation of the CMC matrix, leading to solid-like behavior at rest.

B.2 Colloid-dominated regime ($r < r_c$)

Let us now consider the case $r < r_c$, where the CMC-CB hydrogel microstructure is formed by a space-spanning network of CB particles decorated with CMC polymers [see Fig. 3.5(a)]. The viscoelastic spectrum of two representative gels containing $c_{CMC} = 10^{-2}\%$ and $x_{CB} = 6$ and 8%, respectively are illustrated in Figs. 3.10(a) and 3.10(b). For both gels, G' is merely frequency independent, whereas G'' decreases with increasing frequency, and shows a flattening or even a slight upturn in the high-frequency limit [see Fig. 3.10(a)], which is the signature of the solvent viscosity and Brownian motion of the CB particles [276]. Such a frequency spectrum, along with the logarithmic aging dynamics reported in Section 3.C.1, shows that CMC-CB hydrogels display a glassy-like behavior for $r < r_c$, similar to that reported for jammed assemblies of soft particles [218], or fractal colloidal gels [41, 277]. Therefore, we fit the viscoelastic spectrum reported in Figs. 3.10(a) and 3.10(b) using a modified version of the Soft Glassy Rheology (SGR) model, which is well known to capture such a behavior and reads [213, 214, 217, 219]:

$$G' = \mathcal{G}_0 \left(1 - (\omega\tau)^{x-1}\right) + c\omega^{1/2} \tag{3.5}$$

$$G'' = \mathcal{G}_0 (\omega\tau)^{x-1} + c\omega^{1/2} + \eta_\infty \omega \tag{3.6}$$

where x corresponds to a mean-field noise temperature, τ denotes the effective sample age, and the terms $c\omega^{1/2}$ and $\eta_\infty\omega$ account respectively for Brownian motion, and for the solvent viscous contribution [223]. The data are fitted using Eqs. (3.5) and (3.6)

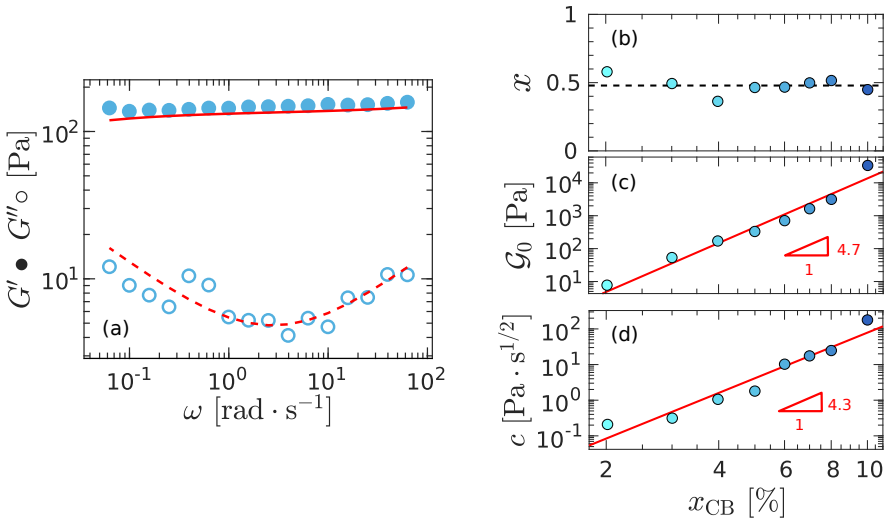

Figure 3.10: Viscoelastic spectrum in the colloid-dominated regime. (a) Frequency dependence of the elastic and viscous moduli, G' and G'' resp., of a CB-CMC hydrogel at $c_{CMC} = 0.01\%$ & $x_{CB} = 6\%$. The red curves are the best fits of the data to a modified SGR model [see Eqs. (3.5) and (3.6)] with $\tau = 1200$ s, $x = 0.50$, $c = 1.4$ Pa.s$^{1/2}$ in (a), and $\tau = 1200$ s, $x = 0.53$, $c = 41$ Pa.s$^{1/2}$ in (b). (c) Fit parameter x, which is constant $x = 0.5 \pm 0.1$, irrespective of the CB content as shown by the dashed line. (d) Fit parameter $\mathcal{G}_0$, which increases as a power law of x_{CB} with an exponent 4.7 ± 0.7. (e) Fit parameter c, which increases as a power law of x_{CB} with an exponent 4.3 ± 0.9.

with $\mathcal{G}_0$, x, and c as free parameters. The parameter $\tau = 1200$ s is the time elapsed since the end of the rejuvenation step and $\eta_\infty = 2.10^{-3}$ Pa.s is the viscosity of the CMC solution at $c_{CMC} = 0.01$ %, measured independently with an Ubbelholde viscosimeter. Fitting our experimental data for samples prepared with a CB content ranging between 2% and 12%, yields a constant effective temperature, $x \simeq 0.5 < 1$ [Fig. 3.10(c)], that is characteristic of a yield stress fluid [219], and a reference modulus $\mathcal{G}_0$ that grows as a power-law of the CB weight fraction, with an exponent 4.7 [Fig. 3.10(d)]. First, the latter value is much larger than 1.8, which allows us to rule out a microstructure involving polymer-bridged nanoparticles [69, 70]. Second, the exponent 4.7 is consistent with that reported for CB gels in aprotic solvents, e.g., mineral oils, in which the elasticity also originates from a percolated network of CB particles [56, 117], as well as in depletion gels [278]. Similarly, the Brownian parameter c follows a power-law of the CB content as shown in Fig. 3.10(e). The power-law exponents in both $\mathcal{G}_0$ and c are comparable within the uncertainties, it suggests that the Brownian contribution scales as the typical elasticity and the Brownian diffusion timescale does not depend on the CB content.

Varying the polymer concentration as well as the CB content, we observe that the gel reference modulus falls onto a master curve when plotted as a function of $(r_c - r)^\xi x_{CB}^\beta$, as illustrated in Fig. 3.11 with $\xi = 3.8$ and $\beta = 8.2$. This expression accounts for the scalings displayed in Fig. 3.4 (a) and for the fact that, as $r \to r_c$, the elastic properties vanish, for the CB particles and clusters become isolated in the CMC matrix. Note that these exponents are fully consistent with the power-law dependence of $\mathcal{G}_0$ found in Fig. 3.10.

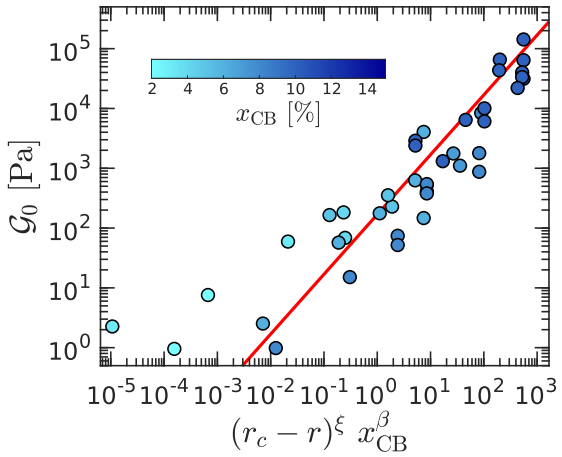

Figure 3.11: Scaling of the elastic modulus in the colloid-dominated regime. Elastic modulus $\mathcal{G}_0$ vs $(r_c - r)^\xi x_{CB}^\beta$ for $r < r_c$, where $r_c = 0.037$, $\xi = 3.8 \pm 0.5$, and $\beta = 8.2 \pm 0.6$ (consistent with Fig. 3.4). Color levels code for the CB content ranging between 2 and 10%. The red line shows the best linear fit of the data.

B.3 Influence of the composition on the scattering patterns of CB-CMC hydrogels

We now investigate further the microstructure proposed for both colloidal and polymer regimes. Direct visual experiments are not available as the CB particles absorb too much the light. SAXS experiments were conducted to witness any signature of the depercolation transition when r crosses r_c.

a X-ray scattering intensity patterns

We first report on the transition between the two regimes and we have a look at the scattering intensities at fixed CB content for different polymer concentrations. The scattering intensities have been rescaled in order to collapse at $q = 0.1$ nm^{-1}, in the range of the form factor. The results are shown as a Kratky plot in Fig. 3.12 to emphasize the differences. Regardless of the CB concentration [Fig. 3.12(a)-(b)], there is a clear transition when r crosses r_c. Within each regime, the dependence on the composition is less striking [Fig. 3.12(c)-(d)]. In the colloidal regime (green curves), the peak intensity occurs at a higher q than the one in the polymer regime (brown curves). This peak may be understood as the signature of a typical correlation length in the structure of the CB particles. It means that the CB particles are closer in the colloidal than in the polymer regime, which remarkably supports the idea of a depercolation transition. Unfortunately the q range is too small to probe the existence of a percolated network, but the data still show evidence of a change in the microstructure at the scale of a few CB particles (∼500 nm, see Fig. 2.1 in Chapter 4.13). There is also a clear difference in the lowest q range below $q = 0.01$ nm^{-1} where the scattering intensity reaches a minimum. In the colloidal regime, the upturn in the low q range is very sharp and suggests that the structure of the CB is correlated over a large distance as expected for a CB network [256]. On the other hand, in the polymer regime the curves are weakly decreasing in this q range, which suggests there is no structure larger than a few CB particles. These features are consistent with the sketches proposed in Fig 3.5.

To quantify these observations, we extracted from the Kratky plots the coordinates of the maximum (q_{max}, $K_{max} = I_{max} q_{max}^2$) and of the minimum ($q_{min}$, $K_{min} = I_{min} q_{min}^2$).

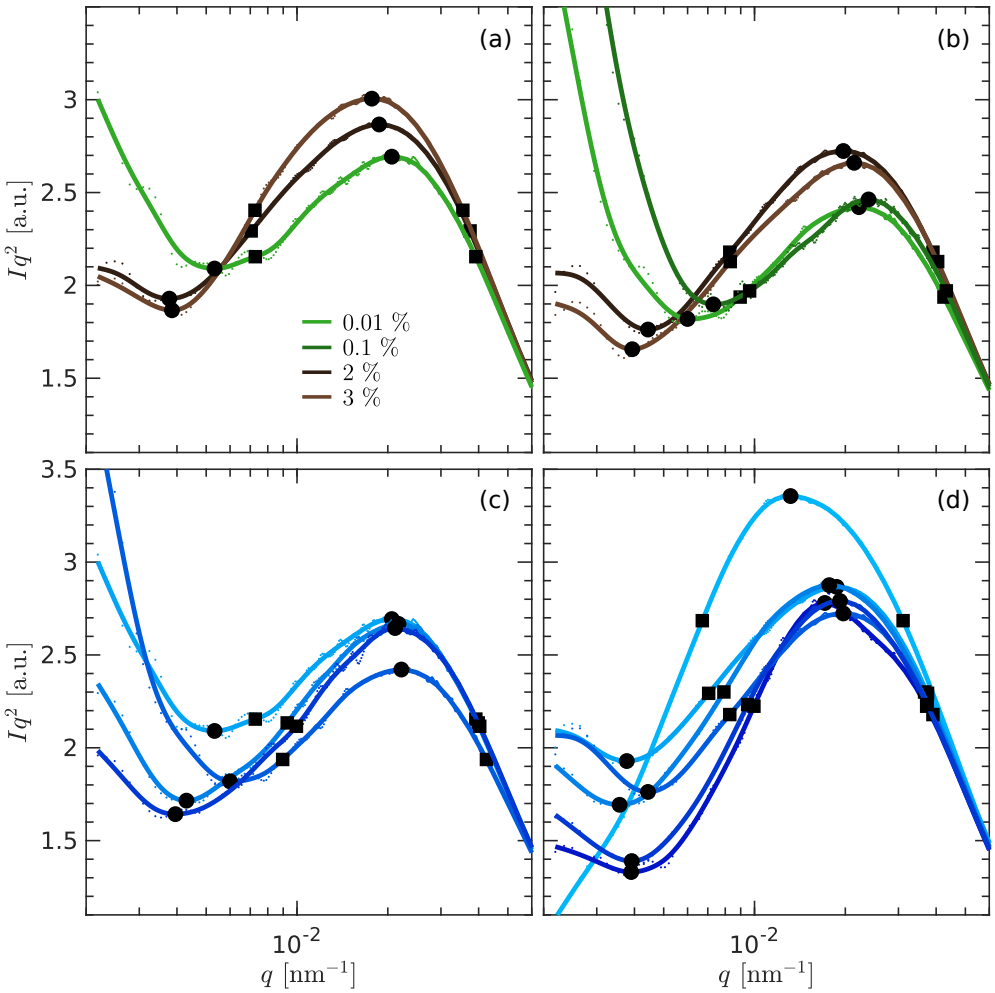

Figure 3.12: Kratky representation of the scattering intensity of the CB only in CB-CMC dispersions at different compositions. The circles represent $q_{\min}$ and $q_{\max}$ ($q_{\min} < q_{\max}$) and the squares represent q_1 and q_2 ($q_1 < q_2$). The CB content is fixed at $x_{CB} = 2\%$ (a) and $x_{CB} = 6\%$ (b) with different $c_{CMC} = 0.01, 0.1, 2$ and 3%. The colloidal regime is depicted in green and the polymer regime in brown. The CMC concentration is fixed at $c_{CMC} = 0.01\%$ (c) and $c_{CMC} = 2\%$ (d) with different x_{CB} from 1 to 10%. Darker color correspond to higher CB content, according to the color bar in Fig. 3.7.

As the peak is well determined for the maximum, we also look at the broadness of the peak through q_1 defined as the position of the inflexion point between $q_{\min}$ and $q_{\max}$ together with q_2 the position where the Kratky plot have the same value as at q_1 on the other side of the peak. The value q_1 determines the transition between the correlation length and the void correlation length. The ratio q_2/q_1 informs on the broadness of the peak. The data are reported for several compositions in Fig. 3.13. The qualitative results described above hold for all the compositions explored, which emphasizes the relevance of the depercolation transition scenario. The maximum peak around $K_{\max}$ is more pronounced, broader and occurs at lower q [Fig. 3.13(a),(c),(f)] in the polymer regime than in the colloidal regime. These features mean that the CB network has a better defined correlation lengthscale in the colloidal regime, suggesting that the CB clusters in the polymer regime are more distributed in size. As for the minimum peak, it also appears more pronounced and occurs at lower q [Fig. 3.13(b),(d)] in the polymer regime than in the colloidal one. The transition between the dense ($q_{\max}$) and the less

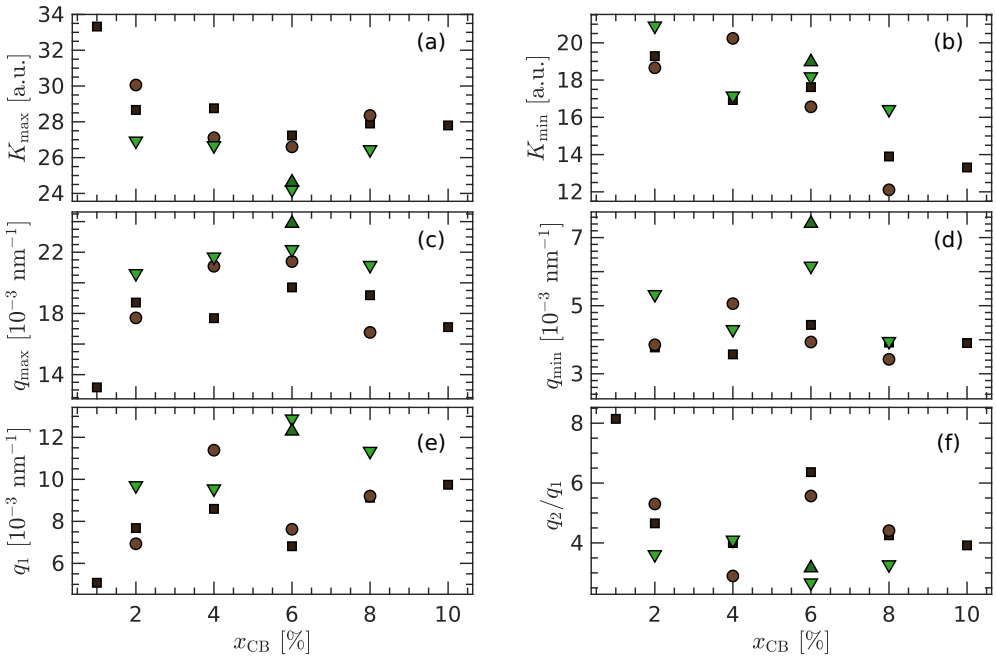

Figure 3.13: Noteworthy quantities of interest in the Kratky plots for different polymer concentrations $c_{CMC} = 0.01, 0.1, 2$ and 3% as a function of the CB content. The values of Iq^2 at the maximum K_{max} (a) at the minimum K_{min} (b) and their corresponding abscissa q_{max} (c) q_{min} (d). The inflexion point q_1 (e) and the q_2/q_1 ratio (f).

dense (q_{min}) correlation lengthscales is reported by q_1 in Fig. 3.13(e). The values of q_1 are shifted to the low q values in the polymer regime with compared to the colloidal regime.

The CB content however has limited impact on the previous values. K_{min} being a decreasing function of x_{CB} with q_{min} roughly constant is consistent with the zero limit $K_{min}/q_{min}^2 \simeq I(q \to 0) \propto \chi_T$ the isothermal compressibility, which decreases as a function of the concentration [279]. However the position of the maximum correlation and its value seem to follow a bell curve which maximum is around $x_{CB} = 6\%$ for all the CMC concentrations probed. It suggests that more CB leads to denser clusters until $x_{CB} = 6\%$, and then the clusters spread more with increasing CB content. It may arise from a longer range of interaction which inhibits the dense aggregation of CB when the bulk contains too many of them. There is however no clear trend for the broadness of the peak and the position of the minimum correlation.

Finally, the scattering intensity of the dilute solution in the polymer regime (c_{CMC} = 2% & $x_{CB} = 1\%$) is strikingly different from the others [lightest blue Fig 3.12(d)]. The correlation lengthscale and the peak broadness are two times bigger than in any other sample. The decorrelation is also much more marked and the minimum is outside the accessible q range. This suggests that the CB are isolated in the polymer matrix and well dispersed with a typical distance that fluctuates a lot.

b Influence of the composition on X-ray Photon Correlation Spectroscopy

Here we discuss the impact of the sample composition on the structure dynamics at the nanoscale, conducted with X-ray Photon Correlation Scattering (XPCS). The goal of the experiments is to quantify how long the microstructure remains correlated, through comparison of scattering patterns measured at a high frequency. The experi-

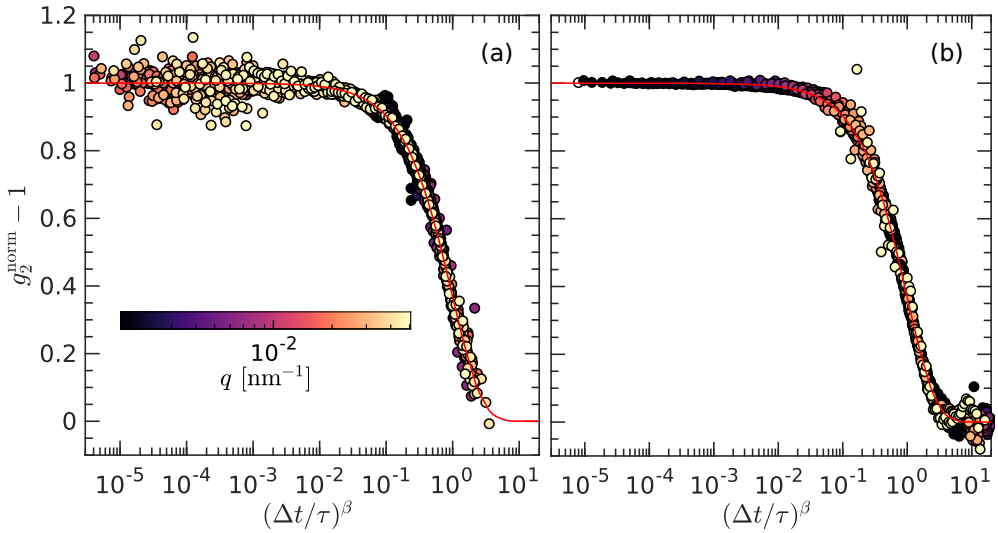

Figure 3.14: XPCS master curve of the normalized auto-correlation function $g_2^{\mathrm{norm}} - 1$ as a function of rescaled lag time $(\Delta t/\tau)^{\beta}$, where β and τ are obtained through an individual fit of the data of the form $g_2^{\mathrm{norm}} - 1 = \exp((-\Delta t/\tau)^{\beta})$. As represented by the colormap, brighter colors correspond to higher q-values ranging from $q = 2.10^{-3}$ to 2.10^{-2} nm^{-1}. The red curve shows a simple decreasing exponential function. Two typical samples are shown: either in the colloidal regime ($r < r_c$) with $c_{\mathrm{CMC}} = 0.01\%$ and $x_{\mathrm{CB}} = 6\%$ (a), or in the polymer regime ($r > r_c$) with $c_{\mathrm{CMC}} = 2\%$ and $x_{\mathrm{CB}} = 8\%$ (b). The values of τ and β are plotted in Fig. 3.15.

ment and analysis are detailed in 2.G.4. The typical data obtained with the procedure therein are shown in Fig. 3.14 as a form of a master curve for all the wavevector amplitudes probed to emphasize the accuracy of data modeling with generalized exponential functions. The rescaled lag time $(\Delta t/\tau)^{\beta}$ is obtained through the individual fit of the data with the expression of eq.(2.96), which values of τ and β are plotted in Fig. 3.15. Almost full decorrelation is observed over the maximum range of lag-time (up to 10^4 s), which ensures a proper determination of τ and β. The decorrelation depends on q, which suggests that there is indeed an effect of the composition on the nanoscale dynamics. However artifacts due to the degradation of the polymer under the X-rays may also impact the decorrelation.

The decorrelation occurs at very different timescales in the colloidal regime and in the polymer regime. Typical values of τ are around $10^4 - 10^5$ s in the former regime and around $1 - 10^2$ s in the latter one. These timescales correspond to the dynamics of the CB particles, since the diffraction intensity is due to the CB in the CB-CMC mixtures. These typical values support the microstructures depicted in Fig.3.5. The decorrelation in the colloidal regime is extremely long, which is consistent with an arrested structure for the CB, namely a glassy structure [280]. However the results presented here show only one timescale, which might be due to experimental limitations. The nanoparticles are tightly held together and there is not much possibility for them to wiggle around, leading to long decorrelation times. The decorrelation time τ plotted in Fig. 3.15(a) scales roughly as $\tau \sim q^{-1}$, which corresponds to a hyperdiffusive process, consistent with other nanoparticle systems reported in the literature, e.g. glasses composed of grafted nanoparticles [281, 282] or grafted nanoparticles in a polymer matrix [283]. Luca Cipelletti et al. [284] studied polystyrene colloidal gels and attributed this hyperdiffusivity to a global shrinkage of the bulk, namely caused by syneresis. However the exponent reported here of the generalized exponential

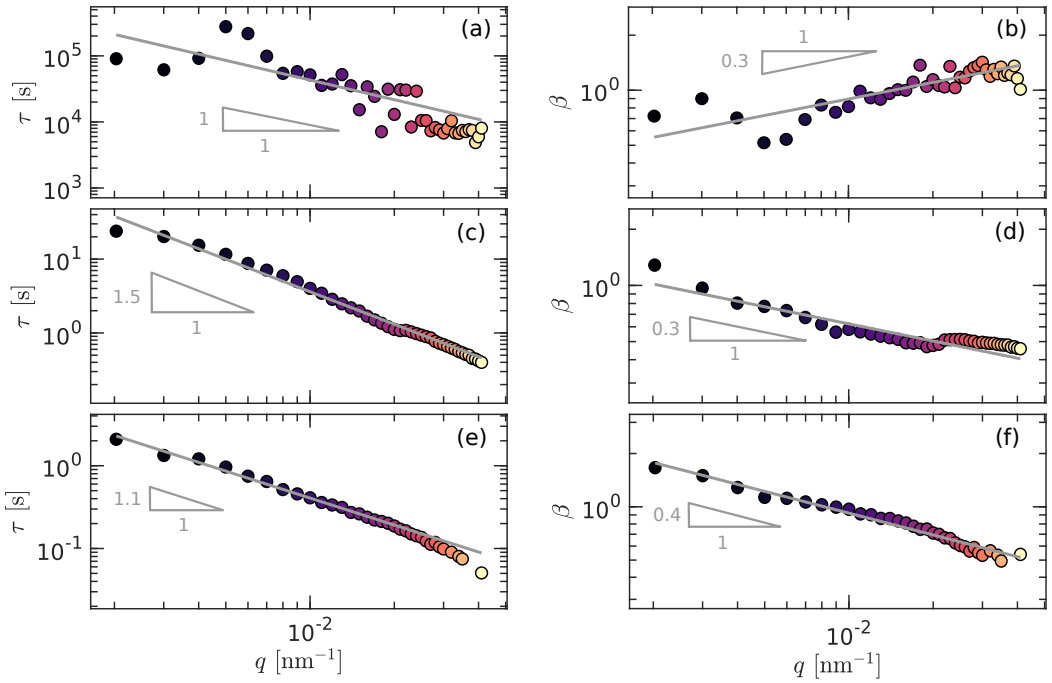

Figure 3.15: XPCS fitting parameters extracted from the fit of the autocorrelation function g_2^{norm} as a generalized exponential function with a timescale τ (left) and exponent β (right) for representative samples: $c_{\text{CMC}} = 0.01\%$ & $x_{\text{CB}} = 6\%$ (a-b), $c_{\text{CMC}} = 2\%$ & $x_{\text{CB}} = 8\%$ (c-d) and $c_{\text{CMC}} = 2\%$ & $x_{\text{CB}} = 2\%$ (e-f). The grey lines correspond to the best power-law fitting of the data, which exponent are given on the graphs and reported in Table 3.1. One should emphasize that data above $q > 3.10^{-2}$ nm^{-1} should be considered with cautious, see Section 2.G.

$\beta \simeq 1$ weakly depends on q, in contrary to $\beta > 1$ observed in the examples cited above.

In the polymer regime ($r > r_c$), same experiments have been conducted for different composition, which results are summarized in Table 3.1. Representative examples are shown in Fig. 3.14(b). The main discrepancy between the two regimes is the relaxation time, which is more than 100 times smaller in the polymer regime than in the colloidal one. It supports the vision of isolated clusters of particle moving in a polymer matrix, the structure is not arrested. Besides, apart from the sample with polymer content $c_{\text{CMC}} = 2\%$ and CB (Vulcan PF) content $x_{\text{CB}} = 8\%$, all data are consistent with the expected trends. The typical timescale increases either with both the CB and polymer contents as the solvent increases in viscosity[1]. In this polymer regime, the process is also hyperdiffusive with τ decaying as power-law of q with an exponent between 1 and 2. On the other hand, the exponent β in the generalized exponential function goes from $\beta \simeq 2$ (compressed exponential) to $\beta \simeq 0.3$ (stretched exponential) as q increases. This kind of behavior has been reported in experiments with polymer-nanoparticles systems [283, 285] and numerical simulations of colloidal gels [286], but there is not clear interpretation of such feature.

Although these results are consistent with the previous ones and reliable, we miss XPCS data for the CMC solution in both regimes to rule out the contribution of its degradation to the decorrelation timescales. However, the CMC does not scatter much with X-rays so data would be too noisy (intensity of the incident beam must not

[1]Similarly, with the smaller particles Vulcan PF, we measured smaller decorrelation times.

c_{CMC} [%]	x_{CB} [%]	τ [s]	β	exponent τ vs q	exponent β vs q
0.01	6	$10^4 - 10^5$	0.8-1	1	-0.3
2	2	$10^{-2} - 1$	0.2-1	1.8	0.5
	4	$10^{-2} - 1$	0.3-2	1.6	0.5
	8	$10^{-1} - 20$	0.3-2	1.5	0.5
3	4	$1 - 10^2$	1-2	1	0.2
	8	$1 - 10^2$	0.6-2	1.8	0.4
2	8 (PF)	$1 - 10^2$	0.5-1.5	1.2	0.3
3	8 (PF)	$10^{-1} - 10$	0.5-1.5	2.3	0.2

Table 3.1: **Typical XPCS results** extracted from the fit of the autocorrelation function g_2^{norm} as a generalized exponential function. Several CMC and CB contents are tested with two different kinds of CB: XC72R and Vulcan PF, a smaller sized CB particles (typically a 40 nm radius).

change since it impacts the polymer degradation).

X-ray scattering experiments bring to light the underlying microscopic differences between the polymer and colloidal gels. Within each regime the impact of the composition is however not clear and calls for experiments probing larger scales, which are however difficult to reach in SAXS. Light scattering fits nicely in this end, but it would require to replace the CB particles with non-light absorbing samples, such as Fumed Silica which has similar properties compared to the CB. However we can take advantage from the electrical conductivity of the CB and investigate the influence of the composition onto the electrical properties of the CB-CMC hydrogels.

B.4 Influence of the composition on the electrical properties of CB-CMC hydrogels

Here, we report on the impact of the CMC concentration at fixed CB content (8%) on the four parameters σ_{CB}, σ_{ion}, n and Q extracted from the fit of the impedance spectra by Eq. (1) in the main text. Figure 3.16(a) is identical to Fig. 4(b) in the main text. Figure 3.16(b) shows that the ionic conductivity, mostly related to sodium cations, follows the same trend as σ_{CB}; it decreases upon approaching $r \simeq r_c$, while it increases linearly with the CMC content in the polymer-dominated regime, because CMC is added in the form of a sodium salt. Figure 3.16(c) shows that n increases monotonically from $n = 0.7$ to $n \simeq 0.8$ in the “colloid-dominated regime" (i.e., $r < r_c$), and shows large fluctuations before stabilizing to $n = 0.8$ in the “polymer-dominated regime" (i.e., $r > r_c$). This observation suggests that the capacitance associated with the electrolyte-electrode contact tends to behave more ideally with increasing content in sodium ions (through the increase of the Na-CMC concentration), while such a capacitance is independent of the CMC concentration in the concentrated regime. Finally, Fig. 3.16(d) shows that Q is relatively insensitive to the CMC concentration over the entire range investigated here.

Finally, CMC-CB hydrogels in the colloid-dominated regime (i.e., $r < r_c$) are electrically conductive at zero frequency [Fig. 3.4(b)]. In Figure 3.17, we compare their mechanical and electrical properties, and observe that the electrical conductivity σ_{CB} conferred upon the sample by the percolated network of CB particles increases as a power law of the reference modulus $\mathcal{G}_0$, with an exponent of about 0.6. Note that a compatible exponent of 0.6 was robustly observed with the same type of CB parti-

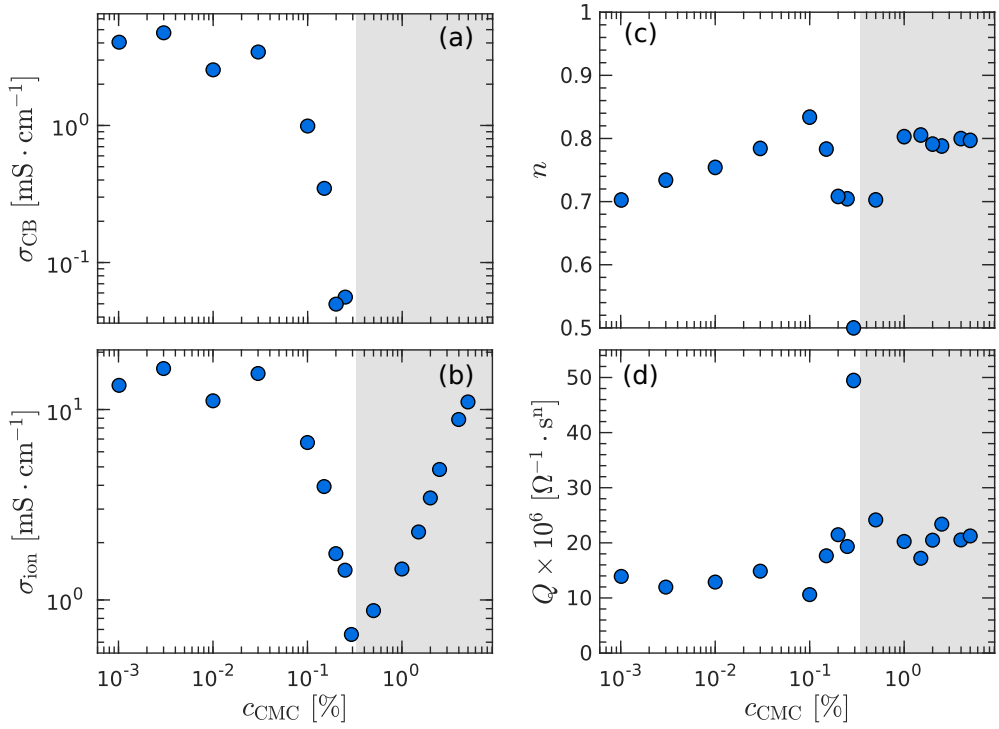

Figure 3.16: Impact of the polymer concentration on the electrical parameters (a) σ_{CB}, (b) σ_{ion}, (c) n, and (d) Q extracted by fitting the impedance spectra of CB-CMC mixtures at fixed CB content (8 %) and various CMC concentrations to Eq. (1) in the main text. The grey zone highlights the polymer-dominated regime in which $\sigma_{CB} = 0$, and corresponding to $c_{CMC} > 0.32\%$ (computed using $r_c = 0.037$ at $x_{CB} = 8\%$).

cles dispersed in mineral oil at various weight fractions in the absence of any dispersant, and for various shear histories [121]. This comparison strongly suggests that, for $r < r_c$, CMC only serves to stabilize the CB network in water, without affecting the link between the mechanical and electrical properties, at least for $r \ll r_c$. Yet, one should emphasize that CMC-CB hydrogels display much lower conductivity values ranging between 10^{-4} and 10^{-2} mS.cm^{-1}, compared to that measured for CB in mineral oil (between 10^{-2} and 2 mS.cm^{-1}), at similar weight fractions. This discrepancy most likely results from the coating of the CB particles by the CMC, which lowers the conductivity.

Electrical and mechanical properties both increase as power-laws of the CB mass fraction. They are indeed highly correlated because they both arise from the CB network, however conductivity and elasticity do not scale with the same exponent with respect to x_{CB}: at $c_{CMC} = 0.01\%$ the exponent is 2.8 ± 0.4 for the conductivity and 4.7 ± 0.7 for the elasticity. It has been shown that the key parameter for the elasticity in a colloidal gel is the bending of the network, which has barely no impact on the electrical conductivity. Hence, a higher connectivity due to a higher CB concentration will lead to a denser network that is more electrically conductive due to geometrical considerations only, whereas the elasticity increase both because the network is denser and connections are less likely to bend [287, 288]. This is consistent with the larger exponent for $\mathcal{G}_0$ versus x_{CB} than the one for σ_{CB}.

We presented the properties *at rest* of the CB-CMC hydrogels and identified two different types of system depending on the CMC-to-CB ratio. In soft matter systems are scarcely in a stationary state and they might evolve with time. We will focus on

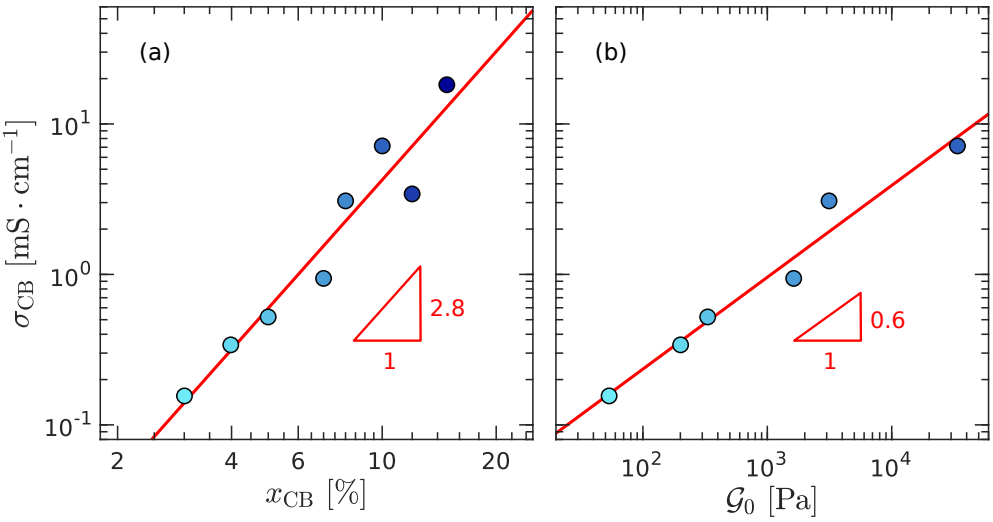

Figure 3.17: Electrical conductivity of the CB network σ_{CB}. (a) Conductivity against the CB content, the colors indicate the values of x_{CB} using the same scale as Fig. 3.11. The red line is the best power-law fit with an exponent 2.8 ± 0.4. (b) Conductivity against elasticity scale $\mathcal{G}_0$. The red line is the best power-law fit with an exponent 0.6 ± 0.2.

the dynamic evolution of the mechanical, structural and electrical properties of these gels in the following.

C Dynamics of recovery of CMC-CB hydrogels

C.1 Mechanical aging

To study the mechanical properties, a shear rejuvenation is applied before each experiment. The system is then let at rest to reach a state, which time evolution is

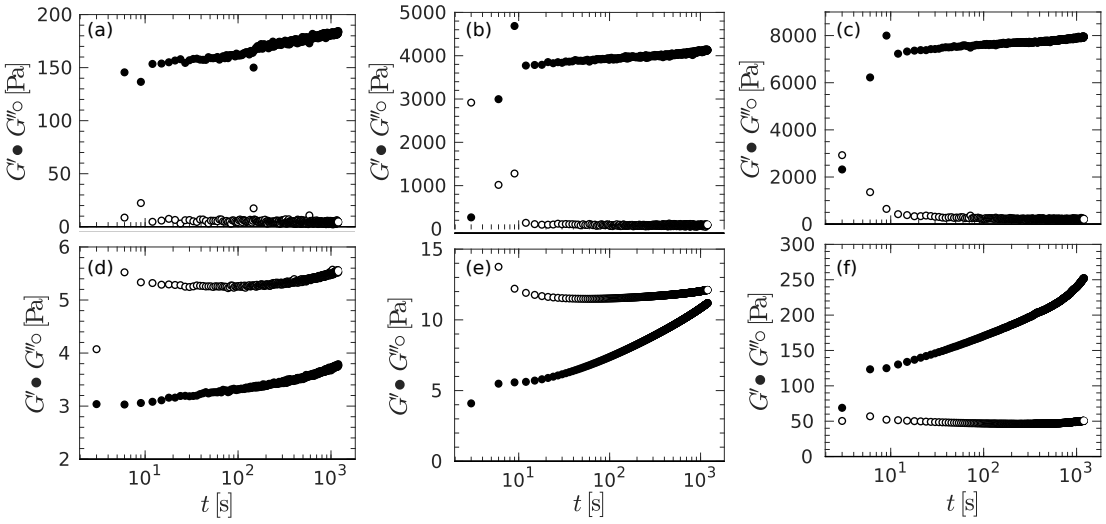

Figure 3.18: Recovery following a preshear at $\dot{\gamma} = 500$ s^{-1} during 180 of CMC-CB hydrogels: time evolution of the elastic and viscous moduli G' and G'' respectively, measured at $\omega = 2\pi$ rad.s for two different CMC concentrations: $c_{CMC} = 0.01$ % with (a) $x_{CB} = 4\%$, (b) $x_{CB} = 6\%$, (c) $x_{CB} = 8\%$, and $c_{CMC} = 2\%$ with (d) $x_{CB} = 6\%$, (e) $x_{CB} = 8\%$, (f) $x_{CB} = 10\%$.

negligible. This is a so-called “quasi-stationary" state. Formally the goal is to reach a case where the Mutation number $Mu = t_{exp}/\tau_{aging}$ is negligible [199, 200], where t_{exp} and τ_{aging} are respectively the typical timescale for the experiment and the typical aging timescale of the system. If $Mu \ll 1$ the system does not evolve much during the time of the experiment so that the system can be seen at rest while the experiment is performed.

The goal of this section is to grasp the typical timescale τ_{aging} for several compositions of CB-CMC hydrogels. Moreover the way the linear viscoelastic properties evolve as a function of time are insightful on the microstructure aging processes. Following a preshear at $\dot{\gamma} = 500\ s^{-1}$ during 180 s, CMC-CB hydrogels display two different types of recoveries depending on the relative content of CMC and CB, as illustrated in Fig. 3.18. For $r < r_c$, the sample elastic modulus at $\omega = 2\pi$ rad.s verifies $G' \gg G''$ in less than a few seconds, and grows logarithmically as a function of time [Fig. 3.18(a)-(c)]. Such dynamics are robust and merely depend on the CB content. It is highly reminiscent of a colloidal gel behavior as seen in [289]. Such a logarithmic evolution corresponds to a scaling $\tau_{aging} \sim t$ where the reference time is the end of the preshear. The evolution timescale is therefore of the order of the age of the sample. Aging effects are likely to be neglected in our experiments in which we let the samples rest for 20 min before any experiment, and the latter never exceeds 15 min.

In contrast, for $r > r_c$, the recovery is faster than logarithmic, and strongly depends on the CB content: the crossover time of G' and G'' at $\omega = 2\pi$ rad.s drops for increasing CB content [Fig. 3.18(d)-(f)]. The Mutation number is therefore difficult to evalu-

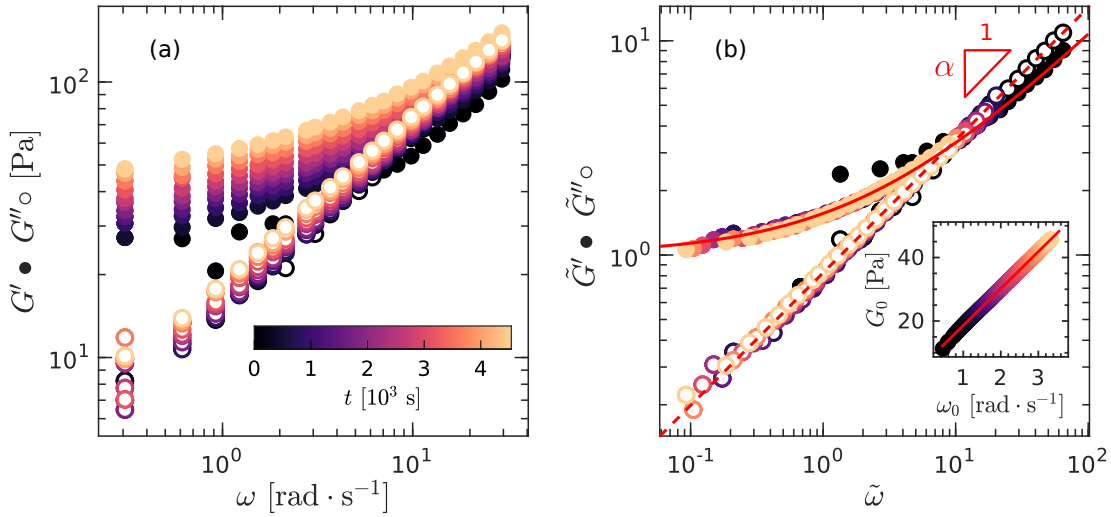

Figure 3.19: Time resolved viscoelastic spectroscopy (a) Time evolution of the viscoelastic spectra of a CMC-CB hydrogel in the polymer regime ($c_{CMC} = 3$ % and $x_{CB} = 8$%) following a preshear at $\dot{\gamma} = 500\ s^{-1}$ during 180 s. Elastic and viscous moduli G' and G'' respectively, are measured using an OWCh sequence with $r_{OWCh} = 0.1$ and $t_w = 1$ s so that the frequencies range from $\omega = 0.3$ to 30 rad.s. The colors encode the time elapsed after the preshear as represented in the colorbar. (b) Master curve for the frequency dependence of the viscoelastic moduli of this sample at different time, obtained by normalizing both the moduli and the frequency: $\tilde{G}' = G'/G_0$, $\tilde{G}'' = G''/G_0$, and $\tilde{\omega} = \omega/\omega_0$ with $\omega_0 = (G_0/\mathbb{V})^{1/\alpha}$, extracted from the FKV [eq. (3.4)] fit of the data with fixed $\alpha = 0.62$. The red curves correspond to the normalized FKV model $\tilde{G}^\star = 1 + (i\tilde{\omega})^\alpha$ with $\alpha = 0.62$. Inset: G_0 vs. ω_0; the red continuous line is the best linear fit of the data. In both (a) and (b) only 1/3 of each spectrum and only 1/3 of the total number of spectra is represented for visibility, the inset shows the full data set.

ate. Besides, one should remain extremely cautious with these data: the frequency at which the moduli are measured is arbitrary and the viscoelastic spectra depend a lot on the frequency in the polymer regime $r > r_c$, unlike in the colloidal regime $r < r_c$ [see Figs. 3.7 and 3.11]. Therefore, the time-evolution of the moduli at fixed frequency is not sufficient to decouple the evolution of the modulus scale from the evolution of the frequency scale. This is the aim of the Optimally Windowed chirp (OWCh) protocol introduced in by Geri et. al in 2018 [44] and described in section 2.D.3.

The evolution of the mechanical properties in the polymer regime is rather slow as depicted in Fig. 3.18(d-f). It allows us to send chirp signals long enough (15 s) to reach small frequency down to 0.3 rad.s^{-1}, in the plateau regime of the elastic modulus [see Fig.3.7]. Three hundreds 15 s chirp signals are repeated in order to span an evolution time of 4500 s. The resulting complex moduli thus computed are presented in Fig. 3.19(a) for a sample at $c_{CMC} = 3\%$ & $x_{CB} = 8\%$. The OWCh parameters are set to $r_{OWCh} = 0.1$ and $t_w = 1$ s leading to a frequency range from $\omega = 0.3$ to 30 rad.s^{-1}, which enables to precisely measure the low-frequency elastic plateau. This allows us to nicely fit all of the spectra with a FKV model and extract G_0 and ω_0 as a function of

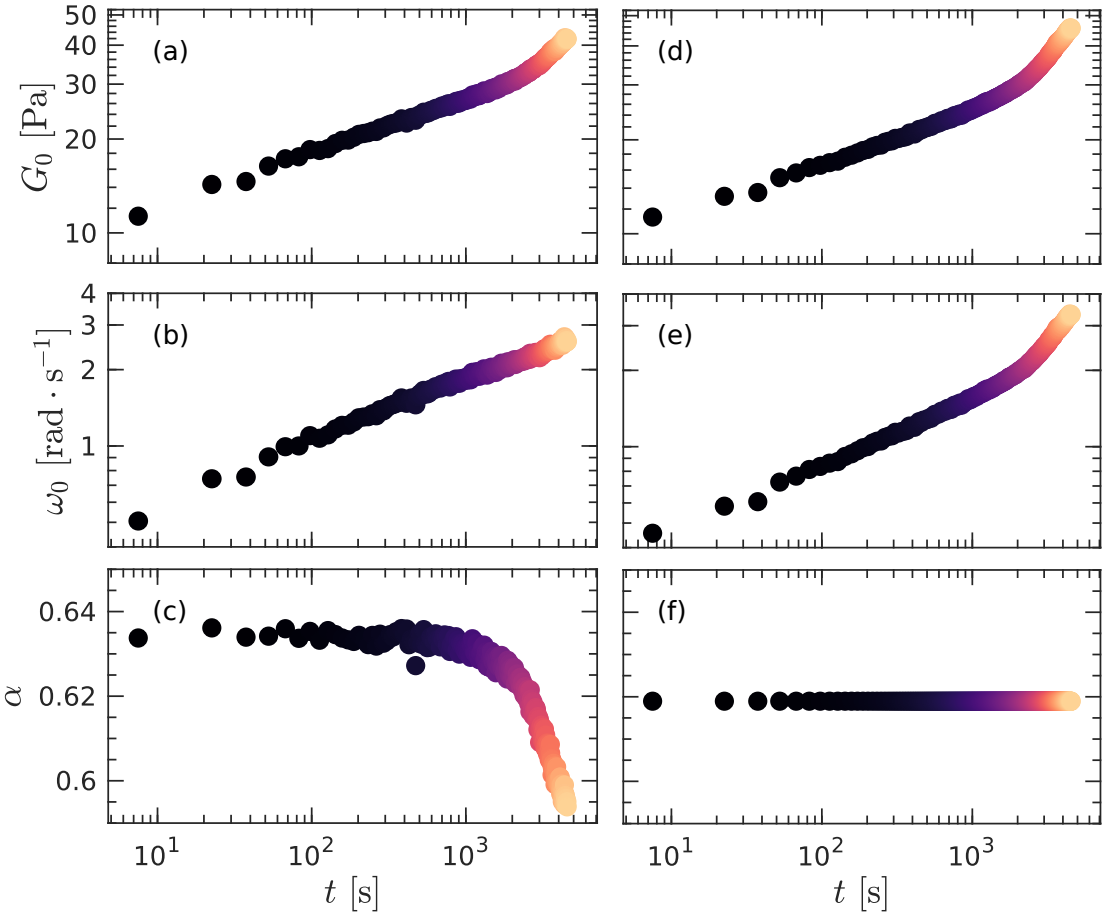

Figure 3.20: Time evolution of the FKVM parameters of a CMC-CB hydrogel in the polymer regime ($c_{CMC} = 3$ % and $x_{CB} = 8\%$) following a preshear at $\dot{\gamma} = 500$ s^{-1} during 180 s. The colors encode the time elapsed after the preshear as represented in the colorbar in Fig. 3.19(a). The parameters G_0 (a), $\omega_0 = (G_0/\mathbb{V})^{1/\alpha}$ (b) and α (c) are extracted from the FKV model [eq. (3.4)] with α as a free parameter, or when α fixed to the mean value in (c): G_0 (d), $\omega_0 = (G_0/\mathbb{V})^{1/\alpha}$ (e) and $\alpha = 0.62$ (f).

time. Normalized spectra are shown in Fig. 3.19(b) to emphasize the relevance of the FKV model.

The time evolution of the scaling KFV parameters G_0, ω_0 and α are plotted in Fig. 3.20(a-c) with α as a free parameter and Fig. 3.20(d-f) with fixed $\alpha = 0.62$, which corresponds to the mean value in Fig. 3.20(c). It remains unclear if the evolution of α is physically meaningful or if it comes from the fitting method applied: as the spectra shift horizontally with time the fits are made in a different part of the FKV model, which may induce variations. Namely, as the FKV model is a good but not perfect description of the data, the slope in the data could evolve slightly with the frequency so that changing the frequency range for the fit would necessarily yield to a different apparent slope, and ultimately a different value for α. As the master curve [Fig. 3.19(b)] is very robust with fixed α and the evolution of $\omega_0(t)$ is more correlated to the one $G_0(t)$ [Fig. 3.20(a-b) vs (d-e)], we chose to consider $\alpha = 0.62$ with a uncertainty of ± 0.02 given by the standard deviation in Fig. 3.20(c). This experiment allows us to clearly highlight two regimes in the aging process of this polymer-dominated hydrogel, with a well defined, i.e., frequency-independent, sharp transition at around $t \simeq 3000$ s [see the upturn in Fig. 3.20(d-e)]. This two-step aging has already been reported in colloidal star polymer glasses but the mechanism is, to our knowledge, still an open question [290].

Finally, this master curve translates a time-connectivity superposition principle [41], whose scaling is compatible with a linear relationship between G_0 and ω_0. Applied here, the superposition principle suggests an equivalence between the increase of the CB content and the aging since similar master curves for the viscoelastic spectra are obtained in both cases [see Fig. 3.7 in Section. 3.B]. We assume that the underlying mechanism is attributed to the evolution of the number of cross-links in the network, which increases both with increasing CB content or aging.

C.2 SAXS evidence of the microstructure evolution

The previous section has shown a clear mechanical signature that CB-CMC hydrogels from the polymer regime evolve over a long timescale. The goal of this section is to look for any change in the microstructure during such an aging process. We applied the same preshear protocol (i.e., constant shear rate $\dot{\gamma} = 500$ s^{-1} applied for 180 s) to the same sample ($c_{CMC} = 3\%$ & $x_{CB} = 8\%$) on the rheometer available at ID02 beamline (ESRF). Following the preseahr, the complex modulus is recorded as a function of time at fixed frequency $\omega = 2\pi$ rad.s^{-1} [Fig. 3.21(a)]. The scattered intensity of X-rays is recorded in situ as a function of time as well. The rheometer is equipped with a 1 mm gap Couette geometry. The state at the end of the preshear may thus be different in this geometry from the one in the cone-and-plate used above in the previous section, which could explain the slight discrepancy in the values of the complex moduli. The X-ray beam hits the sample radially (in the $\boldsymbol{v} \times \text{rot}\, \boldsymbol{v}$ direction). Synchronization is ensured thanks to a triggering of the SAXS through the rheometer software. A typical scattering intensity spectrum is represented in Kratky plot Iq^2 vs. q in Fig. 3.21(b), from which q_{max}, q_1 and q_2 are highlighted. These values are introduced in Section 2.G.2 in Chapter 2.

The scattered intensity weakly evolves during the hydrogel recovery. Namely, the main change is an increase of q_{max} of about 10%, 5h30 after the start of the recovery. This value is attributed to the typical size of CB clusters in the polymer matrix, which gets smaller as time goes by as q_{max} increases. Such a small change in the cluster size impacts dramatically the mechanical properties and suggests complex interac-

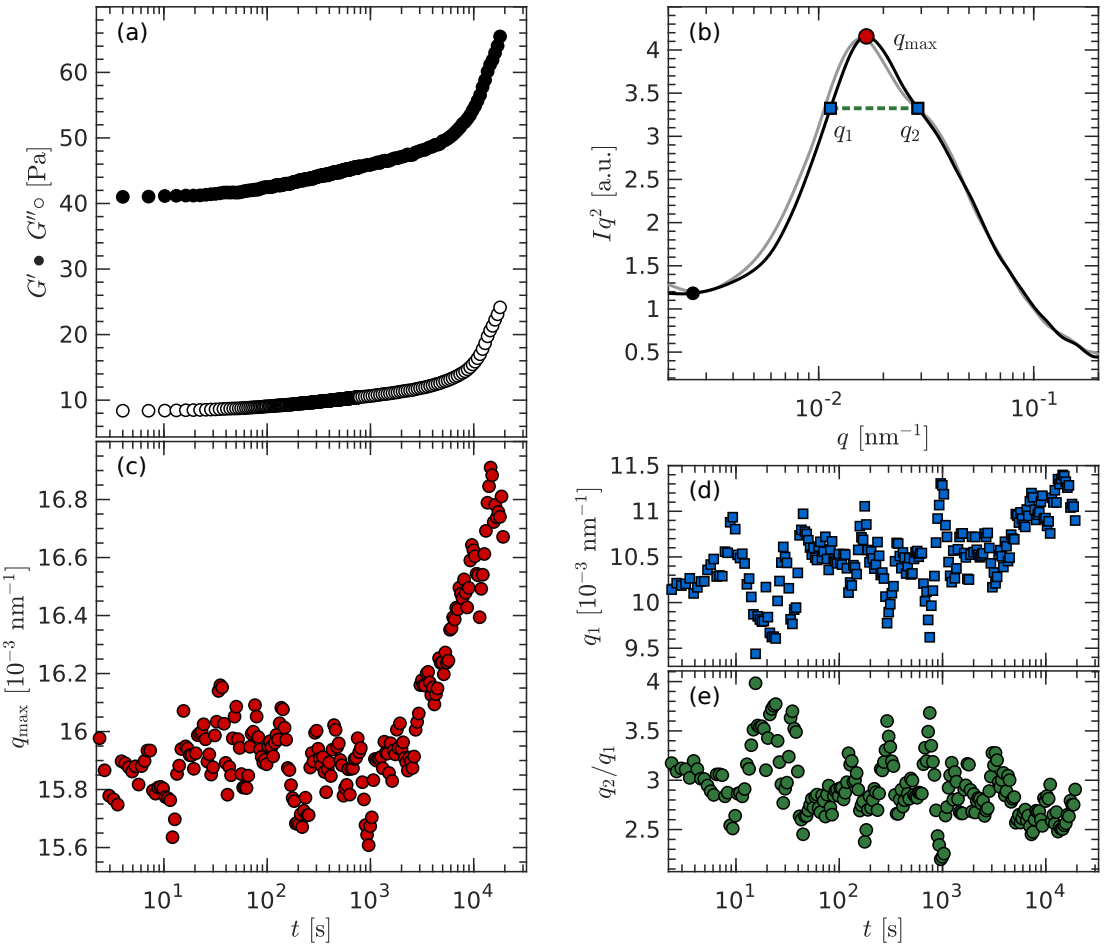

Figure 3.21: Time resolved SAXS. (a) Time evolution of the viscoelastic moduli G' (filled circles) and G'' (open circles) of a CMC-CB hydrogel in the polymer regime ($c_{CMC} = 3$ % and $x_{CB} = 8$%) following a preshear at $\dot{\gamma} = 500$ s^{-1} during 180 s. (b) In situ measurement of the scattering intensity in a radial configuration. The black (resp. grey) line corresponds to the last (resp. first) spectrum measured. The red circle shows the maximum of the peak at q_{max}, the blue squares are q_1 and q_2 defined in section 2.G.2. The green dashed line represents the distance between q_1 and q_2. The extracted values q_{max} (c), q_1 (d) and q_2/q_1 (e) are plotted against the time.

tions between the CB clusters and the polymer network. Remarkably, two regimes are observed in the dynamics of the microstructure during the recovery. A first regime during which q_{max} does not evolve much (for $t < 3000$ s) followed by a sharp increase (after $t > 3000$ s). This critical time is very similar to the one found during time-resolved mechanical spectroscopy experiments (Fig. 3.21). The evolution of G' and G'' at $\omega = 2\pi$ rad.s^{-1} [Fig. 3.21(a)] shows a critical timescale around 7.10^3 s, which should not be mistaken for a relevant value as it is recorded at a single arbitrary frequency. Finally, the broadness of the peak exhibits the same behavior, with a slight narrowing of the peak for $t > 3000$ s [Fig. 3.21(d)-(e)]. As the CB-CMC hydrogel ages, CB clusters tend to reach the optimal size that minimizes the total free energy of the system, which selects the typical sizes and narrows their distribution. The delay before the evolution of the microstructure remains unexplained, but could be attributed to an aggregation of the CB due to their diffusion in the polymer matrix together with an adsorption of the CMC hydrophobic patches onto the CB.

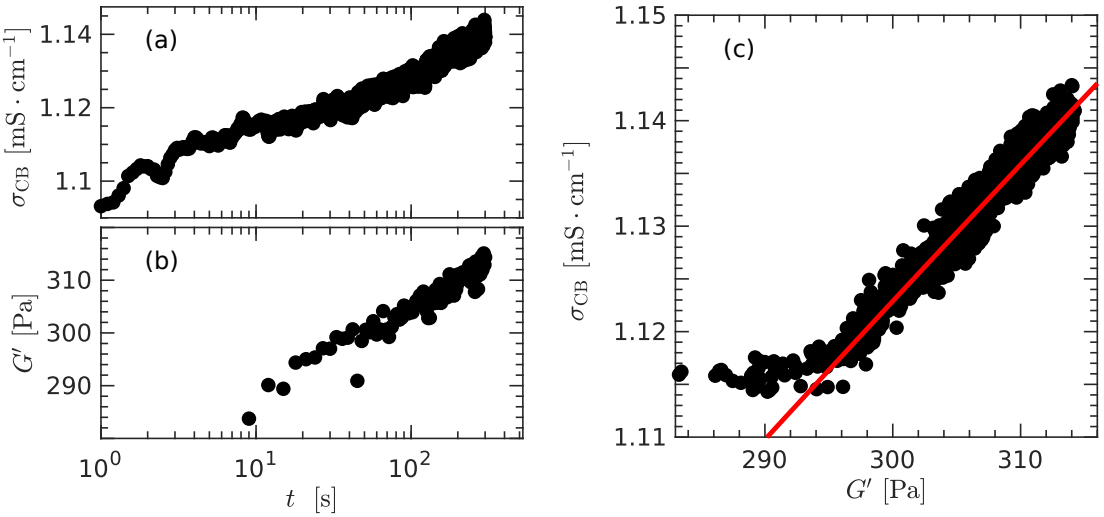

Figure 3.22: Time evolution of the DC electric conductivity σ_{CB} (a) and the elastic modulus G' at $\omega = 2\pi$ rad.s^{-1} (b) of a CB-CMC dispersion in the colloid regime ($c_{CMC} = 0.01\%$ and $x_{CB} = 6\%$). The data were recorded after a preshear at $\dot{\gamma} = 200$s^{-1} for 60 s followed by an oscillatory shear at an amplitude 300% and a frequency $\omega = 2\pi$ rad.s^{-1} for 180 s. (c) σ_{CB} versus G' during this measurement. The elastic modulus data were extrapolated with a linear approximation between the real measurements to match the sampling rate of the conductivity. The red line correspond to the best fit of the data with a power-law (for $G' > 290$ Pa), which exponent is fixed to 0.6 compatible with the scaling $\sigma_{CB} \sim \mathcal{G}_0^{0.6}$ reported in Fig. 3.17.

To elucidate this scenario, we could look into the microstructure of the polymer rather than the CB, especially at higher q values. Because of the fractal geometry of the CB, we can expect a complex adsorption dynamics of the polymer onto the surface of the CB. Contrast matching in a rheo-SANS experiment would be extremely insightful. Unfortunately, CB matching was never achieved, and we could not probe the evolution of the CMC microstructure within CB-CMC hydrogel.

C.3 Evolution of the electrical properties

To complete the study of the dynamics of the CB-CMC hydrogels we now discuss their dielectrical properties. In both polymer-dominated and colloid-dominated regimes, we will see that they do not evolve much with time. In terms of the electric model, it means that the parameters R_{ion}, Q, and n are constant and solely depend on the composition as shown in Fig. 3.16. Hence, in the polymer-dominated regime ($r > r_c$), the impedance spectra are supposedly independent of the time. In DC measurements it means that the conductivity remains close to zero. However, in the colloid-dominated regime ($r < r_c$), the mechanical properties and the DC conductivity σ_{CB} arise both from the CB network, which slowly evolves with time according to the previous sections.

To reset the samples, they were rejuvenated in situ in the shear cell through a preshear at $\dot{\gamma} = 200$ s^{-1} for 60 s, before applying an oscillatory shear at an amplitude 300% and a frequency $\omega = 2\pi$ rad.s^{-1} for 180 s. It corresponds to the first step of the protocol detailed in Chapter 4.A.3. Then, σ_{CB} together with G' are recorded. Both are observed to increase logarithmically with time, as shown in Fig. 3.22(a-b). Such a trend should be compared with the scaling $\sigma_{CB} \sim \mathcal{G}_0^{0.6}$ previously reported in Fig. 3.17, and obtained for variable CB contents. Such scaling at fixed composition but increasing

sample age is compatible with the restricted range of G' explored here. This suggests that the underlying evolution of the microstructure is similar whether we observe the impact of the CB content at rest or the impact of time at fixed concentration. As time passes or concentration increases, the network gets denser and more connected in a similar way hinting to a time-concentration-connectivity superposition principle. It would be interesting to test further this scenario and check if this scaling is still relevant when the temperature is changed. The time evolution of the electrical properties has also been studied at different frequencies.

Colloid-dominated regime

These experiments were conducted in the dielectric cell, out of the shear cell connected to the rheometer so that the sample did not undergo any specific preshear step, apart from the mixing induced by the pipetting step, and by shaking vigorously the container. Although the initial state is not well controlled, the time evolution is still insightful on the dynamics of the system. After loading, the complex impedance of the CB-CMC hydrogel is measured every 10 s for 1 hour at several frequencies from 1 Hz to 1 MHz. The results are shown in Fig. 3.23. For all the frequencies tested, the time dependence is small, within a few percent. To better grasp the results, we shall recall the asymptotic scaling for the real and imaginary parts of the complex impedance, below and above the cutoff frequency [see Eq. (2.57)] defined as $f_c = 1/2\pi[Q(R_{CB} + R_{ion})]^{1/n} \simeq 500$ Hz for the current experiment.

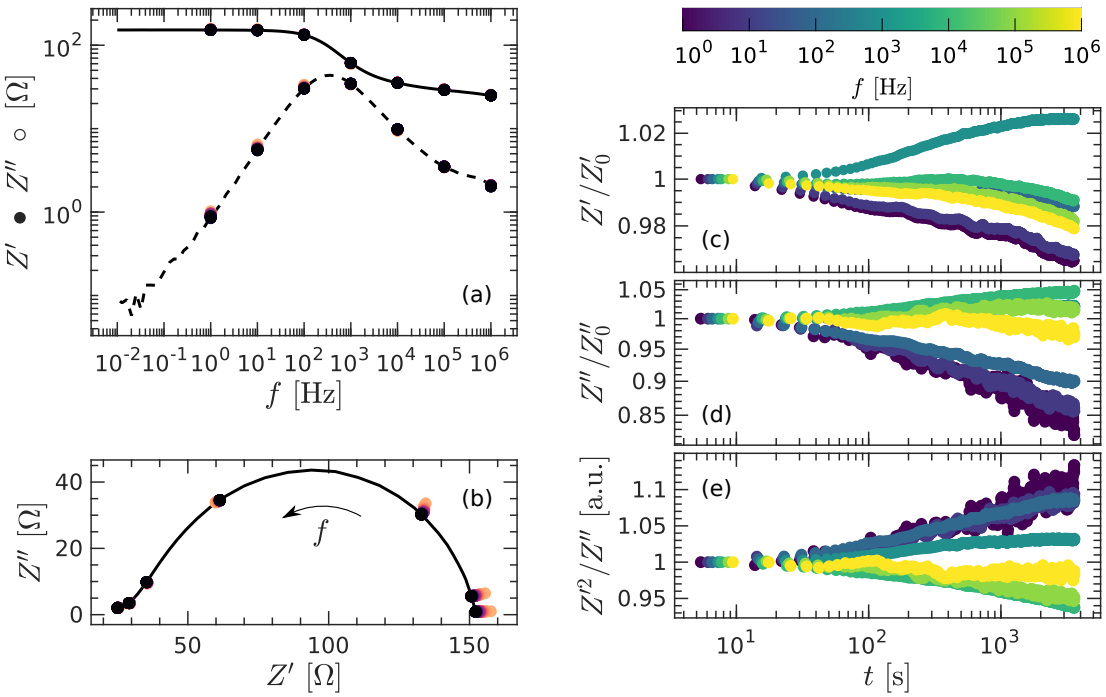

Figure 3.23: Time evolution of the complex impedance $Z^\star = Z' - iZ''$ of a CB-CMC hydrogel in the colloid-dominated regime ($c_{CMC} = 0.01\%$ & $x_{CB} = 8\%$) in Bode representation (a) and Nyquist representation (b). The circles correspond to the evolution of the impedance at f ranging from 1 Hz to 1 MHz (1 point per decade); darker colors mean longer time. The black solid (resp. dashed) line corresponds to the final measurement of Z' (resp. Z'') over an extended frequency range. The time evolution of Z' (c), Z'' (d), and Z'^2/Z'' (e) normalized with the initial value Z'_0 and Z''_0 are plotted against time for different frequencies, which values are represented in the color bar.

In the low-frequency limit, the complex impedance reads:

$$Z'(f \ll f_c) = R_{CB} \tag{3.7}$$

$$Z''(f \ll f_c) = \sin\frac{n\pi}{2} R_{CB}^2 Q(2\pi f)^n \tag{3.8}$$

so that $Z' \propto R_{CB}$ and $Z'' \propto R_{CB}^2$. It explains why Z'' decreases faster with time than Z' for the blue colors in Fig. 3.23(c-d). However, assuming R_{CB} is the only time-dependent variable is not accurate. Indeed this idealized framework Z'^2 should scale as Z'', which is not what is observed as plotted in Fig. 3.23(e). As Z'^2/Z'' depends on time, it suggests that Q and n may evolve slightly with time. A more detailed analysis with more frequencies at each point in time would be required to quantify the evolution of the full set of parameters (e.g., by using chirp sequences). Unfortunately, it was not available with the dielectric setup.

In the high-frequency limit, the complex impedance reads:

$$Z'(f \gg f_c) = \frac{R_{CB}R_{ion}}{R_{CB}+R_{ion}} \tag{3.9}$$

$$Z''(f \gg f_c) = \frac{R_{CB}R_{ion}}{R_{CB}+R_{ion}} \frac{\sin\frac{n\pi}{2}}{(R_{CB}+R_{ion})Q(2\pi f)^n} \tag{3.10}$$

Indeed, we observe in Fig. 3.23(c) that Z' does not depend much on time for high frequencies. In the limit where $R_{CB} \ll R_{ion}$, $Z'(f \gg f_c) \simeq R_{ion}$ and therefore we can conclude that R_{ion} does not depend much on time.

Finally, in the intermediate region where $f \simeq f_c$ (green colors), Z' increases with time. It should be really understood as a signature of the evolution of the cutoff frequency, so that the time evolution comprises horizontal and vertical shifts since Z' is frequency-dependent in this region.

Polymer-dominated regime

In the polymer-dominated regime ($r > r_c$), as $R_{CB} \to \infty$, the complex impedance reads:

$$Z^\star(f) = R_{ion} + \frac{1}{Q(i2\pi f)^n} \tag{3.11}$$

The evolution at low frequency is, therefore, the image of the evolution of Q and n, whereas at high frequency it rather corresponds to the evolution of R_{ion}. The results are summarized in Fig. 3.24, and a minute time dependence is observed although $R_{CB} \to \infty$ in this regime. A remarkable feature is the frequency dependence on the time evolution of Z' Fig. 3.24(c), which is stronger for the lowest frequencies. It means that mainly Q and n are evolving, and R_{ion} remains roughly constant.

The observations on the dielectric properties both in the colloid-dominated and polymer-dominated regimes highlight that the main evolution in the system is due to the CB network depicted by R_{CB}, thus negligible in the polymer-dominated regime. However, some weak evolution is still observed on the other parameters R_{ion}, Q, and n, which suggests that the overall sample is still not in steady state. In the colloid-dominated regime, rearrangements of the CB network are likely to change the dielectric constant of the medium impacting Q mainly. Moreover, as the network geometry evolves, the contacts between the CB and the electrodes may change as well, leading to a change in Q and n. In the polymer-dominated regime, the dielectric measurements exhibit an evolution mainly due to Q and n. It gives evidence that the system is

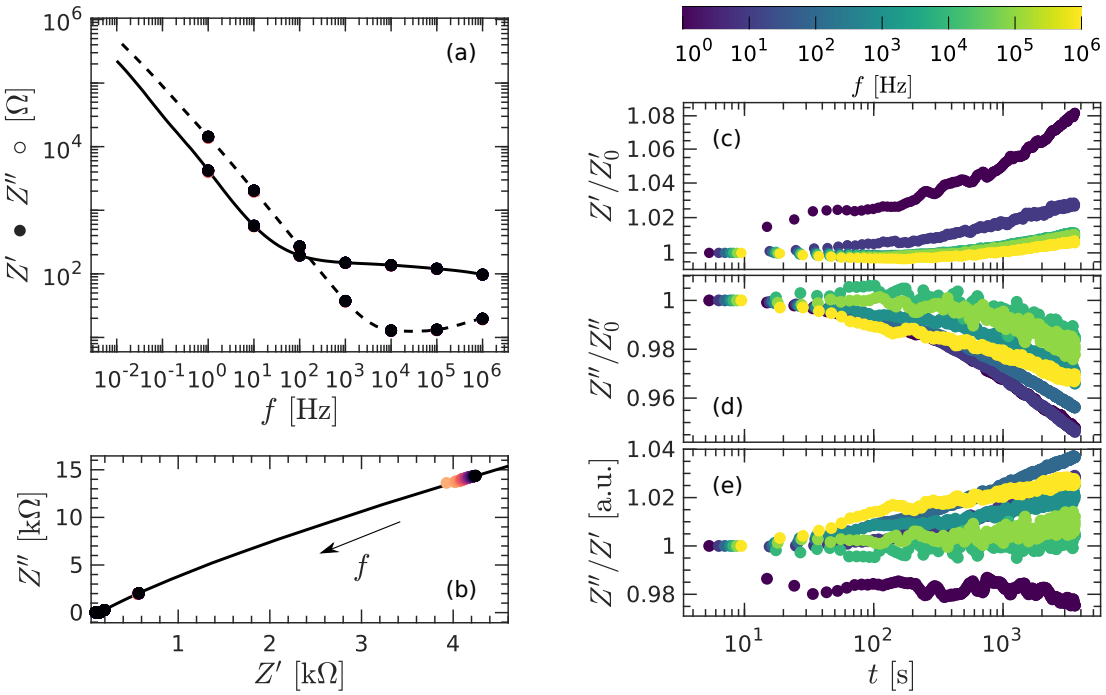

Figure 3.24: Time evolution of the complex impedance $Z^\star = Z' - iZ''$ of a CB-CMC hydrogel in the polymer-dominated regime ($c_{CMC} = 2\%$ $x_{CB} = 8\%$) in Bode representation (a) and Nyquist representation (b). The circles correspond to the evolution of the impedance at f ranging from 1 Hz to 1 MHz (1 point per decade), darker colors mean longer time. The black solid (resp. dashed) line corresponds to the final measurement of Z' (resp. Z'') on an extended frequency range. The time evolution of Z' (c), Z'' (d), and Z''/Z' (e) normalized with the initial value Z'_0 and Z''_0 are plotted against time for different frequencies, which values are represented in the color bar.

still restructuring, in agreement with the previous rheological and scattering results. Finally, R_{ion} seems to not depend much on time. This result is consistent with its interpretation as ionic leakage of the charge accumulation at the interface. Ions are located at the surface of the polymers (and potential impurities coming along with the CB or the CMC), and their contribution is not much impacted by the change of the structure since it takes place at the nanoscale.

D Conclusion

By performing a fundamental and extensive study of water-based dispersions of CMC and CB particles, we have identified the range of polymer and particle contents for which the mixture forms hydrogels. These soft solids show two strikingly different microstructures and mechanical responses depending on the ratio r that quantifies the relative content of polymers and CB particles.

For $r \ll r_c$, i.e., relatively low CMC concentrations, the gel viscoelasticity is governed by the CB particles, which form a space-spanning network. Such a particulate network, which is responsible for the conductive properties of the hydrogel, is decorated and thus stabilized by the CMC. In this regime, the viscoelastic properties of the CMC-CB hydrogel, which are well-described by the SGR model, display weak aging properties, which might be due to the slow reorganization of the particulate network.

In contrast, for $r \gg r_c$, i.e., relatively high CMC concentrations, the gel viscoelastic-

ity originates from two independent contributions, namely the entangled CMC matrix on the one hand, and the CB particles on the other hand. In this regime, CB particles are dispersed as individual particles or clusters inside the CMC matrix, where they act as cross-linkers through hydrophobic interactions. In consequence, the sample is not electronically conductive. Moreover, the viscoelastic spectrum of these CMC-CB hydrogels is frequency dependent and can be rescaled onto a master curve, which is very well described by a Fractional Kelvin-Voigt (FKV) model with an exponent $\alpha = 2/3$ that characterizes the high-frequency viscoelastic response. The mechanical properties show a non-trivial time dependence that suggests a two-step aging process, with little to no evidence at the structural or dielectric level.

The present Chapter paves the way for the rational design of CMC-based slurries in which CMC is used as a binder, e.g., for lithium-ion batteries [160, 291, 292], and more generally for CMC-based hydrogels involving various types of fillers such as graphene oxide, metallic nanoparticles, etc. [293–295].

CHAPTER

4

CB-CMC HYDROGELS NON-LINEAR RHEOLOGY

This chapter aims to understand better the two types of CB-CMC hydrogels previously identified. Their non-linear behavior is highly informative to refine the microscopic description of the system. We will first examine the yielding process of both types of gels under Large Amplitude Oscillatory Shear (LAOS) and get additional insights on the microscopic scenario underpinning the yielding transition using several techniques such as rheo-dielectric measurements and rheo-scattering experiments in Section 4.A. Finally, we explore in Section 4.B the behavior under flow of these complex fluids and the way flow may modify the properties of the gel, motivated by the interest for applications in flow batteries.

A Yielding under Large Amplitude Oscillatory Shear

A.1 General description and key features

In the first section, we focus only on the response under Large Amplitude Oscillatory Shear of CB-CMC hydrogels depicted in the previous chapter. The goal is to understand what happens to the microstructure of the gels when they are strongly mechanically solicited.

So far, we have restricted ourselves to the linear regime, where both G' and G'' are independent of the strain amplitude. In this regime, deformations are reversible, and the material is not damaged. For this reason, it is essential to carry out these measurements in the linear regime, which has to be determined. In practice, the span of the linear regime is usually estimated under oscillatory shear by sweeping the strain amplitude, as done in the present section. However, when the strain increases too much, the material is damaged. It can be witnessed by a macroscopic change of the sample (e.g., fracture, shear bands, etc.) or at the microscopic scale (e.g., *local* reorganization of a colloidal network). In rheological measurements, it shows through the evolution of the viscoelastic properties of the sample, namely G' and G'' now depend on the shear amplitude (both strain and stress). At even larger amplitudes, the sample can even start to flow; the details of such a yielding process highly depend on the microstructure of the gel at rest, and on the interactions within the gel under shear.

This section aims to grasp the characteristic steps before and after the yielding during strain sweep experiments, while we record G' and G'' as a function of the

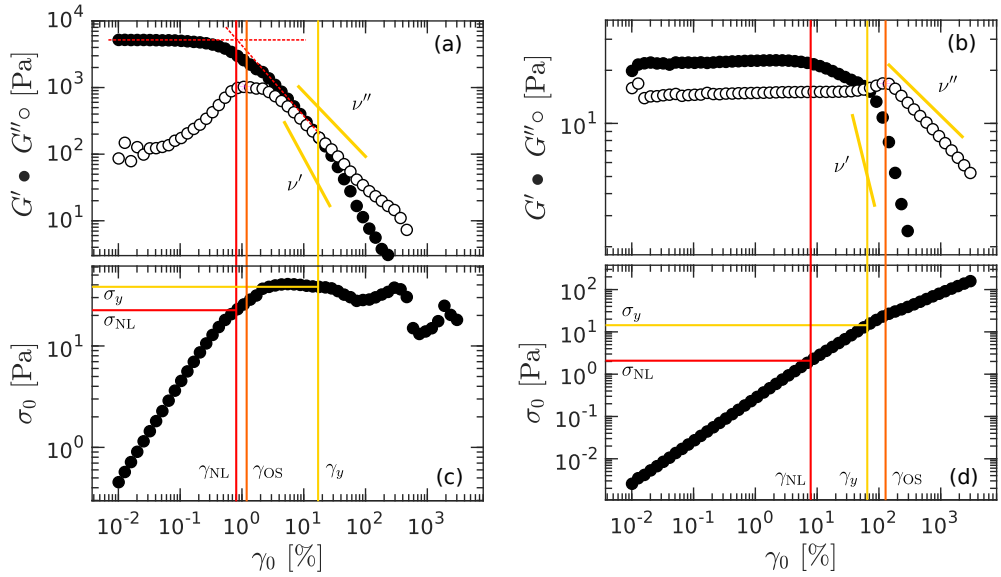

Figure 4.1: Yielding under LAOS. Elastic and viscous moduli vs. strain amplitude γ_0 under oscillatory shear at $\omega = 2\pi$ rad.s^{-1} for CB-CMC hydrogels from (a) the colloid-dominated regime ($r < r_c$ at $c_{CMC} = 0.01\%$ & $x_{CB} = 8\%$) and (b) the polymer-dominated regime ($r > r_c$ at $c_{CMC} = 2\%$ & $x_{CB} = 8\%$). The corresponding stress amplitude σ_0 is plotted in (c) and (d). The vertical red lines indicate the departure from the linear regime; the vertical orange lines mark the position of the maximum in G'', and the yellow lines highlight the yielding point defined by the crossover of G' and G''. The exponent ν' (resp. ν'') characterizing the power-law decay of G' (resp. G'') vs. γ_0 are shown as yellow lines. The horizontal red dashed lines correspond to the geometrical construction used to determine the characteristic strain γ_{NL} defining the onset of non-linearity.

strain. Namely, some specific strains are noteworthy, such as the onset of the non-linear regime γ_{NL}, the yield strain γ_y and the overshoot strain γ_{OS} as defined in Section 2.D.6. Their dependence on the composition is widely studied to refine the comprehension of the system, especially with respect to the critical CMC-to-CB ratio r_c. One should keep in mind that all these results depend on the frequency, which was fixed to $\omega = 2\pi$ rad.s^{-1}.

For Small Amplitude Oscillatory Shear (SAOS), the elastic modulus G' is constant for hydrogels prepared in both colloidal and polymer regimes [Fig. 4.1(a)-(b)]. However, G'' might increase before G' starts to drop, especially in gels that belong to the colloidal regime. Therefore, we chose a geometrical definition G' based on the intersection between its plateau value and a power-law approximation right after the yielding, see section 2.D.6. As the viscous modulus is way smaller than the elastic modulus, this is not clearly visible in the evolution of stress amplitude vs. the strain amplitude [Fig. 4.1(c)]. On the other hand, for gels prepared in the polymer regime,

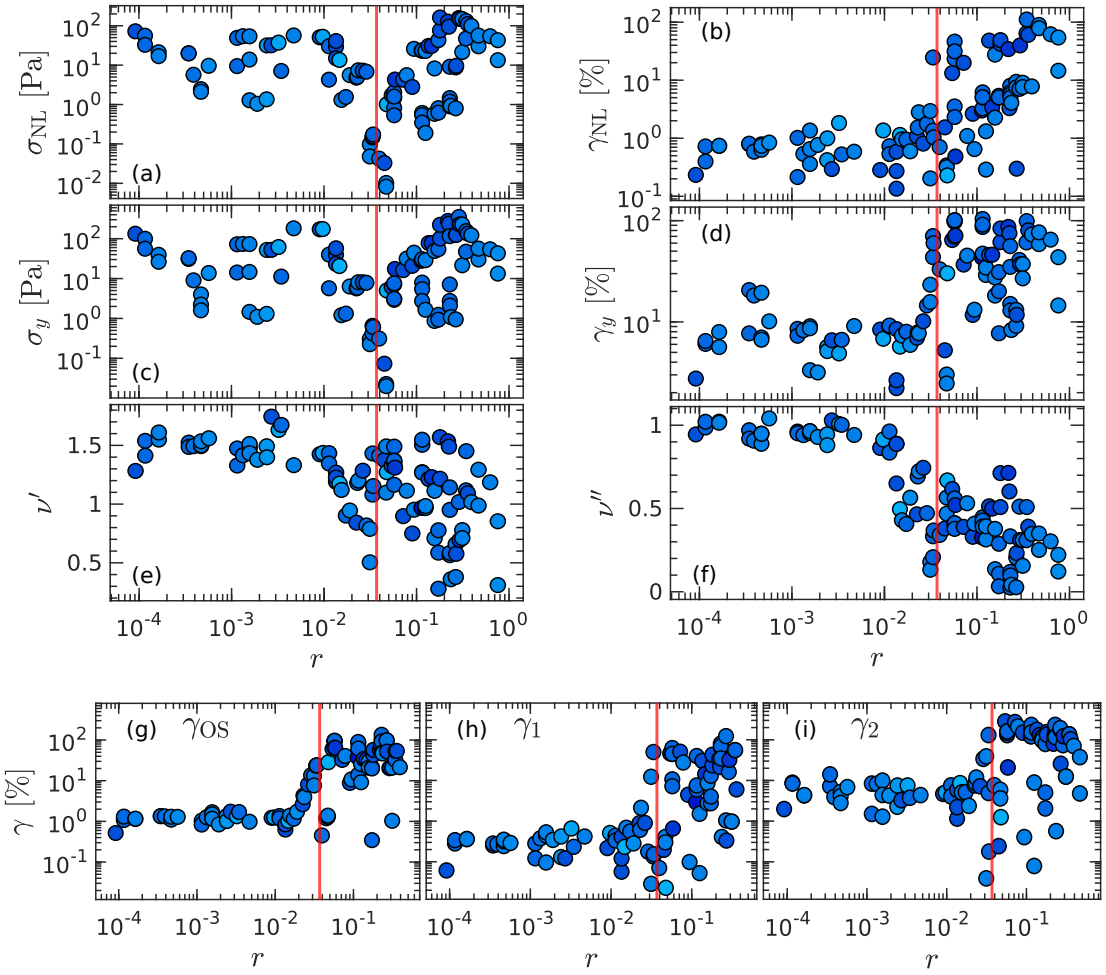

Figure 4.2: Yielding characteristics of CB-CMC hydrogels plotted against the CMC-to-CB ratio r. Limit of the linear regime: (a) stress σ_{NL} and (b) strain γ_{NL}. Values of interest around the yielding: (c) yield stress σ_y, (b) yield strain γ_y, (c) power-law exponent of G' and (d) power-law exponent of G''. Values of interest around the G'' overshoot: (g) strain γ_{OS} for the maximum value of G'', (i) critical strain before the overshoot γ_1 and (j) critical strain after the overshoot γ_2. Colors encode for the CB content; darker colors correspond to larger x_{CB}. The red line represents the critical ratio $r_c \simeq 0.037$.

the linear approximation for the stress versus strain plot remains valid over a decade in strain beyond γ_{NL}, mainly because the elastic and viscous moduli have the same order of magnitude and do not evolve much right after γ_{NL} [Fig. 4.1(d)]. The geometrical definition of γ_{NL} appears then as a crude approximation of the linear strain limit. It means that in order to remain in the linear regime, we have to stick to a strain amplitude at least much smaller than γ_{NL}, we arbitrarily chose a factor 10. The characteristic strain γ_{NL} is still insightful on the sensitivity of the microstructure to a mechanical solicitation. Namely, γ_{NL} is about 1% for a hydrogel in the colloidal regime, whereas it is worth 10% to 100% for a hydrogel in the polymer regime. This result reflects the change in the hydrogel microstructure between these two regimes. These observations are plotted in Fig. 4.2.

For strain amplitude $\gamma_0 \simeq \gamma_{NL}$, this corresponds to the "Medium-Amplitude Oscillatory Shear" (MAOS) regime. Upon increasing the strain amplitude, G' and G'' eventually cross, which defines the yield strain γ_y, and the yield stress $\sigma_y = \sigma(\gamma_y)$. Similarly to the dependence of γ_{NL} with the CB-CMC hydrogel composition, $\gamma_y \simeq 5 - 10\%$ for hydrogels prepared in the colloidal regime and $\gamma_y \simeq 30 - 100\%$ for hydrogels prepared in the polymer regime, which suggests a more fragile microstructure in the former regime than in the latter one [296]. Around the yield point, G'' shows a non-monotonous behavior, which is the hallmark of a type III yielding scenario [224]. Such an overshoot in G'' is also referred to as the Payne effect for composite materials [297]. The overshoot of G'' indicates an excess of dissipation during the yielding process, and the locus of the maximum $\gamma = \gamma_{OS}$ is roughly identical to γ_y [see Fig. 4.2]. The presence of a peak in G'' informs on the plastic reorganization of the microstructure bearing the elasticity, leading to unrecoverable dissipation [298]. An increasing amplitude of the overshoot in G'' corresponds to a more heterogeneous failure scenario.

This picture proposed in ref. [298] is supported by the evolution of the relative amplitude of the overshoot $\Delta G''/G''$ as a function of the hydrogel composition, as shown in Fig. 4.3. In the colloidal regime, i.e., at low CMC content, the maximum of G'' is about five times larger than the linear value, and it neither depends on the CMC concentration nor on the CB content [Fig. 4.3(a), (c) and (d)]. Approaching the depercolation transition, the overshoot vanishes as the network of CB particles becomes weaker and less connected. However, in the polymer regime at fixed CMC concentration [Fig. 4.3(b)], the overshoot amplitude increases as the CB fraction increases and does not depend much on the CMC concentration, equivalently it decreases with increasing r [Fig. 4.3(d)]. Finally, the overshoot is negligible until high CB contents (say typically 10%). This result is consistent with a scenario in which CB clusters cross-link a CMC matrix: the G'' overshoot is due to heterogeneity arising from the CB clusters.

Around the yield point, and regardless of the hydrogel composition, i.e., for hydrogels prepared in either the colloidal or the polymer regime, G' decreases monotonically with the strain amplitude, while G'' goes through a maximum before decreasing[1]. In the limit of large deformations, for $\gamma_0 \gtrsim \gamma_y$, both the elastic and viscous moduli exhibit a power-law decay for increasing strain amplitude γ_0 that reads: $G' \sim \gamma_0^{-\nu'}$ and $G'' \sim \gamma_0^{-\nu''}$. In several cases reported in the literature, this is characterized by a single exponent $\nu' = 2\nu''$ [228]. This phenomenology is explained by a decrease in the relaxation time of the gel microstructure around the breaking point. It assumes there is one dominating around this point. For CB-CMC hydrogels in the colloidal regime,

[1]There are a few hydrogel compositions in the polymer regime where G' overshoots as well. Such compositions correspond to a low CMC concentration and a high CB content ($r \gtrsim r_c$).

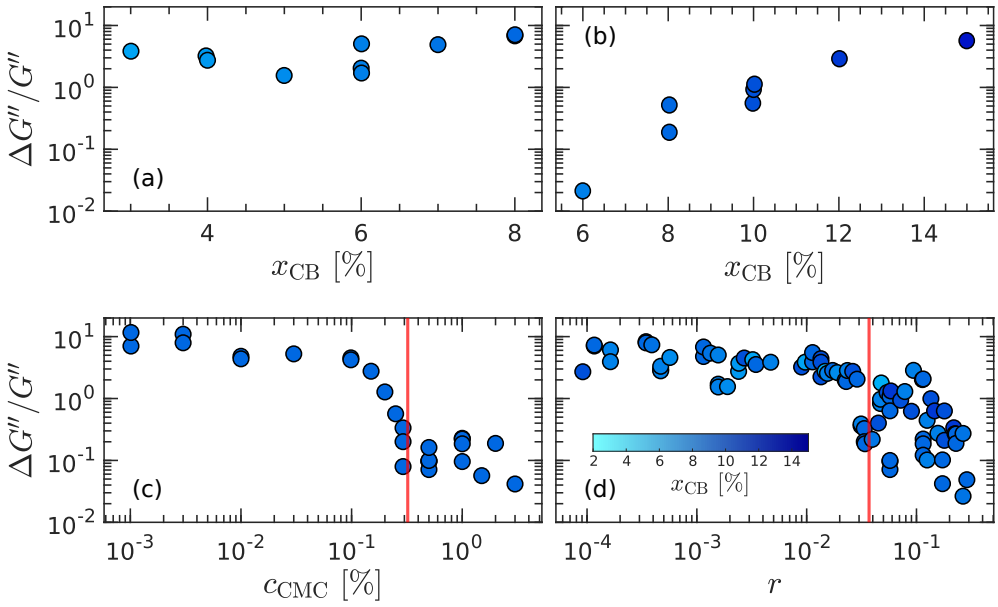

Figure 4.3: Viscous modulus overshoot in LAOS. Relative amplitude of the overshoot in G'' measured at the yield point of CMC-CB hydrogels and reported as a function of the CB content x_{CB} for a fixed CMC concentration: (a) $c_{CMC} = 0.01\%$ and (b) $c_{CMC} = 2\%$, and (c) as a function of the CMC concentration c_{CMC} for a fixed CB content $x_{CB} = 8\%$; (d) as a function of the CMC-to-CB ratio r for all compositions probed. Colors code for the CB content. The vertical red line indicates $r = r_c$, which separates the colloid-dominated regime ($r < r_c$) from the polymer-dominated regime ($r > r_c$) as identified from linear viscoelastic measurements.

we find $\nu' \simeq 1.5$ and $\nu'' \simeq 1$ with little dependence on the composition. In contrast, for CB-CMC hydrogels in the polymer regime, $\nu' \lesssim 1$ with a lot of dispersion, and $\nu'' \lesssim 0.5$ decrease with increasing r [Fig. 4.2(e-f)]. The dispersion of the data is significantly more visible in the polymer regime than in the colloidal one. It might arise from the arbitrary choice of the frequency, which has more impact on the polymer regime, as observed with the linear viscoelastic spectra.

Finally, we observe a two-step yielding scenario in several strain sweep experiments conducted on CB-CMC hydrogels whose composition belongs to the polymer-dominated regime. Here, it appears as a bump in the $G'(\gamma_0)$ well before the yield point. The bump is visible around γ_{NL} in Fig. 4.1(b) and emphasized in Fig. 4.4. This feature is referred to as "double yielding" in the literature [227, 299, 300]. In glassy systems, the scenario is usually the following: the first yielding step is attributed to the breaking of large-scale links between clusters, while the second yielding step corresponds to the breaking of the links within the clusters. Such a double yielding is surprisingly seen for CB-CMC hydrogels in the polymer-dominated regime only, and not in the colloidal-dominated regime, which is supposedly more glassy[2]. Here, because the sample microstructure consists in a polymer network cross-linked by CB particles, we must propose another scenario. To further understand it, we examine the result of strain sweep experiments conducted at different frequencies [Fig. 4.4]. The underlying motivation relies on the frequency dependence of $G^\star$ in the linear regime: the highest frequencies (i.e., for $\omega > \omega_0$ the frequency scale[3]) probe the fluid surrounding

[2]Note that few CB-CMC hydrogels that belong to the colloidal-dominated regime exhibit a double yielding. However, they are not representative and would require a more systematic and dedicated study to conclude upon the existence of this feature or if it is just an artifact.

[3]obtained with the fractional Kelvin-Voigt model in the linear viscoelastic spectrum.

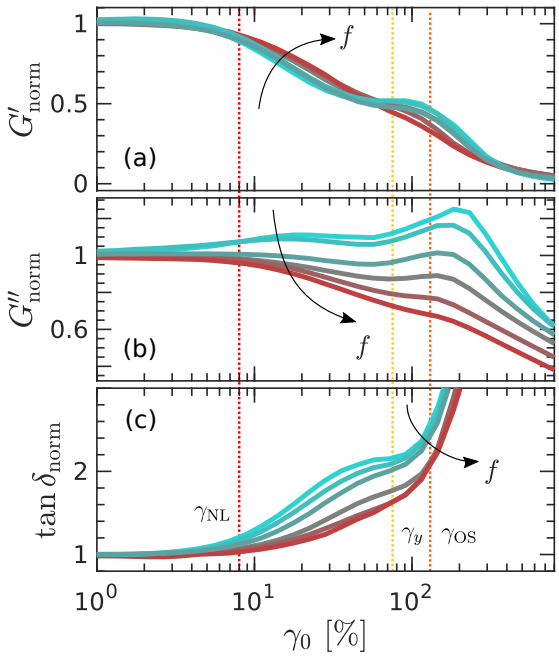

Figure 4.4: Impact of the frequency on the LAOS response in the polymer regime. (a) Normalized elastic modulus $G'_{\rm norm}$, (b) normalized viscous modulus $G''_{\rm norm}$ and (c) their ratio $\tan\delta_{\rm norm} = G''_{\rm norm}/G'_{\rm norm}$ as a function of the strain amplitude γ_0 for experiments conducted at different frequencies on CB-CMC hydrogels in the polymer-dominated regime ($r > r_c$) of composition: $c_{\rm CMC} = 2\%$ & $x_{\rm CB} = 8\%$. The frequencies explored range from from 0.3 rad.s^{-1} (blue colors) to 60 rad.s^{-1} (red colors). Each point is averaged over two cycles, and G' and G'' are normalized by their respective values in the linear regime. The natural frequency scale for this gel is $\omega_0 \simeq 1$ rad.s^{-1}. The vertical dashed lines indicate $\gamma_{\rm NL}$, γ_y and $\gamma_{\rm OS}$ at $\omega = 2\pi$ rad.s^{-1}.

the stress-bearing network, whereas the lowest frequencies (i.e., for $\omega < \omega_0$) probe the CMC network cross-linked by CB clusters. This picture is supported by seminal works on carbon black gels (dispersed in mineral oil without polymer) [56]. At high frequency, where the polymer solvent dominates the stress response, neither the double yielding nor the overshoot in G'' is observed, as opposed to the behavior at low frequency. The strain at which the first yielding occurs (say around 5%) is very similar to the value found for hydrogels that belong to the colloidal-dominated regime where there is no polymer network. This observation suggests that the first yielding is due to the breaking of the CB clusters, hence the second one must come from the breaking of the polymer network. Moreover, the second yielding occurs at around 100%, which is in line with acid-induced CMC gels that do not contain any particles (see Chapter 5).

A.2 Analysis of LAOStrain "intra-cycle" waveforms

To further understand the non-linear behavior of CB-CMC hydrogels, we now go beyond the strain sweep, which is only an average of the mechanical response over the full oscillation cycle. We now study the mechanical response of CB-CMC hydrogels within an oscillation cycle for different maximum strain amplitudes, usually called an "intra-cycle" analysis, following the seminal work reported in ref [195].

For increasing strain amplitudes under oscillatory shear, the departure from the linear regime translates into the growth of harmonics in the stress signal. The details of our analysis have been presented in section 2.D.6. A common way to represent the data is to plot the Lissajous-Bowditch (LB) curves, which represent the instantaneous stress as a function of the instantaneous strain (or shear rate). The shape of these parametric plots allows us to grasp the evolution of the mechanical behavior during a cycle for different maximum strain amplitudes γ_0, as shown in Fig. 4.5. The stress versus strain plot emphasizes the elastic response of the system, (remember that a pure Hookean solid corresponds to a straight line in that LB representation). In contrast, the stress versus shear rate plot emphasizes the viscous response of the system (remember that for a purely Newtonian fluid, LB curves as $\sigma \sim \dot{\gamma}$ are straight lines). Elliptical

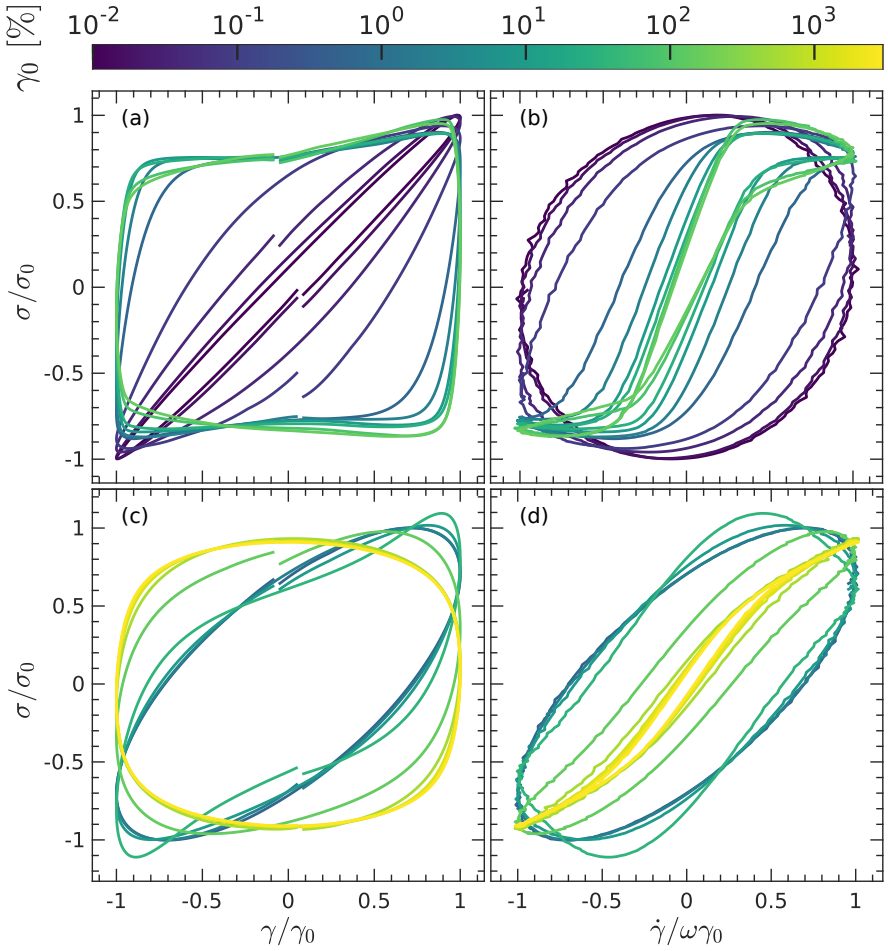

Figure 4.5: Lissajous-Bowditch plots of the normalized stress response to a sinusoidal strain at $\omega = 2\pi$ rad.s^{-1} for CB-CMC hydrogels in the colloidal-dominated regime ($c_{CMC} = 0.01\%$ & $x_{CB} = 8\%$) (a-b), and in the polymer-dominated regime ($c_{CMC} = 3\%$ & $x_{CB} = 8\%$) (c-d). The left (resp. right) column corresponds to the total instantaneous stress vs. the instantaneous strain (resp. shear rate). All values are normalized by the fundamental amplitude at ω, extracted from a Fourier transform of the data. Colors encode the fundamental strain amplitude γ_0 as shown in the color bar.

shapes are expected for viscoelastic fluids in the linear regime that will deform in the non-linear regime, as observed for polymer CB-CMC hydrogels [Fig. 4.6(c)-(d)]. Note that trajectories in LB plots may not be closed: this is the signature of a transient state as the system evolves within the cycle. We neglected this effect and kept the same protocol for all measurements (10 points per decade and 2 cycles per strain value) as a compromise between sample evolution (e.g., aging or evaporation) and this transient feature.

Beyond the linear regime, we witness the solid-to-liquid transition in LB curves. For CB-CMC hydrogels in both the colloidal-dominated and polymer-dominatedregimes, when γ_0 increases, ellipses widen in the $\sigma(\gamma)$ plot, whereas they shrink in the $\sigma(\dot{\gamma})$ plot. Indeed, the area enclosed by a trajectory corresponds to the viscous energy loss in the σ vs γ plot and to the stored elastic energy in the σ vs $\dot{\gamma}$ plot [225]. Moreover, at even larger amplitudes, the stress is a more complicated function of the strain, which translates into additional harmonics in the Fourier decomposition of the stress response. This ultimately leaves a mark on the Lissajous curves, whose shape departs

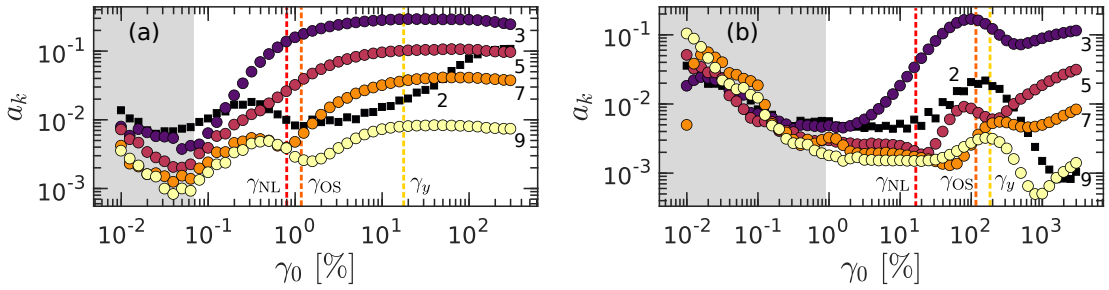

Figure 4.6: Fourier decomposition of the stress as a response to a sine strain at $\omega = 2\pi$ rad.s^{-1} for CB-CMC hydrogels in the colloid-dominated regime ($c_{CMC} = 0.01\%$ & $x_{CB} = 8\%$) (a), and in the polymer-dominated regime ($c_{CMC} = 3\%$ & $x_{CB} = 8\%$) (b). The Fourier coefficients are normalized by the stress amplitude of the fundamental $k = 1$ (such that $a_1 = 1$). The values of k are indicated, and lighter colors correspond to increasing values of k (either 2, 3, 5, 7, or 9). The value $k = 2$ is plotted in smaller squares as it is the only even coefficient with a different physical meaning. The vertical dashed lines indicate γ_{NL}, γ_y and γ_{OS}. The shaded areas emphasize the data with a low signal-to-noise ratio.

from ellipses.

To understand these changes better, we shall rather look at the elastic and viscous stresses separately. This is done numerically using a Fourier decomposition of the total stress response. The normalized amplitude a_k of the k-th harmonic (such that the amplitude of the fundamental is $a_1 = 1$) are plotted in Fig. 4.6. We see that the harmonic $k = 2$ is well below the harmonic $k = 3$ for both types of hydrogels in the colloid-dominated and polymer-dominated regimes. This result holds for all even higher harmonics, but only $k = 2$ was represented for the sake of concision. Even harmonics are usually attributed to artifacts in the measurements, e.g., wall slip [301, 302]. Wall slip seems to be absent during all of the experiments, except for large strain amplitudes (i.e., $\gamma_0 \gtrsim 100\%$) in CB-CMC hydrogels that belong to the colloid-dominated regime. This is in line with the upturn at very large γ_0 of the data in the $\sigma_0(\gamma_0)$ plot reported in Fig. 4.1(c). From now on, we shall only focus on the odd harmonics in the stress Fourier decomposition. As expected they are all negligible in the linear regime, the high values at very low γ_0 arise from a low signal-to-noise ratio when the stress signal is too weak. For CB-CMC hydrogels from both the colloidal-dominated and polymer-dominated regimes, the 3rd harmonic starts to grow at low strain values, about a decade lower than γ_{NL}, which means that non-linearities are growing, but they are not yet visible. For CB-CMC hydrogels from the colloid-dominated regime, the shapes of $a_k(\gamma_0)$ are similar for all the different harmonics [Fig. 4.6(a)]: they all grow within a decade in strain γ_0 before reaching a plateau, which value depends on the rank of the harmonic. Such simultaneous growth of the non-linearities for increasing strain amplitude suggests a homogeneous yielding scenario in time and potentially in space. In sharp contrast, $a_k(\gamma_0)$ all show a non-monotonic evolution for hydrogels from the polymer-dominated regime [Fig. 4.6(b)], which depends on the rank of the harmonic. Such a behavior is perfectly consistent with the double-yielding scenario reported above and will be discussed in more detail in the rest of the text.

Thanks to this Fourier decomposition, we can now compute the elastic and viscous stresses as detailed in Section 2.D.6, written σ_{elast} and σ_{visc} respectively. Namely, this point of view aims at identifying the part of the stress that is either an odd function of the strain for σ_{elast} or an odd function of the shear rate for σ_{visc}. Built this way, these stresses are straight lines in the LB plots in the linear regime, as shown in Fig. 4.7 (note

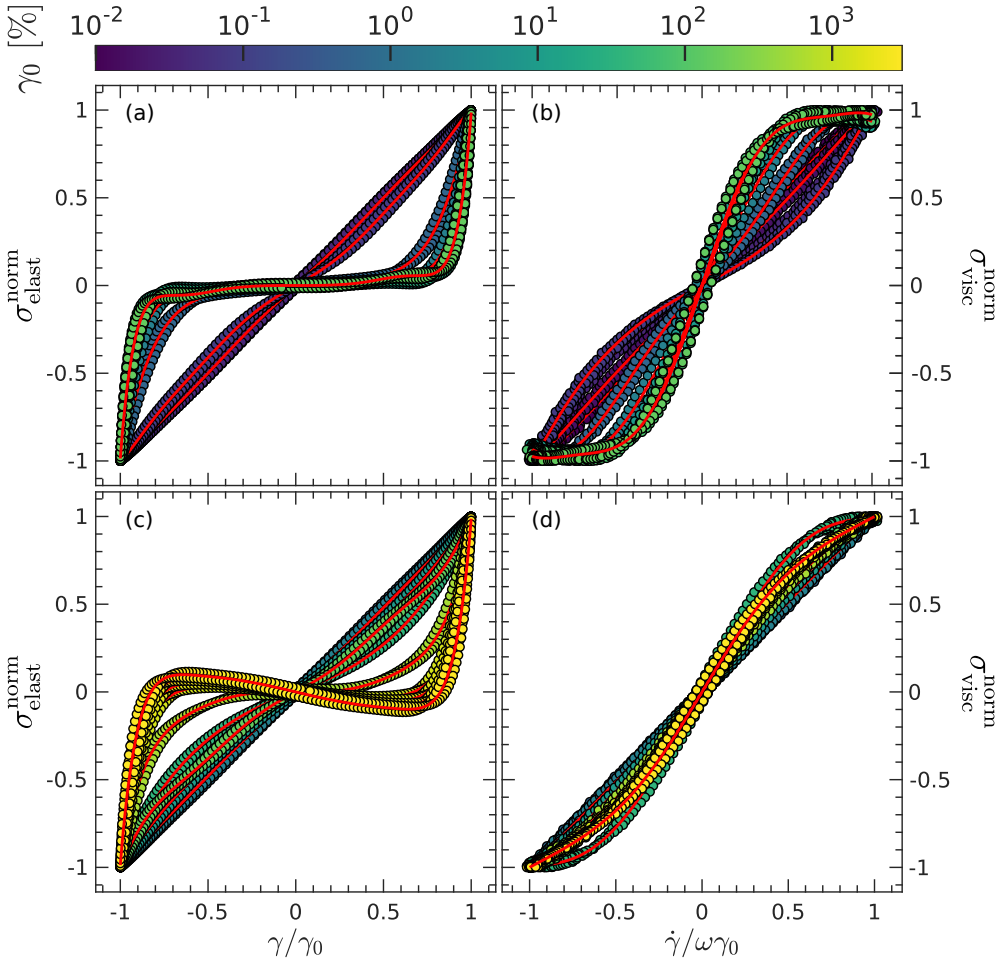

Figure 4.7: Decomposed Lissajous-Bowditch plots of the normalized stress response to a sinusoidal strain at $\omega = 2\pi$ rad.s^{-1} for CB-CMC hydrogels (a-b), in the colloid-dominated regime ($c_{\text{CMC}} = 0.01\%$ & $x_{\text{CB}} = 8\%$), and (c-d) in the polymer-dominated regime ($c_{\text{CMC}} = 3\%$ & $x_{\text{CB}} = 8\%$). The left (resp. right) column corresponds to the normalized elastic σ_{elast} (resp. viscous σ_{visc}) instantaneous stress as a function of the instantaneous strain (resp. shear rate), extracted from the Fourier analysis. The red curves correspond to the Chebyshev description of the data. All values are normalized by their maximal value. Colors encode the fundamental strain amplitude γ_0, as shown in the color bar.

that stresses are normalized by the extremal values for each curve, the slopes can not be used to compare the moduli). This decomposition emphasizes the non-linearities and differentiates the non-linearities in the elastic and viscous stress responses. One can already observe a big difference in non-linear response between the hydrogels from the colloid-dominated regime and that from the polymer-dominated regime: the elastic stress has a positive slope in the vicinity of $\gamma = 0$ in the former regime and not in the latter [Fig. 4.7(a)-(c)]. Moreover, the curvature around $\dot{\gamma} = \omega\gamma_0$ in the viscous stress changes sign as γ_0 increases in the former regime, whereas it remains the same for the latter [Fig. 4.7(b)-(d)].

To better quantify these observations, each σ_{elast} is fitted by a polynomial function of γ, similarly with σ_{visc} and $\dot{\gamma}$. An efficient way of proceeding is to use a Chebyshev basis for the polynomial function, as detailed in Section 2.D.6. From this description, we extract the set of coefficients e_k (expressed in Pa) for the elastic stresses and v_k (expressed in Pa.s) for the viscous stresses, which are plotted in Fig. 4.8. The k-th Cheby-

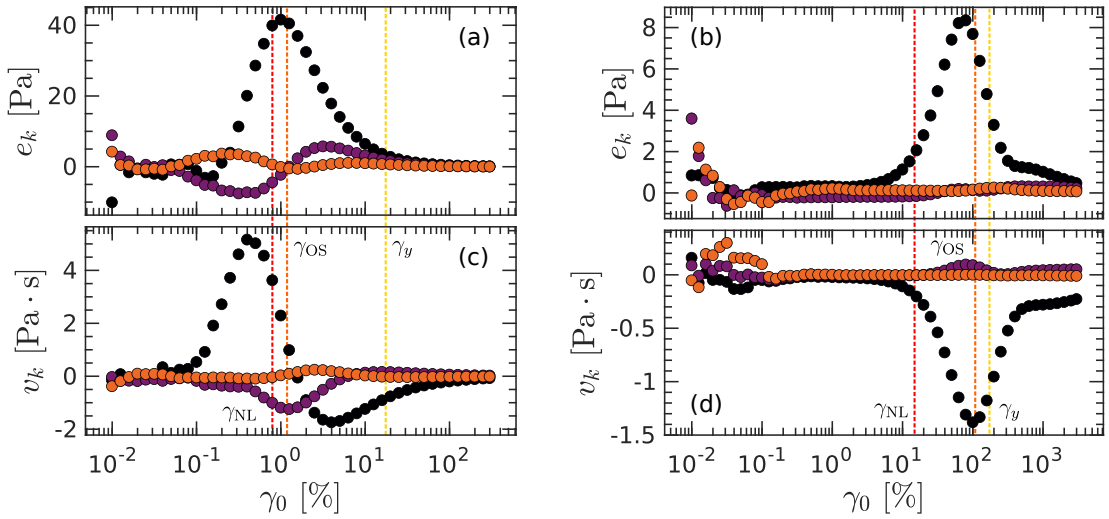

Figure 4.8: Chebyshev coefficients obtained from the LB curve for CB-CMC hydrogels in the colloid-dominated regime ($c_{CMC} = 0.01\%$ & $x_{CB} = 8\%$, left column) and in the polymer-dominated regime ($c_{CMC} = 3\%$ & $x_{CB} = 8\%$, right column). The frequency is fixed at $\omega = 2\pi$ rad.s^{-1}. Lighter colors correspond to a higher value of k (either 3, 5, or 7). The vertical dashed lines indicate γ_{NL}, γ_y and γ_{OS}.

shev polynomial is the first one in which γ^k appears, but as it also contains lower exponents of γ, care should be taken in the interpretation of the e_k and v_k coefficients. Here only $k = 1$, 3, and 5 were used to fit the data; the contributions above $k = 7$ are negligible. The fits are plotted in red onto the stresses in Fig. 4.7. The e_k and v_k coefficients (see Fig. 4.8) are close to zero in the linear regime for $k > 1$. Their overall shape is hard to grasp, and as there is no clear interpretation of these coefficients, we should instead have a look at more physically meaningful values, which are detailed in Section 2.D.6 and summarized in Table 4.1.

Value	Definition	Chebyshev expression	Physical meaning
G_L	$\left.\frac{\sigma_{elast}}{\gamma}\right\|_{\gamma=\gamma_0}$	$e_1 + e_3 + e_5$	Large-strain elastic modulus
G_M	$\left.\frac{\mathrm{d}\,\sigma_{elast}}{\mathrm{d}\gamma}\right\|_{\gamma=0}$	$e_1 - 3e_3 + 5e_5$	Minimum-strain elastic modulus
η_L	$\left.\frac{\sigma_{visc}}{\dot\gamma}\right\|_{\dot\gamma=\omega\gamma_0}$	$v_1 + v_3 + v_5$	Large-rate dynamic viscosity
η_M	$\left.\frac{\mathrm{d}\,\sigma_{visc}}{\mathrm{d}\dot\gamma}\right\|_{\dot\gamma=0}$	$v_1 - 3v_3 + 5v_5$	Minimum-rate dynamic viscosity
S	$\frac{G_L - G_M}{G_L}$	$\frac{4e_3 - 4e_5}{e_1 + e_3 + e_5}$	Intra-cycle strain-stiffening ratio
T	$\frac{\eta_L - \eta_M}{\eta_L}$	$\frac{4v_3 - 4v_5}{v_1 + v_3 + v_5}$	Intra-cycle shear-thickening ratio
G_{cage}	$\left.\frac{\mathrm{d}\,\sigma}{\mathrm{d}\gamma}\right\|_{\sigma=0}$	numerical estimation	Effective cage modulus

Table 4.1: Summary of the intra-cycle parameters analyzed with their definition, expression in terms of the Chebyshev coefficients, and their physical interpretation. The Chebyshev decomposition is limited to $k = 5$.

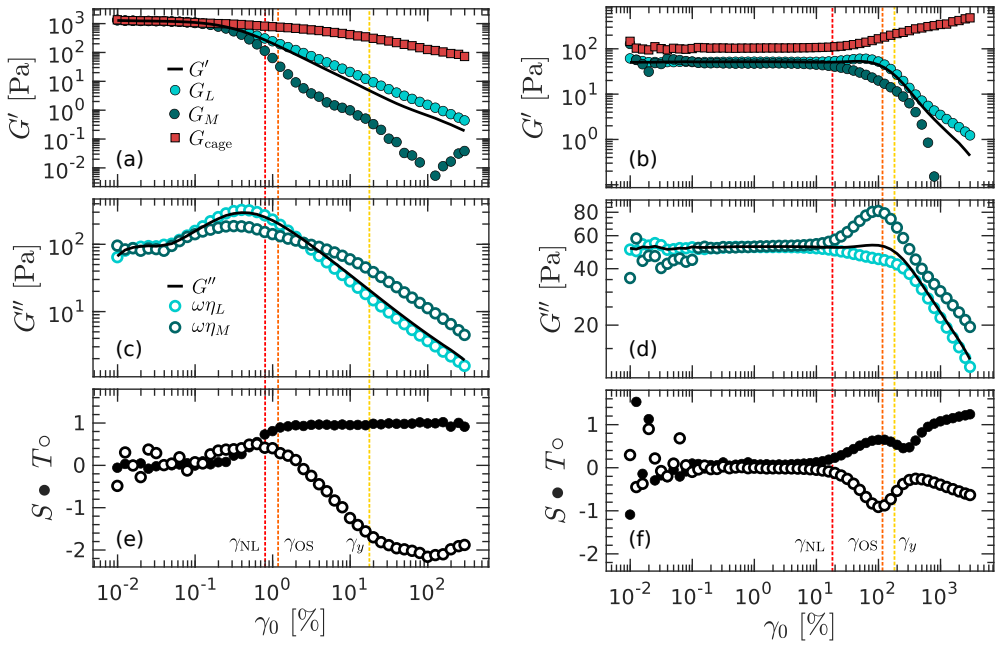

Figure 4.9: LAOStrain intra-cycle analysis for CB-CMC hydrogels from the colloid-dominated regime ($c_{\mathrm{CMC}} = 0.01\%$ & $x_{\mathrm{CB}} = 8\%$, left column) and the polymer-dominated regime ($c_{\mathrm{CMC}} = 3\%$ & $x_{\mathrm{CB}} = 8\%$, right column). The frequency is fixed at $\omega = 2\pi$ rad.s^{-1}.(a-b) Elastic moduli as a function of the strain amplitude γ_0. Black curves correspond to G', which is the modulus computed using only the fundamental frequency. The light (resp. dark) blue circles correspond to G_L (resp. G_M). The red squares correspond to G_{cage}. (c-d) Viscous moduli as a function of the strain amplitude γ_0. Black lines correspond to G'', which is the modulus computed using only the fundamental frequency. The light (resp. dark) blue circles correspond to $\omega\eta_L$ (resp. $\omega\eta_M$). (e-f) Strain-stiffening S (filled circles) and shear-thickening T (open circles) intra-cycle ratios as a function of γ_0.

These intra-cycle values should be compared to the traditional values of G' and G'' plotted for LAOStrain experiments, and as reported in Fig. 4.9. Recall that G' and G'' are the moduli computed considering only the fundamental amplitude of the stress, omitting the harmonics. In the linear regime $\sigma_{\mathrm{elast}} \sim \gamma$ and the different elastic moduli are equivalent $G_L = G_M = G'$ (similarly $\eta_L = \eta_M = G''/\omega$). As the strain amplitude increases, this equality eventually fails as the Lissajous curves of the elastic and viscous stresses deform.

We shall first look at CB-CMC hydrogels from the colloid-dominated regime, corresponding to the left column in Fig. 4.7. At the maximum strain during the shear oscillation, we look at G_L (corresponds to $\gamma = \gamma_0$) and $\omega\eta_M$ (corresponds to $\dot{\gamma} = 0$). They both follow the trend of G' or G'' and are always above except for $\omega\eta_M$ near the overshoot. At zero strain, the shear rate is maximum, and we look at G_M and $\omega\eta_L$ ($\dot{\gamma} = 0$), which also follow the trends of G' and G'' being always smaller than them. These features can be interpreted in the light of the glassy picture of this colloid-dominated hydrogel. At large strains, the cages stiffen, leading to higher values of G_L and η_M compared to G' and G''. On the other hand, at zero strain, the shear rate is maximum, and all cages are broken, leading to lower values of G_M and η_L compared to G' and G'', especially $G_M \ll G'$ because of the case breaking. These results are summarized in the S and T plot [Fig. 4.7(e)]. They both depart from zero (linear regime) near γ_{NL}, the strain-stiffening ratio S reaches a plateau around 1, whereas the shear-thickening T decreases below 0. At large amplitudes, the system evolves into a dynamic glassy

system in which the cages continuously break and reform at each cycle [229]. It is manifested by the high constant value $S = 1$ ($G_M \ll G_L$), which indicates that most of the cages are broken during a cycle at large amplitude. T is strongly negative ($\eta_M > \eta_L$) and decreases[4] with γ_0 when the cages are fully broken the system behaves as a shear-thinning fluid η_L decreases with $\dot{\gamma}$ faster than η_M, consistent with the flow behavior of this system that will be presented in Section 4.B. Further experiments at different frequencies may confirm this interpretation.

Let us now examine the response of CB-CMC hydrogels in the polymer-dominated regime, corresponding to the right column in Fig. 4.9. The elastic moduli G_L and G_M also follow the trend of G' with $G_L > G' > G_M$, yet keeping roughly similar values. At very high strain amplitudes $\gamma_0 > 300\%$ G_L and G_M significantly depart from G', up to a point where $G_M < 0$ as expected by the negative slopes around $\gamma_0 = 0$ in Fig. 4.7(c). As for the viscous moduli, they all follow the same trend with $\omega\eta_M > G'' > \omega\eta_L$ apart for the region around the yielding where η_M strongly overshoots and η_L drops. At the largest strain within the cycle, the CB clusters may break and cause the bigger values for G_L and $\omega\eta_M$ compared to G' and G''. The intra-cyle strain hardening S and shear thickening T ratio are very different in this polymer-dominated regime compared to the colloid one [Fig. 4.9(e-f)]. S and T are zero up to $\gamma_0 \simeq \gamma_{NL}$ and then S remains positive whereas T remains negative, which translates a structure that is broken by the shear rate but hardened by the strain. The yielding is visible on the plots where a non-monotonous dependence on the strain amplitude, which emphasizes the two-step yielding scenario proposed above. It would be insightful to see if this non-monotonous behavior depends on the frequency to confirm this interpretation, namely according to Fig. 4.4, we would expect the effect to be less visible at high frequency.

Finally, the effective cage modulus G_{cage} is also computed and should be interpreted as a rough evaluation of the elastic modulus due to the cages in a glassy system. For CB-CMC hydrogels in the colloid-dominated regime, G_{cage} remains comparable to the linear value of G' before decreasing by a factor 10 beyond the yield strain. This result is consistent with the fact that $S = cste$ beyond the yield strain. Indeed, cages are fully broken within a cycle for $\gamma_0 > \gamma_y$, leading to an even larger reorganization of the sample microstructure for increasing strain amplitudes. Therefore, the apparent cage modulus appears, in turn, weakens with increasing strain values. For CB-CMC hydrogels from the polymer-dominated regime, G_{cage} can be computed, yet it is physically meaningless as indicated by the fact that $G_{cage} \neq G'$ in the linear regime. Nonetheless, such a difference reflects the profound change of microstructure in CB-CMC hydrogels between the polymer-dominated and colloid-dominated regimes.

Electrical properties have been highly insightful in the linear regime, and we will now probe their evolution during the same mechanical protocol.

A.3 Insights from rheo-electrical experiments

a First observations

To probe the electrical properties of CB-CMC hydrogels during a LAOStrain experiment, we repeat the experiments with the rheo-electric setup depicted in Section 2.E.

[4] T may reach a plateau value at very high γ_0, but we have shown that slip may occur around these strain amplitudes for the colloid-dominated regime. Thus one cannot conclude yet on the existence of this plateau.

However, one cannot measure the full spectrum $Z^\star(f)$ as it takes too long to measure, especially since the most interesting value is σ_{CB} accessible only for vanishingly low frequencies. As detailed in Section 2.E.1, we instead applied a constant voltage $U_0 = 100$ mV and recorded the current I to compute the effective instantaneous electrical DC conductivity $\sigma_{DC}(t) = kI(t)/U_0$, with k the cell constant. This value is a direct image of the connectivity of the CB network since the electrical response time (around 10 ms for the colloidal gels) is way smaller than the evolution timescale during the strain sweep (the lowest bound is set by the frequency, that is to say around 1 s).

We first discuss the case of CB-CMC hydrogels from the colloid-dominated regime, for which we have already shown that there is a CB-percolated network responsible for the electrical conductivity of the system. In this regime, elasticity and electrical conductivity are correlated. They indeed start to drop around the same strain amplitude, i.e., $\gamma \simeq 0.2\%$, regardless of the CB content (see Fig. 4.10). However, for the lowest CB content (4%), the electrical conductivity increases before the yielding of the gel, whereas for the highest CB content (8%), the conductivity monotonically decreases through the yielding transition. Beyond the yield point, the conductivity drops, and there is no systematic trend depending on x_{CB}. Wall slip may occur during this experiment as the parallel plate geometry used has smooth boundary conditions to limit the impact of the wall roughness on the electrical measurements. Similar observations have been reported in the literature for experiments. Indeed, Helal *et al.* observed that applying a constant shear stress to CB gels in mineral oil leads to an increase in their electrical conductivity as well as their apparent viscosity before it yields, after which the conductivity oscillates a lot before reaching a constant value [239]. The increase in conductivity is interpreted as a change either in the bulk microstructure or in the contact between the sample and the electrodes before the yielding. The subsequent evolution of the conductivity corresponds to a transient regime where slip and microstructure reorganization dominate the response until reaching a stationary state. For both the present LAOStrain experiments and the creep tests conducted by Helal *et al.*, the proposed scenario could be tested with the complete measurement of electrical spectrum $Z^\star(f)$ at different points in time, especially through the evolution of the constant phase element characteristics. Unfortunately, mechanical non-linearities may impact the electrical measurements, prohibiting the use of frequency-rich signals to measure $Z^\star(f)$ faster.

Finally, at large strain amplitudes, i.e. $\gamma_0 \gtrsim 40\%$, the electrical conductivity shows an abrupt upturn, which may be due to a *dynamical* CB network formed by CB particles and/or clusters in close proximity but not necessarily in mechanical contact and, therefore, not transmitting much stress. Indeed, such a dynamic network is electrically conductive since the CB are close enough to let the current pass (e.g., via electronic tunneling). This picture is supported by previous rheo-electrical work on CB gels in oil, where it was shown that the percolation electrical percolation threshold is lower than the mechanical one in terms of CB content [125, 239].

b Fourier analysis of the DC electrical response

Here, we proceed to a deeper analysis of the DC electrical response, which has in itself a rich behavior as shown in Fig. 4.10(c-d). The mechanical frequency of the oscillatory shear is 1 Hz, and we find only harmonics of this frequency in the Fourier analysis of the electrical conductivity. The coupling between the mechanical input and the electrical measurements has already been observed experimentally in [303] and pre-

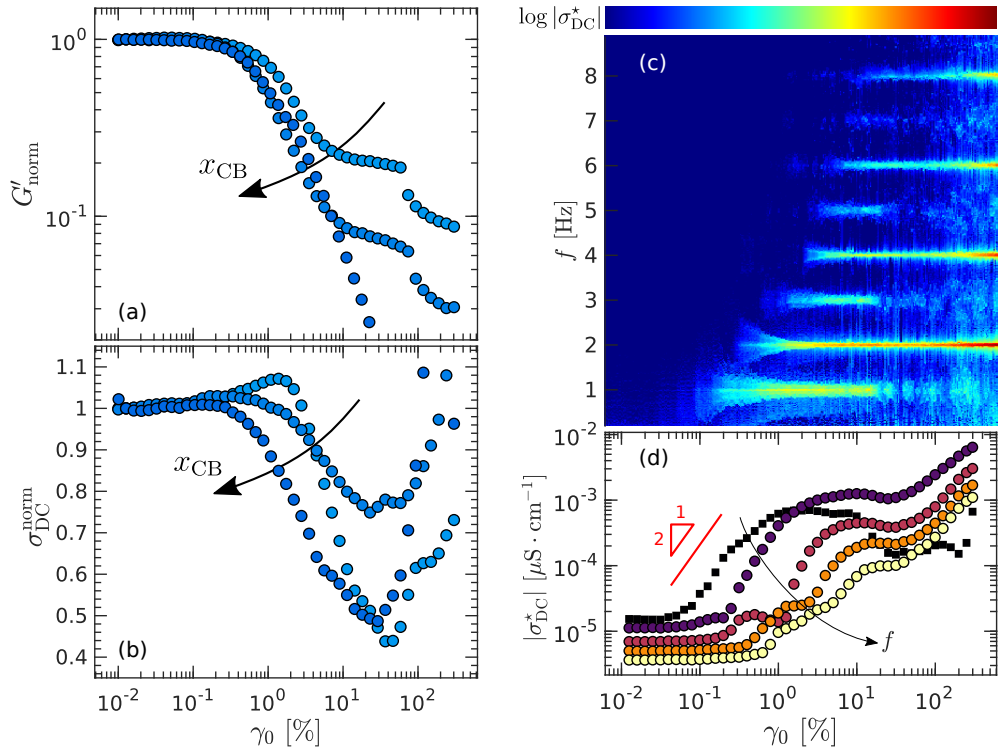

Figure 4.10: Rheo-electrical analysis under LAOStrain for CB-CMC hydrogels from the colloid-dominated regime at $c_{CMC} = 0.01\%$ for $x_{CB} = 4, 6$ and 8% (darker colors correspond to higher x_{CB}). The frequency is set to $\omega = 2\pi$ rad.s^{-1}. The data are averaged over the total number of oscillations applied by the rheometer for each step of strain amplitude γ_0. (a) Elastic moduli normalized by its linear value versus γ_0. Note that mechanical measurements at large γ_0 are affected by the wire closing the electrical circuit, especially when G' is small as observed for lower x_{CB}. (b) Electrical conductivity σ_{DC} versus γ_0. The electrical conductivity is normalized by its initial value. (c) Strain-frequency plot showing the amplitude of the electrical conductivity in the Fourier space $|\sigma^{\star}_{DC}|$ as a function of the Fourier frequency f and the strain amplitude γ_0 (sample at $c_{CMC} = 0.01\%$ & $x_{CB} = 8\%$). Colors encode the amplitude in log scale and arbitrary units. (d) Main harmonics amplitude $|\sigma^{\star}_{DC}(f = p\omega/2\pi)|$ against γ_0 with p being either 1, 2, 4, 6, or 8. They correspond to the brightest lines in (c). Lighter colors correspond to higher harmonics. The case $p = 1$ is plotted in smaller squares as it is the only odd coefficient, which has a different physical meaning than the even values of p. The red line is a guideline for the eye showing a power law of exponent 2.

dicted theoretically [304] for polymer solutions. There is, however, no clear indication of the functional form the electrical conductivity should take with the instantaneous strain $\gamma(t)$.

In Fig. 4.10(c), we present the frequency analysis of the electrical conductivity signal over a 15 s moving window along the LAOStrain experiment and replot the result as a function of the strain amplitude. In other words, each vertical line corresponds to the Fourier transform of σ_{DC} around each strain value γ_0. The zero frequency term has a significantly higher amplitude and is not represented for the sake of readability; besides, it is equivalent to σ_{DC} in Fig. 4.10. For increasing strain amplitude, the amplitude of every even harmonic becomes noticeable, while it stays relatively small for all odd harmonics. In our case, the only odd harmonic that stands out is the fundamental frequency $f = 1$ Hz, which dies out after $\gamma_0 = 10\%$ far after the yielding. Moreover, higher harmonics $f = 2, 4, 6$ and 8 Hz appear at larger γ_0; this feature is reminiscent of

what is observed in the Fourier analysis in the intra-cycle study [Fig. 4.6(a)]. Strikingly enough, the shape of $a_k(\gamma_0)$ and the one of $|\sigma^\star_{\mathrm{DC}}(\gamma_0)|$ are very similar as well, including the scaling $|\sigma^\star_{\mathrm{DC}}| \sim \gamma_0^2$ at the onset of the non-linear regime. This comparison is supported by the idea that mechanical and DC electrical properties are intertwined in the colloidal regime, for they both originate from the CB percolated network.

The even harmonics prevail in the spectrum $|\sigma^\star_{\mathrm{DC}}|$. The $p = 2$ harmonic corresponds to the mechanical perturbation on the electrical measurement. Indeed, the electrical behavior is independent of the shear sign, so it should be an even function of the strain, hence the doubling of the frequency. The $p = 1$ appears then as an asymmetry between the positive and negative shear. This can hardly be attributed to an artifact in the experimental setup, e.g., due to the wire being connected to the rotor, since the stretching of the wire may not be the same in the positive and negative shear directions. It might thus come from partial slip of the CB-CMC hydrogel at the wall of the parallel-plate geometry, which occurs more frequently during the shear oscillation as the amplitude increases. There is no clear physical interpretation of the higher harmonics, but they have to arise from the mechanical stress because it is the only perturbation that brings higher frequencies. Further investigation is required to disentangle the different contributions to the electrical response: what has the most impact between the stress, the strain, and the shear rate? Running experiments at different frequencies and as a function of stress would enlighten a lot in that sense.

For CB-CMC hydrogels in the polymer-dominated regime, $\sigma_{CB} \to 0$ at rest, since the CB particles are isolated within the CMC matrix, hence nothing much was expected with the same protocol. Surprisingly, the electrical conductivity grows by almost 2 orders of magnitude beyond the yield point [Figs. 4.11(a) and (b)], and the same behavior is observed for all even harmonics $p \leq 2$. The fact that even harmonics are negligible confirms that this feature is not an artifact[5]. We explain this increase in the hydrogel conductivity by the formation of a transient percolated network of CB particles. Such a colloidal network forms when the polymers are highly stretched at large enough γ_0. Indeed, the polymers are much more flexible than the CB clusters, hence, when the CB-CMC hydrogel is highly strained it is easier for the CMC matrix to deform. As the volume fraction in CB particles is relatively high, CB clusters are brought into contact by the strain to eventually form a weakly percolated network throughout the whole sample. This *dynamic percolated network* of CB particles is however less connected than the network in CB-CMC hydrogels from the colloidal-dominated regime since the conductivity is three orders of magnitude below: at $x_{\mathrm{CB}} = 8\%$ we measure $\sigma_{\mathrm{DC}} \simeq 0.1\ \mu\mathrm{S.cm}^{-1}$ at the end of the strain sweep [Fig. 4.11(b)] for $c_{\mathrm{CMC}} = 3\%$ against $\sigma_{\mathrm{CB}} \simeq 30\ \mathrm{mS.cm}^{-1}$ at rest for $c_{\mathrm{CMC}} = 0.01\%$ [Fig. 3.17(a)].

These results call for additional experiments such as measuring a complete dielectric spectrum of CB-CMC hydrogels under oscillatory shear. It would bring insightful results on the emergence of such a dynamic percolated network. Yet, as mentioned above this measurement is really challenging. Moreover, it would also be interesting to investigate the impact of the sample composition on the electrical conductivity reached under oscillatory shear, especially for a sample with a value of x_{CB} chosen below the sol-gel transition.

Finally, following the end of the strain sweep experiments, the sample are set to rest. As a preliminary observation, we monitor the relaxation of the electrical con-

[5] In contrast, the vertical lines in the frequency-strain plot shown in Fig. 4.11(c) correspond to random events, enhanced by the fact that the current measured in the polymer regime is extremely low (around 100 nA).

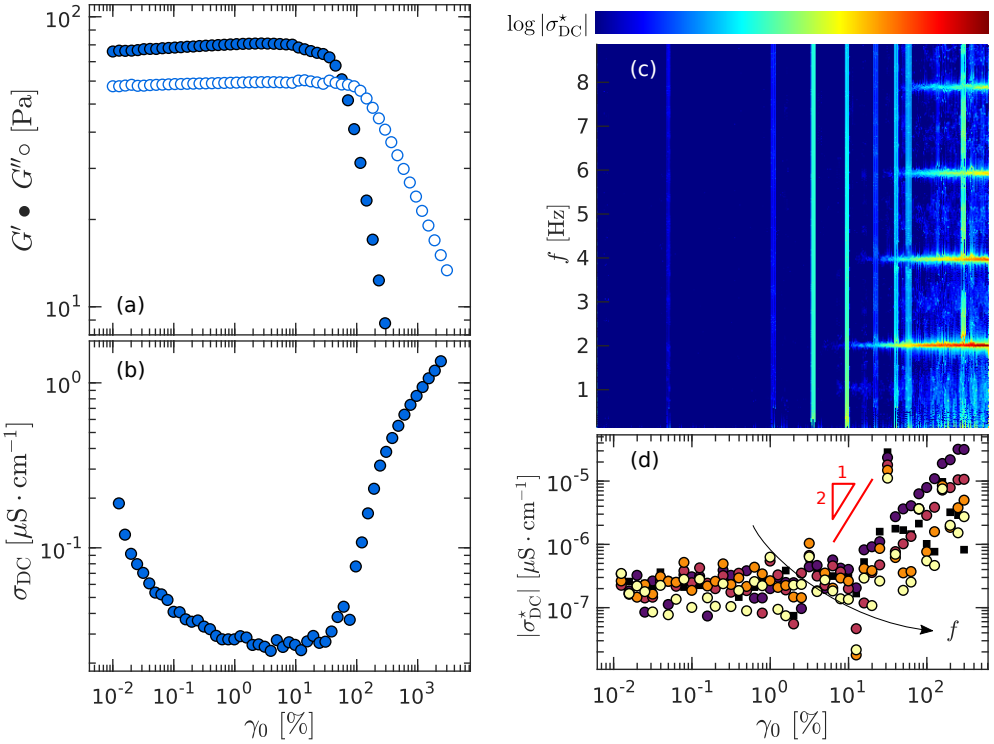

Figure 4.11: Rheo-electrical analysis of a strain sweep experiment conducted on a CB-CMC hydrogel from the polymer-dominated regime ($c_{CMC} = 3\%$ & $x_{CB} = 8\%$). The frequency is set to $\omega = 2\pi$ rad.s^{-1}. The data are averaged over the total number of oscillations applied by the rheometer for each step of strain amplitude γ_0. (a) Elastic modulus normalized by its linear value vs. γ_0. (b) Electrical conductivity σ_{DC} vs. γ_0. The electrical conductivity is normalized by its plateau value between $\gamma_0 = 1 - 10\%$. Note that the initial values of σ_{DC} correspond to a transient current as a response to a step voltage applied at the beginning of the experiment. The typical electrical timescale is very large in the polymer regime (see discussion in Section 2.E.1). (c) Strain-frequency plot showing the amplitude of the electrical conductivity in the Fourier space $|\sigma^\star_{DC}|$ as a function of the Fourier frequency f and the strain amplitude γ_0. Colors encode the amplitude in log scale and arbitrary units. (d) Main harmonics amplitude $|\sigma^\star_{DC}(f = p\omega/2\pi)|$ against γ_0 with p either 1, 2, 4, 6, or 8. Lighter colors correspond to higher harmonics. The $p = 1$ is plotted in smaller squares as it is the only odd coefficient, which has a different physical meaning than the even values of p. The red line shows a power law of exponent 2 for comparison.

ductivity right after the last step of the strain sweep, where the potential dynamic network is the most visible. For hydrogels prepared either in the colloid-dominated or polymer-dominated regime, we observe an abrupt relaxation of the conductivity within 1-10 s, which is in line with the transient nature of the shear-induced dynamic network during the LAOS.

In conclusion of this section, electrical conductivity measurements conducted during strain sweep experiments have allowed us to propose a microscopic scenario for the LAOStrain response of the two types of CB-CMC hydrogels, first identified in Chapter XX, thanks to static dielectric measurements. These experiments also suggest that LAOS on non-conductive CB-CMC hydrogels may trigger the formation of a transient CB network, which is electrically conductive but does not contribute much to the mechanical properties of the composite. In fact, this feature occurs in both types of CB-CMC hydrogels. In the next section, we further investigate this scenario by

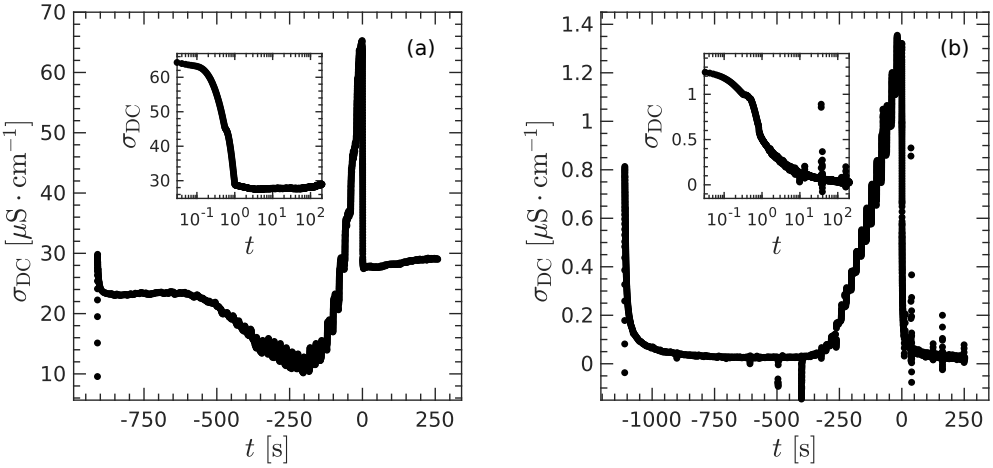

Figure 4.12: Relaxation of the electrical conductivity after a strain sweep. The LAOS experiment is stopped at $t = 0$ and the DC electrical conductivity σ_{DC} is plotted as a function of time for a CB-CMC hydrogel: (a) in the colloid-dominated regime at $c_{CMC} = 0.01\%$ & $x_{CB} = 8\%$ and (b) in the polymer-dominated regime at $c_{CMC} = 3\%$ & $x_{CB} = 8\%$. The insets show a zoom around $t = 0$, the units are the same as the ones in the corresponding main graph.

performing rheo-scattering experiments during LAOStrain experiments.

A.4 Insights from rheo-SAXS experiments

The goal of the rheo-SAXS experiments is to look for any change in the microstructure of CB-CMC hydrogels during the strain sweep. In fact, there are several key features of CB-CMC hydrogels, specifically those from the polymer-dominated regime (e.g., double yielding and the shear-induced formation of transient CB network) that motivated this study. To do so, we recorded the scattering intensity patterns of the sample in the rheometer, as detailed in Section 2.G.3 from Chapter 2. We decided to look at the full scattering intensity I rather than the structure factor. Further work may be done in the future in that sense. To investigate further the evolution of the microstructure under LAOStrain, we looked at the regular strain sweep studied above and following this protocol we applied the same strain sweep but backwards, i.e., sweeping the strain from the largest amplitude down to the lowest (everything else kept the same). We ensured there is no discontinuity between the two protocols.

a Rheo-SAXS on CB-CMC hydrogels from the polymer-dominated network

We shall first discuss the regular strain sweep by increasing values of strain amplitude γ_0, whose results are represented by the circles in Fig. 4.13(a-d). Looking at the scattering intensities in the Kratky representation Iq^2 vs q, where q is the wave vector, we see a continuous shift of the shape Iq^2 as the strain amplitude increases [Fig. 4.13(e)]. Focusing on the center of the q range, we see that the broad peak around $q = 0.2$ nm^{-1} is shifted to the right and it sharpens as γ_0 increases. We quantified this observation with the position of its maximum q_{max} and the ratio q_2/q_1, which corresponds to an estimation of the broadness[6]. Surprisingly, q_{max} continuously in-

[6]Note that the initial value does not match exactly the value for the same sample in Fig. 3.21 (see Section 2.G.4). Indeed, the experiments were conducted with the same loading such that about 5 hours elapsed between the strain sweep and the time sweep with lots of experiments in between. Even with

crease, while q_2/q_1 decreases in the linear regime [Fig. 4.13(a) and (b)]. They both reach a plateau value around γ_{NL} and there seem not to have any specific signature around γ_y. To interpret this behavior, one should recall that the mechanical properties are mainly due to the CMC matrix, whereas in SAXS we solely probe the CB particles. This suggests that the CB clusters may break even in the linear regime such that their mean size decreases (equivalently q_{max} increases). Besides, the shear also induces a more selectivity on this typical size as the broadness of the peak decreases. At large enough strain amplitude, i.e., $\gamma_0 > \gamma_{NL}$, the clusters size reaches its final value, while increasing even more γ_0 cannot reduce any further the size of the clusters as it approaches the size of a single CB (around 500 nm, which roughly translates to $q \simeq 0.01$ nm^{-1}). Note that this final value of q_{max} is comparable to the one in the colloidal regime where $q_{max} \simeq 22.10^{-3}$ nm^{-1} [see Fig. 3.13(c)], to be compared with the typical size for a single CB particle (around 500 nm, which roughly translates to $q \simeq 0.01$ nm^{-1}). This confirms the scenario of a dynamic percolated network of CB particles at large strain amplitude suggested by the rheo-electrical measurements.

To investigate further this dynamic percolated network, we shall look at the data at very low q. They are of great value but unfortunately extremely noisy and artifacts may occur close to the beam stop, especially in the rheometer, hence we did not extract quantitative results from this region of the spectra. However, one clearly sees a sharp peak at the lowest q for large strain amplitudes, which is highly reminiscent of the scattering intensities of the colloidal-dominated regime even though the position of the minimum q_{min} is larger in the latter case (Fig. 3.12). It remarkably supports the idea of a percolated CB network in the polymer gel under large shear. Note however that this upturn in the scattered intensity happens at slightly lower q values in the sheared CB-CMC hydrogel from the polymer-dominated regime than in the CB-CMC hydrogel from the colloid-dominated regime at rest (around 3.10^{-3} vs around 5.10^{-3} nm^{-1}). In an attempt of quantification, we take advantage of the invariant Q_{SAXS}, which represents the area under the Kratky plot over the whole spectrum. Q_{SAXS} has to be constant as the system composition does not change during the experiment [250]. We computed a part of this area $Q_{\delta q}$ within a given region symbolized by the dashed lines[7] in Fig. 4.13(e-f). The Kratky plots do not evolve much at larger q values than that in the region considered, as it corresponds to length scales within the CB particles (form factor). Hence the decrease of $Q_{\delta q}$ as γ_0 increases observed in Fig. 4.13(d) must be compensated by a higher scattering intensity at lower q values, potentially outside of the probed q range. This supports as well a formation of CB clusters at larger scale when γ_0 is large enough, consistent with a CB percolated network.

Following the strain sweep of increasing amplitude, we decrease the strain amplitude. We observe similar trends for the quantity extracted from the scattering experiments [diamonds in Fig. 4.13(a-d) and 4.13(f)]. Starting from the high strain amplitudes, they all plateau until γ_0 is small enough, from which q_{max} decreases, q_2/q_1 increases, and $Q_{\delta q}$ increases as γ_0 decreases. This defines a critical strain that is comparable to γ_y, contrary to γ_{NL} found in the increasing sweeping described above. Finally, when γ_0 reaches γ_{NL}, these values reach another plateau value. Moreover, the final state is slightly different than the initial state, especially the final value for q_{max} is

the preshear, there might still remain some memory effects of the previous experiments, which have an impact on the gel microstructure.

[7] This region corresponds to the minimal value of q_1 and the maximal value of q_2 measured in the whole experiment.

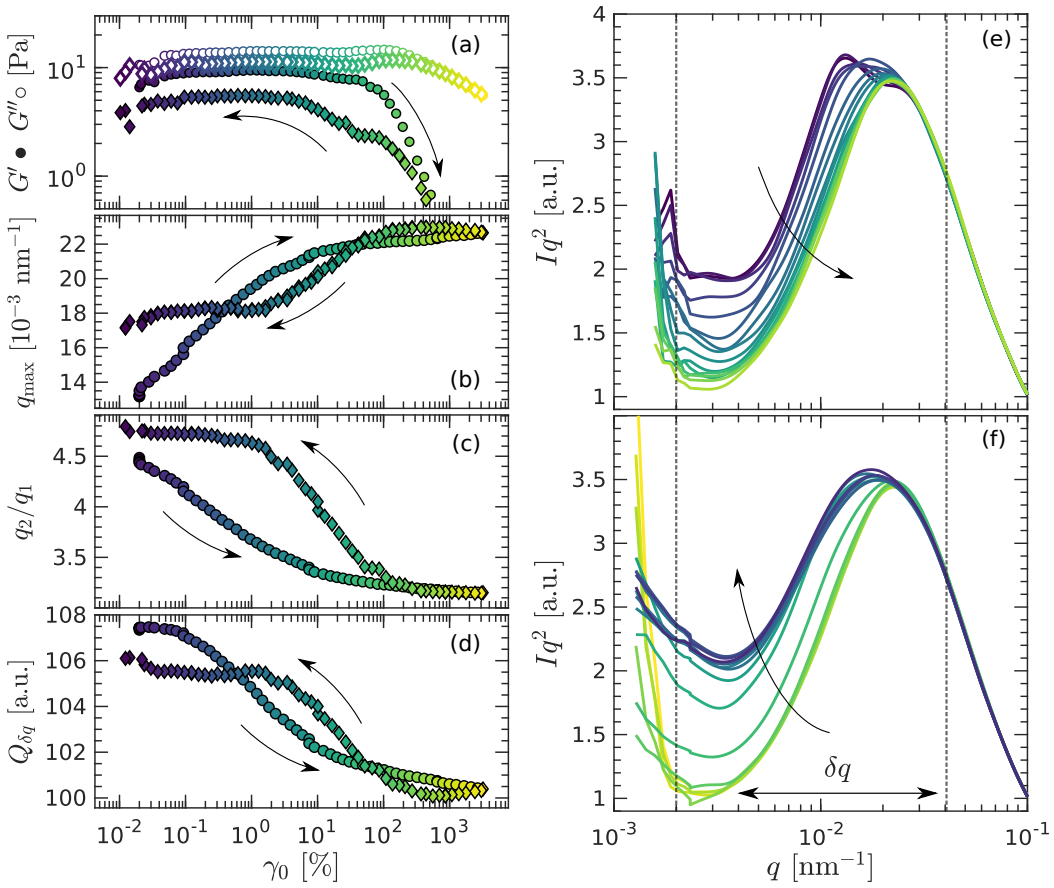

Figure 4.13: Rheo-SAXS analysis of a strain sweep on a CB-CMC hydrogel from the polymer-dominated regime at$c_{CMC} = 2\%$ & $x_{CB} = 8\%$) The strain sweep is applied by increasing values of strain amplitude γ_0 (circles) and then decreasing values (diamonds) as indicated by the black arrows. The frequency is set to $\omega = 2\pi$ rad.s^{-1}. (a) Elastic (filled symbols) and viscous (empty symbols) moduli. (b) Position of the maximum q_{max} in the Kratky plot Iq^2 vs q of the scattering intensity I and (c) broadness of the peak q_2/q_1, with q_1 and q_2 the positions of the inflexion points in the Kratky plot around q_{max}. (d) Area $Q_{\delta q}$ below the Iq^2 plot for q between the dashed lines represented in (e) and (f). The right columns shows the Kratky plots Iq^2 vs q during the increasing step of the strain sweep (e) and during the decreasing step (f). Lighter colors correspond to higher value of γ_0.

larger at the end of the return step than at the beginning of the first increasing ramp. It means that there are is a shear-induced *memory effects* in the structure [106, 239]. Such an increase of q_{max} has been observed during the aging of the sample (Fig. 3.21), but here the moduli are lowered by the shear, as opposed to their increase by aging. This suggests that the memory effect changes the microstructure in a different way compared to aging.

Finally, the two-step yielding observed above for the polymer gel can be deduced from the present SAXS experiments. Indeed, during the ramp up the clusters are well formed and they start to break below γ_{NL}, and then the CB microstructure does not evolve much, which corresponds to a stationary state for the clusters microstructure as they can not be broken further. During the ramp down, the clusters start to reform slowly below γ_y, which corresponds to a shear induced aggregation from the yielded state. Sweeping rate may probably have an impact on the hysteresis between the ramp up and the ramp down.

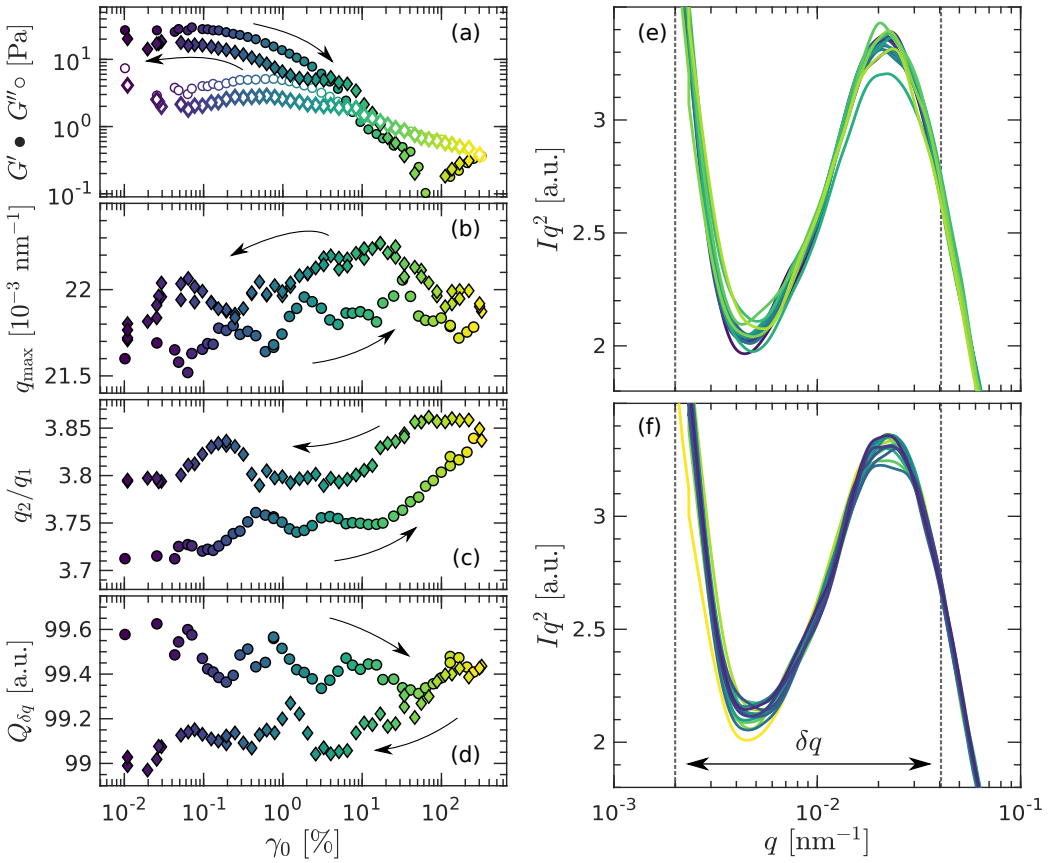

Figure 4.14: Rheo-SAXS analysis of a strain sweep for a CB-CMC hydrogel in the colloidal-dominated regime at $c_{CMC} = 0.01\%$ & $x_{CB} = 6\%$. The strain sweep is applied by increasing values of strain amplitude γ_0 (black circles) and then decreasing values (red squares) as indicated by the black arrows. The frequency is set to $\omega = 2\pi$ rad.s^{-1}. (a) Elastic (filled symbols) and viscous (empty symbols) moduli. (b) Position of the maximum q_{max} in the Kratky plot Iq^2 vs q of the scattering intensity I and (c) broadness of the peak q_2/q_1, with q_1 and q_2 the positions of the inflexion points in the Kratky plot around q_{max}. (d) Area below the Iq^2 plot for q between the dashed lines represented in (e) and (f). The right columns shows the Kratky plots Iq^2 vs q during the increasing step of the strain sweep (e) and during the decreasing step (f). Lighter colors correspond to higher value of γ_0.

b Rheo-SAXS on CB-CMC hydrogels from the colloid-dominated network

For a CB-CMC hydrogel from the colloidal-dominated regime, the structure does not evolve much during the strain sweep [Fig. 4.14]. The variations in all the key parameters presented above remain below 5%, which is difficult to extract from the noise of the data. This means that the differences in the mechanical properties must arise from changes at bigger or smaller scales than the ones probed here. Since the sample is flowing at large strain amplitude, there cannot be a percolated CB network, lower q ranges should present at smaller intensities compared to the measurement at rest. Moreover, we witnessed an increase in electrical conductivity at large strain, meaning there might be changes in the contact between the CB particles, which should be visible at a higher q range, i.e., at very small scales.

In conclusion to this section, the study of yielding under oscillatory shear enabled to settle the difference in nature between the polymer and colloidal-dominated regimes. Moreover we ere able to prove the existence of a transient percolated CB net-

work in both the colloidal and polymer regimes, which is electrically conductive but not strongly connected enough to give the systems solid-like behavior. In the following we will discuss the impact of the shear when applied continuously rather than in an oscillatory fashion.

B Yielding under Continuous Shear

In this second section, we consider the response of CB-CMC gels to *continuous shear*, that is, a constant shear rate $\dot{\gamma}$ is applied, and the response stress σ is measured. It corresponds to most of the applications, especially in the context of flow batteries. The goal is to understand the main characteristics of the flow behavior and study them in light of the results in the previous sections. We will first describe the flow curves, then look into the impact of the flow onto the viscoelasticity and finally we will study the recovery once the flow ceases.

B.1 Flow behavior

Two representative flow curves are shown in Figs. 4.15(a) and (b) for a CB-CMC hydrogel from the polymer-dominated regime and the colloid-dominated regime, respectively. To ensure a stationary state is reached at each applied $\dot{\gamma}$, the flow curve is measured by decreasing values of $\dot{\gamma}$ (see Section 2.D.7.a). An estimate of the viscosity scale η_{500}, i.e., the viscosity at $\dot{\gamma} = 500$ s^{-1} is represented onto the map of all compositions explored [Fig. 4.15(c)]. There is no obvious signature of the sol-gel

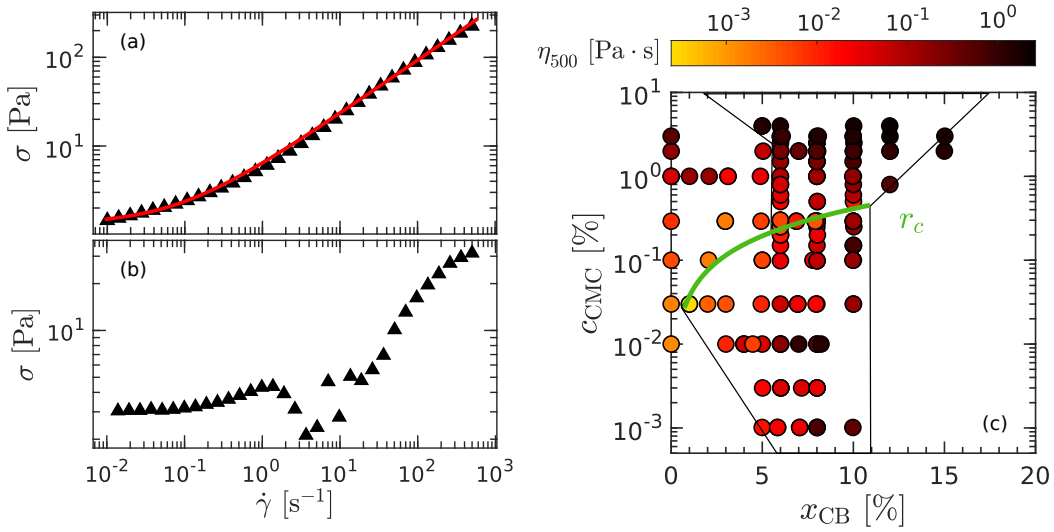

Figure 4.15: Typical flow curves of CB-CMC hydrogels from the polymer-dominated regime ($c_{CMC} = 2\%$ & $x_{CB} = 8\%$) (a) and from the colloid-dominated regime ($c_{CMC} = 0.1\%$ & $x_{CB} = 8\%$) (b). The shear rate is applied stepwise for 10 s with 7 points per decade from $\dot{\gamma} = 500$ to 0.01 s^{-1}. The red curve correspond to the best Hershel-Bulkley fit of the data $\sigma = \sigma_y[1 + (\dot{\gamma}/\dot{\gamma}_c)^n]$ [see Eq. (4.1)], yielding $\sigma_y = 1.0 \pm 0.2$ Pa, $n = 0.59 \pm 0.03$, and $\dot{\gamma}_c = 0.02 \pm 0.01$ s^{-1}. (c) Effective viscosity $\eta_{500} = \sigma/\dot{\gamma}$ at $\dot{\gamma} = 500$ s^{-1} mapped onto the (x_{CB}, c_{CMC}) plane. Darker colors correspond to higher values of η_{500} as represented by the color bar on top. The black lines delimit the gel region, and the green curve represents the frontier $r = r_c$ separating the colloid-dominated regime from the polymer-dominated one, as detailed in Section 3.A.

transition in this map with η_{500} continuously varying with the composition between the sol and gel phases. However there is a clear demarcation between the polymer-dominated and colloid-dominated regimes, with significantly higher viscosity values for the former. At this shear rate, one expects to break any space-spanning network, which means the trends described here are likely to arise mainly from the polymer state (the semi-dilute entangled regime starts around $c_{CMC} = 0.3\%$ and the concentrated regime starts around $c_{CMC} = 2\%$, see Section 2.B). We shall look more precisely into the series of flow curves at various CMC contents if we find any signature of a depercolation transition.

In the case of CB-CMC hydrogels from the colloid-dominated regime, the flow curve shows a complex shape, which suggests that non-trivial flow profile may happen. The large fluctuations of stress between 1 s^{-1} and 10 s^{-1} are strongly reminiscent of stick-slip or shear-banding instabilities[305, 306]. Moreover, the shape of the flow curves at high shear rates (typically for $\dot{\gamma} \gtrsim 100$ s^{-1}) are consistently smoother within all the colloid-dominated regime, thus η_{500} appears as a trustworthy value. It is consistent with the slip scenario, which occurs mainly at low shear rate [233]. We did not look any further into the flow curves of CB-CMC hydrogels from the colloid-dominated regime, which would necessitate the use of a local probe to measure the flow profile simultaneously to the rheology.

In contrast, the flow curves of CB-CMC hydrogels from the polymer-dominated regime show typical features of a yield stress fluid with a stress plateau as $\dot{\gamma} \to 0$ and a power-law dependence with $\dot{\gamma}$ at high shear rates. The exponent of this power-law is lower than 1, indicating a shear-thinning behavior[8]. In the polymer-dominated regime, the flow curves of CB-CMC hydrogels are well described by an Herschel-Bulkley (HB) model [230]. The stress is modeled by the following equation:

$$\sigma = \sigma_y + \sigma_y \left(\frac{\dot{\gamma}}{\dot{\gamma}_c} \right)^n \tag{4.1}$$

with σ_y the yield stress, $\dot{\gamma}_c$ a critical shear rate and n the Herschel–Bulkley exponent [see Section 2.D.7.a for more details]. The values of the fit parameters are reported in Fig. 4.16 as a function of the composition within the polymer-dominated regime. In addition, CB-CMC hydrogels in the polymer-dominated regime are likely to slip at the walls, with a characteristic kink in the flow curve for low shear rates, as shown in Section 2.D.7.a [232]. Wall slip occurs mainly at relatively low shear rate so that the HB model still gives relevant values when used for fitting a limited portion of the flow curve at larger shear rates. Let us now discuss the dependence of the HB parameters with the composition of the CB-CMC hydrogel.

First, the yield stress of CB-CMC hydrogels increases with the CB content and the CMC concentration [Fig. 4.16(a-b)]. It is well described by fitting σ_y as a power-law of $(x_{CB} - x_c)$, with $x_c = 5\%$ and an exponent 3.7 ± 0.5, in good agreement with the scaling of G_0 determined in the linear regime (Fig. 3.9), which follows the same scaling with an exponent 3.0 ± 0.5. The yield stress represents the solid-like behavior of the system at rest, therefore the similarities between G_0 and σ_y confirm these two quantities both arise from the elastic polymer network, which is reinforced as the CB content increases. In the polymer matrix CB particles play the role of cross-linkers, the latter must have a large enough density in order to lead to a solid-like behavior at rest. Moreover Fig. 4.16(b) indicates a dependence of σ_y with c_{CMC} in disagreement with

[8] In this case, $\eta = \sigma/\dot{\gamma}$ decreases as $\dot{\gamma}$ increases.

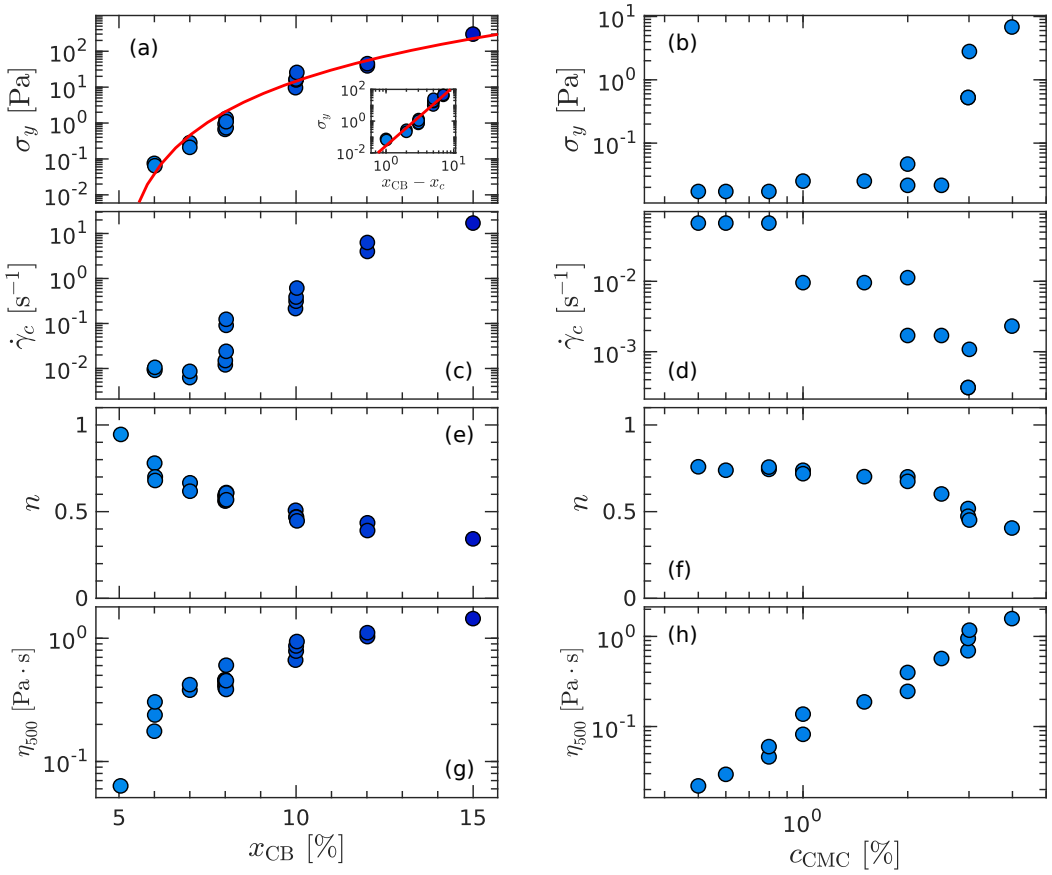

Figure 4.16: Herschel–Bulkley parameters for CB-CMC hydrogels from the polymer-dominated regime, at (left column) fixed $c_{CMC} = 2\%$ as a function of x_{CB} or (right column) fixed $x_{CB} = 6\%$ as a function of c_{CMC}: (a-b) yield stress σ_y, (c-d) critical shear rate $\dot{\gamma}_c$ (c-d) and (e-f) the Herschel–Bulkley exponent n. The red curve is the best power-law fit of σ_y vs $x_{CB} - x_c$ with $x_c = 5\%$, which is represented as an inset of (a), with an exponent of 3.7 ± 0.5.

the scaling between G_0 and c_{CMC} as a power-law 2.4 ± 0.4 obtained in the previous chapter [Fig. 3.9]. As the yield stresses are extremely small (around 0.01 Pa), it would require further investigation to speculate on this potential discrepancy between the elastic modulus at rest G_0 and the yield stress estimated from a flow curve, i.e., dynamically. Moreover, the yield stress values are significantly lower than the typical elasticity scale G_0 for the same composition[9], which may be attributed to aging [see Section 3.19]. The linear value G_0 is measured after a 20 min resting time, whereas, here, σ_y is measured dynamically at the end of the flow curve; there is virtually little to no resting time.

Second, the critical shear rate $\dot{\gamma}_c$ [Fig. 4.16(c-d)] increases with the CB content and decreases with the CMC concentration. This value can be understood as a shear rate above which the influence of the yield stress is negligible in the total stress. Since we are examining CB-CMC hydrogels from the polymer-dominated regime in Fig. 4.16(c), an increasing CB content corresponds to more cross-linkers within the polymer matrix. Larger shear rates are, therefore, required to obtain a flow independent of the yield stress. In contrast, in Fig. 4.16(d), an increasing concentration in CMC at fixed CB content leads to a smaller $\dot{\gamma}_c$, which may translate the increase of the background

[9] Typically here $G_0 \simeq 10\sigma_y$ comparing Fig. 4.16(b) and the inset of Fig. 3.7(c).

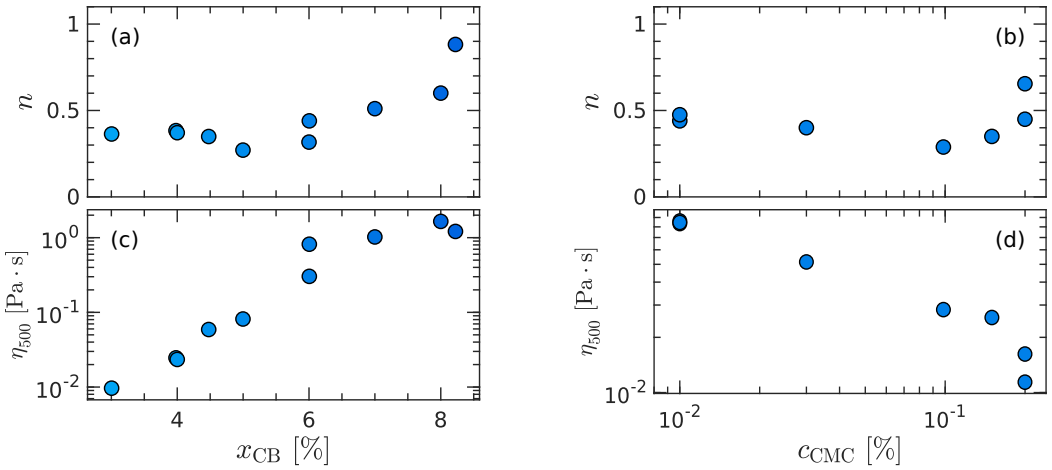

Figure 4.17: Flow curves noteworthy values in the colloid-dominated regime. Shear thinning exponent n (a) as a function of the CB content x_{CB} at fixed $c_{CMC} = 0.01\%$ and (b) as a function of the CMC concentration c_{CMC} content at fixed $x_{CB} = 6\%$. Viscosity η_{500} evaluated at $\dot{\gamma} = 500$ s^{-1} (c) as a function of the CB content x_{CB} at fixed $c_{CMC} = 0.01\%$ and (d) as a function of the CMC concentration c_{CMC} content at fixed $x_{CB} = 6\%$.

viscous contribution to the total stress.

Third, the Herschel-Bulkley exponent n [Fig. 4.16(e-f)] decreases with the CB content at fixed CMC concentration, with typical values between 1 for the less concentrated samples and down to 0.4 for the highest concentrations. A similar trend is observed for the dependence with respect to the CMC concentration at fixed CB content, with a slight difference that there is a plateau value $n \simeq 0.7$ for $c_{CMC} < 2\%$. Lower n values mean an increase of the shear-thinning behavior[10]. In both cases, it translates that the decrease of the viscosity for an increasing shear rate is stronger at a higher volume fraction of either CB or CMC, suggesting more connected microstructures. Note that the end of the plateau value for n vs c_{CMC} at $c_{CMC} = 2\%$ also corresponds to the slope break in the sol-gel frontier of the phase diagram. It supports the idea that the organization of the microstructure is responsible for the value of n.

Finally, the high shear rate viscosity η_{500} smoothly increases with the volume fraction of either CB or CMC [Fig.4.15(g-h)]. This observation is consistent with an increase in the interactions between the CB, the CMC, and the solvent. We shall not discuss further this value as the shear rate is chosen arbitrarily, hence the η_{500} dependence on the composition mixes the changes of the viscosity scale and the shear rate scale. Note that no high shear rate plateau viscosity was ever observed in any of the samples probed at shear rates up to 500 s^{-1}.

In the colloid-dominated regime, $n \simeq 0.5$ and neither depends on the CB fraction nor the CMC concentration to a good approximation [Fig. 4.17(a-b)]. This value of n is in agreement with the values obtained with gels using the same CB XC72R at similar mass fractions dispersed in oil [117]. Besides it corresponds to the lowest value found in the polymer regime, which supports the idea this exponent comes from the CB in the latter regime. The dependence of η_{500} on the composition is plotted in Fig. 4.17(c-d). This high-shear viscosity at fixed CMC concentration increases with the CB content as expected for a colloidal suspension [307]. However, η_{500} surprisingly decreases with

[10] For $\dot{\gamma} \ll \dot{\gamma}_c$ the viscosity $\eta = \sigma/\dot{\gamma} \sim \dot{\gamma}^{n-1}$, which decreases faster for lower values of n.

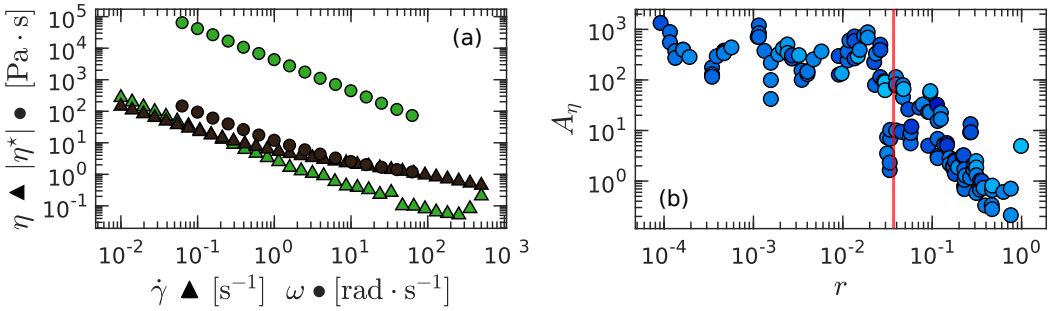

Figure 4.18: Check of the Cox-Merz criterion. (a) $\eta = \sigma/\dot{\gamma}$ extracted from a flow curve as a function of $\dot{\gamma}$ (represented as triangles) and the complex viscosity $|\eta^\star| = |G^\star|/\omega$ extracted from a frequency sweep as a function of ω (represented as circles). (b) Normalized area A_η between the two curves as a function of the CMC-to-CB ratio r. The area is computed over the full range of ω. The vertical red line indicates the value of r_c.

increasing polymer concentration at fixed CB content [Fig. 4.17(d)]; it can be seen as a signature of the depercolation transition. In the colloid-dominated regime, adding polymer to the CB-CMC suspension results in better coating the surface of the CB particles, which screens the inter-particle interactions. This is consistent with the decrease of the linear elastic modulus for increasing CMC concentration [Fig. 3.6(a)]. It suggests that the properties of the colloidal gel under continuous shear are dominated by the CB interactions; this conclusion should hold as well for oscillatory rheology.

In fact, continuous shear and linear oscillatory rheology are, in some cases, directly comparable. This is the meaning of the so-called "Cox-Merz rule" [237], introduced in the previous Section 2.D.7.a. The rule compares the viscosity measured in continuous shear $\eta(\dot{\gamma})$ to the complex viscosity $|\eta^\star(\omega)|$ measured under oscillatory shear, and claims that the measurements are equivalent as long as the same timescale is probed:

$$|\eta^\star(\omega = \dot{\gamma})| = \eta(\dot{\gamma}) \tag{4.2}$$

We observe that the Cox-Merz rule fails for samples in the colloid-dominated regime but holds quite nicely in the polymer-dominated regime [Fig. 4.18(a)]. We quantify the validity of the Cox-Merz rule by the value A_η (see definition in Section 2.D.7.a), which represents the normalized area between the two viscosity curves. The better the validity of the Cox-Merz rule, the smaller A_η. Indeed, this rather area is large for CB-CMC hydrogels in the colloid-dominated regime and significantly smaller for CB-CMC hydrogels in the polymer-dominated regime.

More generally, this rule has been validated in the case of polymer solutions and polymer melts [308], and verified experimentally for a large variety of systems [309–311]. In practice, this rule often fails for complex fluids that exhibit deformation-dependent microstructure (e.g., for associating polymers, suspensions, or hydrogen-bonding polysaccharides). When the rule fails, usually $|\eta^\star| > \eta$ as the shear may break this underlying microstructure [312]. For CB-CMC hydrogels in the colloid-dominated regime, the colloidal network is broken under shear and $|\eta^\star| \gg \eta$. However, for hydrogels in the polymer-dominated regime, the structure is dominated by the entanglement of the CMC such that the Cox-Merz rule holds. The discrepancy at low frequencies between $|\eta^\star|$ and η in the polymer-dominated regime may arise from the CB clusters, whose contribution is relatively large with respect to the polymer at low frequencies, as discussed in the previous chapter. Finally, we observe that the larger the CMC-to-CB ratio, the better the agreement of the Cox-Merz rule as depicted

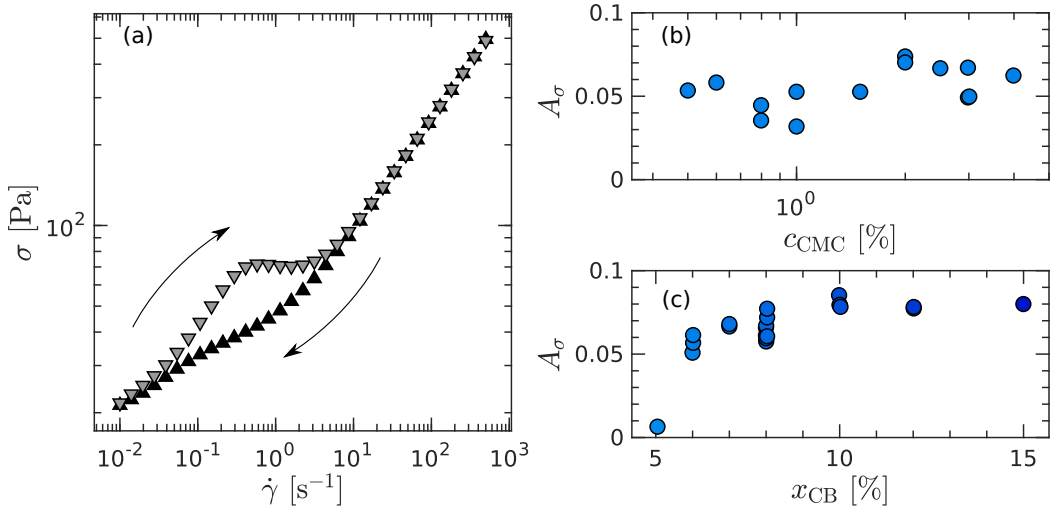

Figure 4.19: Hysteresis between the ramp up and ramp down during a flow curve. (a) Stress σ versus the shear rate $\dot{\gamma}$ for a CB-CMC hydrogel from the polymer-dominated regime ($c_{\mathrm{CMC}} = 2\%$ & $x_{\mathrm{CB}} = 10\%$). The shear rate is applied stepwise for 10 s with 7 points per decade from $\dot{\gamma} = 500$ to 0.01 s^{-1} during the ramp down (black upwards triangles) immediately followed by a ramp up from $\dot{\gamma} = 0.01$ to 500 s^{-1} with the same parameters (gray downwards triangles). (b) Normalized area A_σ between the two curves as a function of the CMC-to-CB ratio at fixed $x_{\mathrm{CB}} = 6\%$ as a function of c_{CMC} (b) or at fixed $c_{\mathrm{CMC}} = 2\%$ as a function of x_{CB} (c).

by the decrease of A_η with r [Fig. 4.18(b)]. This supports the idea that the CMC drives the mechanical response in the polymer regime and that the departure from the Cox-Merz rule in this regime must be attributed to the CB. Future work should consider the Rutgers Delaware rule, which appears as a promising outlook [313, 314] to compare further the colloid-dominated and polymer-dominated regimes. It corresponds to an extension of the Cox-Merz rule in the non-linear regime and accounts for the strain amplitude γ_0 in the complex viscosity $|\eta^\star(\omega = \dot{\gamma}/\gamma_0)| = \eta(\dot{\gamma})$.

So far, we have only considered flow curves measured by decreasing values of $\dot{\gamma}$ as it probes the stress in a way that is as close as possible to a stationary state. The results may be different when sweeping the shear rate by increasing values as shown in Fig. 4.19(a). Typically during the ramp up transient phenomena may reflect in the stress response, such as of the stress overshoot between each $\dot{\gamma}$ step or inhomogeneous flow such as shear banding arising from a partially fluidized sample [120]. For CB-CMC hydrogels from the polymer-dominated regime, we observe this kind of behavior with a stress measured in the ramp up always larger than the one measured in the ramp down. Similarly to what was done with the Cox-Merz rule (see Section 2.D.7.a) we quantify the hysteresis by the normalized area between these two curves A_σ. Flow curves were conducted at fixed sweeping rate and we shall here only consider the influence of the composition of the CB-CMC hydrogel. At fixed CB content, the hysteresis is roughly independent of the CMC concentration [Fig. 4.19(b)]. Furthermore, at fixed polymer concentration, increasing the CB content leads to an increase in the size of the hysteresis. One can imagine that an increasing amount of carbon black particles leads to a broader relaxation spectrum, hence increasing the hysteresis area, at fixed scanning rate.

We shall now investigate the evolution of the microstructure of CB-CMC hydrogels along the rheological hysteresis, by means of rheo-SAXS experiments. For hydrogels

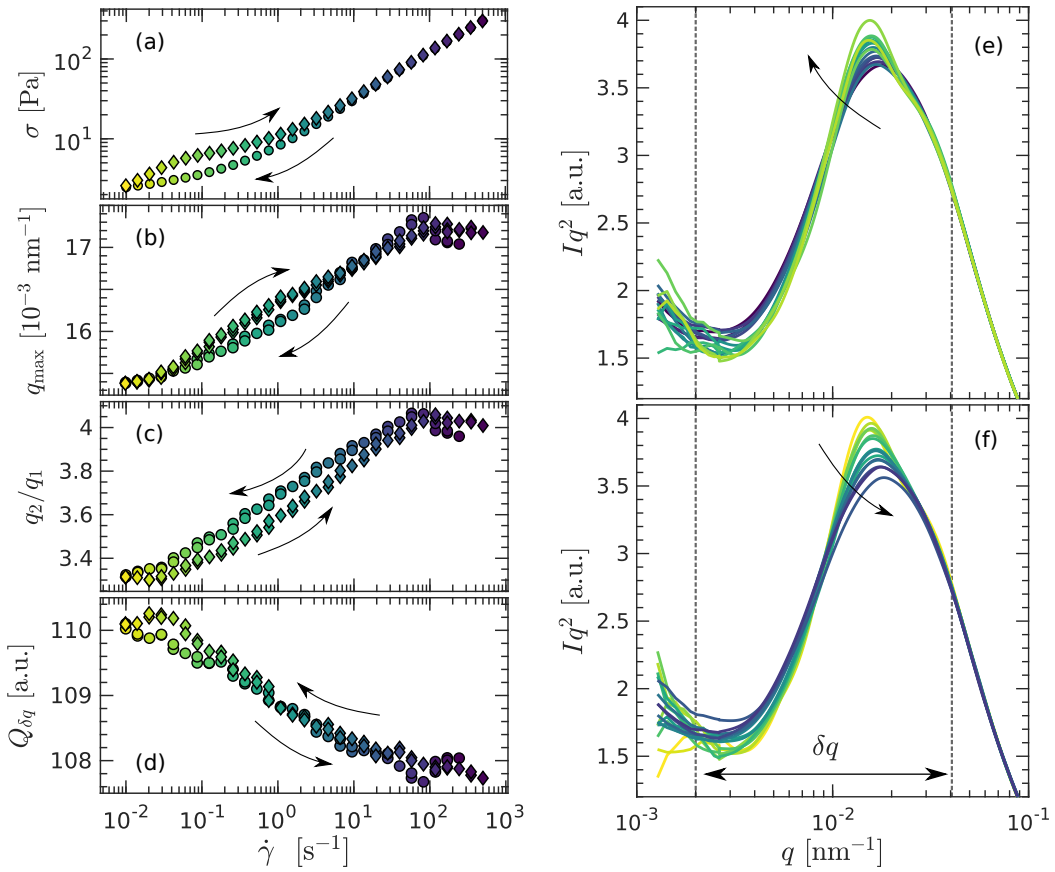

Figure 4.20: Rheo-SAXS analysis of a flow curve for a CB-CMC hydrogel in the polymer regime at $c_{CMC} = 2\%$ & $x_{CB} = 8\%$. The shear rate is applied stepwise for 10 s with 7 points per decade from $\dot{\gamma} = 500$ to 0.01 s^{-1} during the ramp down (circles) and then from $\dot{\gamma} = 0.01$ to 500 s^{-1} during the ramp up (diamonds) as indicated by the black arrows. (a) Stress σ. (b) Position of the maximum q_{max} in the Kratky plot Iq^2 vs q of the scattering intensity I and (c) broadness of the peak q_2/q_1, with q_1 and q_2 the positions of the inflexion points in the Kratky plot around q_{max}. (d) Area below the Iq^2 plot for q between the dashed lines represented in (e) and (f). The right columns shows the Kratky plots Iq^2 vs q during the ramp down of the flow curve (e) and the during the following ramp up of the flow curve (f). Lighter colors correspond to larger values of $\dot{\gamma}$.

from the polymer-dominated regime, the shape of the scattering intensity evolves continuously as the shear rate changes, as represented in Fig. 4.20. Following a decreasing ramp of shear rate, the shear rate is increased back to its orignal value. In both ramp down and up, for larger values of $\dot{\gamma}$ the position of the maximum q_{max} in the Kratky representation Iq^2 vs. q increases and the peak widens as illustrated by the increase of q_2/q_1 [Fig. 4.20(b)]. Finally, $Q_{\delta q}$ as defined in the previous section, decreases with $\dot{\gamma}$, suggesting a growth of the intensity in the low q range below 8.10^{-3} nm^{-1} when the sample is sheared [Fig. 4.20(d)]. These observations point toward a shear-induced densification of the CB clusters, similar to the results presented in LAOS. There are, however, big differences in the absolute values of q_{max} between the two types experiments. Namely, in continuous shear, q_{max} does not overcome 17.10^{-3} nm^{-1} whereas, in LAOS, it saturates around 22.10^{-3} nm^{-1}, to be compared with the typical size for a single CB particle (around 500 nm, which roughly translates to $q \simeq 0.01$ nm^{-1}). To compare both results, we shall consider the shear rate amplitude $\omega\gamma_0$ in LAOS, which

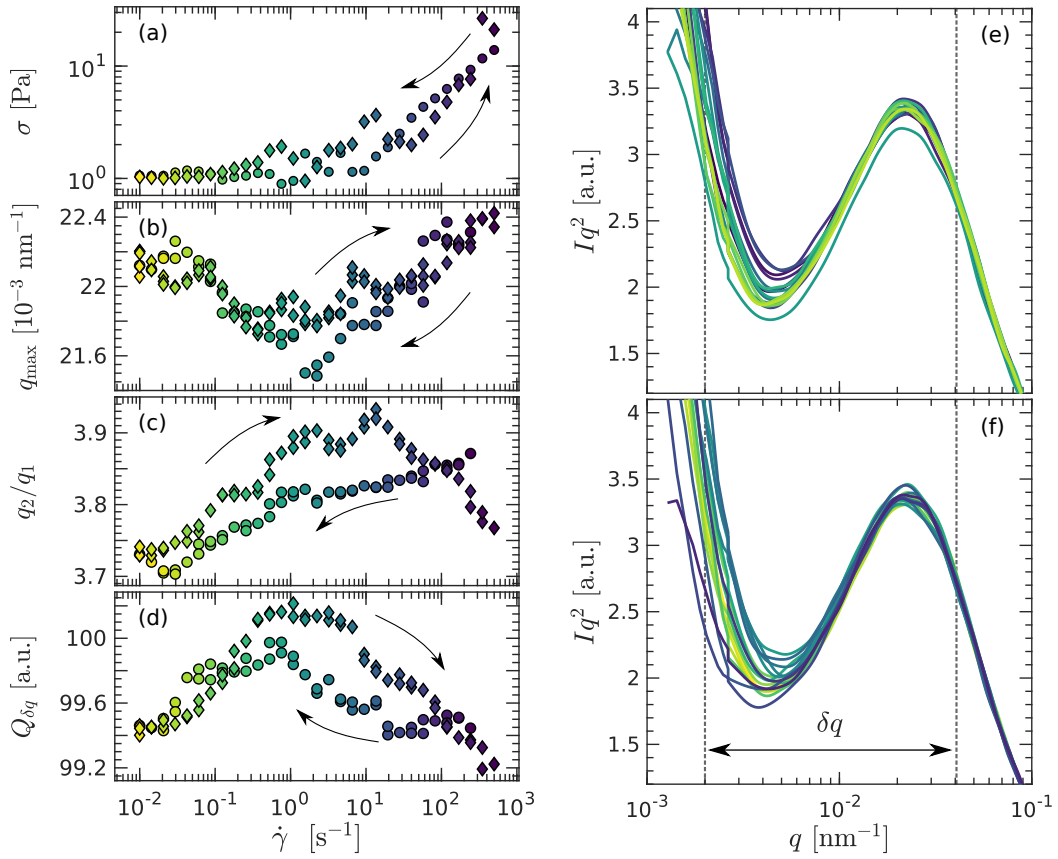

Figure 4.21: Rheo-SAXS analysis of a flow curve for a CB-CMC hydrogel from the colloid-dominated regime ($c_{CMC} = 0.01\%$ & $x_{CB} = 6\%$). The shear rate is applied stepwise for 10 s with 7 points per decade from $\dot{\gamma} = 500$ to 0.01 s^{-1} during the ramp down (circles) and then from $\dot{\gamma} = 0.01$ to 500 s^{-1} during the ramp up (diamonds) as indicated by the black arrows. (a) Stress σ. (b) Position of the maximum q_{max} in the Kratky plot Iq^2 vs q of the scattering intensity I and (c) broadness of the peak q_2/q_1, with q_1 and q_2 the positions of the inflection points in the Kratky plot around q_{max}. (d) The area below the Iq^2 plot computed for the range of q comprised between the dashed lines represented in (e) and (f). The right column shows the Kratky plots Iq^2 vs q during the ramp down of the flow curve (e) and the during the following ramp up of the flow curve (f). Lighter colors correspond to higher values of $\dot{\gamma}$.

maximum value is about 200 s^{-1} (with $\gamma_0 = 3.10^3\%$ oscillating at $\omega = 2\pi$ rad.s^{-1}). This value is comparable to the maximum shear rate $\dot{\gamma} = 500$ s^{-1} reached during the flow curve. The dependence of q_{max} with the shear rate is also stronger in LAOS than in continuous shear[11]. Finally, the low-q region of the scattered intensity changes a lot in LAOS but almost not in continuous shear [compare Fig. 4.21(e-f) and Fig. 4.14(e-f)]. This is consistent with the rather small variation of $Q_{\delta q}$ within the experiment and suggests that the main changes of the microstructure in both LAOS and continuous shear occur for q values between within δq, around 10^{-3} and 3.10^{-2} nm^{-1}. Together with the fact the evolution of $Q_{\delta q}$ is smaller for continuous shear than LAOS. All of these features lead to the conclusion that LAOS is much more efficient than continuous shear to organize the CB at the cluster scale.

For CB-CMC hydrogels from the colloid-dominated regime, there is little impact

[11] In practice, at constant ω, computing the shear rate amplitude out thje strain amplitude corresponds to a horizontal shift in Fig. 4.13(b), so that the slopes in LAOS and continuous shear can be compared directly in lin-log plots.

on the scattering intensity of the continuous shear similarly to the observations in LAOS. Fluctuations of the intensity are, however, much stronger in the LAOS case, especially in the low q region in Fig. 4.20(e-f). It is consistent with the scattered data seen in rheology with lots of fluctuations in the flow curves as well.

Further investigation in both the polymer-dominated and colloid-dominated regimes would be very interesting in order to enrich the comparison between flow and LAOS, namely the correspondence between the HB values with their counterparts in LAOS and whether it correlates to the observations made in SAXS. In this direction, we characterized the linear viscoelastic properties of CB-CMC hydrogels when submitted to a flow thanks to orthogonal superposition rheology.

B.2 Linear viscoelasticity under flow: orthogonal superposition rheometry

The goal here is to understand the evolution of $G^\star$ as the sample is submitted to shear, namely how different the viscoelastic spectra measured under flow is from the one at rest and how it depends on the shear rate. To do so we used orthogonal superposition (OSP) rheometry, which is described in Section 2.D.4. This method consists in applying a continuous shear at given $\dot{\gamma}$ –as for a regular flow curve– and measure in the meantime the viscoelastic spectrum $G^\star_\perp$ along the direction orthogonal to the flow. We refer to the direction of the flow as the parallel direction. The perpendicular modulus $G^\star_\perp$ is the fingerprint of the system *in the orthogonal direction* and corresponds in

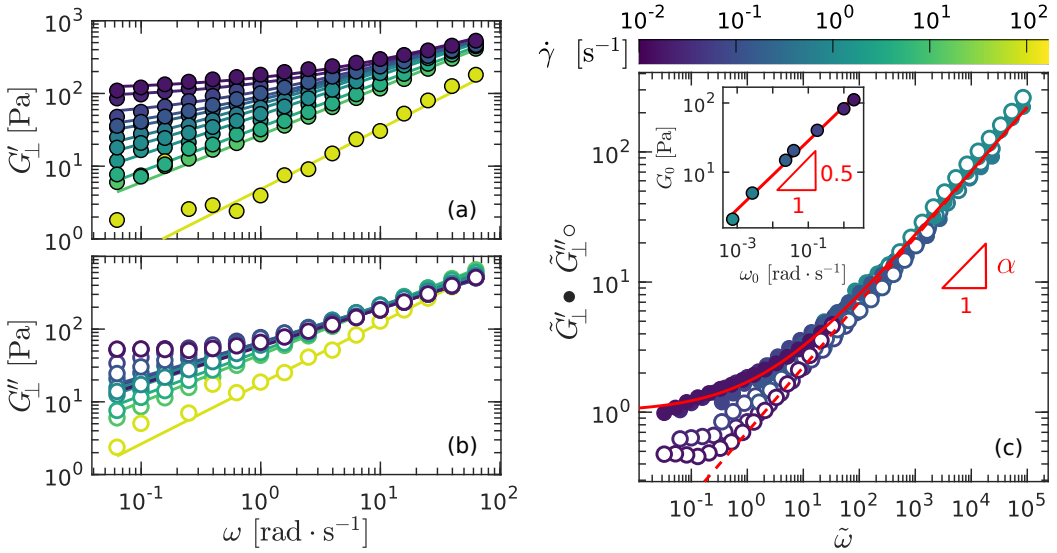

Figure 4.22: Linear viscoelastic spectra under flow of a CB-CMC hydrogel in the polymer regime at $c_{CMC} = 2\%$ & $x_{CB} = 10\%$. The perpendicular elastic modulus $G'_\perp$ (a) and the perpendicular viscous modulus $G''_\perp$ (b) are fitted by an FKVM represented by the solid lines. Lighter colors correspond to large values of the applied shear rate $\dot{\gamma}$ as represented by the colorbar. (c) Master curve of the viscoelastic spectra for different $\dot{\gamma} < \dot{\gamma}^\star = 1\,s^{-1}$ after rescaling by the modulus scale G_0 and frequency scale ω_0 extracted from the FKVM fits, which results are plotted in Fig. 4.23. The red curves correspond to the normalized FKVM with $\alpha = 0.5$ the average value for the spectra in the master curve. The modulus and frequency scales are plotted against one another as an inset, where the red line shows the best power-law fit yielding an exponent of 0.5.

the case of isotropic systems to the regular $G^\star$ discussed so far–*in the parallel direction*[12].

We seek to investigate the dependence of $G^\star_\perp$ on the applied flow. As the flow curves of the CB-CMC gels from the colloid-dominated regime are too irregular, we only focus here on samples from the polymer-dominated regime. The perpendicular modulus $G^\star_\perp$ is plotted in Fig. 4.22 for different shear rates in the parallel direction from $\dot\gamma = 0.01$ to $100\ \mathrm{s}^{-1}$. At high frequencies, all spectra are similar, especially for the viscous modulus $G''_\perp$. At low frequencies, there is a continuous evolution of $G'_\perp$ and $G''_\perp$ towards lower values as $\dot\gamma$ increases. It is consistent with the point of view developed previously in this manuscript or in the literature [56]. The lower frequencies correspond to the polymer network cross-linked by CB clusters, which breaks under shear, whereas the higher frequencies correspond to the solvent behavior mainly dominated by the polymer interactions less influenced by the shear.

The perpendicular modulus $G^\star_\perp$ is remarkably well fitted by a Fractional Kelvin-Voigt Model (FKVM), similarly to the parallel modulus at rest (see Fig. 3.8 in Chapter 3). This means the microstructure does not dramatically change upon shear, at least for shear rates below a critical shear rate $\dot\gamma^\star \simeq 1\ \mathrm{s}^{-1}$. Indeed, for higher values of $\dot\gamma$, the spring element G_0 vanishes, and the FKVM turns into a single springpot element,

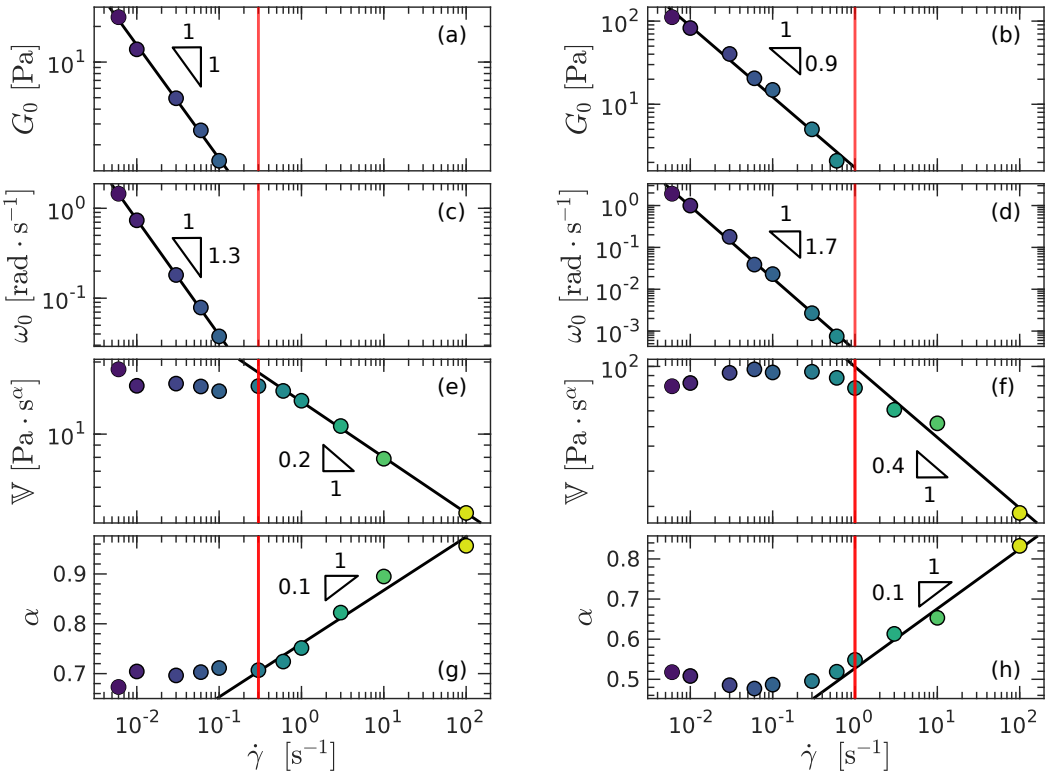

Figure 4.23: Impact of the flow on the FKVM parameters of CB-CMC hydrogels from the polymer-dominated regime at $c_{CMC} = 2\%$ & $x_{CB} = 8\%$ (left column) or $c_{CMC} = 2\%$ & $x_{CB} = 10\%$ (right column). The red lines correspond to $\dot\gamma^\star = 0.3\ \mathrm{s}^{-1}$ for $x_{CB} = 8\%$ and $\dot\gamma^\star = 1\ \mathrm{s}^{-1}$ for $x_{CB} = 10\%$. (a-b) Modulus scale G_0, (c-d) frequency scale ω_0, (e-f) quasi-property of the springpot $\mathbb{V}$ and (g-h) exponent α. The black lines correspond to the best power-law fits of the data either below or above $\dot\gamma^\star$, which exponent are indicated onto the plots.

[12] It has been shown that preshear may induce some anisotropy [315], such that $G^\star$ should rigorously be noted $G^\star_{||}$ to emphasize the potential anisotropy included in the measurement.

with no modulus nor frequency scale. For $\dot{\gamma} < \dot{\gamma}^\star$, these scales are defined, and the spectra plotted onto a master curve probing six orders of magnitude in rescaled frequency [Fig. 4.22(c)]. The typical modulus scales as $G_0 \sim \omega_0^{0.5}$ in stark contrast with the results found at rest for different compositions where $G_0 \sim \omega_0$ [Figs. 3.7 and 3.8], which could be attributed to a change of the network connectivity under shear.

Such time-shear rate superposition principle has already been observed for CB and fumed silica dispersions in organic solvents [201]. However, in this seminal study, solely the frequency was rescaled and the shift factor corresponds to the viscosity of the sample. The authors concluded that viscosity sets the timescales at stake in their colloidal gels. Here, the viscoelastic spectra are shifted horizontally *and* vertically. It should, however, be noted that the two shifts correspond actually to the single evolution of G_0 in the FKVM as represented in Fig. 4.23. We see that for $\dot{\gamma} < \dot{\gamma}^\star$ the springpot characteristics $\mathbb{V}$ and α remain constant, hence the frequency scale $\omega = (G_0/\mathbb{V})^{1/\alpha}$ depends only on G_0[13]. The rescaling depicted here has therefore a profoundly different meaning from the one described in the colloidal gels [201]. It may rather point out an evolution of the cross-linking within the polymer network upon shear. Under continuous shear, the CB clusters are less efficient to promote the elastic network as they may stick and unstick dynamically to the polymers. This effect is enhanced with the shear, hence the decrease of G_0 with $\dot{\gamma}$.

The same features are observed for two different compositions in the polymer regime at $c_{CMC} = 2\%$ & $x_{CB} = 8$ or 10% [Fig. 4.23], with similar dependence of the FVKM parameters with $\dot{\gamma}$ below $\dot{\gamma}^\star$. Above $\dot{\gamma}^\star$ the elastic element goes to zero, $\mathbb{V}$ decreases and α increases when $\dot{\gamma}$ increases. This indicates the sample fluidization at larger $\dot{\gamma}$. The exponent α increases towards 1 meaning the springpot turns into a regular dashpot, which could be attributed to a screening of the interactions by the hydrodynamic forces due to the flow.

The main difference between the two CB contents is the value of $\dot{\gamma}^\star$, which is significantly smaller for the lowest content (around 0.3 vs 1 s^{-1}). It remains unclear how this $\dot{\gamma}^\star$ should be interpreted. It could be seen either as a typical timescale for the formation of the clusters or as an energy scale induced by the flow. Further experiments with an extended range of compositions will be insightful in finding the relevant dimensionless parameter describing this transition.

We observed that the continuous shear impacts the properties of the gels in the polymer regime. We shall now investigate the mechanical response when the flow is stopped.

B.3 Recovery after flow cessation

In general, the mechanical properties of a complex fluid is impacted by the shear history it has undergone [316–319]. This is known as a memory effect, which means that the sample somewhat "remembers" the shear experienced prior to flow cessation, and the state at rest may depend on it. We study this effect in the case of CB-CMC hydrogels with a flow cessation protocol: starting from a steady sate under shear at $\dot{\gamma}_{SS}$ associated with a steady-state stress σ_{SS}, the shear geometry is then set to $\dot{\gamma} = 0$ at $t = 0$ and we record the stress relaxation as a function of time (see Section 2.D.7.b). For a viscoelastic liquid, the stress relaxes to zero. However, in gels and soft glasses flow cessation may lead a stress relaxing to a finite value called the *residual stress* σ_{res} [317, 320–322].

[13] From this one recovers the scaling $G_0 \sim \omega_0^{0.5}$ in Fig. 4.22 as $\alpha \simeq 0.5$ for this sample.

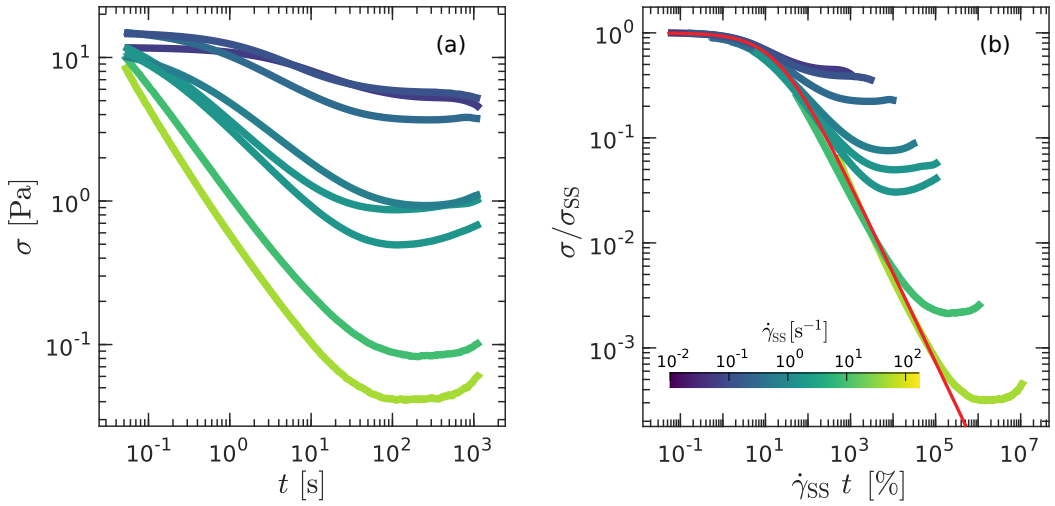

Figure 4.24: Stress relaxation during flow cessation of a CB-CMC hydrogel from the polymer-dominated regime ($c_{CMC} = 2\%$ & $x_{CB} = 8\%$). Lighter colors correspond to larger values of steady-state shear-rate $\dot{\gamma}_{SS}$ prior to flow cessation. (a) Stress σ as a function of time t for different values of $\dot{\gamma}_{ss}$. (b) Normalized stress σ/σ_{SS} vs strain $\dot{\gamma}_{SS}t$. The red curve corresponds to the fit of the envelop of the relaxation, i.e., far from the residual stress plateau according to the Eq. (4.3), with $\gamma_c = 20 \pm 5\%$ and $p = 0.8 \pm 0.1$.

The stress relaxation for a CB-CMC hydrogel from the polymer-dominated regime is presented in Fig. 4.24. Larger values of $\dot{\gamma}_{SS}$ lead to lower residual stresses, consistent with the acknowledged scenario in the literature [323]. Lower shear rates form larger structures, which are less likely to reorganize hence the lower stress relaxation. The CB clusters might play the role of the said structures in the CB-CMC hydrogels.

Remarkably, the stress relaxations collapse onto the same master curve for all values of $\dot{\gamma}_{SS}$ when the stress is normalized by σ_{SS}, i.e., its value at $t = 0$, and the horizontal axis is expressed in term of effective[14] strain $\dot{\gamma}_{SS}t$. This master curve plotted Fig. 4.24(b) can be modeled far from the residual stress by the following phenomenological expression:

$$\frac{\sigma}{\sigma_{SS}} = \frac{1}{1 + (\dot{\gamma}_{SS}t/\gamma_c)^p} \tag{4.3}$$

where γ_c is a critical strain depicting the departure from the plateau value of σ at small t and p an exponent corresponding to the exponent of the power-law decay at large t in the transient regime. It means that the early stage of the relaxation is driven by the inherited motion of the particles from the steady shear, which speed is set by $\dot{\gamma}_{SS}$ [321, 322].

Two different scalings have been proposed for σ_{res} vs. $\dot{\gamma}_{SS}$ to build rescaled master curves. A first scenario suggests that the residual stress is driven by the hydrodynamic forces, such that σ_{res} should scale as the ratio between hydrodynamic stress and the yield stress through $\eta_{bg}\dot{\gamma}_{SS}/\sigma_y$ with η_{bg} the viscosity of the background solvent [322]. A second scenario proposes that the residual stress is driven by the excess stress above the yield stress, such σ_{res} is expected to scale as[15] $(\dot{\gamma}_{SS}/\dot{\gamma}_c)^n$ with n the Herschel-Bulkley exponent of the system and $\dot{\gamma}_c$ its critical shear rate [321]. With the present system, one observes a scaling $\sigma_{res} \sim \dot{\gamma}_{SS}^{0.5}$ [see Fig. 4.25], which seems to be

[14] It corresponds to the strain the sample would have undergone if the shear rate was not stopped.
[15] In the Herschel-Bulkley model $\dot{\gamma}^n = \dot{\gamma}_c^n(\sigma - \sigma_y)/\sigma_y$.

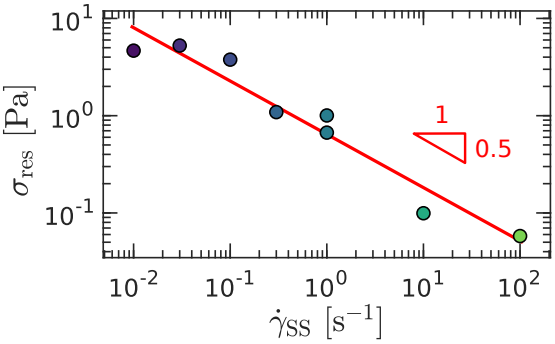

Figure 4.25: Residual stress after flow cessation vs. $\dot{\gamma}_{SS}$ for a CB-CMC hydrogel from the polymer-dominated regime at $c_{CMC} = 2\%$ & $x_{CB} = 8\%$. The red lines correspond to the best power-law fit of the data, yielding to exponent of 0.5 ± 0.1.

more consistent with the latter description since $n \simeq 0.5$ for this system. Further experiments including different samples with different Herschel-Bulkley parameters would be required to confirm this observation.

We now look for the signature of the residual stress into the viscoelastic spectra after the flow cessation. $G^\star$ is measured at the end of the protocol, that is 1200 s after the zero shear rate is applied. Regardless of $\dot{\gamma}_{SS}$ all of the spectra are described by a FKVM whose parameters are correlated to the residual stress as shown in Fig. 4.26(b-d). Namely the modulus scale G_0 grows as $\sigma_{res}^{0.3}$, which strongly contrasts with the linear scaling[16] observed in colloidal gels over a similar range of modulus and residual stress [317]. The smaller exponent reflects a weaker impact of the residual stress onto the final modulus scale in the present CB-CMC hydrogels. The experiment has been conducted for a similar gel with a larger CB content ($c_{CMC} = 2\%$ & $x_{CB} = 10\%$), yielding to an even smaller exponent between 0.1 and 0.2 In such polymer cross-linked gel, the residual stress has less impact onto the elasticity scale G_0 for larger CB contents, it suggests a very complex link between the microstructure frustration and the final elasticity.

Still, the modulus shift factor G_0 and the frequency shift factor ω_0 exhibit a scaling close to a linear relationship. This is highly reminiscent of what was observed with the time-concentration time-age superposition principles reported in the previous Chapter 3, resp. in Fig. 3.7 and Fig. 3.19. It suggests that the overall same mechanism dictates the mechanical behavior of this CB-CMC hydrogel in the polymer-dominated regime, that we assume to be linked to the connectivity of the network. In this framework, it is equivalent to increase the CB content, to let the system age than to induce a larger residual stress in the structure: the connectivity in the network is enhanced.

C Conclusion

The properties of the CB-CMC hydrogels beyond the linear viscoelasticity have been studied in detail in this chapter. The results obtained are perfectly consistent with the previous observations performed in the linear viscoelastic regime, namely the existence of a colloid-dominated and a polymer-dominated regime. This nonlinear analysis has further enhanced our understanding of the microstructure in each regime.

[16] Note the scaling proposed in [317] includes a constant term.

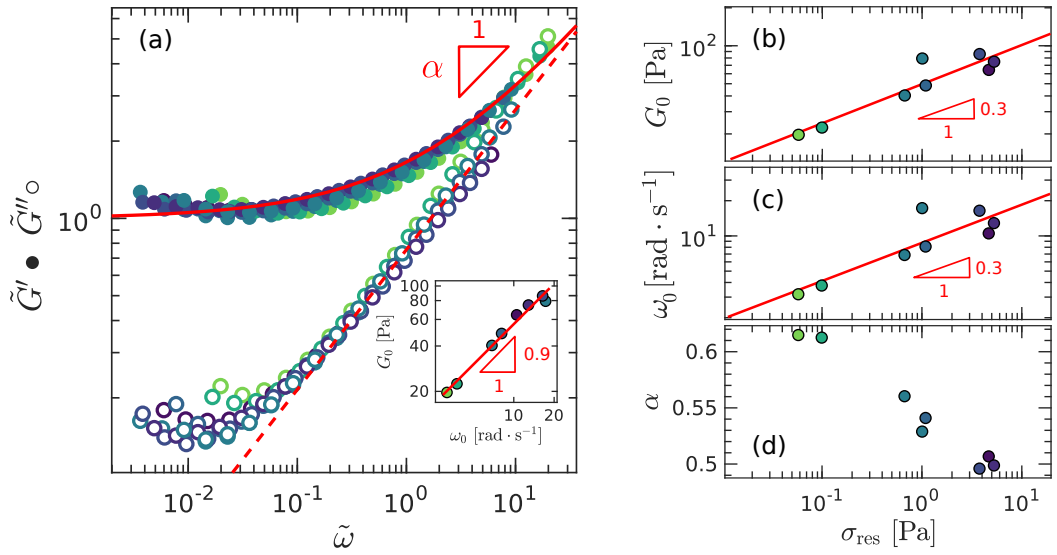

Figure 4.26: Viscoelastic spectra after flow cessation: dependence on the shear rate $\dot{\gamma}_{SS}$ for a CB-CMC hydrogel from the polymer-dominated regime at $c_{CMC} = 2\%$ & $x_{CB} = 8\%$. (a) Rescaled elastic and viscous moduli $\tilde{G}'$ and $\tilde{G}''$ as a function of the reduced frequency $\tilde{\omega}$ as detailed in Section 3.B.1. The red curves correspond to the normalized FKVM with $\alpha = 0.55$. The inset shows the scaling $G_0 \sim \omega_0^{0.9}$. The FKVM parameters G_0 (a), ω_0 (c) and α (d) are plotted as a function of the residual stress σ_{res}. The red lines correspond to the best power-law fit of the data, with a slope 0.3 ± 0.1 for both G_0 and ω_0.

In the colloid-dominated regime, we observed strong similarities under LAOS and continuous shear with glassy-like systems. Moreover, the evolution of the electrical properties is non trivial and implies subtle reorganization at the contact scale between CB particles. Adhesion to the interfaces is a huge problem to tackle for this system and it requires further investigation, namely regarding its impact onto the electrochemical properties for the application of flow batteries.

In the polymer-dominated regime, the non-linear behavior is extremely rich. The response to LAOStrain shows a double yielding transition, which suggests the presence of multiple lengthscales in the microstructure. The polymer-dominated regime is therefore more heterogeneous than the colloid-dominated regime. Moreover, this two-step yielding process have been observed in other polymer-nanoparticles systems and building a general framework seems to be a complex problem as the characteristics depend a lot on the type of interaction at stake. Systems with polymer networks cross-linked by nanoparticles [324–326] and depleted colloidal system [299] both show this remarkable feature, but the interpretation is very different. The question of the impact of the hydrophobic interaction remains open.

Finally, we saw in both regimes that a dynamical microstructure might be induced by the shear. This highly motivates the study of memory effects and potential resulting anistropy in both types of hydrogels studied here.

CHAPTER

5

ACID-INDUCED GELS OF CARBOXYMETHYLCELLULOSE SOLUTIONS

In the previous chapters we focused on CB-CMC hydrogels. In the present chapter we aim at understanding what physical properties should be attributed to the CMC alone. In this scope, we study CMC solutions that form gels upon acidification. In the first section, we focus on this transition through many different approaches, namely rheometry, neutron scattering, and NMR relaxometry. Motivated by these results, we propose a microscopic model for the sol-gel transition based on hydrophobic inter-chain association that accounts for the sol-gel boundary over the entire range of CMC content under study. The second section aims at better understanding the rheological properties of such acidified CMC solutions, namely the impact of the temperature and the behavior of CMC gels under LAOStrain.

A Acid-induced phase transition

The properties of the CMC can be tuned via the degree of substitution (DS), which corresponds to the average number of carboxymethyl groups per repeating glucose unit and varies between 0 and 3. Highly substituted polymers, i.e., for DS $\gtrsim$ 1, are hydrophilic and disperse easily in water, yielding rheological features typical of polyelectrolyte solutions[175–178]. In contrast, weakly substituted polymers, i.e., for DS $\lesssim$ 0.9, contain hydrophobic regions, which favor interchain aggregation and the formation of so-called "fringed micelles" in aqueous solution [180], yielding thixotropic and even gel-like properties at high enough concentrations [181–186]. In practice, the gelation of CMC solution can be induced by lowering the pH, which decreases the charge density along the CMC chain and promotes the formation of multichain aggregates [187]. At a low enough pH, CMC solutions thus behave as soft solids that experience a solid-to-liquid transition at large deformations [188, 189]. While much is known about the flow properties of highly substituted CMC aqueous solutions, the acid-induced gelation of less substituted CMC solutions, and the resulting gel properties remain poorly understood in terms of mechanical and structural properties.

Here, combining complementary techniques, we perform an in-depth characterization of the acid-induced sol-gel transition in aqueous solutions of weakly substituted CMC. Rheological measurements allow us to identify the gelation point and build a phase diagram over a broad range of pH and CMC content. Moreover, the scattered intensity measured by small-angle neutron scattering (SANS) shows an abrupt change at the sol-gel transition, suggesting the presence of a heterogeneous percolated network of disordered fibrils formed through a microphase separation. Building upon this scenario, we devise a simple model based on physical crosslinks at the locus of hydrophobic patches along the polymer chain, which yields an equation for the sol-gel boundary in excellent agreement with the phase diagram. Viscoelastic spectra measured in the gel phase at different pH exhibit similar features. Following a time-composition superposition principle, these spectra can be rescaled onto a remarkable master curve, which hints at a self-similar microstructure in which the CMC chains follow a Rouse-like dynamics. Finally, low-field NMR spectroscopy reveals that the sol-gel transition is associated with a decrease in the proton transverse relaxation time T_2, whose temperature dependence remains Arrhenius-like across the transition. Yet, the corresponding energy scale reveals a sharp drop by more than 60% at the transition, showing that the aqueous solvent is affected in the *bulk* by the sol-gel transition, echoing the excellent water retention capacity of CMC-based gels [327–329].

A.1 Rheological evidence of a sol-gel transition

a Phase diagram

Aqueous solutions of CMC for DS = 0.88 are prepared at ambient temperature, and their linear viscoelastic properties are measured by rheometry following the protocols described in Section 2.D.2. Figure 5.1(a) shows the linear viscoelastic spectrum in the form of the loss factor, i.e., $\tan\delta = G''/G'$ vs. ω, for a series of CMC solutions at $c_{CMC} = 3\%$ with different pH values ranging between pH= 0.6 and 6.7. For pH $\geq$ 3, the loss factor is a decreasing function of the frequency, with $\tan\delta > 1$ for vanishing frequencies, i.e., the sample response is mainly liquid-like. In contrast, for pH $<$ 3, the loss factor increases for increasing frequency, with $\tan\delta < 1$ at low frequencies, which is the hallmark of a solid-like response. These results highlight a

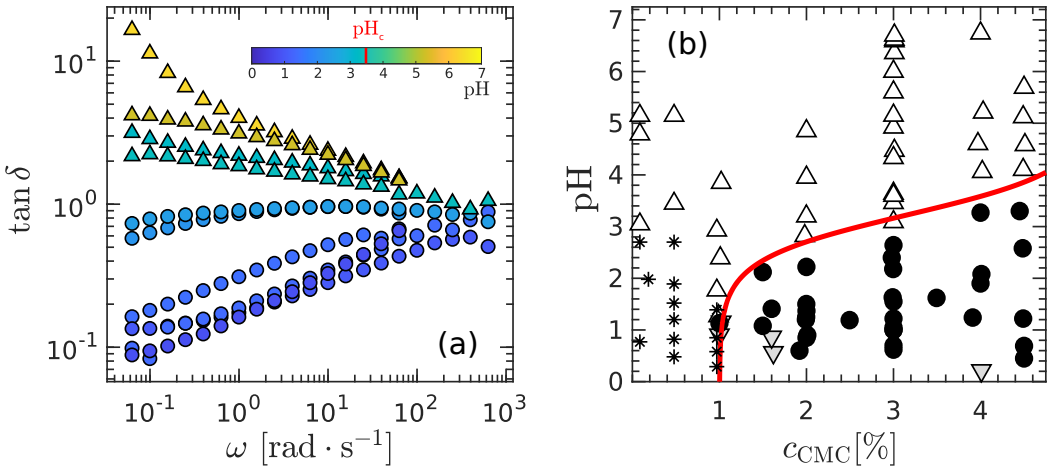

Figure 5.1: Phase diagram of the sol-gel transition for acidified CMC solutions. (a) Loss factor $\tan\delta = G''/G'$ vs. frequency ω for 3% CMC solutions at various pH ranging from 0.6 to 6.7 (see color bar). Triangles stand for viscoelastic liquid ($\tan\delta > 1$ at low frequencies), whereas circles correspond to gels ($\tan\delta < 1$ at low frequencies). (b) Phase diagram pH vs. CMC concentration comprising four phases: ($*$) phase-separated samples, ($\triangle$) viscoelastic liquids, ($\bullet$) gels, and ($\triangledown$) Newtonian solutions. The latter case corresponds to over-acidified CMC solutions in which the CMC is chemically degraded. The red curve separating the sol and gel phases corresponds to the model discussed described by Eq. (5.10) with $Y = 0.18$.

critical pH value, $pH_c \simeq 3$, at which the loss factor is independent of the frequency, hence demonstrating that the present CMC solution displays a sol-gel transition at pH_c [330]. Note that for vanishing pH (i.e., pH $\lesssim 1$), the CMC solutions behave as Newtonian liquids due to the chemical degradation of the polymer [331, 332]. This degraded CMC solutions are translucent, and their viscosity drops by several orders of magnitude compared to gels and non-degraded viscoelastic liquid-like samples, with a typical viscosity $\eta \simeq 1 - 10$ mPa.s for the degraded CMC solutions. We used this Newtonian behavior as a criterion to classify these samples as degraded. They display *irreversible aging*, i.e., their viscosity decreases with increasing sample age on a typical timescale of one or two days following their preparation. Therefore, we conclude that visual inspection, together with viscosity measurements, provide robust qualitative and quantitative criteria for identifying the degraded samples.

Repeating this analysis over a broad range of CMC concentrations allows us to build the phase diagram pH vs. CMC content reported in Fig. 5.1(b). The gel-like region is observed beyond a critical CMC content of about 1 %, and over a growing span of pH for increasing CMC concentration. For CMC solutions at $c_{CMC} < 1$ % and various values of pH we find that for pH $\gtrsim 3$, samples are homogeneous viscoelastic liquids. However, for pH $\lesssim 3$, solutions are not stable in time and CMC quickly sediments. We observe a watery supernatant and soft micrometric clumps at the bottom of the recipient [see Fig. 5.2(a)]. Note that, in contrast, samples in the gel phase are homogeneous, as illustrated, e.g., for $c_{CMC} = 1.5$ % in Figs. 5.2(b) and 5.2(c). We assume that the clumps observed for pH$\lesssim 3$ and $c_{CMC} < 1$ % are CMC aggregates, which do not form a gel because the polymer concentration is lower than the percolation threshold. Indeed, the value 1% is comparable to the concentration separating the semi-dilute unentangled regime from the semi-dilute entangled regime [178]. Therefore, our observation suggests that acid-induced gelation only occurs in entangled samples. These samples are displayed in Fig. 5.1 as ($*$) symbols.

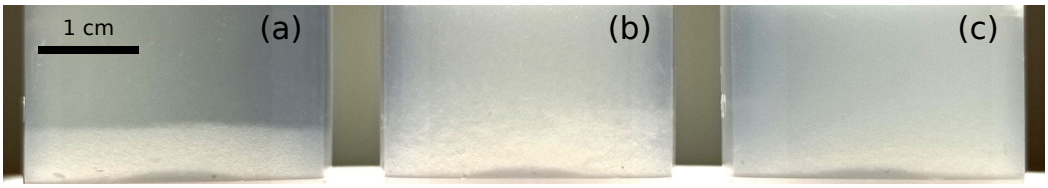

Figure 5.2: Illustration of the phase separation at low CMC concentration. Picture of samples at pH $= 2.0 \pm 0.1$ and (a): $c_{CMC} = 0.5\%$, (b): $c_{CMC} = 1\%$, and (c): $c_{CMC} = 1.5\%$. Sample (a) is inhomogeneous: CMC has sedimented in the form of clumps; in contrast, samples (b) and (c), which contain a sufficiently high CMC concentration, form a gel.

b Modeling the sol-gel frontier

The equation of the sol-gel phase boundary can be derived using a mean-field approach, in which gelation occurs beyond a critical density of active hydrophobic patches, which serve as cross-linkers. Assuming that the number of active hydrophobic patches increases with both the CMC content and the number of carboxymethyl group, we can derive an equation $pH_c(c_{CMC})$ that depends only on three parameters. The result shown as a red curve in Fig. 5.1(b) is in excellent agreement with the available data. We shall emphasize that the presence of clumps at small c_{CMC} strongly supports this model. Here, we explicit the assumptions of the model used to describe the sol-gel boundary of the phase diagram. This model constitutes a simple description of the sol-gel transition, based on experimental elements available, and on the following assumptions:

• **First assumption.** The sol-gel transition occurs when the total concentration of hydrophobic patches, i.e., the number $\mathcal{N}$ of patches per unit volume, exceeds a given threshold $\mathcal{N}_{crit}$. As the CMC solution is in the semi-dilute entangled regime, we assume that $\mathcal{N}_{crit}$, which corresponds to a given average functionality of the patches, neither depends on the CMC content nor on the pH. In other words, we neglect the changes in the interaction energies associated with a change in polymer or HCl concentrations. Moreover, we define f_{OFF} $(= 1 - f_{ON})$ as the probability for a hydrophobic patch to be disconnected from the elastically active network (e.g., patches connected within the same polymer or patches that are isolated). This fraction is dictated by the conformation of the polymer and, in particular, by its degree of coiling. Therefore, f_{OFF} should mainly depend on the pH, and presumably much less on the CMC concentration c_{CMC}. Finally, the hydrophobic crosslinks have a finite lifetime, i.e., on average, there is a fraction f_τ of patches that are effectively connected at a given time. In that framework, the sol-gel transition occurs when

$$f_{ON} f_\tau \mathcal{N} = \mathcal{N}_{crit}\,. \tag{5.1}$$

• **Second assumption.** For the sake of simplicity, we consider that the probability for a hydrophobic patch to be active is constant, i.e., $f_{ON} = cst$. This assumption is supported by the fact that (i) the weight fraction of CMC in the gels does not exceed 4%, so that the system remains in the semi-dilute regime, and (ii) we focus on the vicinity of the sol-gel transition so that the coiling of the polymer should be quite similar regardless of the CMC concentration or the pH. Furthermore, we consider that the

active hydrophobic patches are active most of the time, i.e., $f_\tau \simeq 1$. The typical values for f_{ON} and f_τ are actually not important, as they are considered constant, which is equivalent to consider an effective $\mathcal{N}_{\mathrm{crit}}^{\mathrm{eff}} = \mathcal{N}_{\mathrm{crit}}/(f_{\mathrm{ON}} f_\tau)$, and set $f_{\mathrm{ON}} = f_\tau = 1$ thereafter. For clarity, we shall still keep f_{ON} and f_τ explicitly below.

• **Third assumption.** We now express the concentration of hydrophobic patches n as a function of c_{CMC} and pH to compute the equation of the sol-gel boundary. We propose the following form, introducing c_{COOH} the concentration of substituted groups that are in their acidic form:

$$\mathcal{N} = A c_{\mathrm{CMC}} + B c_{\mathrm{COOH}}\,, \tag{5.2}$$

where A and B are positive prefactors. Both concentrations c_{CMC} and c_{COOH} are expressed in mol.L^{-1} (proportional to the number of entities per unit volume). The prefactor A corresponds to the number of patches introduced by the CMC itself without altering the pH of the solution; A depends mostly on the degree of substitution (DS) of the CMC, and on the molecular weight M_w of the CMC. In contrast, B denotes the additional number of hydrophobic patches when a COO^- group is protonated. Hence, B should depend not only on DS and M_w, but also on the patch density along the polymer chain, if many COOH groups are formed in a dense environment of patches, they might increase the length of already existing patches rather than creating a new one.

• **Fourth assumption.** We consider A and B to be constant, independent of c_{CMC} and pH. c_{COOH} is linked to the pH through the following two equations that capture respectively the atom conservation (when a mole of CMC is introduced, it introduces $\Psi = N \times \mathrm{DS}$ moles of COOH or COO^-, with N the number of monomers, proportional to M_w), and the acido-basic chemistry with an acidity constant K_A:

$$c_{\mathrm{COOH}} + c_{\mathrm{COO^-}} = \Psi\, c_{\mathrm{CMC}}\,, \tag{5.3}$$

$$K_A = \frac{10^{-\mathrm{pH}}\, c_{\mathrm{COO^-}}}{c_{\mathrm{COOH}}}\,. \tag{5.4}$$

Combined with Eq. (2), this leads to the following expressions of c_{COOH} and $\mathcal{N}$:

$$c_{\mathrm{COOH}} = \frac{\Psi\, c_{\mathrm{CMC}}}{1 + 10^{\mathrm{pH}-\mathrm{pK_A}}}\,, \tag{5.5}$$

$$\mathcal{N} = c_{\mathrm{CMC}} \left(A + \frac{B\Psi}{1 + 10^{\mathrm{pH}-\mathrm{pK_A}}} \right). \tag{5.6}$$

Combining Eqs. (5.1) and (5.6) then yields the equation for the sol-gel boundary:

$$\mathrm{pH_c} = \mathrm{pK_A} + \log_{10} \frac{(A + B\Psi) f_{\mathrm{ON}} f_\tau c_{\mathrm{CMC}} - \mathcal{N}_{\mathrm{crit}}}{\mathcal{N}_{\mathrm{crit}} - A f_{\mathrm{ON}} f_\tau c_{\mathrm{CMC}}}\,. \tag{5.7}$$

• **Fifth assumption.** $\mathcal{N}_{\mathrm{crit}}$ is related to the critical CMC concentration below which no gel can be obtained, irrespective of the pH. Here, we observe experimentally that $c_{\mathrm{crit}} \simeq 1\%$. In Eq. (5.5), the largest possible value of c_{COOH} is ξc_{CMC}, for which $\mathcal{N} \simeq c_{\mathrm{CMC}}\,(A + B\xi)$, so that an estimation of $\mathcal{N}_{\mathrm{crit}}$ can be expressed as follows:

$$\mathcal{N}_{\mathrm{crit}} \simeq f_{\mathrm{ON}} f_\tau\, (A + B\Psi)\, c_{\mathrm{crit}} \tag{5.8}$$

Based on this estimate, we can express the equation of the sol-gel boundary as follows:

$$\mathrm{pH_c} = \mathrm{pK_A} + \log \frac{c_{\mathrm{CMC}} - c_{\mathrm{crit}}}{c_{\mathrm{crit}} - \dfrac{A}{A + B\Psi}\, c_{\mathrm{CMC}}} \tag{5.9}$$

$$= \mathrm{pK_A} + \log \frac{c_{\mathrm{CMC}} - c_{\mathrm{crit}}}{c_{\mathrm{crit}} - \mathrm{Y} c_{\mathrm{CMC}}}\,. \tag{5.10}$$

with $\mathrm{Y} = A/(A + B\Psi) < 1$.

Finally, we use Eq. (5.10) to fit the boundary of the sol-gel phase diagram reported in Fig. 5.6. The best agreement with the experimental data is obtained for $\mathrm{Y} = 0.18$ and $\mathrm{pK_A} = 2.5$, consistently with $\mathrm{pK_A}$ values reported in Ref. [190].

• **Final remark.** Note that in Eq. (5.10) $\mathrm{pH_c}$ diverges when $c_{\mathrm{CMC}} = c_{\mathrm{crit}}/\mathrm{Y}$, which means that above this concentration, a gel will form regardless of the pH, which is indeed what is observed in the literature for similar DS and M_w of the CMC [189, 333].

A.2 Structural insights

a Small Angle Neutron Scattering

To further elucidate the self-assembly of CMC upon acidification, we use small-angle neutron scattering (SANS) and report the scattering intensity spectra $I(q)$ in Fig. 5.3. For viscoelastic liquids, i.e., at pH $>$ 3, the signal-to-noise ratio is low, and $I(q)$ decays roughly as q^{-2}. This high-q (Porod) regime is reminiscent of non-interacting Gaussian polymer chains in a solvent. For pH $<$ 3, i.e., upon gelation, the scattered intensity increases dramatically, showing that CMC gels scatter neutrons much more efficiently than their liquid counterparts. Moreover, two important observations can be made. First, the Porod regime at low pH switches to $I \sim q^{-2.8}$ indicating the presence of relatively dense objects together with a gradient of scattering length density at the interface with the background [334]. More precisely, the exponent -2.8 represents an intermediate case between Gaussian chains ($I \sim q^{-2}$), where the exponent is related to the volume fractal dimension of the chain, and smooth particles ($I \sim q^{-4}$), where the exponent is related to the surface fractal dimension D_s according to $I \sim q^{-(6-D_s)}$ (where $D_s = 2$ for smooth particles). This result is compatible with the presence of fringed micelles [180] that are characterized by a dense core formed by the aggregation of hydrophobic CMC strands surrounded by a sparse, hairy shell of polymer chains. Second, fitting the scattering intensity of gel samples with an empirical Guinier-Porod model [260] enables us to extract the inflection point of the scattering intensity, providing $q^* \simeq 8.4\ 10^{-3}\text{Å}^{-1}$ (see also inset in Fig. 5.3) corresponding to a length scale $d^* = 2\pi/q^* \simeq 75$ nm that we assign to the diameter of the fringed micelles section. At $q < q^*$, the scattering intensity scales as $I \sim q^{-1.5}$ suggesting that the micelles can be seen as flexible rod-like objects characterized by an aspect ratio larger than about 10, in good agreement with the schematic view proposed in Ref. [179] for CMC of low DS, spontaneously gelling in concentrated solutions. Here, the largest characteristic size of the fringed micelles is larger than 600 nm since no plateau is visible at the smallest accessible q values. Focusing on gel samples in the low q range, the scattering intensity increases slightly but monotonically with decreasing pH, which suggests that the mass of the fringed micelles, or the fractal dimension of the network they form, tend to grow progressively even well beyond the gel point. This result indicates that while most of the hydrophobic patches tend to aggregate at the sol-gel

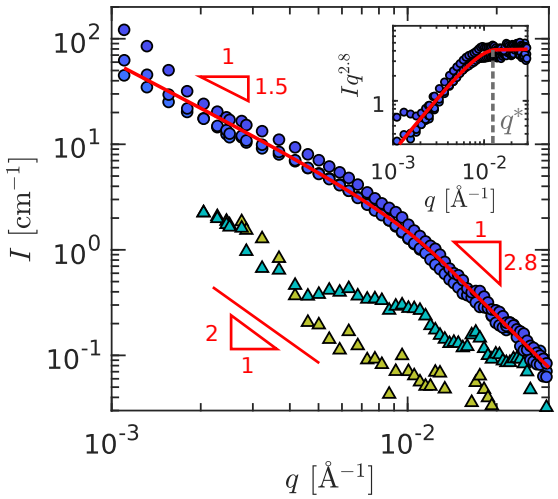

Figure 5.3: Small angle neutron scattering intensity I as a function of the wavevector q for samples prepared at pH $<$ pH$_c$ (○) and pH $>$ pH$_c$ (△). Same color code as in Fig. 5.1. The red solid line is the best fit by a Guinier-Porod model[260], see SI. Inset: Kratky-like representation $Iq^{2.8}$ vs. q of the scattering data of the gel phase presented in the main graph. The vertical dashed line highlights q^*.

transition, forming the so-called fringed micelles, a fraction of them remain available in the gel state.

b Low-field Nuclear Magnetic Resonance

Finally, we examine the sol-gel transition from the *solvent perspective* using molecular probes. Low-field NMR experiments allow us to assess the dynamics of the water molecules[1] for different pH. We observe that irrespective of the sample pH, the spin relaxation following a 90° pulse (see Section.2.F in Chapter. 2) is a decreasing function of time [see inset in Fig. 5.4(a)]. The data are fitted with a single mode decreasing exponential function, i.e., $I(t) = I_0 \exp(-t/T_2)$, where I_0 is the signal intensity at $t = 0$. In contrast to similar measurements on colloidal dispersions [335], or hydrogels based on methylcellulose [336], chitosan [337], biological tissues [338], and synthetic homo- and co-polymers [339, 340], we find that an excellent fit of the relaxation data can be achieved with a single exponential term. CMC samples in both the sol and gel phase are therefore characterized by a *single* transverse (spin-spin) relaxation time T_2. Repeating the same experiments at various temperatures reveals that T_2 increases for increasing temperature [see Fig. 5.4(a)], which we attribute to a higher mobility of the water molecules regardless of their environment. More specifically, $T_2(T)$ is well fitted by an Arrhenius law, i.e., $T_2 = T_2^0 \exp(-E_a/RT)$, yielding an apparent activation energy E_a for each sample composition. Remarkably, E_a shows an abrupt jump at the sol-gel transition, from $E_a \simeq 14$ kJ.mol^{-1} for liquid-like samples (pH > 3) to $E_a \simeq 9$ kJ.mol^{-1} for solid-like samples (pH < 3). Moreover, as shown in the inset of Fig. 5.4(b), a decrease in the CMC concentration at fixed pH $<$ pH$_c$ results in a continuous increase of E_a up to about 14 kJ.mol^{-1}, similar to the value measured for pH $>$ pH$_c$ at $c_{CMC} = 3\%$. Note, however, that the apparent activation energy E_a cannot be understood as a bonding energy as often proposed to rationalize Arrhenius

[1] In fact, the recorded magnetization is directly proportional to the number of protons in the sample, the signals measured on the hydrogels are thus strongly dominated by the water molecules.

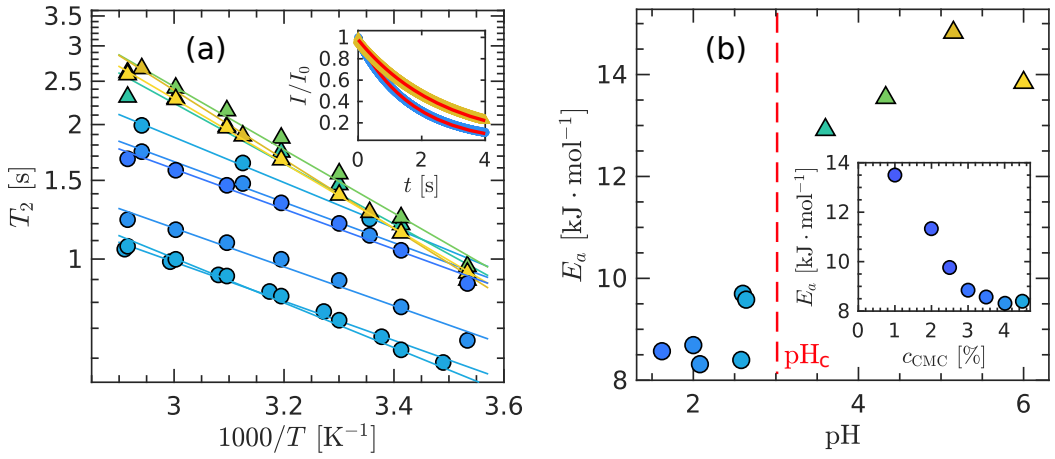

Figure 5.4: Low-field Nuclear Magnetic Resonance: spin relaxation. (a) Transverse NMR relaxation time T_2 of CMC solutions at $c_{CMC} = 3\%$ and different pH as a function of the inverse of the temperature plotted in semilogarithmic scale. Solid lines correspond to the best Arrhenius fit of the data $T_2 \sim \exp(-E_a/RT)$. Same color code as in Fig. 5.1. Inset: intensity I of the transverse magnetic field as a function of time t (normalized by its initial value I_0). Solid lines correspond to the best fit of the data with an exponential fit $I/I_0 = \exp(-t/T_2)$. (b) Parameter E_a obtained from the Arrhenius fit in (a) as a function of pH at fixed $c_{CMC} = 3\%$. Inset: E_a vs. c_{CMC} at fixed $c_{HCl} = 0.15$M. Triangles (resp. disks) correspond to the liquid (resp. gel) phase. Same color code as in Fig. 5.1.

dependence observed in rheology [341–343]. Here, low T_2 values accompanied by low E_a are indicative of the formation of rigid systems, in which the dynamics of the water molecules are slowed down and poorly sensitive to temperature. Such a picture is in good qualitative agreement with the formation of a percolated network at low pH, which causes a decrease *in bulk* of the average water molecules diffusivity. On the other hand, increasing the pH or decreasing the CMC concentration results in looser networks of fringed micelles, and eventually non-percolated systems, where the mobility of water molecules is enhanced and effectively more sensitive to temperature.

There are clear rheological and structural indications of the sol-gel transition upon acidification, which suggests the emergence of fringed micelles at low enough pH. We represented this microstructure in Fig. 5.5. We shall now study their rheological properties focusing mainly in the gel region.

B Rheological properties of acid-induced carboxymethylcellulose hydrogels

Physical gels are ubiquitously found in a broad range of products, from foodstuff to biomedical products. They consist in assemblies of colloids or polymers displaying attractive interactions, hence forming a percolated network incorporating large amounts of solvent [2, 344]. The very nature of the attractive forces between the constituents plays a key role in the gel properties, for they impact the strength and connectivity of the gel network. In practice, attractive interactions come in different flavors usually sorted by their strength [51]. Physical gels built from colloids and/or polymers include various types of non-covalent bonds: metal-ligand [345–347], hydrogen bonds [342, 348–350], ionic bonds [351–353], depletion interactions [67], van-der-Waals interactions, and hydrophobic interactions [354]. The latter case is of primary impor-

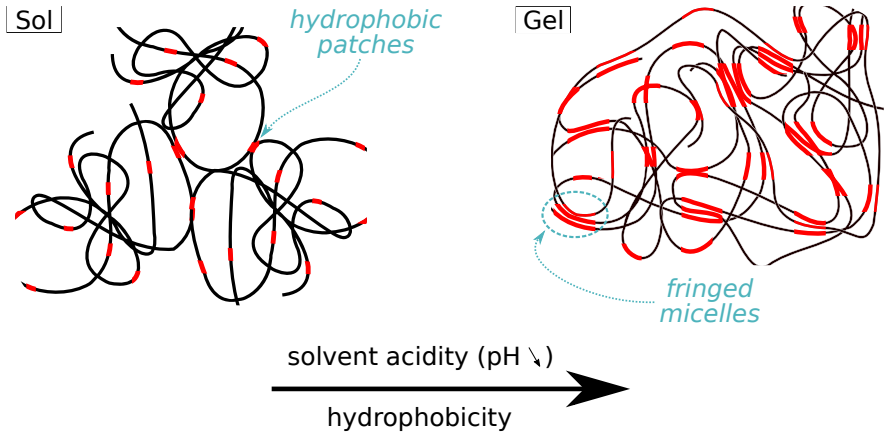

Figure 5.5: Microstructure across the sol-gel transition of acidified CMC solution. The black lines represent the CMC chains, which are entangled. The red part of these chains represent the hydrophobic patches, which grow when the pH is lowered. One fringed micelle is highlighted in blue.

tance, for hydrophobic interactions are pivotal in the self-assembly of numerous biological systems, e.g., structure of proteins and DNA [355, 356]. However, gels formed by hydrophobic interactions remain less studied than their counterpart formed from the other interactions listed above, and their specific characteristics are yet to be fully understood.

Here we tackle the case of hydrogels formed by hydrophobic interactions between CMC. In practice, CMC is obtained from natural cellulose by etherification, using sodium hydroxide and monochloroacetate [165]. As a result, each anhydroglucose repeating unit of CMC displays up to three hydroxyl groups substituted by a carboxymethyl group. Such substitution is scattered along the polymer chain, yielding hydrophobic regions, which corresponds to the less substituted ones [182]. The *average* number of substituted hydroxyl groups defines the degree of substitution (DS) of the CMC, which typically ranges between 0.5 and 1.5 for commercial grades. Blocks of unsubstituted cellulose region along the chain backbone are mainly observed for DS $\lesssim$ 0.9 [179]. These unsubstituted regions facilitate transient chain associations, responsible for a pronounced thixotropic behaviour under flow, and the formation of gels at large concentrations [179, 182, 183, 186, 189].

At fixed CMC content, gel formation in suspensions of weakly substituted CMC can further be controlled by adjusting the pH of the suspension. Indeed, lowering the pH of the CMC suspension diminishes the charge density of the polymer chains, thereby reducing its dimensions and promoting the formation of multi-chain aggregates [187]. In the preivous section, we have provided a comprehensive description of such an acid-induced gelation of carboxymethylcellulose [357]. Building upon seminal observations [188, 331], we introduced a mean-field model based on hydrophobic interchain association that accounts remarkably well for the sol-gel boundary over a broad range of CMC concentrations, up to 5% [Fig. 5.6]. Finally, neutron scattering experiments confirmed the picture of a gel network built from flexible rod-like structure involving fuzzy colloidal structures composed of a dense core surrounded by a sparse, hairy shell of polymer chains strongly reminiscent of fringed micelles [180, 358].

In the present section, we focus on the rheological properties of CMC suspensions across the sol-gel transition. We show in Section 5.B.1 that the linear viscoelastic spectrum of CMC suspensions in the liquid phase display a broad power-law spectrum,

which can be rescaled onto a master curve following a time-temperature superposition principle. The rescaling factors obey an Arrhenius dependence with the temperature that allows us to infer an activation energy that is compatible with hydrophobic interactions. A similar analysis in the gel phase reveals that acid-induced CMC gels verify the theory of rubber elasticity. Finally, in the last section of this section, we examine the shear-induced yielding transition of CMC gels to Large Amplitude Oscillatory Shear. Intra-cycle analysis offers a detailed account of the yielding transition that we discuss at various pH.

B.1 Linear Rheology

a Impact of the composition onto the linear viscoelastic properties in the gel phase

Aqueous suspensions of Carboxymethylcellulose form gels upon acidification. In the previous section, we have performed an extensive characterization of the sol-gel transition varying both the CMC content and the pH of these solutions [357]. Measuring the linear viscoelastic spectrum of these suspensions, i.e., $G'(\omega)$ and $G''(\omega)$ allows us to identify the gel point, which corresponds to sample compositions such that $\tan\delta = G''/G'$ is frequency independent [330], while gel samples are defined by $\tan\delta < 1$ in the limit $\omega \to 0$. This criterion allowed us to build a phase diagram reported in Fig. 5.6 in which the gel phase corresponds to CMC suspensions of concentration larger than 1% and sufficiently low pH to induce the aggregation of the CMC. Suspensions with a CMC concentration lower than 1% do not form gels but turbid heterogeneous dispersions of macroscopic aggregates due to the lack of polymer (see gray region in Fig. 5.6), whereas CMC suspensions of sufficiently high pH form homogeneous viscoelastic liquids (see blue region in Fig. 5.6). In the following, we examine in more detail the linear viscoelastic spectrum of both the liquid and gel phases and test their robustness to a change in temperature.

In the gel state, the viscoelastic spectra are all well described by a fractional Kelvin-

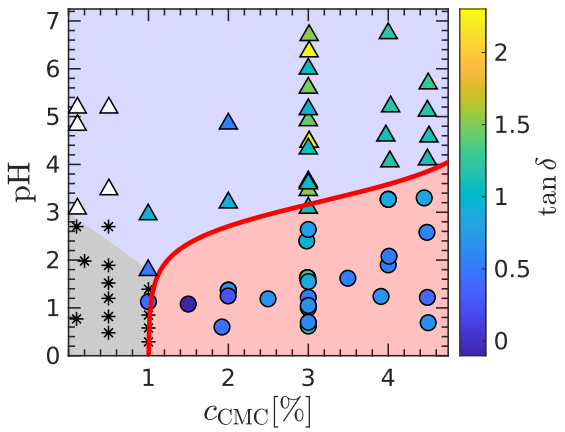

Figure 5.6: Map of aqueous CMC suspensions mechanical properties. The four different phases are represented: gel [(•) with a red background], viscoelastic liquid [(Δ) with a blue background], phase-separated samples [(⋆) with a gray background], and Newtonian solutions (▽). Color levels code for the loss factor $\tan\delta = G''/G'$ of the gel sample determined by small amplitude oscillatory shear at $\omega = 2\pi$ rad.s^{-1}. The white triangles denote viscoelastic liquids whose rheological properties were not measured. The red curve separating the viscoelastic liquid phase from the gel phase corresponds to the model discussed in Eq. (5.10) with Y = 0.18.

Voigt model (FKVM) [210, 270] already encountered in this manuscript. The fitted viscoelastic spectra and their parameters G_0, ω_0 and α are given in Fig. 5.7. This is highly reminiscent of the CB-CMC hydrogels studied in chapter 3. The main difference is the exponent $\alpha = 0.5$ obtained with the current acidified CMC gels, which is significantly smaller than the typical value $\alpha \simeq 2/3$ for CB-CMC hydrogels. The FKV model is characterized by a single timescale ω_0, which allows us to collapse all the loss factor data onto a master curve when plotted against $\tilde{\omega} = \omega/\omega_0$ [Fig. 5.7(j)]. Moreover, using normalized moduli, i.e., $\tilde{G}' = G'/G_0$, $\tilde{G}'' = G''/G_0$, we also uncover a universal master curve for the viscoelastic spectrum of all gels obtained at pH $<$ pH$_c$ [Fig. 5.7(k)]. This master curve is, in turn, well described over 8 orders of magnitude

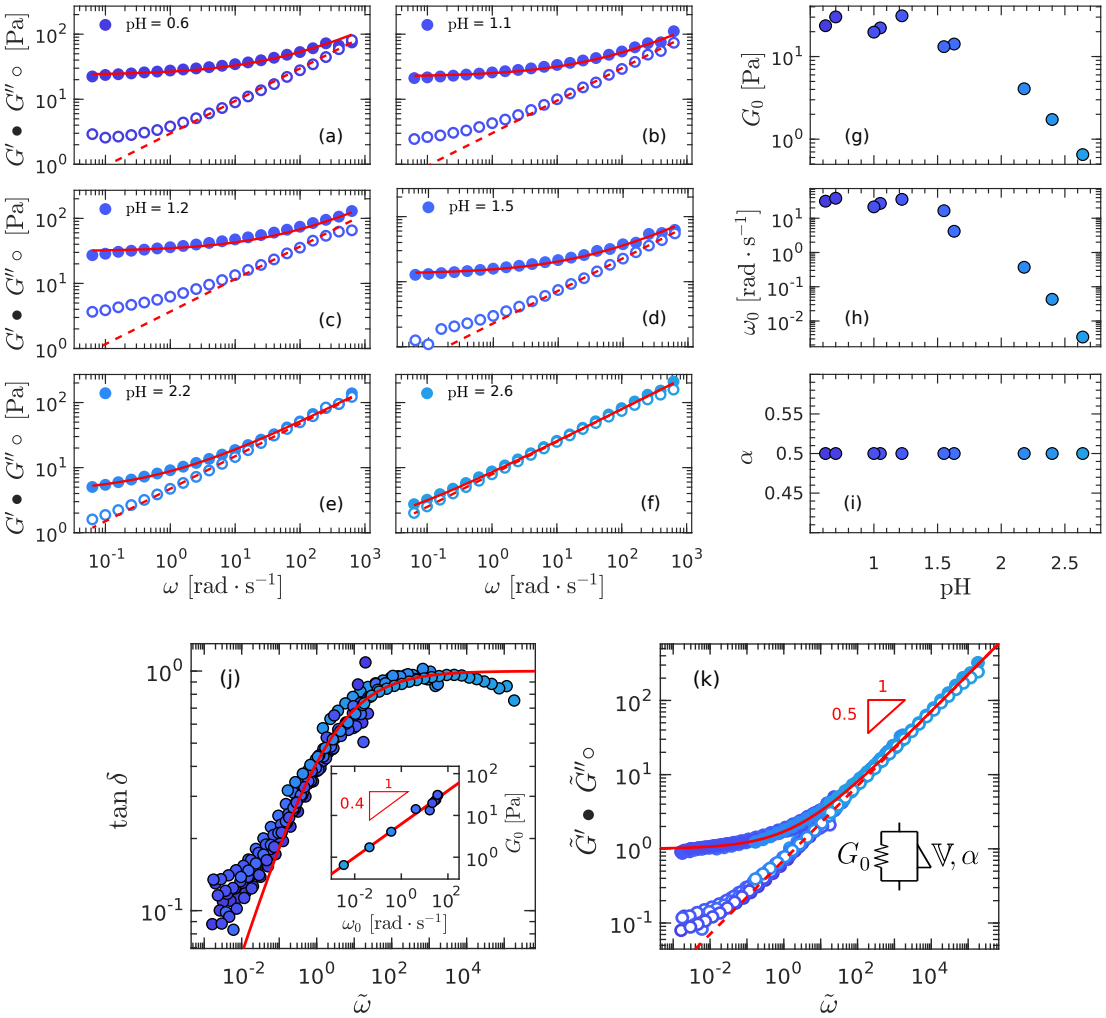

Figure 5.7: Linear viscoelatic properties of acidified CMC hydrogels. (a-f) Viscoelastic spectra of CMC solutions at fixed polymer content $c_{CMC} = 3\%$ and pH ranging from 0.6 to 2.6. The solid (resp. dashed) red curve corresponds to G' (resp. G'') when fitting the complex modulus to eq. (1) in the main text. The three fitting parameters are plotted against the pH: (g) G_0, (h) ω_0, and (i) α. The latter is fixed to $\alpha = 0.5$. (j) Master curve for the loss factor tan δ versus reduced frequency $\tilde{\omega} = \omega/\omega_0$ for a 3% CMC gels at various pH $<$ pH$_c$ ranging between 0.6 and 2.6. Inset: G_0 vs. ω_0; the red line is the best power-law fit of the data, yielding an exponent 0.4. (k) Master curve for the frequency dependence of the normalized viscoelastic moduli of acid-induced CMC gels. The red curve is the best fit of the data by the FKV model with $\alpha = 0.5$.

of reduced frequency by the fractional Kelvin-Voigt model pictured as red curves in Fig. 5.7(k).

Remarkably, the modulus and frequency scales depend a lot on the pH for pH $\gtrsim$ 1.5 but are almost constant below [Fig.5.7(g-h)]. It suggests a saturation effect of the pH, which is consistent with our microscopic vision of the system. The network is reinforced by lowering the pH because it increases the number or the length of the hydrophobic patches, but once most of the carboxylate groups are acidified lowering the pH further does not have much impact onto the mechanical properties of the gel.

These results show that irrespective of the pH, acid-induced CMC gels display a common underlying hierarchical microstructure, which is characterized by the power-law dependence of G_0 vs. ω_0 with an exponent 0.4 [inset in Fig. 5.7(j)] much smaller than the value reported for other polymer gels, e.g., protein gels [60]. Moreover, in the high-frequency limit, $\tilde{G}' \sim \tilde{G}'' \sim \tilde{\omega}^{1/2}$, which is reminiscent of the power-law rheology of critical gels [330], and in remarkable agreement with a Rouse scaling. This high-frequency response also contrasts with the 2/3 scaling exponent reported for CMC (and polyacrylamide) hydrogels crosslinked by colloidal particles [273, 274, 359]. In fact, a closer look at CMC gel viscoelastic properties measured over the course of two months reveals that CMC gels are slowly reinforcing, which results in a slow decrease of α from $\alpha = 0.55$ a sample of a few days old to $\alpha = 0.4$ at two months age [see Fig. 5.8]. Therefore, the discrepancy between our previous results is only apparent, and one should keep in mind that due to the slow reinforcement of acid-induced CMC gels, comparison among various sets of data must be done at similar sample ages.

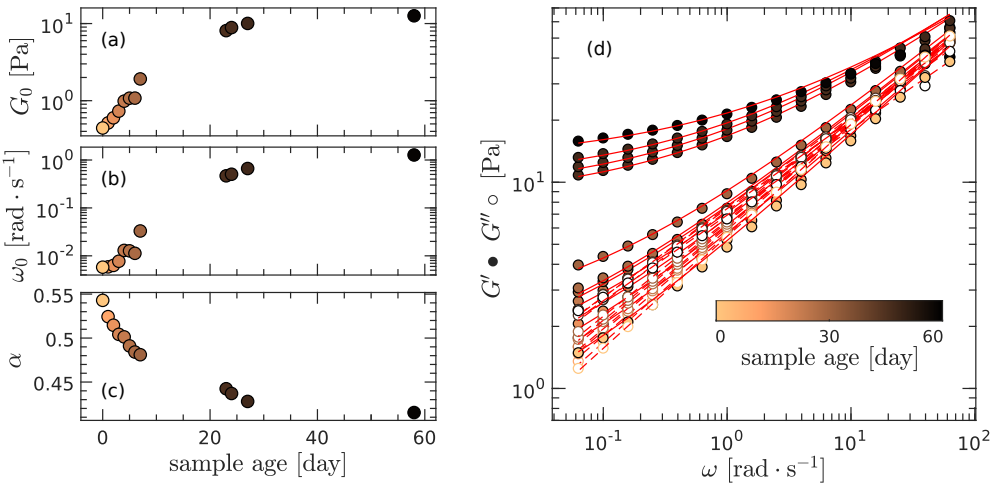

Figure 5.8: Long time evolution of the viscoelastic spectrum in the gel phase, which properties are extracted from a fit of the data to a fractional Kevlin-Voigt (FKV) model [see Eq. (3.4)]. (a) modulus scale G_0, (b) frequency scale ω_0, and (c) exponent α as a function of the sample age, defined as the time elapsed from the preparation date. The samples are CMC gels at fixed composition from the same batch ($c_{CMC} = 3\%$ and pH = 1.6) at fixed temperature T = 22°C. (d) Corresponding spectra, the red curves are the FKV fits with the parameters plotted in (a-c). Colors encode the sample age as shown in the colorbar.

b Time-temperature superposition

Analysis in the gel phase

When varying the temperature, the FKVM remains relevant to describe the vis-

coelatic spectra for CMC acidified hydrogel at $c_{CMC} = 3\%$ CMC gel at pH $= 1.6$ [Fig. 5.9(a) and 5.9(b)]. Interestingly, the power-law exponent α is independent of the temperature, which prompts us to set it constant $\alpha = 0.4$, which reduces the number of fitting parameters to two: G_0 and $\mathbb{V}$. The latter parameter can be replaced by $\omega_0 = (G_0/\mathbb{V})^{1/\alpha}$, which has a physical dimension much easier to grasp. Moreover, using normalized coordinates, i.e., $\tilde{G}' = G'/G_0$, $\tilde{G}'' = G''/G_0$, and $\tilde{\omega} = \omega/\omega_0$, we obtain a master curve for the viscoelastic spectra measured at various temperatures. Such a master curve, which is the hallmark of a time-temperature superposition principle, calls for several remarks.

First, we obtained an identical master curve, while varying the pH at fixed temperature and CMC concentration [357]. This result suggests that pH and temperature affect the same binding element, which are the hydrophobic groups along the polymer chain. The sole difference between our previous study and the present one is the value of α (0.5 vs. 0.4, respectively).

Finally, we examine the temperature dependence of the rescaling factors, i.e., G_0 and ω_0. The elastic modulus G_0 increases with the temperature in a way that is compatible with the theory of rubber elasticity, i.e., $G_0 \sim k_B T/\xi^3$, where ξ denotes the average distance between two nodes of the gel network [Fig. 5.10(a)]. Here, the best fit of the data yields $\xi \simeq 40$ nm. This length scale is comparable with the size of fringed micelles, as determined recently by neutron scattering on the very same samples [357]. This observation suggests that fringed micelles would act as hydrocolloids forming a percolated network rather than being dispersed as separate crosslinks in the polymer suspension. More generally, seminal work on CMC hydrogels with $0.8 \lesssim \mathrm{DS} \lesssim 1$, and formed at sufficiently large CMC concentrations have shown that the dependence of the elastic modulus with the polymer concentration is compatible with Flory's theory and the theory of rubber elasticity [188]. Our results therefore extend these conclu-

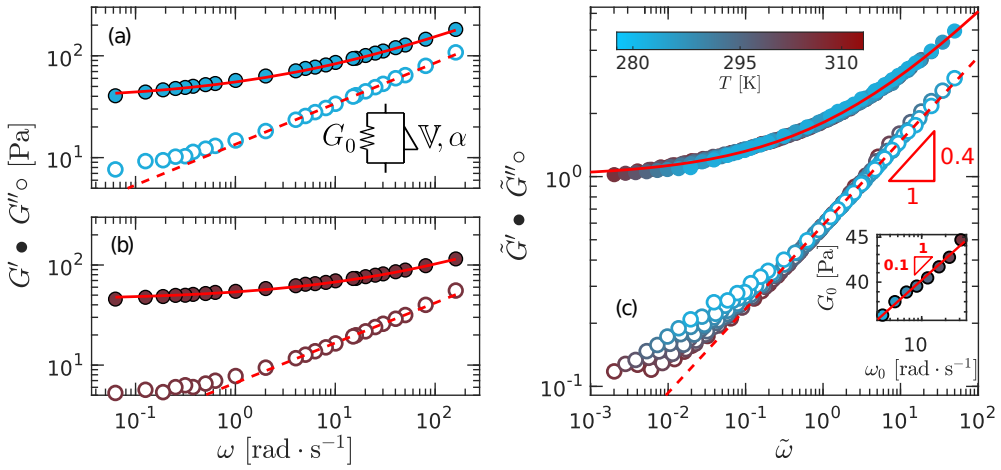

Figure 5.9: Impact of the temperature on the viscoelastic spectrum of an acidified CMC hydrogel at 3% CMC and pH$=$ 1.6. G' and G'' vs. ω for at a temperature $T = 5°$C (a) and $T = 40°$C (b). The red curves are the best fits of the data with a Fractional Kelvin-Voigt (FKV) model [see Eq. (3.4)], which is sketched in (a). (c) Master curve for the frequency dependence of the viscoelastic moduli obtained by normalizing both the viscoelastic moduli and the frequency, i.e., $\tilde{G}' = G'/G_0$, $\tilde{G}'' = G''/G_0$, and $\tilde{\omega} = \omega/\omega_0$ with $\omega_0 = (G_0/\mathbb{V})^{1/\alpha}$ for eight different temperatures ranging from $T = 5°$C to 40°C and coded in color. The red curves correspond to the normalized FKV model, $\tilde{G}^\star = 1 + (i\tilde{\omega})^\alpha$ with $\alpha = 0.4$. Inset: G_0 vs. ω_0; the red continuous line is the best power-law fit of the data with an exponent 0.1.

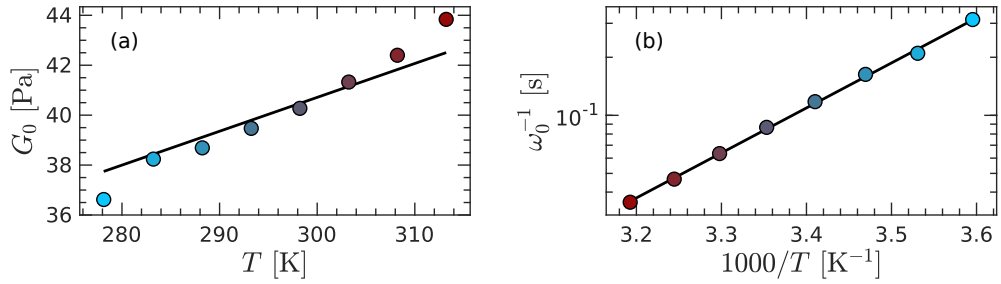

Figure 5.10: Temperature dependence of the scaling factors G_0 and ω_0 from the Fractional Kelvin-Voigt model shown in Fig. 5.9. (a) G_0 vs. T. The black line shows the best fit of the data assuming a rubber elasticity model, i.e., $G_0 = k_B T/\xi^3$, yielding $\xi \simeq 46$ nm. (b) ω_0^{-1} vs. $1/T$. The black line in the best fit of the data with an Arrhenius model that reads $\omega_0^{-1} \propto \exp(-E_a/k_B T)$, yielding an activation energy $E_a = 43 \pm 3$ kJ.mol^{-1}. Colors code for the temperature. Same color code as in Fig. 5.9.

sions to the case of acid-induced CMC gels (at fixed CMC concentration), while explicitly testing the temperature dependence, which, to the best of our knowledge, had not been reported yet.

Analysis in the sol phase

We then examine the linear viscoelastic properties of acidified CMC suspensions in liquid phase, and the entangled regime. Figure 5.11(a) illustrates the typical frequency dependence of G' and G'' in the case of a liquid 3% CMC suspension at pH $= 3.6$. Such a broad power-law spectrum is in line with previous rheological measurements performed on CMC suspensions at similar concentrations for various counter ions and for CMC of different molecular properties, i.e., various degrees of substitution and molecular weights [174, 185, 186, 189, 360, 361]. The power-law viscoelastic response of the CMC suspension is remarkably well-captured by a Fractional Maxwell (FM) model that consists of two spring pots – or Scott-Blair element– in series [see sketch as an inset in Fig. 5.11(a)]. Each spring pot is characterized by a quasi-property and a dimensionless exponent, noted ($\mathbb{V}$, κ) and ($\mathbb{B}$, β), respectively, where we assume $\kappa < \beta$. The corresponding complex modulus reads [210, 270]:

$$G^\star = \frac{\mathbb{K}\,(i\omega)^\kappa\,\mathbb{B}\,(i\omega)^\beta}{\mathbb{K}\,(i\omega)^\kappa + \mathbb{B}\,(i\omega)^\beta} \tag{5.11}$$

The complex modulus can be re-written as follows:

$$G^\star = \eta_0 \omega \frac{(i\omega/\omega_0)^{\kappa+\beta-1}}{(i\omega/\omega_0)^\kappa + (i\omega/\omega_0)^\beta} \tag{5.12}$$

where $\eta_0 = (\mathbb{K}^{\beta-1}/\mathbb{B}^{\kappa-1})^{1/(\beta-\kappa)}$ and $\omega_0 = (\mathbb{K}/\mathbb{B})^{1/(\beta-\kappa)}$. In the low-frequency limit, i.e., $\omega \ll \omega_0$ the CMC suspension displays a critical-like response, i.e., $G'(\omega) \sim G''(\omega) \sim \omega^\beta$, with $\beta = 0.72$ [15]. This behavior strongly contrasts with the response expected for a monodisperse polymer solution, for which $G''(\omega) \sim \omega$, while $G'(\omega) \sim \omega^2$ [15]. Such a discrepancy can be related to the presence of hydrophobic patches along the polymer chains that lead to some degree of physical binding between the polymers, bringing the suspension close to the gel point.

This response is robustly observed over a broad range of temperatures, from $T =$ 5°C to 40°C [see Fig. 5.11(b)], which hints at some universal feature in the linear mechanical response of CMC suspensions. Indeed, the viscoelastic spectrum obtained at

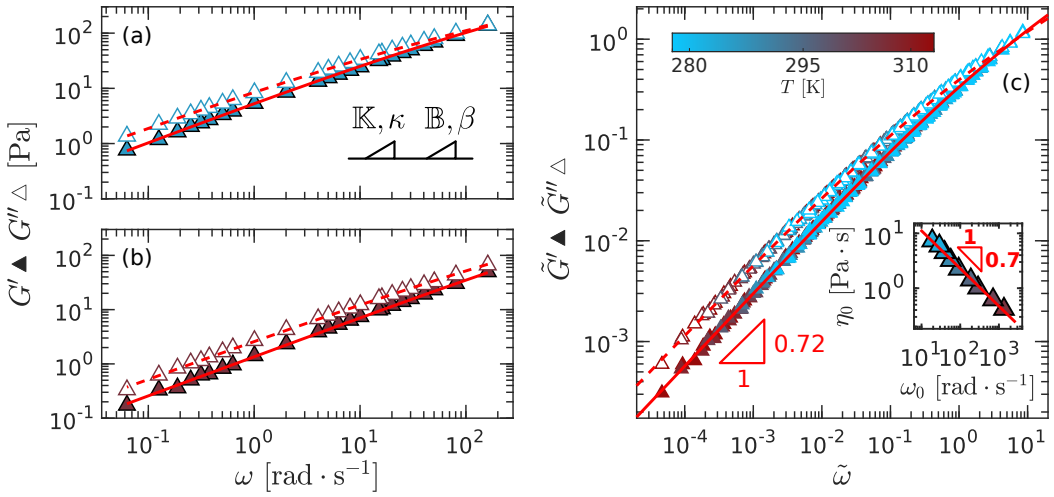

Figure 5.11: Impact of the temperature on the viscoelastic spectrum of an acidified CMC solution at 3% CMC and pH= 3.6. Frequency dependence of the elastic and viscous moduli, G' and G'' resp., at a temperature T = 5°C (a) and T = 40°C (b). The red curves are the best fits of the data to a Fractional Maxwell (FM) model [see Eq. (5.11)], which is sketched in (a). (c) Master curve for the frequency dependence of the viscoelastic moduli obtained by normalizing both the moduli and the frequency: $\tilde{G}' = G'/(\eta_0\omega_0)$, $\tilde{G}'' = G''/(\eta_0\omega_0)$, and $\tilde{\omega} = \omega/\omega_0$ with $\eta_0 = (\mathbb{K}^{\beta-1}/\mathbb{B}^{\kappa-1})^{1/(\beta-\kappa)}$ and $\omega_0 = (\mathbb{K}/\mathbb{B})^{1/(\beta-\kappa)}$ for different temperatures ranging from T = 5°C to 40°C. The red curves correspond to the normalized FM model: $\tilde{G}^\star = (i\tilde{\omega})^{\kappa+\beta}/[(i\tilde{\omega})^\kappa + (i\tilde{\omega})^\beta]$ with $\kappa = 0.39$ and $\beta = 0.72$. Inset: η_0 vs. ω_0; the red line is the best fit of the data with a decreasing power-law of exponent 0.7.

various temperatures can be rescaled into a master curve by normalizing the elastic and viscous modulus by $\eta_0\omega_0$, and the frequency by ω_0, as illustrated in Fig. 5.11(c). Such a rescaling confirms the existence of a time-temperature superposition, which is here–in the terminal regime– governed by the CMC strands dynamical association as originally proposed in the Sticky reptation model [341, 362]. Moreover, we find that these two rescaling factors are connected by a power law that reads $\eta_0 \sim \omega_0^{-0.7}$ or equivalently, in terms of elastic scale, $\eta_0\omega_0 \sim \omega_0^{0.3}$.

Interestingly, similar master curves were reported for CMC suspensions prepared with various salt concentrations, and various types of monovalent salts, e.g., NaCl, and divalent salts, e.g., $CaCl_2$, $MgCl_2$, etc., which hints at a time-salt superposition principle [360]. Yet, these master curves were obtained by shifting manually the viscoelastic spectra along the sole horizontal –frequency– axis, and the shift factor depends on the nature of the salt. The microscopic scenario underpinning this superposition principle has been attributed to the formation of a complex between the added ions and some functional groups along the polymer chains, working as intermolecular crosslinks, and leading to reduced chain mobility. These observations support our scenario according to which varying the temperature affects the number of physical crosslinks between the CMC chains. Moreover, in our case, obtaining a master curve requires an additional rescaling of the viscoelastic spectrum along the vertical axis, which suggests that a more complex scenario is at stake.

The impact of temperature on the viscoelastic spectrum is captured by the temperature dependence of the two parameters η_0 and ω_0 that is reported in Figure 5.12. These two parameters can be interpreted as the zero-shear viscosity and the terminal frequency (i.e., the inverse of a terminal relaxation time). Both η_0 and ω_0^{-1} are well described by an Arrhenius equation from which the respective apparent activation en-

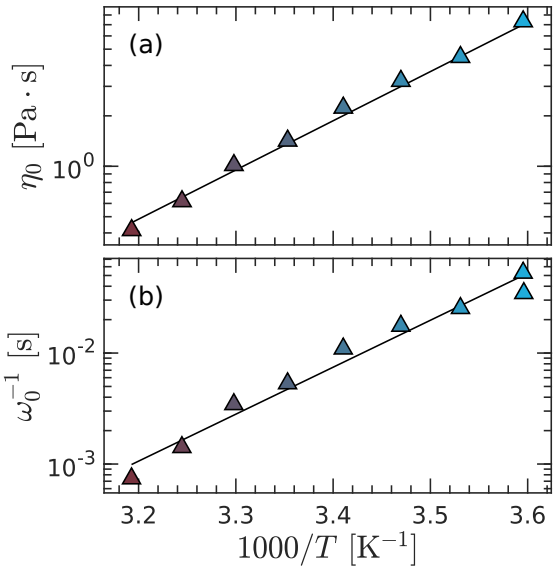

Figure 5.12: Temperature dependence of the rescaling parameters η_0 and ω_0 extracted from the Fractional Maxwell model. (a) η_0 and (b) ω_0^{-1} vs. $1/T$ in semi-logarithmic scale to highlight the exponential scaling. The black lines correspond to the best fit of the data with an Arrhenius-like scaling, i.e., $X \sim \exp(-E_a/k_BT)$, where $X = \eta_0$ or ω_0^{-1}, and E_a stands for the activation energy, and k_B is the Boltzmann constant. We obtain $E_a = 56$ kJ.mol^{-1} and $E_a = 81$ kJ.mol^{-1} for η_0 and ω_0, respectively.

ergies are found to be $E_a = 56$ kJ.mol^{-1} and $E_a = 81$ kJ.mol^{-1}. These values are similar to what is generally observed for polymer melts at $T > T_g + 100$ °C [18]. Note that because of the utilization of the fractional model, both values are not expected to match whereas it is generally the case since $\eta_0(T) \sim G_0/\omega_0(T)$, where $G_0 = G(\omega = \omega_0)$ and the dependence in temperature is inherent to the monomeric friction coefficient $\zeta(T)$ satisfying $\zeta \sim \eta_0 \sim \omega_0^{-1}$ regardless of the chain topology [18]. Said differently, the quasi-property character of η_0 (i.e., $\kappa = 0.89$ and $\beta = 0.72$) breaks its parallel evolution with respect to ω_0 when changing the temperature, which suggests a complex microstructure.

Finally, one should notice that $\kappa = 0.4$ is similar to $\alpha = 0.4$; these exponents might be linked since the high-frequency relates to short length scales where both liquid suspensions and gels display some structural similarity, i.e., patchy polymers with some degree of attraction.

C Non-linear rheology of acid-induced CMC gels

C.1 Reversibility of the yielding transition

In this section, we examine the non-linear rheological response of acid-induced CMC gels. We first test the reversibility of the shear-induced solid-to-liquid transition of a 3% gel prepared at pH=2.2, by imposing a series of consecutive large amplitude oscillatory shear (LAOS) of amplitude $\gamma_0 = 300\%$ for 180 s followed by a period of rest at small amplitude oscillatory shear (SAOS) $\gamma_0 = 1\%$ for 1200 s. Both steps are conducted at $f = 1$ Hz. The results are illustrated in Fig. 5.13(a) where we report the loss factor $\tan\delta = G''/G'$ as a function of time over 5 successive LAOS and SAOS cycles.

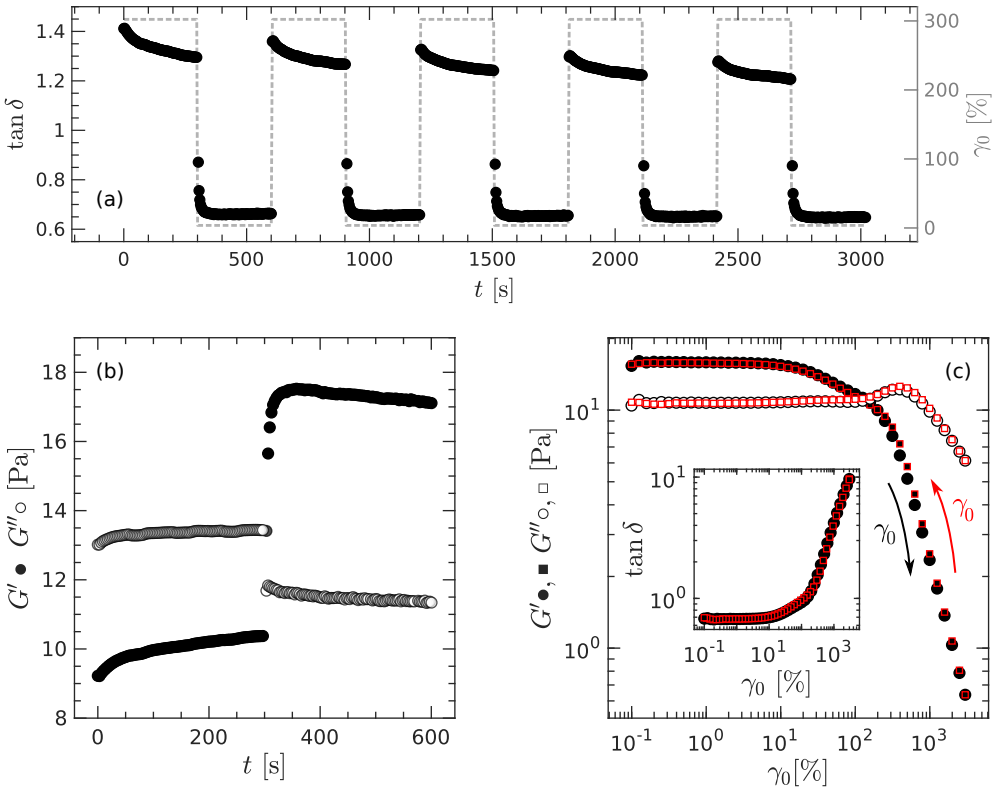

Figure 5.13: Reversibility of the yielding transition under LAOS. (a) Temporal evolution of the loss factor $\tan\delta$ of a CMC gel under oscillatory shear at $f = 1$ Hz during 5 steps of 300 s alternating large strain amplitude of 300% and small strain amplitude of 1%. The loss factor is represented in black (left axis) while the strain amplitude γ is represented in blue (right axis). (b) Elastic (filled circles) and viscous (open circles) moduli measured at $f = 1$ Hz corresponding to the first 600 s of the graph. (c) Elastic and viscous moduli measured at $f = 1$ Hz for an increasing ramp of strain amplitude (black circles) followed by a decreasing ramp of strain amplitude (red squares). The strain amplitude is varied between 0.01% and 3000% with 10 steps per decade; each strain amplitude is applied for 3 cycles. Experiments conducted on a CMC gel prepared with $c_{\mathrm{CMC}} = 3\%$ and pH = 2.2.

Under LAOS, the CMC gel flows as a viscous liquid ($\tan\delta > 1$) and exhibits a time-dependent response [Fig. 5.13(a)]. The loss factor decreases during the 1 s of the test, without reaching a steady state. In practice, examining the individual evolution of G' and G'' shows that G'' is roughly constant, whereas G' increases [see Fig. 5.13(b)]. These observations show that acid-induced CMC gels flow like liquids under large amplitude oscillations, while their microstructure keeps rearranging under shear over a timescale larger than 300 s, most likely due to the association/dissociation dynamics of hydrophobic patches.

Upon flow cessation and switching to SAOS, the loss factor displays a rapid drop with $\tan\delta < 1$ associated with the sol-gel transition before reaching a quasi steady-state in about 20 s [Fig. 5.13(a)]. The crossover of G' and G'' occurs within seconds, which shows that sol-gel transition is rapid, while $G'(t)$ subsequently shows a mild overshoot with a maximum after about 50 s [see Fig. 5.13(b)]. These observations suggest that the sol-gel transition corresponds to some dynamical arrest of the fringed micelles; and we can further hypothesize that it is followed by *local* and/or cooperative microstructural rearrangements leading to he slow relaxation of G'.

Repeating these alternative cycles of LAOS and SAOS reveals first that acid-induced

CMC gels reversibly yield under external shear and reform upon flow cessation, and second that the state reached upon flow cessation poorly depends on the shear history experienced by the sample. To further illustrate the absence of memory in the rheological response of acid-induced CMC gels, we perform a strain-sweep experiment on the same 3% CMC gel first by increasing the amplitude before immediately decreasing it. The result is shown in Fig. 5.13(b).

Increasing the strain amplitude at $f = 1$ Hz by discrete steps spaced logarithmically between 0.1% to 3000% leads to a shear-induced yielding transition [Fig. 5.13(b)]. In practice, the elastic modulus G' is constant in the linear deformation region, and decreases monotonically beyond a strain amplitude of about 10%. Conversely, the viscous modulus G'' constant and lower than G' at first, crosses G' at a critical strain γ_y of about 150%, before showing a maximum at $\gamma \simeq 400\%$ followed by an abrupt drop. The overshoot in G'' is referred to as the "Payne effect" in filled polymer composites [363, 364], while the overall response is classified as Type III, and commonly observed in a broad range of colloidal particulate and polymer gels [226]. Interestingly, performing a decreasing ramp of strain following an identical strain path as during the increasing ramp leads to the very same viscoelastic response of the gel, confirming the "reversibility" of the shear-induced solid-to-liquid transition, as demonstrated by alternating periods of LAOS and SAOS.

C.2 Analysis of LAOStrain waveforms

In this section, we further quantify the shear-induced yielding of acid-induced CMC gels upon increasing the strain amplitude during LAOStrain experiments. The evolution of G' and G'' vs. the strain amplitude γ_0 is shown in Fig. 5.14(a) together with the stress amplitude $\sigma(\gamma_0)$ in Fig. 5.14(b). The stress grows linearly up to the crossover of G' and G'', which defines the yield strain $\gamma_y \simeq 200\%$ and the yield stress $\sigma_y \simeq$40 Pa. Additionally, we report the growth of harmonics in the stress signal: both the third and fifth harmonics grow quadratically with the strain amplitude up to the yield point. At the yield point, G'' shows a maximum [see inset in Fig. 5.14(a)], while for $\gamma_0 > \gamma_y$ both G' and G'' display a power-law decay highlighted with red lines in Fig. 5.14(a). In practice, $G' \sim \gamma_0^{-\nu'}$ and $G'' \sim \gamma_0^{-\nu''}$, with $\nu' = 0.8$ and $\nu'' = 0.6$, with $\nu'/\nu'' \simeq 1.3$. Remarkably, these values contrast with predictions from Mode Coupling Theory (MCT) following which, one should expect $\nu'' \simeq 0.9$ and $\nu' = 2\nu''$ [228]. Such a discrepancy suggests that the shear-induced rearrangements of the polymer network, especially at the locus of hydrophobic patches might play a key role in the yielding process since MCT does not take into account local rearrangements of particles occurring via the crossing of activated barriers. Yet, acid-induced CMC gels are not an isolated case, for the prediction $\nu' = 2\nu''$ has been reported to fail in several experimental studies on colloidal gels [318] and denser suspensions of soft repulsive particles, i.e., colloidal glasses [365–367].

To provide a more detailed picture of the yielding transition, we turn to the intra-cycle analysis of the LAOStrain experiments. Typical waveforms for the intra-cycle response of an acid-induced CMC hydrogel are reported in Fig. 5.15 as Lissajous-Bowditch (LB) plots that parametrically show the measured instantaneous stress against the instantaneous strain γ and strain rate $\dot{\gamma}$ within a period of oscillation [368]. We report LB plots for three different strain amplitudes along the strain sweep experiment, i.e., $\gamma_0 = 10\%, 100\%,$ and 1000%. For increasing strain amplitude, this representation illustrates very well the growth of harmonics in the stress signal and the transition

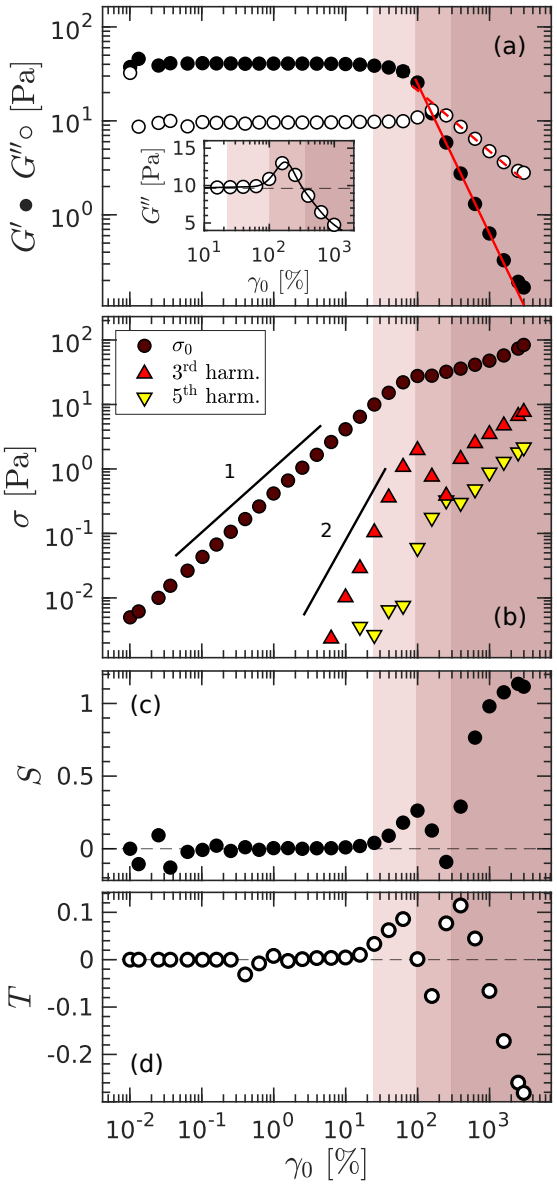

Figure 5.14: LAOStrain experiment and intra-cycle analysis on a 3% CMC gel (pH= 0.6) (a) Viscoelastic moduli G' (•) and G'' (○) vs. strain amplitude γ_0. The red lines show the best power-law fit of the data beyond the crossover of G' and G'', i.e., $G' \sim \gamma_0^{-\nu'}$ and $G'' \sim \gamma_0^{-\nu''}$, with $\nu' = 0.8$ and $\nu'' = 0.6$. Inset: zoom on G'' overshoot near the yield point defined by the crossover of G' and G'' in the main figure. (b) Stress amplitude σ_0 as well as the third and fifth harmonic of the stress response vs. strain amplitude γ_0. Black lines emphasize a linear and quadratic increase. (c) Strain-stiffening ratio $S = (G'_L - G'_M)/G'_L$, with $G'_M = (d\sigma/d\gamma)\,|_{\gamma_0}$ the minimum-strain modulus, and $G'_L = (\sigma/\gamma)\,|_{\gamma=\pm\gamma_0}$ the large-strain modulus. $S > 0$ implies intra-cycle strain-stiffening, while $S < 0$ corresponds to intra-cycle strain-softening behavior. (d) Shear-thickening ratio $T = (\eta'_L - \eta'_M)/\eta'_L$. $T > 0$ implies intra-cycle shear-thickening, while $T < 0$ corresponds to intra-cycle shear-thinning behavior. In (c) and (d), the horizontal dashed line highlights $S = T = 0$. In (a)–(d), the non-linear response is divided into three regions of strain highlighted by vertical stripes. The first region ($\gamma_0 \gtrsim 25\%$) marks the onset of non-linearity based on the intra-cycle analysis (defined by $S > 0$ and $T > 0$). The second region ($\gamma_0 \gtrsim 100\%$) marks the onset of non-linearity based on the strain-dependence of the stress amplitude $\sigma(\gamma_0)$. The third region ($\gamma_0 \gtrsim 300\%$) corresponds to the established non-linear response beyond the minimum of S (and maximum of T).

from the linear regime, i.e., $\sigma(\gamma)$ close to a straight line and $\sigma(\dot{\gamma})$ close to a circle, to the non-linear regime where $\sigma(\gamma)$ and $\sigma(\dot{\gamma})$ display more complex shapes. In order to quantify the intra-cyle evolution of the sample response, we use two additional elastic moduli introduced in ref. [195], which are the elastic modulus computed at the minimum strain within the cycle, i.e, $G'_M = (\mathrm{d}\sigma/\mathrm{d}\gamma)\,|_{\gamma=0}$, and the elastic modulus computed at the largest strain applied to the sample, i.e., $G'_L = (\sigma/\gamma)\,|_{\gamma=\gamma_0}$ [see Fig. 5.15(b)]. The gel response within an oscillation is well captured by the strain-stiffening ratio S, a dimensionless quantity defined as $S = (G'_L - G'_M)/G'_L$, where $S > 0$ indicates intra-cycle strain-stiffening, whereas $S < 0$ corresponds to an intra-cycle strain-softening behavior. The same approach can be used on the waveform $\sigma(\dot{\gamma})$ to define the minimum rate dynamic viscosity $\eta'_M = (d\sigma/d\dot{\gamma})\,|_{\dot{\gamma}=0}$ and the large rate dynamic viscosity $\eta'_L = (\sigma/\dot{\gamma})\,|_{\dot{\gamma}=\omega\gamma_0}$ [see Fig. 5.15(e)]. The corresponding di-

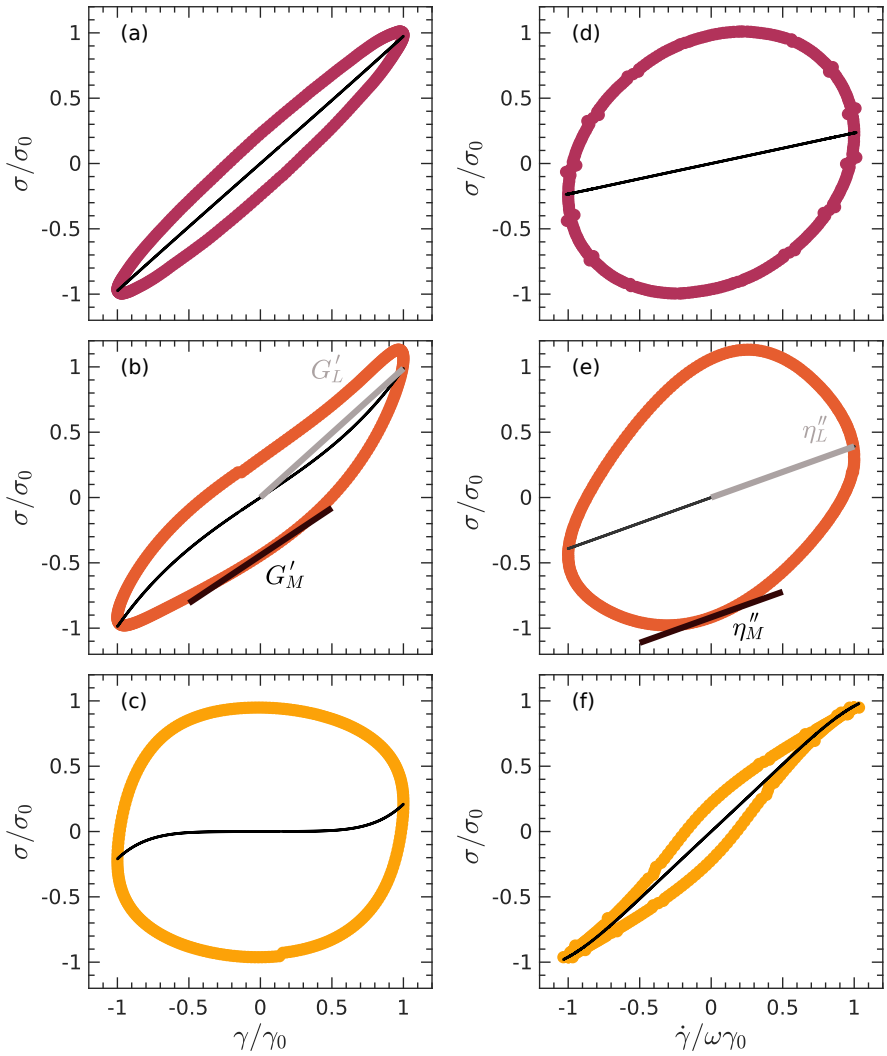

Figure 5.15: Selected waveforms of the stress response to large-amplitude strain deformations of a 3% CMC gel (pH= 0.6) at various strain amplitudes: $\gamma_0 = 10\%$ (a,b), 100% (c,d), and 1000% (e,f). The normalized stress σ/σ_0 is reported as a function of either the normalized strain γ/γ_0 in (a), (c), and (f), or the normalized shear rate $\dot{\gamma}/(\omega\gamma_0)$ in (b), (d), and (f). The black curves show the elastic (resp. viscous) part of the stress response in (a), (c), and (e) [resp. (b), (d), and (f)]. In (b), we define the elastic modulus at the minimum strain $G'_M = (d\sigma/d\gamma)\,|_{\gamma=0}$, and the elastic modulus at the largest strain $G'_L = (\sigma/\gamma)\,|_{\gamma=\gamma_0}$. In (e), we define the minimum rate dynamic viscosity $\eta'_M = (d\sigma/d\dot{\gamma})\,|_{\dot{\gamma}=0}$ and the large rate dynamic viscosity $\eta'_L = (\sigma/\dot{\gamma})\,|_{\dot{\gamma}=\omega\gamma_0}$. These moduli and viscosities are used to compute the parameters S and T shown in Fig. 5.14(c) and 5.14(d).

mensionless ratio, i.e., the shear-thickening ratio, is defined as $T = (\eta'_L - \eta'_M)/\eta'_L$, where $T > 0$ implies intra-cycle shear-thickening, whereas $T < 0$ corresponds to an intra-cycle shear-thinning behavior.

The parameters S and T are computed along the oscillatory strain ramp shown in Fig. 5.14(a) and reported in Figs. 5.14(c) and 5.14(d), respectively. At low strain amplitude, $S = T = 0$; this linear regime extends up to $\gamma_0 \simeq 25\%$, which defines the onset of the non-linear response beyond which $S > 0$ and $T > 0$ (see first vertical stripe in Fig. 5.14). Such intra-cycle strain-hardening and intra-cycle shear-thickening responses suggest that the polymer network responds non-linearly to the increasing

deformation, although the increase in stress amplitude remains linear [Fig. 5.14(b)]. Both parameters S and T increase up to a maximum reached at $\gamma_0 = 100\%$, beyond which $\sigma(\gamma_0)$ shows a sublinear increase. Then, the parameters S and T drop abruptly to become negative at the yield point $\gamma = \gamma_y \simeq 200\%$ defined by the crossover of G' and G''. The gel response is both intra-cycle strain-softening and shear-thinning, which most likely reflects the loss of integrity of the gel and its failure due to the unbinding of a sufficiently large number of hydrophobic patches. Finally, for $\gamma_0 \gtrsim 300\%$, the gel displays an intra-cycle shear-thinning response ($T < 0$), which captures the fact that the fringed micelles align under flow, together with an intra-cycle strain-hardening response ($S > 0$). The latter behavior appears paradoxical for a gel, whose constituents have been fluidized by the large amplitude oscillations. Yet, one should keep in mind that the fringed micelles composing the gel at rest can still assemble into aggregates likely to deform and respond non-linearly over the course of an oscillation.

C.3 Impact of pH on the key LAOStrain features

In this last section, we examine the role of pH on the response of acid-induced CMC gels. We focus on a 3% CMC gel and report the key features of the LAOStrain experiments in Figure 5.16, namely the onset of non-linearity γ_{NL}, the yield strain γ_y and the yield stress σ_y, the normalized amplitude of the maximum in G'' at the yield point, and the exponents characterizing the power-law decay of G' and G'' beyond the yield point. The sol-gel transition occurs at $pH_c \simeq 3$ at this CMC concentration (see Fig. 5.6). The gel properties strengthen for decreasing values of the pH as we get deeper into the gel state. Such a strengthening occurs down to pH $\simeq 2.2$ below which

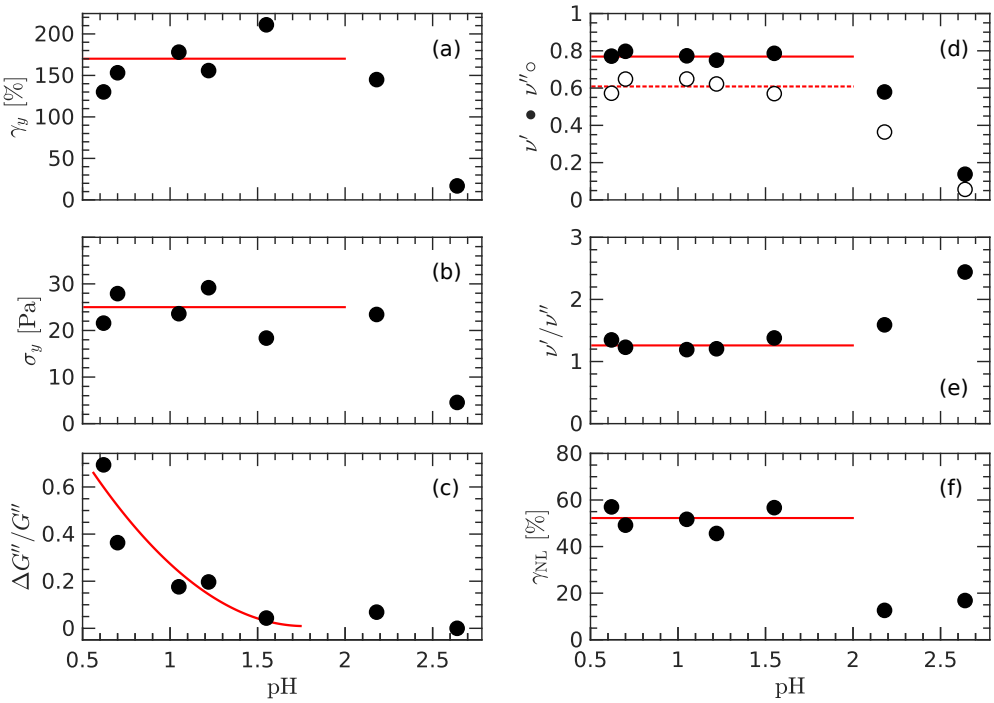

Figure 5.16: Non-linear noteworthy properties of a 3% CMC gel reported as a function of the pH. (a) yield strain γ_y and (b) yield stress σ_y defined by the crossover of G' and G'' [see Fig. 5.14(a)]. (c) Normalized amplitude of the maximum in G''. (d) Exponents ν' and ν'' characterizing the power-law decay of G' and G'' beyond the yield point; (e) ratio ν'/ν''. (f) Onset of non-linearity γ_{NL}. Red curves are guides for the eyes.

all the properties are constant: $\gamma_{NL} \simeq 55$ Pa, $\gamma_y \simeq 150$ Pa, and $\sigma_y \simeq 25$ Pa, while $\nu' \simeq 0.8$, $\nu'' \simeq 0.6$, and $\nu'/\nu'' \simeq 1.3$. However, the amplitude of the G'' overshoot at the yield point keeps growing for decreasing pH, meaning that the viscous dissipation becomes more and more pronounced as the pH of the CMC gel decreases. From a microscopic perspective, the overshoot in G'' is linked to plastic flow and originates in the *continuous* transition from recoverable to unrecoverable strain accumulation [298]. In that framework, the progressive increase of the amplitude in the G'' overshoot for decreasing pH can be interpreted as the relative decrease of the viscoelastic solid dissipation compared to the unrecoverable dissipation due to plastic flow. This result strongly suggests that the yielding transition of acid-induced CMC gels becomes spatially more heterogeneous for decreasing pH, which remains to be tested by performing time and spatially-resolved measurements across the yielding transition [369, 370].

D Conclusion

Put together, our observations offer a comprehensive picture of the acid-induced sol-gel transition. Upon acidification, CMC assemble into fringed micelles that serve as precursors for the formation of a percolated network made of CMC fibers, as evidenced by SANS measurements and strongly reminiscent of the fibrous microstructure reported for heat-induced methylcellulose gels[336, 371]. The sol-gel transition, which relies on the binding of hydrophobic patches spread along the CMC molecules, is *abrupt* both from the perspective of the gel microstructure (SANS experiments) and from that of the solvent (low-field NMR experiments). These observations support the picture of a sol-gel transition taking place at a critical density of activated hydrophobic patches, as introduced above to account for the equation of the boundary separating the sol from the gel region in the phase diagram of Fig. 5.1(b). Beyond the gel point, decreasing the pH increases the number of hydrophobic patches involved in the gel microstructure, which also induces a change in the CMC conformation. These additional crosslinkers contribute to reinforcing the gel elastic properties over a limited range of pH beyond which the elastic modulus G_0 saturates towards a plateau [see, e.g., Fig. 5.7(j) at pH < 1.5 for a 3% CMC solution]. This suggests that some hydrophobic patches, although active, do not contribute to the gel elastic properties, either due to steric constraints or to intramolecular binding. Our results provide solid ground for designing CMC-based soft composites with more complex compositions.

We have shown that acidified aqueous suspensions of carboxymethylcellulose obey a time-temperature superposition principle across the sol-gel transition. In the sol phase, the viscoelastic spectrum displays a power-law frequency dependence that is well-captured by a Fractional Maxwell model, while the viscoelastic spectrum is captured by a Kelvin-Voigt fractional model. In both cases, the activation energies extracted from the temperature dependence of the rescaling factors are compatible with the presence of hydrophobic patches along the polymer chain, driving the association of the CMC. While these two fractional models show a common power-law exponent, it remains unclear whether these two descriptions can be unified into a single model capturing the viscoelastic spectrum across the sol-gel transition, in the spirit of recent work on the sol-gel transition in aqueous dispersions of cellulose nanocrystals [58].

Acid-induced CMC gels follow the rubber elasticity model, which extends the seminal work performed on CMC gels obtained by increasing the CMC content at neutral pH [188]. Moreover, these gels display a reversible shear-induced yielding transition, which follows a Type III response under LAOStrain. Beyond the yield

point, the viscoelastic moduli display a decreasing power-law response for increasing strain amplitude. The exponents are not captured by MCT, which prompts proposing an alternative description of the shear-induced solid-to-liquid transition.

CHAPTER 5. ACID-INDUCED GELS OF CMC SOLUTIONS

CHAPTER

6

CONCLUSION

In this manuscript, we have studied a water-based dispersion of Carbon Black (CB) motivated by the application of flow batteries. This dispersion is stabilized with an associative bio-sourced polymer, namely Carboxymethylcellulose (CMC). The rheological, dielectric, and structural properties were investigated during this PhD. Hydrophobic interactions appear as a key feature in this system and they have been examined in a simpler case, which consists of acidified CMC solutions in the absence of CB particles.

Summary of the results

In Chapter 3, we presented the phase diagram of CB-CMC dispersions for different compositions ranging from CB content up to 15% and CMC concentration from 10^{-3}% to 5%. Within this phase diagram, we focused on the hydrogel region and reached for a sufficient CMC concentration to stabilize the CB, and large CB content to obtain a percolated network. We pointed out two different kinds of hydrogels depending on the CMC-to-CB ratio r. Below a critical ratio r_c, the hydrogel is electrically conductive and has a glassy mechanical behavior that displays physical aging. Above r_c, the hydrogel is not electrically conductive, and the mechanical properties arise from a polymer network cross-linked by CB clusters. We interpret the transition between these two types of gels upon increasing r as a "depercolation" transition. Scattering experiments confirmed this scenario.

In Chapter 4, we studied the CB-CMC hydrogels under large deformations, where both colloid-dominated and polymer-dominated regimes identified in the previous chapter also show a very different behavior. We followed the evolution of the structural and electrical properties to probe the impact of large deformations. These results confirm the glassy behavior of the colloid-dominated regime. In the polymer-dominated regime, the results suggest two different stress-bearing microstructures at different length scales. We implemented a rheo-conductimetry experimental protocol that has, to our knowledge, never been conducted on electronically conductive gels.

In Chapter 5, we studied acidified CMC solutions without CB. We identified signatures of a sol-gel transition with a broad array of experimental techniques including rheology, scattering, and NMR experiments. We investigated the temperature depen-

dence of the mechanical properties in the sol and gel phases. Time-temperature superposition nicely applies in both cases, and we extracted typical energies of activation which confirms that the leading interactions in the CMC are hydrophobic. Finally, the gel phase shares a lot of mechanical features with the CB-CMC hydrogels in the polymer-dominated regime, which confirms that CB particles in this regime act as cross-linkers in the polymer matrix, driven by the hydrophobic interactions between CB and CMC.

Outlooks

With the present work, we aimed to understand a novel class of CB hydrogels for potential application to flow batteries. Here, we benefit from the hydrophobic interactions brought by the CMC to stabilize the CB in water. The CMC being an *associative* polymer that may itself form a gel, our study raises the following fundamental questions.

First, we managed to build several master curves for the different viscoelastic spectra encountered throughout this manuscript. They exhibit a behavior that is very robust to changes in composition and temperature. However, the question of the scaling of the shift factors remains unanswered, and insights from modeling are needed to fully grasp the profound link between the different power-law exponents found therein.

Second, hydrophobic interactions are a highly debated question in soft matter. Further investigation on the impact of such interactions on nanocomposites would be extremely insightful. In this manuscript, we studied only one polymer with a fixed degree of substitution (DS), which we know dictates the strength of the hydrophobic interactions. Exploring the phase diagram of acidified CMC gels with different DS would provide a lot of information on their very impact. Moreover, the model proposed in this manuscript to describe the sol-gel transition explicitly depends on the DS, as the number of hydrophobic patches is set by the DS. In the CB-CMC systems, since the interactions between the CB and the CMC are supposedly hydrophobic, we speculate that the DS should have an impact on the critical ratio r_c. In particular, a lower DS should decrease the number of CMC needed to "depercolate" the CB network, leading to a lower r_c. In that framework, a better control over the spatial distribution of the hydrophobic regions within the polymer would be very helpful. Block copolymers appear as a promising material to inspect the interactions in nanocomposites. Such polymers exhibit exceptional tunability, for they are composed of different units of repetition with chosen properties and spatial arrangement [372].

Third, in the present work, the size of both the nanoparticle and the polymer were kept fixed. We should expect very different behavior depending on their size ratio [373]. For instance, if one considers the extreme case where a CMC coil is much smaller than the CB particles, the polymer may totally coat the CB, hence preventing the formation of an electronically conductive network as was observed for surfactants [89]. In the opposite limit where the CMC coil is much larger than the CB particles, we may expect several scenarios, including the wrapping of the polymer around the CB particles or each polymer bridging multiple particles, leading to completely different properties [68]. All of this ultimately depends on the relative CB-CB, CMC-CMC, CB-CMC, CB-solvent, and CMC-solvent interactions. The CB offers the possibility to change its topology, namely the size of its constitutive nodules and their fractal arrangement, which could be used to tune the interactions. Moreover, some CB are treated to change their surface properties at the nanoscale; some of them are

even hydrophilic (e.g., the PBX Carbon Black series from Cabot). It would be enriching to study the impact of the interactions on the mechanical and electrical properties of the resulting hydrogels. To even go beyond the scope of CB, fumed silica-based nanocomposites could be studied in the light of the present work. Fumed silica are nanoparticles very similar to CB with highly tunable properties as well. Their main advantage remains in their transparency, which allows direct microscopic observation of the microstructure.

Fourth, the depercolation transition deserves a whole fundamental study on its own. Namely, this transition should be studied through the lens of NMR relaxometry, following the present work on the acid-induced gelation of CMC solutions. In a less fundamental perspective, this depercolation transition may also have practical applications as the electrical and mechanical properties are extremely sensitive to the CMC concentration near the transition. With a small increase of the CMC concentration in the colloid-dominated regime near the transition, the system turns from stiff and conductive to very liquid and insulating.

Last but not least, the behavior under flow of CB-CMC hydrogels points towards a shear-induced anisotropy, which could be probed using further orthogonal superposition rheometry and 2D scattering experiments. The link between the anisotropy and the final properties of such a polymer-nanoparticle system would be insightful. The rheo-electrical experiments might also provide further evidence for anisotropy.

BIBLIOGRAPHY

[1]W. Van Saarloos et al., Soft matter: concepts, phenomena, and applications (Princeton University Press, 2024).

[2]Y. Cao et al., "Design principles of food gels", Nature Food **1**, 106–118 (2020).

[3]P. T. Spicer et al., "Complex fluid formulations: a source of inspiration and innovation", Chemical Engineering Progress **116**, 32–38 (2020).

[4]L. N. Jimenez et al., "The rheologically-complex fluid beauty of nail lacquer formulations", Soft Matter **17**, 5197–5213 (2021).

[5]M.-A. Fardin et al., "Dynamic duos: the building blocks of dimensional mechanics", arXiv preprint arXiv:2401.15101 (2024).

[6]C. W. Macosko, "Rheology principles", Measurements and Applications (1994).

[7]R. H. Ewoldt et al., "Designing complex fluids", Annual Review of Fluid Mechanics **54**, 413–441 (2022).

[8]D. Feys et al., "How do concrete rheology, tribology, flow rate and pipe radius influence pumping pressure?", Cement and Concrete Composites **66**, 38–46 (2016).

[9]F. Gastone et al., "Guar gum solutions for improved delivery of iron particles in porous media (part 1): porous medium rheology and guar gum-induced clogging", Journal of contaminant hydrology **166**, 23–33 (2014).

[10]S. M. Sajadi et al., "Direct ink writing of cement structures modified with nanoscale additive", Advanced Engineering Materials **21**, 1801380 (2019).

[11]T. Bhattacharjee et al., "Writing in the granular gel medium", Science advances **1**, e1500655 (2015).

[12]R. Edgeworth et al., "The pitch drop experiment", European Journal of Physics **5**, 198 (1984).

[13]D. Pang et al., "Dna studies using atomic force microscopy: capabilities for measurement of short dna fragments", Frontiers in molecular biosciences **2**, 1 (2015).

[14]J. Wang et al., "Adsorption and conformation of carboxymethyl cellulose at solid–liquid interfaces using spectroscopic, afm and allied techniques", Journal of Colloid and Interface Science **291**, 75–83 (2005).

[15]R. G. Larson, The structure and rheology of complex fluids, Vol. 150 (Oxford university press New York, 1999).

[16]C. McCarthy et al., "Ecological considerations of per-and polyfluoroalkyl substances (pfas)", Current Pollution Reports **3**, 289–301 (2017).

[17]Q.-F. Guan et al., "An all-natural bioinspired structural material for plastic replacement", Nature communications **11**, 5401 (2020).

[18]M. Rubinstein et al., Polymer physics (Oxford university press, 2003).

[19]F. Sciortino, "One liquid, two glasses", Nature materials **1**, 145–146 (2002).

[20]V. Trappe et al., "Jamming phase diagram for attractive particles", Nature **411**, 772–775 (2001).

[21]L. J. Kaufman et al., "Direct imaging of repulsive and attractive colloidal glasses", The Journal of chemical physics **125** (2006).

[22]P. Coussot, Rhéophysique la matière dans tous ses etats (EDP sciences, 2012).

[23]J. Mewis et al., "Thixotropy", Advances in colloid and interface science **147**, 214–227 (2009).

[24]D. Z. Rocklin et al., "Elasticity of colloidal gels: structural heterogeneity, floppy modes, and rigidity", Soft Matter (2021).

[25]R. G. Larson et al., "A review of thixotropy and its rheological modeling", Journal of Rheology **63**, 477–501 (2019).

[26]J. F. Brady et al., "Dynamic simulation of hydrodynamically interacting suspensions", Journal of Fluid Mechanics **195**, 257–280 (1988).

[27]N. J. Wagner et al., "Shear thickening in colloidal dispersions", Physics Today **62**, 27–32 (2009).

[28]E. Brown et al., "Shear thickening in concentrated suspensions: phenomenology, mechanisms and relations to jamming", Reports on Progress in Physics **77**, 046602 (2014).

[29]D. Bonn et al., "Yield stress materials in soft condensed matter", Reviews of Modern Physics **89**, 035005 (2017).

[30]P. J. Lu et al., "Colloidal particles: crystals, glasses, and gels", Annu. Rev. Condens. Matter Phys. **4**, 217–233 (2013).

[31]E. Del Gado et al., "Colloidal gelation", Fluids, Colloids and Soft Materials: An Introduction to Soft Matter Physics, John Wiley & Sons, Hoboken, 279–292 (2016).

[32]P. J. Lu et al., "Gelation of particles with short-range attraction", Nature **453**, 499–503 (2008).

[33]D. Robinson et al., "Long range order in two dimensional fractal aggregation", Physical review letters **71**, 715 (1993).

[34]L. C. Johnson et al., "Influence of structure on the linear response rheology of colloidal gels", Journal of Rheology **63**, 583–608 (2019).

[35]M. Bantawa et al., "The hidden hierarchical nature of soft particulate gels", Nature Physics **19**, 1178–1184 (2023).

[36]P. N. Pusey et al., "Phase behaviour of concentrated suspensions of nearly hard colloidal spheres", Nature **320**, 340–342 (1986).

[37]P. Pusey, "Colloidal glasses", Journal of Physics: Condensed Matter **20**, 494202 (2008).

[38]J. Bergenholtz et al., "Nonergodicity transitions in colloidal suspensions with attractive interactions", Physical Review E **59**, 5706 (1999).

[39]E. Zaccarelli et al., "Colloidal glasses and gels: the interplay of bonding and caging", Proceedings of the National Academy of Sciences **106**, 15203–15208 (2009).

[40]J. Bergenholtz et al., "Gelation in model colloid- polymer mixtures", Langmuir **19**, 4493–4503 (2003).

[41]B. Keshavarz et al., "Time–connectivity superposition and the gel/glass duality of weak colloidal gels", Proc. Natl. Acad. Sci. U.S.A. **118**, e2022339118 (2021).

[42]H. H. Winter et al., "Analysis of linear viscoelasticity of a crosslinking polymer at the gel point", Journal of rheology **30**, 367–382 (1986).

[43]F. Chambon et al., "Linear viscoelasticity at the gel point of a crosslinking pdms with imbalanced stoichiometry", Journal of Rheology **31**, 683–697 (1987).

[44]M. Geri et al., "Time-resolved mechanical spectroscopy of soft materials via optimally windowed chirps", Physical Review X **8**, 041042 (2018).

[45]J. Bauland et al., "Two-step aging dynamics in enzymatic milk gels", arXiv preprint arXiv:2403.10176 (2024).

[46]S. Liu et al., "Thermoreversible gelation and viscoelasticity of κ-carrageenan hydrogels", Journal of Rheology **60**, 203–214 (2016).

[47]H. H. Winter et al., "Rheology of polymers near liquid-solid transitions", Neutron spin echo spectroscopy viscoelasticity rheology, 165–234 (1999).

[48]S. R. Derkach, "Rheology of emulsions", Advances in colloid and interface science **151**, 1–23 (2009).

[49]I. Cantat et al., Foams: structure and dynamics (OUP Oxford, 2013).

[50]B. Schroyen et al., "Stress contributions in colloidal suspensions: the smooth, the rough, and the hairy", Physical review letters **122**, 218001 (2019).

[51]T. Rossow et al., "Supramolecular polymer networks: preparation, properties, and potential", Supramolecular Polymer Networks and Gels, 1–46 (2015).

[52]V. Trappe et al., "Investigation of q-dependent dynamical heterogeneity in a colloidal gel by x-ray photon correlation spectroscopy", Physical Review E **76**, 051404 (2007).

[53]T. Steiner, "The hydrogen bond in the solid state", Angewandte Chemie International Edition **41**, 48–76 (2002).

[54]B. W. Ninham, "On progress in forces since the dlvo theory", Advances in colloid and interface science **83**, 1–17 (1999).

[55]E. E. Meyer et al., "Recent progress in understanding hydrophobic interactions", Proceedings of the National Academy of Sciences **103**, 15739–15746 (2006).

[56]V. Trappe et al., "Scaling of the viscoelasticity of weakly attractive particles", Physical review letters **85**, 449 (2000).

[57]L. Morlet-Decarnin et al., "Slow dynamics and time–composition superposition in gels of cellulose nanocrystals", The Journal of Chemical Physics **156** (2022).

[58]L. Morlet-Decarnin et al., "Critical-like gelation dynamics in cellulose nanocrystal suspensions", ACS Macro Letters **12**, 1733–1738 (2023).

[59]M. Lin et al., "Universality in colloid aggregation", Nature **339**, 360–362 (1989).

[60]S. Costanzo et al., "Tailoring the viscoelasticity of polymer gels of gluten proteins through solvent quality", Macromolecules **53**, 9470–9479 (2020).

[61]J. E. Martin et al., "Viscoelasticity of near-critical gels", Phys. Rev. Lett. **61**, 2620–2623 (1988).

[62]J. E. Martin et al., "Viscoelasticity near the sol-gel transition", Phys. Rev. A **39**, 1325–1332 (1989).

[63]J. Jordan et al., "Experimental trends in polymer nanocomposites—a review", Materials science and engineering: A **393**, 1–11 (2005).

[64]S. Fu et al., "Some basic aspects of polymer nanocomposites: a critical review", Nano Materials Science **1**, 2–30 (2019).

[65]I. Dellatolas et al., "Local mechanism governs global reinforcement of nanofiller-hydrogel composites", ACS nano **17**, 20939–20948 (2023).

[66]T. Jiang et al., "Role of particle size and polymer length in rheology of colloid–polymer composites", Macromolecules **45**, 9791–9803 (2012).

[67]H. N. Lekkerkerker et al., Depletion interaction (Springer, 2011).

[68]M. Fuchs et al., "Structure of colloid-polymer suspensions", Journal of Physics: Condensed Matter **14**, R239 (2002).

[69]M. Surve et al., "Universality in structure and elasticity of polymer-nanoparticle gels", Phys. Rev. Lett. **96**, 177805 (2006).

[70]M. Surve et al., "Polymer-bridged gels of nanoparticles in solutions of adsorbing polymers", J. Chem. Phys. **125**, 064903 (2006).

[71]V. Ganesan et al., "Mean-field models of structure and dispersion of polymer-nanoparticle mixtures", Soft Matter **6**, 4010–4025 (2010).

[72]M. A. Winnik et al., "Associative polymers in aqueous solution", Current opinion in colloid & interface science **2**, 424–436 (1997).

[73]Z. Zhang et al., "Dynamics of associative polymers", Soft Matter **14**, 2961–2977 (2018).

[74]C. Chassenieux et al., "Rheology of associative polymer solutions", Current Opinion in Colloid & Interface Science **16**, 18–26 (2011).

[75]B. Cabane et al., "Shear induced gelation of colloidal dispersions", Journal of Rheology **41**, 531–547 (1997).

[76]J. Zebrowski et al., "Shake-gels: shear-induced gelation of laponite–peo mixtures", Colloids and Surfaces A: Physicochemical and Engineering Aspects **213**, 189–197 (2003).

[77]G. Kraus, "Reinforcement of elastomers by carbon black", Rubber chemistry and Technology **51**, 297–321 (1978).

[78]A.-C. Genix et al., "Enhancing the mechanical properties of glassy nanocomposites by tuning polymer molecular weight", ACS applied materials & interfaces **10**, 33601–33610 (2018).

[79]D. Vlassopoulos et al., "Tunable rheology of dense soft deformable colloids", Current opinion in colloid & interface science **19**, 561–574 (2014).

[80]S. K. Kumar et al., "Nanocomposites: structure, phase behavior, and properties", Annual review of chemical and biomolecular engineering **1**, 37–58 (2010).

[81]J.-C. Majesté, "Rheology and processing of polymer nanocomposites: theory, practice, and new challenges", Rheology and Processing of Polymer Nanocomposites, 69–134 (2016).

[82]A. C. Balazs et al., "Nanoparticle polymer composites: where two small worlds meet", Science **314**, 1107–1110 (2006).

[83]T. M. Narayanan et al., "Low-cost manganese dioxide semi-solid electrode for flow batteries", Joule **5**, 2934–2954 (2021).

[84]G. Assat et al., "Fundamental understanding and practical challenges of anionic redox activity in li-ion batteries", Nature Energy **3**, 373–386 (2018).

[85]H. Parant et al., "Flowing suspensions of carbon black with high electronic conductivity for flow applications: comparison between carbons black and exhibition of specific aggregation of carbon particles", Carbon **119**, 10–20 (2017).

[86]E. N'gouamba, "Rhéologie des suspensions aqueuses de noir de carbone et de fluides à seuil modèles dans leur régime solide", PhD thesis (Paris Est, 2020).

[87]C. Dennison et al., "In situ distributed diagnostics of flowable electrode systems: resolving spatial and temporal limitations", Physical Chemistry Chemical Physics **16**, 18241–18252 (2014).

[88]M. Meslam et al., "Promising aqueous dispersions of carbon black for semisolid flow battery application", Colloids Surf. A: Physicochem. Eng. Asp., 129376 (2022).

[89]K. Lee et al., "Surfactant induced catastrophic collapse of carbon black suspensions used in flow battery application", Journal of Colloid and Interface Science **633**, 712–722 (2023).

[90]S. Porada et al., "Carbon flow electrodes for continuous operation of capacitive deionization and capacitive mixing energy generation", Journal of Materials Chemistry A **2**, 9313–9321 (2014).

[91]K. B. Hatzell et al., "Direct observation of active material interactions in flowable electrodes using x-ray tomography", Faraday discussions **199**, 511–524 (2017).

[92]International Carbon Black Association, Carbon black user's guide, https://www.carbon-black.org/resources-from-icba, [Online; accessed 15-May-2024], 2016.

[93]R. Samson et al., "Structural analysis of soot agglomerates", Langmuir **3**, 272–281 (1987).

[94]H. J. Spinelli, "Polymeric dispersants in ink jet technology", Adv. Mater. **10**, 1215–1218 (1998).

[95]C. Phillips et al., "The effect of graphite and carbon black ratios on conductive ink performance", J. Mater. Sci. **52**, 9520–9530 (2017).

[96]F. Ehrburger-Dolle et al., "Anisotropic ultra-small-angle x-ray scattering in carbon black filled polymers", Langmuir **17**, 329–334 (2001).

[97]J.-C. Huang, "Carbon black filled conducting polymers and polymer blends", Adv. Polym. Technol. **21**, 299–313 (2002).

[98]S. Wen et al., "Partial replacement of carbon fiber by carbon black in multifunctional cement–matrix composites", Carbon **45**, 505–513 (2007).

[99]A. Pandolfo et al., "Carbon properties and their role in supercapacitors", J. Power Sources **157**, 11–27 (2006).

[100]T. A. Silva et al., "Electrochemical biosensors based on nanostructured carbon black: a review", J. Nanomater. **2017** (2017).

[101]R. Kour et al., "Recent advances in carbon nanomaterials as electrochemical biosensors", J. Electrochem. Soc. **167**, 037555 (2020).

[102]F. Arduini et al., "Carbon black as an outstanding and affordable nanomaterial for electrochemical (bio) sensor design", Biosensors and Bioelectronics **156**, 112033 (2020).

[103]M. Duduta et al., "Semi-solid lithium rechargeable flow battery", Adv. Energy Mater. **1**, 511–516 (2011).

[104]Z. Li et al., "Aqueous semi-solid flow cell: demonstration and analysis", Phys. Chem. Chem. Phys. **15**, 15833–15839 (2013).

[105]M. Youssry et al., "Non-aqueous carbon black suspensions for lithium-based redox flow batteries: rheology and simultaneous rheo-electrical behavior", Phys. Chem. Chem. Phys. **15**, 14476–14486 (2013).

[106]A. Narayanan et al., "Mechanical history dependence in carbon black suspensions for flow batteries: a rheo-impedance study", Langmuir **33**, 1629–1638 (2017).

[107]T. M. Narayanan et al., "Low-cost manganese dioxide semi-solid electrode for flow batteries", Joule **5**, 2934–2954 (2021).

[108]S. Khodabakhshi et al., "Carbon black reborn: structure and chemistry for renewable energy harnessing", Carbon **162**, 604–649 (2020).

[109]S.-L. Chou et al., "Small things make a big difference: binder effects on the performance of li and na batteries", Phys. Chem. Chem. Phys. **16**, 20347–20359 (2014).

[110]M. Youssry et al., "Aqueous dispersions of carbon black and its hybrid with carbon nanofibers", RSC advances **8**, 32119–32131 (2018).

[111]M. van der Waarden, "Stabilization of carbon black dispersion in hydrocarbons", J. Colloid Sci. **5**, 317–325 (1950).

[112]P. Hartley et al., "Dispersion of powders in liquids. 1. the contribution of the van der waals force to the cohesiveness of carbon black powders", Langmuir **1**, 651–657 (1985).

[113]V. Trappe et al., "Investigation of q-dependent dynamical heterogeneity in a colloidal gel by x-ray photon correlation spectroscopy", Phys. Rev. E **76**, 051404 (2007).

[114]M. Kawaguchi et al., "Rheological properties of carbon black suspensions in a silicone oil", Langmuir **17**, 6041–6044 (2001).

[115]T. Gibaud et al., "Heterogeneous yielding dynamics in a colloidal gel", Soft Matter **6**, 3482–3488 (2010).

[116]J. Sprakel et al., "Stress enhancement in the delayed yielding of colloidal gels", Physical review letters **106**, 248303 (2011).

[117]V. Grenard et al., "Timescales in creep and yielding of attractive gels", Soft matter **10**, 1555–1571 (2014).

[118]T. Gibaud et al., "Multiple yielding processes in a colloidal gel under large amplitude oscillatory stress", Soft Matter **12**, 1701–1712 (2016).

[119]G. Ovarlez et al., "Rheopexy and tunable yield stress of carbon black suspensions", Soft Matter **9**, 5540–5549 (2013).

[120]T. Divoux et al., "Rheological hysteresis in soft glassy materials", Physical review letters **110**, 018304 (2013).

[121]H. Helal et al., "Simultaneous rheo-electric measurements of strongly conductive complex fluids", Phys. Rev. Applied **6**, 064004 (2016).

[122]G. A. Kelesidis et al., "Process design for carbon black size and morphology", Carbon, 118255 (2023).

[123]F. H. Amon et al., Process of making hydrophilic carbon black, US Patent 2,439,442, Apr. 1948.

[124]P. Z. Ramos et al., "Evaluating the rheo-electric performance of aqueous suspensions of oxidized carbon black", Journal of Colloid and Interface Science **634**, 379–387 (2023).

[125]J. J. Richards et al., "Clustering and percolation in suspensions of carbon black", Langmuir **33**, 12260–12266 (2017).

[126]M. Carmo et al., "Physical and electrochemical evaluation of commercial carbon black as electrocatalysts supports for dmfc applications", Journal of Power Sources **173**, 860–866 (2007).

[127]H. Y. Li et al., "Polymer-encapsulated hydrophilic carbon black nanoparticles free from aggregagtion", Colloid Surf. A: Physicocgem Eng. Aspect **254**, 173–178 (2005).

[128]J. Paredes et al., "Nanoscale investigation of the structural and chemical changes induced by oxidation on carbon black surfaces: a scanning probe microscopy approach", J. Colloid Interface Sci. **288**, 190–199 (2005).

[129]T. Liu et al., "Grafting poly (n-butyl acrylate) from a functionalized carbon black surface by atom transfer radical polymerization", Langmuir **19**, 6342–6345 (2003).

[130]T. Liu et al., "Water-dispersible carbon black nanocomposites prepared by surface-initiated atom transfer radical polymerization in protic media", Macromolecules **39**, 548–556 (2006).

[131]J.-H. Lin et al., "A novel method for grafting polymers on carbon blacks", J. Mater. Chem. **8**, 2169–2173 (1998).

[132]N. Tsubokawa, "Functionalization of carbon material by surface grafting of polymers", Bull. Chem. Soc. Jpn. **75**, 2115–2136 (2002).

[133]Q. Yang et al., "A temperature-responsive carbon black nanoparticle prepared by surface-induced reversible addition–fragmentation chain transfer polymerization", Polymer **48**, 3444–3451 (2007).

[134]Y. Pei et al., "Water structure change-induced expansion and collapse of zwitterionic polymers surface-grafted onto carbon black", Aust. J. Chem. **67**, 1706–1709 (2014).

[135]L. Wang et al., "Surface modification of carbon black by thiolene click reaction for improving dispersibility in aqueous phase", J. Dispers. Sci. Technol. **40**, 152–160 (2019).

[136]F. Tiarks et al., "Encapsulation of carbon black by miniemulsion polymerization", Macromol. Chem. Phys. **202**, 51–60 (2001).

[137]R. M. Casado et al., "Polymer encapsulation of surface-modified carbon blacks using surfactant-free emulsion polymerisation", Polymer **48**, 2554–2563 (2007).

[138]B. R. Alves et al., "Colloid stabilisation by polyelectrolytes. dispersions of carbon black in aqueous poly (acrylic acid) solution", J. Chem. Soc., Faraday Trans. 1 **77**, 889–896 (1981).

[139]M. Iijima et al., "Effect of structure of cationic dispersants on stability of carbon black nanoparticles and further processability through layer-by-layer surface modification", Chem. Eng. Sci. **85**, 30–37 (2013).

[140]Y. Hanada et al., "Analysis of dispersion and aggregation behavior of carbon black particles in aqueous suspension by colloid probe afm method", Adv. Powder Technol. **24**, 844–851 (2013).

[141]T. Ogura et al., "Behavior of surfactants in the suspension of coal components", Bull. Chem. Soc. Jpn. **66**, 1633–1639 (1993).

[142]T. Ogura et al., "The role of surfactants in achieving highly loaded aqueous suspensions of organic particles", Bull. Chem. Soc. Jpn. **67**, 3143–3149 (1994).

[143]S. D. Gupta et al., "Adsorption of surfactants on carbon black-water interface", J. Dispers. Sci. Technol. **26**, 111–120 (2005).

[144]Y. Zhao et al., "Adsorption mechanism of sodium dodecyl benzene sulfonate on carbon blacks by adsorption isotherm and zeta potential determinations", Environ. Technol. **34**, 201–207 (2013).

[145]H. Mizukawa et al., "Effects of perfluorosulfonic acid adsorption on the stability of carbon black suspensions", Langmuir **25**, 11984–11987 (2009).

[146]S. Subramanian et al., "Aqueous carbon black dispersions stabilized by sodium lignosulfonates", Colloid Polym. Sci. **299**, 1223–1236 (2021).

[147]M. Celik, "Adsorption of ethoxylated sulfonate and nonionic homologs on coal", J. Colloid Interface Sci. **129**, 428–440 (1989).

[148]M. Bele et al., "Adsorption of cetyltrimethylammonium bromide on carbon black from aqueous solution", Carbon **36**, 1207–1212 (1998).

[149]W. Porcher et al., "Optimizing the surfactant for the aqueous processing of lifepo4 composite electrodes", J. Power Sources **195**, 2835–2843 (2010).

[150]C. Eisermann et al., "Stabilization of carbon black particles with cetyltrimethylammoniumbromide in aqueous media", Power Technology **253**, 338–346 (2014).

[151]H. Ridaoui et al., "Effect of cationic surfactant and block copolymer on carbon black particle surface charge and size", Colloids Surf. A: Physicochem. Eng. Asp. **278**, 149–159 (2006).

[152]H. Sis et al., "Effect of nonionic and ionic surfactants on zeta potential and dispersion properties of carbon black powders", Colloids Surf. A: Physicochem. Eng. Asp. **341**, 60–67 (2009).

[153]Y. Lin et al., "Adsorption of a rake-type siloxane surfactant onto carbon black nanoparticles dispersed in aqueous media", Langmuir **18**, 6147–6158 (2002).

[154]F. Miano et al., "Adsorption of nonyl phenol propylene oxide—ethylene oxide surfactants on carbon black and the rheology of the resulting dispersions", Colloids Surf. **62**, 111–118 (1992).

[155]S. Yasin et al., "Investigating the effectiveness of peo/ppo based copolymers as dispersing agents for graphitic carbon black aqueous dispersions", Colloids Surf. A: Physicochem. Eng. Asp. **404**, 25–35 (2012).

[156]E. N'gouamba et al., "Yielding, thixotropy, and strain stiffening of aqueous carbon black suspensions", Journal of Rheology **64**, 955–968 (2020).

[157]A. Guerfi et al., "Lifepo4 water-soluble binder electrode for li-ion batteries", J. Power Sources **163**, 1047–1052 (2007).

[158]J.-H. Lee et al., "Effect of carboxymethyl cellulose on aqueous processing of lifepo4 cathodes and their electrochemical performance", Electrochem. Solid-State Lett. **11**, A175 (2008).

[159]W. Porcher et al., "Design of aqueous processed thick lifepo4 composite electrodes for high-energy lithium battery", J. Electrochem. Soc. **156**, A133 (2008).

[160]A. García et al., "Stability and rheological study of sodium carboxymethyl cellulose and alginate suspensions as binders for lithium ion batteries", J. Appl. Polym. Sci. **135**, 46217 (2018).

[161]C. Barrie et al., "Rheology of aqueous carbon black dispersions", J. Colloid Interface Sci. **272**, 210–217 (2004).

[162]Y. Aoki et al., "Rheology of carbon black suspensions. i. three types of viscoelastic behavior", Rheol. Acta **42**, 209–216 (2003).

[163]V. Varshney et al., "Chemical functionalization of cellulose derived from nonconventional sources", Cellulose Fibers: Bio-and nano-polymer composites: Green chemistry and technology, 43–60 (2011).

[164]V. Gupta et al., "Cellulose: a review as natural, modified and activated carbon adsorbent", Bioresource technology **216**, 1066–1076 (2016).

[165]T. Heinze et al., "Studies on the synthesis and characterization of carboxymethylcellulose", Angew. Makromolek. Chem. **266**, 37–45 (1999).

[166]V. Kanikireddy et al., "Carboxymethyl cellulose-based materials for infection control and wound healing: a review", International Journal of Biological Macromolecules **164**, 963–975 (2020).

[167]M. S. Rahman et al., "Recent developments of carboxymethyl cellulose", Polymers **13**, 1345 (2021).

[168]C. Clasen et al., "Determination of viscoelastic and rheo-optical material functions of water-soluble cellulose derivatives", Progress in polymer science **26**, 1839–1919 (2001).

[169]Y. Sheng et al., "Dual-drug delivery system based on the hydrogels of alginate and sodium carboxymethyl cellulose for colorectal cancer treatment", Carbohydr. Polym. **269**, 118325 (2021).

[170]J. S. Yaradoddi et al., "Biodegradable carboxymethyl cellulose based material for sustainable packaging application", Sci. Rep. **10**, 21960 (2020).

[171]L. Jiang et al., "Preparation and characterization of a novel composite containing carboxymethyl cellulose used for bone repair", Mater. Sci. Eng. C **29**, 193–198 (2009).

[172]W.-M. Kulicke et al., "Characterization of aqueous carboxymethylcellulose solutions in terms of their molecular structure and its influence on rheological behaviour", Polymer **37**, 2723–2731 (1996).

[173]M. T. Ghannam et al., "Rheological properties of carboxymethyl cellulose", J. Appl. Polym. Sci. **64**, 289–301 (1997).

[174]A. Benchabane et al., "Rheological properties of carboxymethyl cellulose (cmc) solutions", Colloid and Polymer Science **286**, 1173–1180 (2008).

[175]X. H. Yang et al., "Viscosity properties of sodium carboxymethylcellulose solutions", Cellulose **14**, 409–417 (2007).

[176]C. G. Lopez et al., "Viscosity and scaling of semiflexible polyelectrolyte nacmc in aqueous salt solutions", Macromolecules **50**, 332–338 (2017).

[177]J. S. Behra et al., "Characterization of sodium carboxymethyl cellulose aqueous solutions to support complex product formulation: a rheology and light scattering study", ACS Appl. Mater. Interfaces. **1**, 344–358 (2019).

[178]C. G. Lopez, "Entanglement of semiflexible polyelectrolytes: crossover concentrations and entanglement density of sodium carboxymethyl cellulose", J. Rheol. **64**, 191–204 (2020).

[179]C. G. Lopez et al., "Electrostatic and hydrophobic interactions in nacmc aqueous solutions: effect of degree of substitution", Macromolecules **51**, 3165–3175 (2018).

[180]T. F. Liebert et al., "Exploitation of reactivity and selectivity in cellulose functionalization using unconventional media for the design of products showing new superstructures", Biomacromolecules **2**, 1124–1132 (2001).

[181]E. Ott et al., "Observations on the thixotropy and structural characteristics of sodium carboxymethylcellulose", Die Makromolekulare Chemie: Macromolecular Chemistry and Physics **18**, 352–366 (1956).

[182]E. DeButts et al., "Rheology of sodium carboxymethylcellulose solutions", Industrial & Engineering Chemistry **49**, 94–98 (1957).

[183]J. H. Elliot et al., "Some rheological properties of sodium carboxymethylcellulose solutions and gels", Rheol. Acta **13**, 670–674 (1974).

[184]H. Hakert et al., "Rheological and electron microscopic characterization of aqueous carboxymethyl cellulose gels part i: rheological aging of aqueous gels of carboxymethyl cellulose in the free acid form (hcmc)", Colloid Polym. Sci. **267**, 226–229 (1989).

[185]U. Kastner et al., "Structure and solution properties of sodium carboxymethyl cellulose", Colloids Surf. **123**, 307–328 (1997).

[186]C. Barba et al., "Synthesis and characterization of carboxymethylcelluloses from non-wood pulps ii. rheological behavior of cmc in aqueous solution", Cellulose **9**, 327–335 (2002).

[187]I. Dogsa et al., "Amorphous supramolecular structure of carboxymethyl cellulose in aqueous solution at different ph values as determined by rheology, small angle x-ray and light scattering", Carbohydr. Polym. **111**, 492–504 (2014).

[188]J. Hermans Jr, "Investigation of the elastic properties of the particle network in gelled solutions of hydrocolloids. i. carboxymethyl cellulose", J. Polym. Sci., Part A: Polym. Chem. **3**, 1859–1868 (1965).

[189]C. G. Lopez et al., "Oscillatory rheology of carboxymethyl cellulose gels: influence of concentration and ph", Carbohydr. Polym. **267**, 118117 (2021).

[190]C. Hoogendam et al., "Persistence length of carboxymethyl cellulose as evaluated from size exclusion chromatography and potentiometric titrations", Macromolecules **31**, 6297–6309 (1998).

[191]P. Oswald, Rhéophysique. ou comment coule la matière: ou comment coule la matière (Humensis, 2015).

[192]B. Radovskiy et al., "Relaxation modulus and complex modulus", in (Jan. 2018), pp. 41–72.

[193]R. H. Ewoldt et al., "Large amplitude oscillatory shear of pseudoplastic and elasto-viscoplastic materials", Rheologica acta **49**, 191–212 (2010).

[194]V. H. Rolon-Garrido et al., "The damping function in rheology", Rheologica Acta **48**, 245–284 (2009).

[195]R. H. Ewoldt et al., "New measures for characterizing nonlinear viscoelasticity in large amplitude oscillatory shear", Journal of Rheology **52**, 1427–1458 (2008).

[196]P. Lidon, "Effet d'ultrasons de puissance sur les matériaux mous : vers des matériaux "acousto-rhéologiques"", Theses (Université de Lyon, July 2016).

[197]P. Coussot, "Rheophysics", Matter in all its states, Paris-Est: Springer (2014).

[198]R. H. Ewoldt et al., "Experimental challenges of shear rheology: how to avoid bad data", in Complex fluids in biological systems (Springer, 2015), pp. 207–241.

[199]M. Mours et al., "Time-resolved rheometry", Rheologica Acta **33**, 385–397 (1994).

[200]S. Jamali et al., "The mnemosyne number and the rheology of remembrance", Journal of Rheology **66**, 1027–1039 (2022).

[201]S. H. Sung et al., "Orthogonal superposition rheometry of colloidal gels: time-shear rate superposition", Soft Matter **14**, 8651–8659 (2018).

[202]J. Vermant et al., "Orthogonal superposition measurements using a rheometer equipped with a force rebalanced transducer", Review of scientific instruments **68**, 4090–4096 (1997).

[203]G. Colombo et al., "Superposition rheology and anisotropy in rheological properties of sheared colloidal gels", Journal of Rheology **61**, 1035–1048 (2017).

[204]R. Tao et al., "End effect correction for orthogonal small strain oscillatory shear in a rotational shear rheometer", Rheologica Acta **59**, 95–108 (2020).

[205]J. Song et al., "Non-maxwellian viscoelastic stress relaxations in soft matter", Soft Matter **19**, 7885–7906 (2023).

[206]A. Serra-Aguila et al., "Viscoelastic models revisited: characteristics and interconversion formulas for generalized kelvin–voigt and maxwell models", Acta Mechanica Sinica **35**, 1191–1209 (2019).

[207]R. F. Schmidt et al., "Comparison of classical and fractional viscoelastic models for describing entangled polymer solutions", chemXiv preprint doi:10.26434/chemrxiv-2024-hff6n (2024).

[208]G. S. Blair et al., "Limitations of the newtonian time scale in relation to non-equilibrium rheological states and a theory of quasi-properties", Proceedings of the Royal Society of London. Series A. Mathematical and Physical Sciences **189**, 69–87 (1947).

[209]G. S. Blair et al., "Vi. an application of the theory of quasi-properties to the treatment of anomalous strain-stress relations", The London, Edinburgh, and Dublin Philosophical Magazine and Journal of Science **40**, 80–94 (1949).

[210]A. Jaishankar et al., "Power-law rheology in the bulk and at the interface: quasi-properties and fractional constitutive equations", Proceedings of the Royal Society A: Mathematical, Physical and Engineering Sciences **469**, 20120284 (2013).

[211]G. W. Scott-Blair et al., "On the creep, recovery, relaxation and elastic" memory" of some renneted milk gels", Br. J. Appl. Phys. **10**, 15 (1959).

[212]P. Kollmannsberger et al., "Linear and nonlinear rheology of living cells", Annual review of materials research **41**, 75–97 (2011).

[213]P. Sollich et al., "Rheology of soft glassy materials", Phys. Rev. Lett. **78**, 2020 (1997).

[214]P. Sollich, "Rheological constitutive equation for a model of soft glassy materials", Phys. Rev. E **58**, 738–759 (1998).

[215]J.-P. Bouchaud, "Weak ergodicity breaking and aging in disordered systems", Journal de Physique I **2**, 1705–1713 (1992).

[216]C. Monthus et al., "Models of traps and glass phenomenology", Journal of Physics A: Mathematical and General **29**, 3847 (1996).

[217]E. Purnomo et al., "Linear viscoelastic properties of aging suspensions", Europhys. Lett. **76**, 74 (2006).

[218]E. H. Purnomo et al., "Glass transition and aging in dense suspensions of thermosensitive microgel particles", Phys. Rev. Lett. **101**, 238301 (2008).

[219]S. M. Fielding et al., "Aging and rheology in soft materials", J. Rheol. **44**, 323–369 (2000).

[220]L. Cipelletti et al., "Slow dynamics in glassy soft matter", Journal of Physics: Condensed Matter **17**, R253 (2005).

[221]R. Lionberger et al., "High frequency modulus of hard sphere colloids", Journal of Rheology **38**, 1885–1908 (1994).

[222]I. De Schepper et al., "Viscoelasticity in dense hard sphere colloids", Physical review letters **70**, 2178 (1993).

[223]T. Mason et al., "Linear viscoelasticity of colloidal hard sphere suspensions near the glass transition", Physical review letters **75**, 2770 (1995).

[224]K. Hyun et al., "A review of nonlinear oscillatory shear tests: analysis and application of large amplitude oscillatory shear (laos)", Progress in polymer science **36**, 1697–1753 (2011).

[225]M. Kamkar et al., "Large amplitude oscillatory shear flow: microstructural assessment of polymeric systems", Progress in Polymer Science **132**, 101580 (2022).

[226]K. Hyun et al., "Large amplitude oscillatory shear as a way to classify the complex fluids", Journal of Non-Newtonian Fluid Mechanics **107**, 51–65 (2002).

[227]A. Ahuja et al., "Two step yielding in soft materials", Advances in Colloid and Interface Science **282**, 102179 (2020).

[228]K. Miyazaki et al., "Nonlinear viscoelasticity of metastable complex fluids", EPL (Europhysics Letters) **75**, 915 (2006).

[229]S. A. Rogers et al., "A sequence of physical processes determined and quantified in laos: application to a yield stress fluid", Journal of Rheology **55**, 435–458 (2011).

[230]W. H. Herschel et al., "Konsistenzmessungen von gummi-benzollösungen", Kolloid-Zeitschrift **39**, 291–300 (1926).

[231]M. Caggioni et al., "Variations of the herschel–bulkley exponent reflecting contributions of the viscous continuous phase to the shear rate-dependent stress of soft glassy materials", Journal of Rheology **64**, 413–422 (2020).

[232]S. P. Meeker et al., "Slip and flow in pastes of soft particles: direct observation and rheology", Journal of Rheology **48**, 1295–1320 (2004).

[233]M. Cloitre et al., "A review on wall slip in high solid dispersions", Rheologica Acta **56**, 283–305 (2017).

[234]R. Radhakrishnan et al., "Understanding rheological hysteresis in soft glassy materials", Soft Matter **13**, 1834–1852 (2017).

[235]T. Divoux et al., "Transient shear banding in a simple yield stress fluid", Physical review letters **104**, 208301 (2010).

[236]F. Da Cruz et al., "Viscosity bifurcation in granular materials, foams, and emulsions", Physical Review E **66**, 051305 (2002).

[237]W. Cox et al., "Rheology of polymer melts—a correlation of dynamic and steady flow measurements", in International symposium on plastics testing and standardization (ASTM International, 1959).

[238]J. B. Jorcin et al., "Cpe analysis by local electrochemical impedance spectroscopy", Electrochim. Acta **51**, 1473–1479 (2006).

[239]A. Helal et al., "Simultaneous rheoelectric measurements of strongly conductive complex fluids", Physical Review Applied **6**, 064004 (2016).

[240]J. Jamnik et al., "Treatment of the impedance of mixed conductors equivalent circuit model and explicit approximate solutions", J. Electrochem. Soc. **146**, 4183 (1999).

[241]S. M. R. Niya et al., "On a possible physical origin of the constant phase element", Electrochimica Acta **188**, 98–102 (2016).

[242]M. Schalenbach et al., "Physicochemical mechanisms of the double-layer capacitance dispersion and dynamics: an impedance analysis", J. Phys. Chem. C **125**, 5870–5879 (2021).

[243]J. R. Macdonald et al., Impedance spectroscopy: theory, experiment, and applications (John Wiley & Sons, 2018).

[244]A. Lasia, "The origin of the constant phase element", J. Phys. Chem. Lett. **13**, 580–589 (2022).

[245]R. Garrappa, "Numerical solution of fractional differential equations: a survey and a software tutorial", Mathematics **6**, 16 (2018).

[246]R. W. Brown et al., Magnetic resonance imaging: physical principles and sequence design (John Wiley & Sons, 2014).

[247]H. Y. Carr et al., "Effects of diffusion on free precession in nuclear magnetic resonance experiments", Phys. Rev. **94**, 630 (1954).

[248]S. Meiboom et al., "Modified spin-echo method for measuring nuclear relaxation times", Rev. Sci. Instrum. **29**, 688–691 (1958).

[249]I. Sudreau, "Dispersions de boehmite sous cisaillement : anisotropie structurale, rhéologie et effets mémoire", 2022ENSL0023, PhD thesis (2022).

[250]P. Lindner et al., "Neutron, x-ray and light scattering: introduction to an investigative tool for colloidal and polymeric systems", (1991).

[251]A. Peterlin, "Small angle scattering by a three component system", Die Makromolekulare Chemie: Macromolecular Chemistry and Physics **87**, 152–165 (1965).

[252]R. Coalson et al., "Small angle scattering by a three-component system. testing the theory for light scattering", in Journal of polymer science part c: polymer symposia, Vol. 13, 1 (Wiley Online Library, 1966), pp. 123–131.

[253]R. Ottewill et al., "Small-angle neutron scattering studies on binary mixtures of charged particles", Langmuir **11**, 3757–3765 (1995).

[254]B. Hammouda, "Probing nanoscale structures-the sans toolbox", National Institute of Standards and Technology, 1–717 (2008).

[255]C. G. Lopez et al., "Structure of sodium carboxymethyl cellulose aqueous solutions: a sans and rheology study", Journal of Polymer Science Part B: Polymer Physics **53**, 492–501 (2015).

[256]N. Dagès et al., "Mechanics and structure of carbon black gels under high-power ultrasound", Journal of Rheology **65**, 477–490 (2021).

[257]C. Sorensen et al., "Test of static structure factors for describing light scattering from fractal soot aggregates", Langmuir **8**, 2064–2069 (1992).

[258]D. Mildner et al., "Small-angle scattering from porous solids with fractal geometry", Journal of Physics D: Applied Physics **19**, 1535 (1986).

[259]J. Krzywon, Http://www.sasview.org/.

[260]B. Hammouda, "A new guinier–porod model", J. Appl. Crystallogr. **43**, 716–719 (2010).

[261]P. Munier et al., "Rheo-saxs study of shear-induced orientation and relaxation of cellulose nanocrystal and montmorillonite nanoplatelet dispersions", Soft Matter **18**, 390–396 (2022).

[262]O. G. Shpyrko, "X-ray photon correlation spectroscopy", Journal of synchrotron radiation **21**, 1057–1064 (2014).

[263]P. Alexander et al., "Effect of x-rays and γ-rays on synthetic polymers in aqueous solution", Journal of Polymer Science **23**, 355–375 (1957).

[264]S. Dierker et al., "X-ray photon correlation spectroscopy study of brownian motion of gold colloids in glycerol", Physical Review Letters **75**, 449 (1995).

[265]R. L. Leheny, "Xpcs: nanoscale motion and rheology", Current opinion in colloid & interface science **17**, 3–12 (2012).

[266]B. Le Ouay et al., "Dwcnt-doped silica gel exhibiting both ionic and electronic conductivities", J. Phys. Chem. C **116**, 11306–11314 (2012).

[267]M. Youssry et al., "Suspensions of carbon nanofibers in organic medium: rheo-electrical properties", Phys. Chem. Chem. Phys. **17**, 32316–32327 (2015).

[268]K. S. Cole, "Electric impedance of suspensions of spheres", The Journal of general physiology **12**, 29 (1928).

[269]G. P. Baeza et al., "Depercolation of aggregates upon polymer grafting in simplified industrial nanocomposites studied with dielectric spectroscopy", Polymer **73**, 131–138 (2015).

[270]A. Bonfanti et al., "Fractional viscoelastic models for power-law materials", Soft Matter **16**, 6002–6020 (2020).

[271]B. H. Zimm, "Dynamics of polymer molecules in dilute solution: viscoelasticity, flow birefringence and dielectric loss", J. Chem. Phys. **24**, 269–278 (1956).

[272]R. L. Bagley et al., "A theoretical basis for the application of fractional calculus to viscoelasticity", J. Rheol. **27**, 201–210 (1983).

[273]E. E. Pashkovski et al., "Viscoelastic scaling of colloidal gels in polymer solutions", Langmuir **19**, 3589–3595 (2003).

[274]V. Adibnia et al., "Viscoelasticity of near-critical silica-polyacrylamide hydrogel nanocomposites", Polymer **112**, 457–465 (2017).

[275]R. H. Colby et al., "Chain entanglement in polymer melts and solutions", Macromolecules **25**, 996–998 (1992).

[276]T. G. Mason et al., "Optical measurements of frequency-dependent linear viscoelastic moduli of complex fluids", Phys. Rev. Lett. **74**, 1250 (1995).

[277]S. Aime et al., "Power law viscoelasticity of a fractal colloidal gel", J. Rheol. **62**, 1429–1441 (2018).

[278]V. Prasad et al., "Universal features of the fluid to solid transition for attractive colloidal particles", Faraday Discuss. **123**, 1–12 (2003).

[279]G. P. Baeza et al., "Multiscale filler structure in simplified industrial nanocomposite silica/sbr systems studied by saxs and tem", Macromolecules **46**, 317–329 (2013).

[280]G. Brambilla et al., "Probing the equilibrium dynamics of colloidal hard spheres above the mode-coupling glass transition", arXiv preprint arXiv:0809.3401 (2008).

[281]S. Srivastava et al., "Hyperdiffusive dynamics in newtonian nanoparticle fluids", ACS Macro Letters **4**, 1149–1153 (2015).

[282]A. Jain et al., "Three-step colloidal gelation revealed by time-resolved x-ray photon correlation spectroscopy", The Journal of Chemical Physics **157** (2022).

[283]T. Hoshino et al., "Dynamical crossover between hyperdiffusion and subdiffusion of polymer-grafted nanoparticles in a polymer matrix", Physical Review E **88**, 032602 (2013).

[284]L. Cipelletti et al., "Universal aging features in the restructuring of fractal colloidal gels", Physical review letters **84**, 2275 (2000).

[285]O. D. Parashchuk et al., "Hyperdiffusive dynamics in conjugated polymer blends and fullerene absorbing solutions", Soft Matter **7**, 5585–5594 (2011).

[286]M. Bouzid et al., "Elastically driven intermittent microscopic dynamics in soft solids", Nature communications **8**, 15846 (2017).

[287]P.-K. Kao et al., "Microstructure and elasticity of dilute gels of colloidal discoids", Soft Matter **18**, 1350–1363 (2022).

[288]H. Wu et al., "A model relating structure of colloidal gels to their elastic properties", Langmuir **17**, 1030–1036 (2001).

[289]C. Derec et al., "Aging and nonlinear rheology in suspensions of polyethylene oxide–protected silica particles", Physical Review E **67**, 061403 (2003).

[290]M. E. Helgeson et al., "Viscoelasticity and shear melting of colloidal star polymer glasses", Journal of Rheology **51**, 297–316 (2007).

[291]J.-H. Lee et al., "Effect of carboxymethyl cellulose on aqueous processing of natural graphite negative electrodes and their electrochemical performance for lithium batteries", J. Electrochem. Soc. **152**, A1763 (2005).

[292]M. Dahbi et al., "Sodium carboxymethyl cellulose as a potential binder for hard-carbon negative electrodes in sodium-ion batteries", Electrochem. commun. **44**, 66–69 (2014).

[293]E. Bozaci et al., "Application of carboxymethylcellulose hydrogel based silver nanocomposites on cotton fabrics for antibacterial property", Carbohydr. Polym. **134**, 128–135 (2015).

[294]N. H. Ali et al., "Sodium carboxymethyl cellulose hydrogels containing reduced graphene oxide (rgo) as a functional antibiofilm wound dressing", J. Biomater. Sci. Polym. Ed. **30**, 629–645 (2019).

[295]M. L. Saladino et al., "Graphene oxide carboxymethylcellulose nanocomposite for dressing materials", Materials **13**, 1980 (2020).

[296]F. J. Müller et al., "Toughening colloidal gels using rough building blocks", Nature Communications **14**, 5309 (2023).

[297]A. R. Payne, "The dynamic properties of carbon black-loaded natural rubber vulcanizates. part i", Journal of applied polymer science **6**, 57–63 (1962).

[298]G. J. Donley et al., "Elucidating the g" overshoot in soft materials with a yield transition via a time-resolved experimental strain decomposition", Proceedings of the National Academy of Sciences **117**, 21945–21952 (2020).

[299]N. Koumakis et al., "Two step yielding in attractive colloids: transition from gels to attractive glasses", Soft Matter **7**, 2456–2470 (2011).

[300]K. Pham et al., "Yielding of colloidal glasses", EPL (Europhysics Letters) **75**, 624 (2006).

[301]M. D. Graham, "Wall slip and the nonlinear dynamics of large amplitude oscillatory shear flows", Journal of Rheology **39**, 697–712 (1995).

[302]K. Atalık et al., "On the occurrence of even harmonics in the shear stress response of viscoelastic fluids in large amplitude oscillatory shear", Journal of non-newtonian fluid mechanics **122**, 107–116 (2004).

[303]K. Horio et al., "Rheo-dielectric responses of entangled cis-polyisoprene under uniform steady shear and laos", Macromolecules **47**, 246–255 (2014).

[304]T. Uneyama et al., "A theoretical analysis of rheodielectric response of type-a polymer chains", Journal of Polymer Science Part B: Polymer Physics **47**, 1039–1057 (2009).

[305]J. Persello et al., "Flow of colloidal aqueous silica dispersions", Journal of Rheology **38**, 1845–1870 (1994).

[306]A. Kurokawa et al., "Avalanche-like fluidization of a non-brownian particle gel", Soft Matter **11**, 9026–9037 (2015).

[307]R. Verberg et al., "Viscosity of colloidal suspensions", Physical Review E **55**, 3143 (1997).

[308]M. C. Williams et al., "Three-constant oldroyd model for viscoelastic fluids", The Physics of Fluids **5**, 1126–1128 (1962).

[309]W. Gleissle et al., "Validity of the cox–merz rule for concentrated suspensions", Journal of rheology **47**, 897–910 (2003).

[310]S. Onogi et al., "Rheological properties of polymethyl methacrylate and polyvinyl acetate in the molten state", Kolloid-Zeitschrift und Zeitschrift für Polymere **222**, 110–124 (1968).

[311]T. Al-Hadithi et al., "The relationship between the linear (oscillatory) and nonlinear (steady-state) flow properties of a series of polymer and colloidal systems", Colloid and Polymer Science **270**, 40–46 (1992).

[312]W. .-. Kulicke et al., "Relation between steady shear flow and dynamic rheology", Rheologica Acta **19**, 601–605 (1980).

[313]D. Doraiswamy et al., "The cox–merz rule extended: a rheological model for concentrated suspensions and other materials with a yield stress", Journal of rheology **35**, 647–685 (1991).

[314]I. Krieger, "Correspondence: comments on a manuscript by doraiswamy et al.", Journal of Rheology **36**, 215–217 (1992).

[315]G. Ovarlez et al., "Flows of suspensions of particles in yield stress fluids", Journal of rheology **59**, 1449–1486 (2015).

[316]M. Das et al., "Shear induced tuning and memory effects in colloidal gels of rods and spheres", The Journal of Chemical Physics **157** (2022).

[317]I. Sudreau et al., "Residual stresses and shear-induced overaging in boehmite gels", Physical Review Materials **6**, L042601 (2022).

[318]I. Sudreau et al., "Shear-induced memory effects in boehmite gels", Journal of Rheology **66**, 91–104 (2022).

[319]N. Koumakis et al., "Tuning colloidal gels by shear", Soft Matter **11**, 4640–4648 (2015).

[320]L. Mohan et al., "Microscopic origin of internal stresses in jammed soft particle suspensions", Physical Review Letters **111**, 268301 (2013).

[321]L. Mohan et al., "Build-up and two-step relaxation of internal stress in jammed suspensions", Journal of Rheology **59**, 63–84 (2015).

[322]H. Vinutha et al., "Memory of shear flow in soft jammed materials", arXiv preprint arXiv:2312.00251 (2023).

[323]E. Moghimi et al., "Residual stresses in colloidal gels", Soft Matter **13**, 7824–7833 (2017).

[324]C. Y. Anthony et al., "Structural considerations for physical hydrogels based on polymer–nanoparticle interactions", Molecular Systems Design & Engineering **5**, 401–407 (2020).

[325]A. C. Yu et al., "Physical networks from entropy-driven non-covalent interactions", Nature communications **12**, 746 (2021).

[326]A. K. Grosskopf et al., "Gelation and yielding behavior of polymer–nanoparticle hydrogels", Journal of Polymer Science **59**, 2854–2866 (2021).

[327]Y. Xiao et al., "Development of high-retention water absorbent from cellulosic materials: water absorbent from bleached kraft pulp", J. Wood Sci. **47**, 394–399 (2001).

[328]H. Kono, "Characterization and properties of carboxymethyl cellulose hydrogels crosslinked by polyethylene glycol", Carbohydr. Polym. **106**, 84–93 (2014).

[329]C. Marliere et al., "How water retention in porous media with cellulose ethers works", Cem. Concr. Res. **42**, 1501–1512 (2012).

[330]H. Winter et al., "Rheology of polymers near liquid-solid transitions", Adv. Polym. Sci. **134**, 167–230 (1997).

[331]G. Dürig et al., "Sur la structure des solutions aqueuses de carboxymethylcellulose", Helvetica Chimica Acta **33**, 1106–1118 (1950).

[332]H. Cheng et al., "Rheology of carboxymethylcellulose made from bacterial cellulose", in Macromolecular symposia, Vol. 140, 1 (1999), pp. 145–153.

[333]S. Lim et al., "The effect of binders on the rheological properties and the microstructure formation of lithium-ion battery anode slurries", Journal of Power Sources **299**, 221–230 (2015).

[334]G. Beaucage et al., "Structural studies of complex systems using small-angle scattering: a unified guinier/power-law approach", J. Non-Cryst. Solids **172**, 797–805 (1994).

[335]D. Le Botlan et al., "Quantitative determination of bound water in wheat starch by time domain nmr spectroscopy", Carbohydr. Res. **308**, 29–36 (1998).

[336]D. Besghini et al., "Time-domain nmr elucidates fibril formation in methylcellulose hydrogels", Macromolecules (2023).

[337]D. Capitani et al., "Water in hydrogels. an nmr study of water/polymer interactions in weakly cross-linked chitosan networks", Macromolecules **34**, 4136–4144 (2001).

[338]M. Abrami et al., "Use of low field nmr for the characterization of gels and biological tissues", ADMET and DMPK **6**, 34–46 (2018).

[339]P. Y. Ghi et al., "H nmr study of the states of water in equilibrium poly (hema-co-thfma) hydrogels", Biomacromolecules **3**, 991–997 (2002).

[340]M. Abrami et al., "Physical characterization of alginate–pluronic f127 gel for endoluminal nabds delivery", Soft Matter **10**, 729–737 (2014).

[341]L. Leibler et al., "Dynamics of reversible networks", Macromolecules **24**, 4701–4707 (1991).

[342]G. P. Baeza et al., "Network dynamics in nanofilled polymers", Nat. Commun. **7**, 11368 (2016).

[343]S. Nian et al., "Dynamics of associative polymers with high density of reversible bonds", Phys. Rev. Lett. **130**, 228101 (2023).

[344]Y. S. Zhang et al., "Advances in engineering hydrogels", Science **356**, eaaf3627 (2017).

[345]E. Khare et al., "Transition-metal coordinate bonds for bioinspired macromolecules with tunable mechanical properties", Nat. Rev. Mater. **6**, 421–436 (2021).

[346]L. Jiang et al., "Magneto-responsive nanocomposites with a metal–ligand supramolecular matrix", Macromolecules **55**, 3936–3947 (2022).

[347]F. Zhuge et al., "Decoding the linear viscoelastic properties of model telechelic metallo-supramolecular polymers", Journal of Rheology **61**, 1245–1262 (2017).

[348]G. Cui et al., "Linear shear and nonlinear extensional rheology of unentangled supramolecular side-chain polymers", Journal of Rheology **62**, 1155–1174 (2018).

[349]A. Louhichi et al., "Humidity affects the viscoelastic properties of supramolecular living polymers", Journal of Rheology **61**, 1173–1182 (2017).

[350]L. Bouteiller, "Assembly via hydrogen bonds of low molar mass compounds into supramolecular polymers", Hydrogen bonded polymers, 79–112 (2007).

[351]A. Shabbir et al., "Nonlinear shear and uniaxial extensional rheology of polyether-ester-sulfonate copolymer ionomer melts", Journal of Rheology **61**, 1279–1289 (2017).

[352]Q. Chen et al., "Ionomer dynamics and the sticky rouse model", Journal of Rheology **57**, 1441–1462 (2013).

[353]W. Mei et al., "Anion chemical composition of poly (ethylene oxide)-based sulfonylimide and sulfonate lithium ionomers controls ion aggregation and conduction", Journal of Materials Chemistry C **10**, 14569–14579 (2022).

[354]D. C. Tuncaboylu et al., "Structure optimization of self-healing hydrogels formed via hydrophobic interactions", Polymer **53**, 5513–5522 (2012).

[355]J. Černỳ et al., "Non-covalent interactions in biomacromolecules", Phys. Chem. Chem. Phys. **9**, 5291–5303 (2007).

[356]W. Wang et al., "Bioinspired fabrication of high strength hydrogels from non-covalent interactions", Prog. Polym. Sci. **71**, 1–25 (2017).

[357]G. Legrand et al., "Acid-induced gelation of carboxymethylcellulose solutions", ACS Macro Letters **13**, 234–239 (2024).

[358]T. Liebert et al., "Microscopic visualization of nanostructures of cellulose derivatives", in Macromolecular symposia, Vol. 223, 1 (Wiley Online Library, 2005), pp. 253–266.

[359]G. Legrand et al., "Dual origin of viscoelasticity in polymer-carbon black hydrogels: a rheometry and electrical spectroscopy study", Macromolecules **56**, 2298–2308 (2023).

[360]T. Matsumoto et al., "Influence of added salt on dynamic viscoelasticity of carboxymethylcellulose aqueous systems", Polym. Eng. Sci. **28**, 393–402 (1988).

[361]C. G. Lopez et al., "Influence of divalent counterions on the solution rheology and supramolecular aggregation of carboxymethyl cellulose", Cellulose **26**, 1517–1534 (2019).

[362]M. Rubinstein et al., "Dynamics of entangled solutions of associating polymers", Macromolecules **34**, 1058–1068 (2001).

[363]Z. Xu et al., "Payne effect of carbon black filled natural rubber compounds and their carbon black gels", Polymer **185**, 121953 (2019).

[364]X. Fan et al., "Insight into the weak strain overshoot of carbon black filled natural rubber", Polymer **167**, 109–117 (2019).

[365]M. E. Helgeson et al., "Viscoelasticity and shear melting of colloidal star polymer glasses", J. Rheol. **51**, 297–316 (2007).

[366]V. Carrier et al., "Nonlinear rheology of colloidal glasses of soft thermosensitive microgel particles", J. Rheol. **53**, 245–273 (2009).

[367]N. Koumakis et al., "Direct comparison of the rheology of model hard and soft particle glasses", Soft Matter **8**, 4271–4284 (2012).

[368]K. S. Cho et al., "A geometrical interpretation of large amplitude oscillatory shear response", J. Rheol. **49**, 747–758 (2005).

[369]S. Manneville, "Recent experimental probes of shear banding", Rheol. Acta **47**, 301–318 (2008).

[370]B. Saint-Michel et al., "Local oscillatory rheology from echography", Phys. Rev. Appl. **5**, 034014 (2016).

[371]J. R. Lott et al., "Fibrillar structure in aqueous methylcellulose solutions and gels", Macromolecules **46**, 9760–9771 (2013).

[372]M. R. Bockstaller et al., "Block copolymer nanocomposites: perspectives for tailored functional materials", Advanced materials **17**, 1331–1349 (2005).

[373]J. Tianying et al., "Role of particle size and polymer length in rheology of colloid–polymer composites", (2012).